Selected climate mitigation and adaptation measures and their impact on the climate of the region of Hamburg

Dissertation

zur Erlangung des Doktorgrades

an der Fakultät für Mathematik, Informatik und Naturwissenschaften

Fachbereich Geowissenschaften

der Universität Hamburg

vorgelegt von

Marita Böttcher

aus Hamburg

Hamburg, 2017

Tag der Disputation: 1. November 2017

Folgende Gutachter empfehlen die Annahme der Dissertation:
Prof. Dr. K. Heinke Schlünzen
Prof. Dr. Bernd Leitl

Zusammenfassung

In dieser Arbeit wird der Einfluss ausgewählter Klimaschutz- und Klimaanpassungsmaßnahmen auf das Klima der Metropolregion Hamburg quantifiziert. Als Beispiel für Klimaschutzmaßnahmen sind große, hypothetische Windparks in der Deutschen Bucht ausgesucht und ihr Einfluss auf das regionale Klima mit Schwerpunkt auf die städtische Wärmeinsel (UHI) von Hamburg untersucht worden. Der Einfluss verschiedener Klimaanpassungsmaßnahmen wie Gründächer, höhere Albedo für z. B. Dächer, Straßen und Parkplätze sowie Änderungen der Bebauungsdichte auf meteorologische Größen ist ebenfalls untersucht worden. Drei sozioökonomische Szenarien werden betrachtet: Szenario s1 mit einer sinkenden Bevölkerungszahl und geringer Umsetzung von Klimaanpassungsmaßnahmen; Szenario s2 mit stagnierender Bevölkerungszahl und sporadischer Umsetzung von Klimaanpassungsmaßnahmen und Szenario s3, mit steigender Bevölkerungszahl und flächendeckender Umsetzung von Klimaanpassungsmaßnahmen. Szenario s3 zeigt den größten Einfluss auf das städtische Sommerklima und ist auch für die Wintermonate untersucht worden, um die Bewertung zu vervollständigen.

Der Einfluss von Klimaschutz- und Klimaanpassungsmaßnahmen ist unter Verwendung von statistischer-dynamischer Gitterverfeinerung untersucht worden. Der statistische Teil ist mit zwei statischen Methoden unter der Nutzung des Bewertungsindexes nach Perkins et al. (2007) und eines neu eingeführten bivariaten Bewertungsindexes durchgeführt worden. Der dynamische Teil der Gitterverfeinerung wurde mit dem numerischen Modell METRAS durchgeführt. Ein horizontal nicht-äquidistantes Gitter ist erfolgreich getestet und im Modell angewendet worden. Damit wird die Anzahl der nötigen Schritte für die Gitterverfeinerung von den Ergebnissen eines globalen Modells zu der nötigen hohen Auflösung dieser Studie reduziert. Im Rahmen dieser Arbeit ist METRAS um eine Parametrisierung für Windkraftanlagen erweitert worden, um den Einfluss von Windparks auf das Klima zu untersuchen. Zur Untersuchung der Klimaanpassungsmaßnahmen im Winter ist eine Parametrisierung der Effekte von schneebedecktem Boden auf die Wechselwirkungen zwischen Boden und Atmosphäre entwickelt worden.

Diese Studie zeigt, dass die Einführung großer Windparks in der Deutschen Bucht die klimatische mittlere Lufttemperatur für große Teile Norddeutschlands im Sommer leicht reduziert. Auch wenn die Temperatur im Klimamittel für Hamburg durch die Windparks leicht abnimmt, kommt es zu systematischen Änderungen der Wolkenbedeckung. Durch diese wird die mittlere starke UHI von Hamburg im Sommer verstärkt. Szenario s3 redu-

ziert den Einfluss der städtischen Gebiete von Hamburg auf die meteorologischen Größen in der Region und die UHI in den Sommermonaten. Die Änderungen durch die sozio-ökonomischen Szenarien s1 und s2 sind gering. Während der Wintermonate führt Szenario s3 zu leicht höheren Temperaturen und etwas verstärkter UHI im Winterklimamittel.

Abstract

In this thesis, the impact of selected climate mitigation and adaptation measures on the climate of the metropolitan region of Hamburg is quantified. Hypothetical large wind farms in the German Bight are selected as an example of possible climate mitigation measures. Their impact on the regional climate is assessed, with a focus on the urban heat island (UHI) of Hamburg during summer months. The impact of different climate adaptation measures like green roofs, increased albedo of structures such as roofs, streets and parking areas, and changes in building density is also considered, with an investigation of their effects on meteorological variables. Three socio-economic scenarios are considered: scenario s1, with a decreasing number of inhabitants and few adaptation measures; scenario s2, with a stagnant population and sporadic adaptation measures, and scenario s3, with a growing population, a compact city, and substantially implemented adaptation measures. Scenario s3 shows the highest impact on the urban summer climate and is investigated for the winter months as well to complete the assessment.

The methodology employed to assess the impact of the climate mitigation and adaptation measures is statistical-dynamical downscaling (SDD). The statistical part of the study is performed using two statistical methods: the skill score following Perkins et al. (2007) (SSP) and the newly developed bivariate skill score (BSS). The dynamical part of the downscaling is performed using the mesoscale model METRAS. A horizontal non-uniform grid is successfully tested and employed in the model. This reduces the number of necessary refinement steps for downscaling from global model results to the high horizontal grid resolution necessary for this study. In this study, METRAS is extended with a parametrisation for wind turbines to investigate the impact of wind farms on regional climate. For investigation in the influence of climate adaptation measures on winter climate, a parametrisation of the effects of snow-covered soil on the exchange between soil and atmosphere is developed.

The study shows that the introduction of large wind farms in the German Bight would induce a slight cooling to large areas of Northern Germany. While the climate mean summer temperature of Hamburg is reduced due to the wind farms, there are systematic changes in cloud cover. This increases the mean strong summer UHI of Hamburg. Scenario s3 reduces the effects of the urban areas of Hamburg on the meteorological variables in the region and on the UHI during summer months. The changes introduced by the other two socio-economic scenarios are small. During winter months, scenario s3 leads to slightly

higher temperatures and slightly increases the UHI in the winter climate average.

Table of Contents

List of Figures

List of Tables

1 Introduction

1.1 Motivation

Global climate change has been reported by the Intergovernmental Panel on Climate Change (IPCC) for the past (IPCC's Fifth Assessment Report (AR5), 2013). Climate mitigation and adaptation measures are applied to reduce the impact of global climate change. The metropolitan region of Hamburg (MRH) is affected by the global changes (Daschkeit, 2011). Taking into consideration the regional climate and climate change as well as Hamburg's growth and the influence of its local urban climate, climate mitigation and adaptation measures become important for both Hamburg and the metropolitan region. In this thesis, the impact of selected climate mitigation and adaptation measures on the climate of the metropolitan region of Hamburg is assessed.

1.2 Climate of the metropolitan region of Hamburg

The metropolitan region of Hamburg (MRH) is located in Northern Germany, roughly 100 km from the North Sea and the Baltic Sea. Situated in the westerlies, the main wind direction is from the West where maritime weather conditions are predominant (Daschkeit, 2011). Hamburg has a moderate climate with mild winters and warm summers and moist weather conditions (Kottek et al., 2006). The mean annual temperature at the weather station at the Hamburg airport (Fuhlsbüttel) was 9.0 °C in the climate period from 1971 to 2000 (Daschkeit, 2011; Riecke and Rosenhagen, 2010). The minimum and maximum monthly mean temperatures at Fuhlsbüttel are found in January and July with values of 1.3 °C and 17.4 °C, respectively, for the climate period from 1971 to 2000 (Daschkeit, 2011; Riecke and Rosenhagen, 2010).

Precipitation occurs in MRH the whole year round with slightly higher monthly mean precipitation in summer and winter than in spring and autumn. The maximum monthly mean precipitation of 77 mm/month occurs in June and the minimum monthly mean precipitation of 42 mm/month is in February. This is based on measurements at Fuhlsbüttel in the climate period from 1971 to 2000 (Daschkeit, 2011; Riecke and Rosenhagen, 2010). The mean annual precipitation at Fuhlsbüttel was 772 mm/year in the climate period from 1971 to 2000 (Daschkeit, 2011; Riecke and Rosenhagen, 2010).

In the frame of climate change, the weather conditions for the MRH will change to a warmer and wetter climate with a projected temperature increase for all seasons but especially for winter for the middle of the 21st century (Daschkeit, 2011; Rechid et al., 2014). In winter, the lowest temperatures are projected to increase most and therefore the probability density function (PDF) of the temperature is projected to get smaller (Rechid et al., 2014). Thus, the warming during winter months is projected to be realised by a decreasing number of cold days. For the other three seasons, temperatures will increase uniformly, with a slight tendency for a larger increase of higher temperatures in summer (Rechid et al., 2014).

The mean annual precipitation is projected to increase for the middle of the 21st century (Daschkeit, 2011; Rechid et al., 2014). The largest increase of mean seasonal precipitation is projected for autumn (September, October, November) while for summer (June, July, August) there is no clear signal, with some indication that the precipitation will remain the same or decrease (Rechid et al., 2014). In winter, the precipitation is projected to increase with a decrease of the number of days without precipitation (Rechid et al., 2014). In summer, the number of days without precipitation as well as the number of days with high precipitation are projected to increase (Rechid et al., 2014). Therefore, in summer the probability density function (PDF) of precipitation includes more high precipitation events and more periods of drought (Rechid et al., 2014). The changes in the regional climate are projected to be more intense by the end of the 21st century (Daschkeit, 2011; Rechid et al., 2014).

In the context of the given climate situation for the MRH, Hamburg additionally is a developing city with an increasing number of inhabitants during the last decades (statista, 2017a,b). Therefore, Hamburg has an increasing influence on the regional climate. The differences in the urban climate of a city and its rural surrounding are generated by urban structures and their different physical parameters compared to those of vegetation. Thereby, the buildings in a city affect the atmosphere by increasing the roughness length. This decreases the wind speed in average and affects all atmospheric processes depending on wind speed, e.g., the heat and moisture exchange between surfaces and the atmosphere or urban ventilation. The building structures have a larger amount of heat storage than the vegetation. This influences the surface energy budget and the heating of the atmosphere close to the surface. The influence also results from the albedo of building materials, which is larger for vegetation than for most urban structures. The large sealed areas in a city and less vegetation than in rural areas decrease the evaporation and the humidity in the city. The energy consumption of the citizens results in an anthropogenic heat release which directly increases the temperature in the urban areas compared to the temperature in a rural surrounding. Together, all these processes lead to a difference in the climate of urban and rural areas. Not only the temperature but also, e.g., the wind field, the relative humidity, the precipitation and the air quality are changed.

The current and future urban climate of Hamburg are well investigated with a special focus on the (summer) urban heat island (UHI). Schlünzen et al. (2010) investigated the long-term differences in temperature and precipitation for the MRH and differences in temperature between the city of Hamburg and the more rural suburbs for a shorter time. They calculated the UHI from the daily minimum temperatures for the inner city of Hamburg in the range of 2.5 K to 3 K for summer months and around 1.5 K for winter months. Some studies by Hoffmann et al. (2012), Hoffmann and Schlünzen (2013) and Hoffmann et al. (2016) employed statistical and statistical-dynamical downscaling to investigate the current and the future summer UHI of Hamburg. In Hoffmann et al. (2012), the cloud cover, the wind speed and the relative humidity are found to be important parameters to determine the UHI of Hamburg with a statistical model. The pattern for the current summer UHI, found by Hoffmann et al. (2016) utilising statistical-dynamical downscaling, agrees well with the UHI pattern found by Bechtel and Schmidt (2011) using floristic mapping data as proxy for the temperature. Hoffmann and Schlünzen (2013) and Hoffmann et al. (2016) found no coherent patterns of changes in the future UHI signal.

1.3 Impact of adaptation and mitigation measures

The target of climate adaptation measures is in the best case to balance the impacts of climate change or, at least to reduce them. Reducing the UHI of Hamburg may compensate the increasing temperatures due to global climate change for the city, even if the regional temperatures increase. This can be achieved by climate adaptation measures that reduce the differences in the urban and rural climate. In addition, the physical parameters of urban areas may be modified in a way that human comfort in the urban areas is increased.

In the literature the effect of establishing green spaces in the urban areas is well investigated. Numerical simulations showed that small changes in land use result in large impacts on the latent and sensible heat fluxes and also on to the temperature (Klink and Willmott, 1994; Gill et al., 2007). The influence of green spaces is affected by their arrangement (Honjo and Takakura, 1991). Honjo and Takakura (1991) and Spronken-Smith and Oke (1998) showed that a park in an urban area generates a temperature reduction in an area with the same dimensions as the generating park. The impacts of several small green areas superimpose to produce one large impact with a periodic amplitude (Honjo and Takakura, 1991). This impact is best developed if the downwind distance between the two green areas and has the same dimension as the green areas themselves. The largest impact of green areas is achieved from a wide and irrigated park in a warm and dry climate (Bowler et al., 2010). Due to the large impact of evaporation, the irrigation of the green areas is very important (Spronken-Smith and Oke, 1998). Measurements showed a cooling effect of green areas of the magnitude of 1 K to 2 K in a fetch up to 1000 m (Taha, 1997; Ca et al., 1998; Spronken-Smith and Oke, 1998; Spronken-Smith et al., 2000; Yu and Hien, 2006; Hamdi and Schayes, 2008; Bowler et al., 2010). In some extreme cases a cooling in the range of 8 K is measured (Spronken-Smith and Oke, 1998). The results show the importance of the irrigated green areas. For Hamburg this implies that the water from precipitation should be stored for watering of green areas during a summer drought. This method additionally buffers the rain water run-off from a heavy precipitation event and therefore unloads the rain water sewer network.

Another well investigated climate adaptation measure is the use of building materials with a higher albedo which means a higher reflectivity of the incoming short wave radiation. Thus, the surface energy balance is modified and the surface temperature and the sensible heat flux are reduced. The influence of different building materials is investigated by Takebayashi and Moriyama (2012). They found a reduction of the surface sensible heat flux up to 150 W/m^2, depending on the albedo of the building material. The impact of roofs with a higher albedo was investigated in the regional scale by Georgescu et al. (2013, 2014) and in the global scale by Jacobson and Ten Hoeve (2012). Georgescu et al. (2013) and Georgescu et al. (2014) found a cooling for the regional areas with roofs with high albedo as did Jacobson and Ten Hoeve (2012) for regional areas too. However, Jacobson and Ten Hoeve (2012) found a global warming of 0.07 K. Georgescu et al. (2014) showed that the largest cooling is found for a combination of roofs with high albedo and green roofs.

Due to climate change, mitigation measures like the use of renewable energy become more important. The use of wind energy is mentioned as most important because of the small CO_2 footprint, the efficiency of the technology and the availability of wind power during day and night. Thereby, offshore wind farms, especially in shelf seas in North-West Europe like the North Sea, are preferred because of the higher wind speeds over open water than over land. The wind farms extract and convert kinetic energy from the wind to electricity. Therefore, wind farms are a sink of energy for the atmosphere. The atmosphere smooths the selective energy loss by mixing with the surroundings. Thus, the impact of a wind farms gets distributed. Large wind farms impact a large area, as found by Keith et al. (2004); Wang and Prinn (2010); Christiansen and Hasager (2005). In a very extreme case, global atmospheric motion may be affected (Miller et al., 2011). Due to the location of Hamburg eastward from the North Sea and with prevailing winds from the West, the MRH may by influenced by large offshore wind farms in the North Sea.

1.4 Research questions

In this thesis, the impacts of different mitigation and adaptation measures on the climate of the Metropolregion Hamburg are investigated. Most of the adaptation measures are on a very local scale, e.g., parks or green roofs. The mitigation measures concern large offshore wind farms having a horizontal dimension of several kilometres to some tens of kilometres with each wind turbine having a horizontal dimension of only a few ten meters. Therefore, the scale of both the adaptation and the mitigation measures, are small compared to the horizontal grid resolution of a global or regional model. Thus, a refinement in horizontal grid size from regional climate model results is necessary to assess the impact of the mitigation and adaptation measures. In this thesis, the refinement is realised by statistical-dynamical downscaling. The methods used are described in Chapter 2. In Chapter 3 the influence of large offshore wind farms in the North Sea as a mitigation measure is investigated. The impact of different climate adaptation measures on the summer and winter climate of Hamburg is assessed in Chapter 4 and Chapter 5. The conclusions are given in Chapter 6, where the four questions that follow are discussed:

1. Does the statistical method sufficiently represent the climate of Hamburg?
2. Do climate mitigation measures like wind farms have an impact on the urban summer climate of Hamburg?

3. Are climate adaptation measures able to keep the future urban summer climate of Hamburg in a range where human comfort is achievable?

4. How do climate mitigation and adaptation measures act on the urban winter climate of Hamburg?

Chapter 3 of this thesis has already been published (Boettcher et al., 2015) and Chapter 4 is intended for publication for urban climate journal. Chapter 5 is in preparation for publication. For a better reading of this thesis, the abstracts of the publications are left out and the appendices, the acknowledgements and the references are summarised at the end of this thesis. Cross references to publications that are chapters of this thesis are replaced by using the chapter numbers.

2 Methods applied

Climate is defined as the statistics of weather conditions at a given point, usually considering 30 years. Global climate simulations for the past and the future conditions are often realised over 100 years and more. These global circulation models (GCMs) usually have a horizontal grid resolution of several tens of kilometres. With these grid resolutions, regional aspects like differences in urban structures or local effects of adaptation measures can hardly be represented. For studies dealing with local effects, the regional climate has to be simulated with a much higher horizontal grid resolution. For simulating urban structures, a horizontal grid resolution of a few hundred meters is on demand.

Three methods to simulate the regional climate are described, e.g., by HOFFMANN (2012): dynamical downscaling, statistical downscaling and statistical-dynamical downscaling. The direct simulation of 30 years' climate using dynamical downscaling from GCM results with a high resolution model often needs several downscaling steps to satisfy the nudging approach (HOFFMANN, 2012). Also, simulations using a high horizontal resolution need smaller time steps than models with a coarser resolution, caused by the physics and numerics used. Thus, dynamical downscaling of climate simulations with a high resolution model are very expensive in computational time and money (HOFFMANN, 2012). However, their advantage are consistent meteorological data (HOFFMANN, 2012).

For applying statistical downscaling for localising GCM results, mathematical relationships between GCM results and observational data are formulated for each variable (HOFFMANN, 2012). The computational costs are low but formulating the relationships is mathematically complex and many observational data are needed. The formulations are often physically inconsistent (HOFFMANN, 2012).

One method to combine the advantages of these two downscaling methods is statistical-dynamical downscaling (SDD) (HOFFMANN, 2012). Starting from the results of the GCMs, statistical methods are applied to determine the important weather situations for the climate period of interest. The important weather situations will be simulated with the regional model and the results will be statistically recombined to represent the climate of interest with a high resolution. The computational costs are lower than in the case of dynamical downscaling and the results are physically consistent (HOFFMANN, 2012).

The statistical methods to estimate the important weather situations depend on the target values. Hoffmann and Schlünzen (2013) developed a weather pattern classification to simulate the mean strong summer urban heat island of Hamburg with SDD using the mesoscale transport and stream model of the atmosphere (METRAS) without considering the statistics of the other meteorological variables.

Starting from the method of Hoffmann and Schlünzen (2013), two more universal approaches for calculating the statistics of the meteorological variables are developed and applied along with SDD in this thesis. The dynamical simulations of the important weather situations found by these methods are performed with the numerical model METRAS (Section 2.1). The data used for forcing the simulations and those used for the evaluation and for the statistical methods are described in Section 2.2. The statistical methods applied are given in Section 2.3.

2.1 General characteristics of the applied model METRAS

In this thesis, the numerical model METRAS is used. METRAS is a non-hydrostatic mesoscale transport and stream model of the atmosphere. The model employes momentum, mass and energy conservation and solves equations for momentum, temperature, water vapour and cloud and rain water in three dimensions in terrain-following coordinates. METRAS solves the equations in flux form on an Arakawa-C grid. The equations are Reynolds averaged and approximated for use in the mesocale by using the anelastic assumption and the Boussinesq approximation. Sub-grid scale surface cover effects are considered using a variable number of surface cover classes (SCCs) for each grid cell. The surface fluxes are calculated with the flux aggregation method. In the application of METRAS for this thesis, the Coriolis force is kept constant.

The adaptation measures investigated in this thesis are implemented by changing the SCCs in the model input. The SCCs have different characteristics. They specifically differ in values used for albedo, thermal conductivity and diffusivity, soil water availability, saturation value for soil water content and roughness length. In the following sections, the parametrisations are described with the help of selected equations. Further numerical methods and adjustments of METRAS used for the different applications in this thesis are described in Section 3.2.1, Section 4.2.1 and Section 5.2. A subset of SCCs and their corresponding parameters used with METRAS are given in Section 4.3.1.

The six parameters for each SCC are included in the model in different equations. The SCCs are denoted by an index j in the following. The albedo, α_j, is considered in the calculation of the short wave radiation budget (Section 2.1.1), the roughness length, $z_{0,j}$, in the calculation of the turbulent surface fluxes (Section 2.1.2), the soil water availability, $\alpha_{q,j}$, and the saturation value for soil water content, $W_{k,j}$, in the budget equation of soil moisture (Section 2.1.3) and the thermal conductivity, ν_j, and diffusivity, k_j, in the calculation of the surface temperature (Section 2.1.4).

2.1.1 Parametrisation of atmospheric short wave radiation

The short wave radiation budget is calculated with two different parametrisations in METRAS, depending on the cloudiness (Schlünzen et al., 2012). For a cloudless sky, only at the surface the short wave radiation balance is calculated. Then the net short wave radiation budget at the surface for each SCC, $SW_{net,j}$, is given by Equation (2.1).

$$SW_{net,j} = \mu_j \, I_\infty \, \cos\left(Z(t)\right) \tag{2.1}$$

The incoming solar radiation is given as $I_\infty = 1370$ W/m^2. The parameter μ_j depends on the albedo, α_j, the elevation angle of the sun and the turbidity of the air. Following Golchert (1981), μ_j is defined by Equation (2.2) for a cloudless sky for Northern Germany. The zenith angle of the sun $Z(t)$ is calculated with respect to the geographical latitude of the model area, the time, t, and thus the hour angle, the declination from the day of the year and the slope of the surface.

$$\mu_j = 0.75 \; (1 - \alpha_j) \tag{2.2}$$

In case of cloud development somewhere in the model area, the radiation fluxes are calculated with a two-stream approximation scheme (Bakan, 1994; Schlünzen et al., 2012). The incoming solar radiation flux, E, is calculated from Equation (2.3) with the transmission factors for Rayleigh scattering, T_E, absorption by water vapour, T_V, absorption and scattering by aerosols, T_D, and liquid water, T_L. Equation (2.3) is integrated from the top to the bottom of the atmosphere. Equation (2.3) is calculated twice, for the visible range 1 of solar radiation (wave length < 0.75 μm) and for the near infrared range

2 (wave length > 0.75 μm). The solar constants, E_0, for both ranges are given by E_{01} = 707 W/m^2 and E_{02} = 660 W/m^2. f_A is a function of the albedo and is set to one in METRAS.

$$E = E_0\, T_E\, T_V\, T_D\, T_L\, f_A\, \cos\left(Z(t)\right) \tag{2.3}$$

The reflected solar radiation flux, A, from the surface to the atmosphere is also calculated from Equation (2.3) but integrated from the bottom to the top of the atmosphere. The reflected solar radiation flux is again reflected by the atmosphere and parts of it are redirected towards the surface. To avoid an iterative solution of the incoming and reflected solar radiation fluxes, the fluxes are merged by adding a correction term weighted with the quotient of the fluxes. Then the net solar radiation flux, S, of a layer is calculated from the fluxes at the corresponding layer with Equation (2.4). E_1 and E_2 denote the incoming solar radiation fluxes for the visible and the near infrared range 1 and 2, respectively and A_1 and A_2 for the reflected radiation fluxes in the ranges 1 and 2, respectively.

$$S = E_1 + E_2 - A_1 - A_2 \tag{2.4}$$

With the net solar radiation flux of a layer, given by Equation (2.4), the net short wave radiation budget at the surface is calculated for each SCCs (Equation 2.5). The albedo for each SCC is applied by Equation (2.5) where f_j is the fraction of the SCC in the individual grid cell.

$$SW_{net,j} = \frac{\sum\limits_j (1-\alpha_j)\, S}{\sum\limits_j (1-\alpha_j)\, f_j} \tag{2.5}$$

2.1.2 Surface fluxes and flux aggregation method

The roughness length, $z_{0,j}$, of the different SCCs is considered in the calculation of the surface fluxes of momentum, heat and moisture. With the flux aggregation method, the momentum flux, M, the sensible heat flux, H, and the latent heat fluxes, L, are given by Equation (2.6) to Equation (2.8). The air density of the basic state at the surface is denoted by $\rho_{0,surf}$, the specific heat capacity of dry air at constant pressure by c_p and the latent heat of evaporation of water by l_{21}.

$$M = -\rho_{0,surf}\, u_\star^2 \tag{2.6}$$
$$H = -c_p\, \rho_{0,surf}\, u_\star\, \theta_\star \tag{2.7}$$
$$L = -l_{21}\, \rho_{0,surf}\, u_\star\, q_\star \tag{2.8}$$

In the flux aggregation method, the scaling values for momentum, heat and moisture, $u_\star$, $\theta_\star$ and $q_\star$, respectively, are calculated from the sub-grid scale surface fluxes of the individual SCCs with Equation (2.9) to Equation (2.11).

$$u_\star = \sqrt{\sum_j f_j\, u_{\star,j}^2} \tag{2.9}$$
$$\theta_\star = \frac{1}{u_\star} \sum_j (f_j\, u_{\star,j}\, \theta_{\star,j}) \tag{2.10}$$
$$q_\star = \frac{1}{u_\star} \sum_j (f_j\, u_{\star,j}\, q_{\star,j}) \tag{2.11}$$

The scaling values of the sub-grid scale surface fluxes, $u_{\star,j}$, $\theta_{\star,j}$ and $q_{\star,j}$, are defined by Equation (2.12) to Equation (2.14).

$$u_{\star,j} = \sqrt{\hat{C}_{m,j}}\, V(z_{k=1}) \tag{2.12}$$
$$\theta_{\star,j} = \frac{\hat{C}_{\theta,j}}{\sqrt{\hat{C}_{m,j}}}\, (\theta(z_{k=1}) - \theta_{S,j}) \tag{2.13}$$
$$q_{\star,j} = \frac{\hat{C}_{q,j}}{\sqrt{\hat{C}_{m,j}}}\, (q_1^1(z_{k=1}) - q_{1S,j}^1) \tag{2.14}$$

The magnitude of the horizontal wind speed in the lowest layer is denoted by $V(z_{k=1})$ and the potential temperature in the lowest layer by $\theta(z_{k=1})$. $\theta_{S,j}$ denotes the potential surface temperature for each SCCs. The specific humidity in the lowest layer and at the surface are denoted by $q_1^1(z_{k=1})$ and $q_{1S,j}^1$, respectively. The near-surface effective transfer coefficients of momentum, heat and moisture, $\hat{C}_{m,j}$ and $\hat{C}_{\chi,j}$, where χ may one of θ and q, $\hat{C}_{\theta,j}$ and $\hat{C}_{q,j}$, are given by Equation (2.15) and Equation (2.16).

$$\hat{C}_{m,j} = \frac{\kappa^2}{\left[\ln\left(\frac{l_b}{z_{0,j}}\right)\frac{\ln(z_{k=1}/z_0)}{\ln(l_b/z_0)} - \psi_m\left(\frac{z_{k=1}}{L_{MO,j}}\right)\right]^2} \tag{2.15}$$

$$\hat{C}_{\chi,j} = \frac{\kappa^2}{\left[\ln\left(\frac{l_b}{z_{0,j}}\right)\frac{\ln(z_{k=1}/z_0)}{\ln(l_b/z_0)} - \psi_m\left(\frac{z_{k=1}}{L_{MO,j}}\right)\right]\left[\ln\left(\frac{l_b}{z_{0\chi,j}}\right)\frac{\ln(z_{k=1}/z_{0\chi})}{\ln(l_b/z_{0\chi})} - \psi_h\left(\frac{z_{k=1}}{L_{MO,j}}\right)\right]} \tag{2.16}$$

The near-surface effective transfer coefficients of momentum, heat and moisture are functions of the blending height, l_b, and the stability functions for momentum and heat, ψ_m and ψ_h, respectively. The stability functions depend on the Monin-Obukhov-Length for each SCC, $L_{MO,j}$. The von Karman constant is given by $\kappa = 0.4$. The effective roughness length, z_0, is given by Equation (2.17).

$$\frac{1}{\left(\ln\frac{l_b}{z_0}\right)^2} = \sum_j \frac{f_j}{\left(\ln\frac{l_b}{z_{0,j}}\right)^2} \tag{2.17}$$

The sub-grid scale effective roughness lengths of heat and moisture, $z_{0\theta,j}$ and $z_{0q,j}$, depend on the surface type of the individual SCCs. For surface types not defined as water or urban and for the mean roughness lengths for heat and moisture, $z_{0\theta}$ and z_{0q}, the effective roughness lengths are calculated using Equation (2.18).

$$\frac{z_0}{z_{0\chi}} = 10 \tag{2.18}$$

The roughness length of momentum for water areas depends on the wind speed. In METRAS, the roughness length of momentum for water areas is calculated following

CLARKE (1970) with Equation (2.19).

$$z_{0,water} = \max \begin{cases} 0.0185\, u_\star^2/g \\ \min \begin{cases} 7 \cdot 10^{-5}\ \mathrm{m} \\ \max \begin{cases} 0.032\, u_\star^2/g \\ 1.5 \cdot 10^{-5}\ \mathrm{m} \end{cases} \end{cases} \end{cases} \tag{2.19}$$

The water and urban areas are treated as hydrodynamically rough surfaces. For water the roughness lengths of temperature and moisture are calculated following BRUTSAERT (1975, 1982) from Equation (2.20) and Equation (2.21). For urban surfaces, the roughness length of temperature and moisture are calculated following KANDA et al. (2007) from Equation (2.22) and Equation (2.23).

$$\frac{z_0}{z_{0\theta,water}} = \max \begin{cases} \dfrac{z_0}{442413} \\ \dfrac{z_0}{\exp\left(\kappa\left(7.3 Re_\star^{0.25}\sqrt{0.71} - 5\right)\right)} \end{cases} \tag{2.20}$$

$$\frac{z_0}{z_{0q,water}} = \max \begin{cases} \dfrac{z_0}{442413} \\ \dfrac{z_0}{\exp\left(\kappa\left(7.3 Re_\star^{0.25}\sqrt{0.6} - 5\right)\right)} \end{cases} \tag{2.21}$$

$$\frac{z_0}{z_{0\theta,urban}} = \max \begin{cases} \dfrac{z_0}{442413} \\ \dfrac{z_0}{\exp\left(\kappa\left(3.83 Re_\star^{0.25}\sqrt{0.71} - 5\right)\right)} \end{cases} \tag{2.22}$$

$$\frac{z_0}{z_{0q,urban}} = \max \begin{cases} \dfrac{z_0}{442413} \\ \dfrac{z_0}{\exp\left(\kappa\left(3.83 Re_\star^{0.25}\sqrt{0.6} - 5\right)\right)} \end{cases} \tag{2.23}$$

The roughness Reynoldsnumber, $Re_\star$, is given by Equation (2.24).

$$Re_\star = \frac{u_\star z_0}{\nu} \tag{2.24}$$

2.1.3 Soil moisture budget

In METRAS, the budget equation of soil moisture follows Deardorff (1978) and considers the soil water availability, $\alpha_{q,j}$, and the saturation value for the soil water content, $W_{k,j}$. The humidity at the surface for each SCC is calculated from Equation (2.25) with the saturation value of the humidity at the surface equal to $q^1_{1sat,j}$. Humidity at the surface is restricted to the range given in Equation (2.26).

$$q^1_{1S,j} = \alpha_{q,j}\, q^1_{1sat,j}\,(T_{S,j}) + (1 - \alpha_{q,j})\, q^1_1(z_{k=1}) \tag{2.25}$$

$$0 \leq q^1_{1S,j} \leq q^1_{1sat,j}\,(T_{S,j}) \tag{2.26}$$

The soil water availability, $\alpha_{q,j}$, is calculated from a prognostic equation (Equation 2.27) with the density of water, $\rho_{water} = 1000$ kg/m^3, and the precipitation, P (in kg/m^2). The soil water availability is between zero and one (Equation 2.28).

$$\frac{\partial \alpha_{q,j}}{\partial t} = \frac{-\dfrac{L_j}{l_{21}} + P}{\rho_{water}\, W_{k,j}} \tag{2.27}$$

$$0 \leq \alpha_{q,j} \leq 1 \tag{2.28}$$

2.1.4 Surface temperature and force-restore method

The thermal conductivity, ν_j, and diffusivity, k_j, of soil merged with vegetation (one layer approach) are considered in the calculation of the surface temperature in METRAS. The surface temperature is calculated with the force-restore method from the surface energy balance following Bhumralkar (1975) and Deardorff (1978) for each SCC separately. The surface energy balance of each SCC is given by Equation (2.29) whereas the heat flux to the soil at the surface for each SCC, $G_{S,j}$, is given by Equation (2.30) and F_j denotes the anthropogenic heat emission for each surface cover class.

$$SW_{net,j} + LW_{net,j} + H_j + L_j + G_{S,j} + F_j = 0 \tag{2.29}$$

$$G_{S,j} = -\nu_j \left(\frac{\partial T_{S,j}}{\partial z} \right)_S \tag{2.30}$$

The sensible heat flux and the latent heat flux for each SCC are denoted by H_j and L_j, respectively. The net long wave radiation flux, $LW_{net,j}$, can be calculated with a two-stream approximation scheme (Bakan, 1994; Schlünzen et al., 2012) or more simply for a cloudless sky from the Stefan-Boltzmann-Law (Equation 2.31) with the parameter $\epsilon = 0.22$ and the Stefan-Boltzmann-constant, $\sigma = 5.67\ 10^{-8}\ W/m^2K^4$.

$$LW_{net,j} = -\epsilon\sigma T_{S,j}^4 \tag{2.31}$$

For solving Equation (2.30), a horizontal homogeneous surface within each SCC is assumed. Therefore, a one-dimensional sinusoidal wave is applicable as a solution for a diurnal cycle (Bhumralkar, 1975). Then, the heat flux to the soil at the surface is given by Equation (2.32) where h_j is the depth of the daily temperature wave and T_h the temperature in the depth h_j.

$$G_{S,j} = \frac{\nu_j \sqrt{\pi}}{h_j} \left(\frac{h_j^2}{4\pi k_j} \frac{\partial T_{S,j}}{\partial t} + T_{S,j}(t) - T_h \right) \tag{2.32}$$

The heat conduction to the soil layer with the depth, D_j (Equation 2.34), is given by Equation (2.33) in the depth $D_j/2$.

$$\frac{\partial T_{S,j}(t)}{\partial t} = k_j \frac{\partial^2 T}{\partial z^2} = -\frac{k_j}{\nu_j} \left[\frac{G_{S,j}(0,t) - G_{S,j}(h_j,t)}{\frac{D_j}{2}} \right] \tag{2.33}$$

The heat fluxes to the soil in Equation (2.33) are given by Equation (2.29) and Equation (2.32). With Equation (2.34), Equation (2.33) results in Equation (2.35).

$$D_j = \frac{h_j}{2\sqrt{\pi}} \tag{2.34}$$

$$\frac{\partial T_{S,j}(t)}{\partial t} = \frac{2\sqrt{\pi}k_j}{h_j \nu_j}\left(-G_{S,j}\left(0,t\right) - \frac{\nu_j\sqrt{\pi}}{h_j}\left(T_{S,j}(t) - T_h\right)\right) \tag{2.35}$$

2.2 Data used

The important weather situations found by the statistical methods are dynamically downscaled with METRAS, with the ECMWF analysis data used for meteorological forcing (Section 3.2.4, Section 4.2.2 and Section 5.2.3.3). The data and their preprocessing are described in Section 2.2.1. The sea surface temperatures and the deep soil temperatures used in METRAS are from the NOAA Optimum Interpolation Sea Surface Temperatures V2 (NOAA OISSTs) dataset (Section 2.2.2). The statistics of the meteorological variables use observational data from weather stations in Germany and The Netherlands to be independent from the ECMWF analysis data used for forcing, even if the method allows use of the same data. The observational data are provided by the German Meteorological Service (Deutscher Wetterdienst) (DWD) and are used for evaluating the model simulations forced by the ECMWF analysis data. They are described in Section 2.2.3.

2.2.1 ECMWF analysis data

The forcing of the meteorological variables is realised in a nudging towards realistic weather situations using ECMWF analysis data (ECMWF, 2009, 2010). ECMWF analysis data have a horizontal resolution of about 25 km before 26$^{\text{th}}$ January 2010 and afterwards about 16 km. ECMWF analysis data of before 1$^{\text{st}}$ February 2006 are not employed because the horizontal grid size is coarser than 25 km. The evaluation period considered in this thesis ends on 31$^{\text{st}}$ December 2010. The statistical method for combined meteorological parameter (Section 2.3.2) is introduced to consider non-liner relationships between meteorological variables. Due to climate change, the non-liner relationships between meteorological variables may change. Therefore, ECMWF analysis data after the end of the evaluation period considered in this thesis are excluded from the data pool.

METRAS uses ECMWF analysis data for temperature, horizontal wind components, specific humidity, cloud water and rain water. The variables are given at pressure levels by ECMWF. For use in METRAS, these data are interpolated to the terrain following coordinates and the Arakawa-C grid.

In the simulations discussed in Chapter 3 and Chapter 4, the cloud water and rain water taken from ECMWF analysis data are added to the specific humidity values used to force METRAS as it is done by Hoffmann (2012). This shall allow for small-scale cloud developments. For the simulations discussed in Chapter 5, the cloud and rain water from ECMWF analysis data are forced to the cloud water content in METRAS as suggested by Schoetter (2013). In these simulations, pressure tendencies at the upper model boundary are prescribed for an improved capture of mesoscale phenomena (Schoetter, 2013).

For simulating winter months with snow cover and snow cover-related processes (Chapter 5), additional information about the snow cover is needed. The snow water equivalent, the snow density and the snow albedo are taken from the ECMWF analysis data. These values are given as surface values and are horizontally interpolated to the METRAS grid at surface level. No vertical correction is included despite differences in surface altitude. The data are provided as initial data of METRAS. During the model integration, METRAS calculates the new values from the initial data dependent on the actual meteorological situation (Chapter 5).

The values of snow water content, snow density and snow albedo are given once for each grid cell in the ECMWF model. Therefore, these initial values are prescribed to all SCCs in a grid cell in METRAS, even if METRAS calculates the values for each SCC separately. The values of snow water equivalent are adopted to METRAS after a check for missing values in the preprocessing. The same process is applied for the snow albedo values because the threshold values in the ECMWF model and in METRAS are the same, with a minimum albedo of 0.50 and a maximum albedo of 0.85. The snow density values from the ECMWF model have the same threshold values as in METRAS until the 26th January 2010, with a minimum and a maximum of 100 kg/m^3 and 300 kg/m^3, respectively. After 26th January 2010, the threshold values in the ECMWF model change to 50 kg/m^3 and 450 kg/m^3, respectively. In that case, the values from ECMWF analysis data are set to the limits used in METRAS during preprocessing. This introduces errors in the snow hight calculated from the snow water equivalent and the snow density but keeps the thermal parameters of snow in the range where the model is tested for. If snow water equivalent data are missing, the value is set to zero in METRAS. In case of missing snow albedo or density of snow, the values in METRAS are set to fresh snow with maximum albedo and minimum density of snow. An example of initial data used in METRAS is given in Appendix A.

2.2.2 NOAA OISST data

The sea surface temperatures used in METRAS are taken from the NOAA OISSTs (Reynolds et al., 2002, 2007). The NOAA OISSTs are accessible in two different versions. The weekly averaged NOAA OISSTs have a horizontally grid resolution of one degree while the daily averaged NOAA OISSTs have a horizontal grid resolution of a quarter of a degree. The simulations discussed in Chapter 3 and Chapter 4 are performed with data from the weekly NOAA OISSTs following Hoffmann (2012) while the simulations discussed in Chapter 5 apply the daily NOAA OISSTs following Schoetter (2013).

The average of each weekly NOAA OISSTs is centred on Wednesday. The analyses are performed for all ocean areas and the Great Lakes. The weekly NOAA OISSTs values over land are filled by a Cressman interpolation (Reynolds et al., 2002). For use in METRAS, the weekly NOAA OISSTs are horizontally interpolated to the METRAS grid. For inland water bodies and the deep soil temperature of landmass (Section 2.1.4), the NOAA OISSTs are adjusted for the local altitude as suggested by Bungert (2008).

The daily NOAA OISSTs (Reynolds et al., 2007) are provided only for water areas. For use in METRAS, the averaged water temperatures for the North Sea, the Baltic Sea and the Mediterranean Sea are interpolated over the continent from ocean grid cells near Cuxhaven, Fehmarn, Genoa and Venice as applied by Schoetter (2013) following Bungert (2008). For the land areas, the temperatures are calculated from the three averaged water temperatures, weighted by the distance between the individual land area and each water area (Schoetter, 2013). The daily NOAA OISSTs are horizontally interpolated to the METRAS grid. Furthermore, the temperatures for inland water bodies and the temperature T_h in the depth h_j for soil are adjusted for the local altitude in METRAS.

The simulations using the weekly NOAA OISSTs apply the NOAA OISST data which cover at least two days of simulation period. For the simulations performed with the daily NOAA OISSTs, the NOAA OISST data from the first day of simulation period are applied for the whole period.

2.2.3 DWD observational data

In this thesis, observational data from the German Meteorological Service (Deutscher Wetterdienst) (DWD) are used to develop the statistical method used for downscaling (Section 2.3). The observational data from the DWD are considered for a 30-year time period (1981 to 2010). The dataset includes hourly data of wind speed, wind direction, temperature and relative humidity.

In the Diploma thesis of Martens (2012), 27 weather stations in Northern Germany and the Netherlands were found to have a high rate of sampled data. These 27 weather stations are located in the METRAS model domain used in this thesis. Therefore, the data from these weather stations are used for assessment. Two of the weather stations are located in The Netherlands; the other 25 weather stations are located in Germany (Figure 2.1). A list of the weather stations and their corresponding World Meteorological Organization (WMO) number is given in Appendix B. The quality check for the data is performed following the method developed by Martens (2012).

In order to estimate the differences in the climate statistics between the whole year and the separate seasons, the time series are split into seasons. The spring months are March, April and May (MAM), the summer months are June, July and August (JJA), the autumn months are September, October and November (SON) and the winter months are December, January and February (DJF).

2.3 Statistical methods for determining relevant meteorological situations

The two statistical methods used in this thesis consider the probability density functions PDFs of different meteorological variables. A univariate skill score following Perkins et al. (2007) is applied to assess the differences between the PDFs of the climate time series and the PDFs from a smaller dataset of some important weather situations. Additionally, a bivariate skill score is developed that accounts for the relationship between two

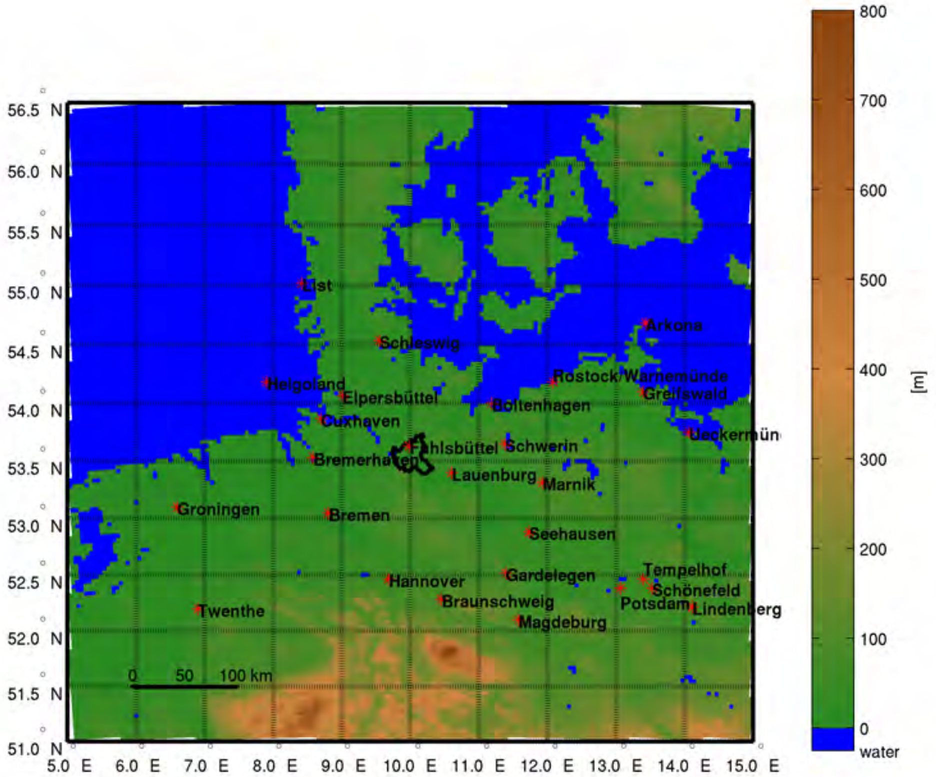

Figure 2.1: Meteorological stations used for statistical analysis of the 30-year time series. Hamburg is located in the centre and marked with a black line.

meteorological variables, e.g., the possible dependency of the relative humidity on wind direction. Both methods are applied with observational data from the DWD but are also applicable to other datasets, e.g., GCM results.

2.3.1 Method for single meteorological parameters

The reliable representation of the climate statistics of meteorological variables and therefore the shape of the PDFs of several meteorological variables is important for assessing the impact of climate mitigation and adaptation measures on the local climate. Perkins et al. (2007) developed a skill score to assess the similarity between two PDFs for one meteorological variable using an easy statistical method that assesses an entire PDF, not only restricted aspects of it. In this thesis, this skill score following Perkins et al. (2007) (SSP) is used for comparison between the PDF of the full dataset of a variable from a

30 year time series with the PDF from a reduced dataset of the same variable from the same time series. The minima of both PDFs for each corresponding bin are summed. The result is the intersection area of both PDFs. If SSP is equal to one, both PDFs agree perfectly and if it is equal zero there is no intersection. If n is the number of bins and Z_{M_i} and Z_{O_i} are the bins of both PDFs, the SSP is given by Equation (2.36) (Perkins et al., 2007). Following their study, a good agreement is an SSP > 0.8 while an SSP $= 0.9$ marks a near-perfect agreement.

$$\mathrm{SSP} = \sum_{i=1}^{n} \mathrm{minimum}(Z_{M_i}, Z_{O_i}) \tag{2.36}$$

The PDFs for the meteorology data described in Section 2.2.3 are analysed with the SSP. The PDFs are defined with 1 K bins for temperature in degree Celsius (TC), 1 m/s bins for wind speed (FF), 5 % bins for relative humidity (RH) and 30° bins for wind direction (DD). The wind direction from the North is used as the first bin with a range of ±15°.

The SSP is resampled with bootstrapping a thousand times for each of the considered 27 weather stations in Northern Germany and The Netherlands (Figure 2.1). The full datasets are used for temperature, relative humidity, wind speed and wind direction to calculate the SSPs of 30 randomly chosen years with the same size of datasets as the full datasets out of the full 30-years datasets. Out of it, the mean SSP is calculated for each variable from all resamples of all weather stations. This mean SSP defines the possible level of accuracy (LOA) and gives a measure of the consistency, robustness and completeness of the time series. The analysis is done for the whole year as well as separately for the seasons. The resulting LOAs are given in Table 2.1. The LOAs are at least 0.97; they are close to one for the whole year as well as for the separate seasons. Thus, following the demand of an SSP > 0.9 for a near-perfect agreement by Perkins et al. (2007), the assessed time series agree very well and robust against the test. The testing of a reduced dataset against the full dataset therefore should achieve a high SSP. The LOA is the value that can be reached with a reduced dataset.

The dependency of the SSPs on the size of the reduced dataset is tested with bootstrapping based on data for randomly chosen full days. For each number of days between one and 300, the SSPs for each variable are resampled for each weather station a thousand times. In Figure 2.2 and Figure 2.3, the mean SSP for each weather station and all variables is shown for the whole year against the number of days per resample. Same figures are given per season in Appendix C. For a low number of days, the SSP is very low. With an increasing number of days, the SSP increases as an asymptotic solution against the LOA. The averaged SSP over all weather stations does not reach the LOA even when 300 randomly chosen days are selected.

The asymptotic solution of the SSPs converges differently against the LOAs for different variables. The LOAs of the wind speed (FF) are the highest for the whole year and each season and the convergence is strongest (Table 2.1, Figure 2.2 and Figure 2.3). Thus, the lowest number of days for reaching the assessment criteria of a good and a near-perfect agreement is needed for wind speed (Table 2.2 and Table 2.3). The increase of the SSP dependent on the number of days is lowest for temperature (TC) (Table 2.1, Figure 2.2 and Figure 2.3); therefore, more days are required to fit the assessment criteria (Table 2.2 and Table 2.3). The behaviour of the LOAs of the relative humidity is similar to the behaviour of the LOAs of wind speed, while the LOAs of wind direction behave similarly to the LOAs of temperature.

Good agreements for the SSPs can be reached with a low numbers of randomly chosen days (Table 2.2). Only four randomly chosen days are required to fit well the PDF for wind speed in the summer months while 24 randomly chosen days (the highest number) are required to fit the PDF of temperature for the whole year. To reach a near-perfect agreement more randomly chosen days are required (Table 2.3). Again, the PDFs for wind speed in summer months and temperature for the whole year provide the extrema, requiring 15 and 93 randomly chosen days.

The number of randomly chosen days needed for SDD is determined by analysis of the convergence and the assessment criteria results. As shown in Table 2.3 and discussed in Section 3.2.4, 40 randomly chosen days fit the near-perfect agreement for the summer months (JJA). Figure C.3 and Figure C.4 show that a further increase of the number of randomly chosen days higher than 40 days will only slightly increase the SSPs.

Weather stations with more maritime climate conditions are marked with blue colours in Figure 2.2, Figure 2.3 and Appendix C while weather stations with more continental climate are marked with red colours. The SSP dependency on the number of randomly chosen days reflect for some variables differences between maritime and continental climate. For the temperatures of the continental weather stations, a higher median SSP is reached with a lower number of randomly chosen days than for the weather stations with more maritime climate (Figure 2.2, Figure 2.3 and Appendix C). The range of the SSPs,

Table 2.1: Level of accuracy (LOA) for the SSPs of 30 years of data per season and for full years.

SSP	LOA TC	LOA RH	LOA FF	LOA DD
MAM	0.98	0.98	0.99	0.98
JJA	0.98	0.98	0.99	0.98
SON	0.97	0.98	0.99	0.98
DJF	0.97	0.98	0.98	0.97
year	0.98	0.98	0.99	0.99

Table 2.2: Minimum number of days needed to reach a good agreement (SSP $>$ 0.8).

SSP	TC	RH	FF	DD
MAM	14	6	5	12
JJA	8	5	4	10
SON	17	6	6	13
DJF	21	7	8	15
year	24	7	6	13

Table 2.3: Minimum number of days needed to reach a near-perfect agreement (SSP $\geq$ 0.9).

SSP	TC	RH	FF	DD
MAM	55	24	19	46
JJA	32	19	15	38
SON	66	22	22	48
DJF	81	26	28	54
year	93	26	22	48

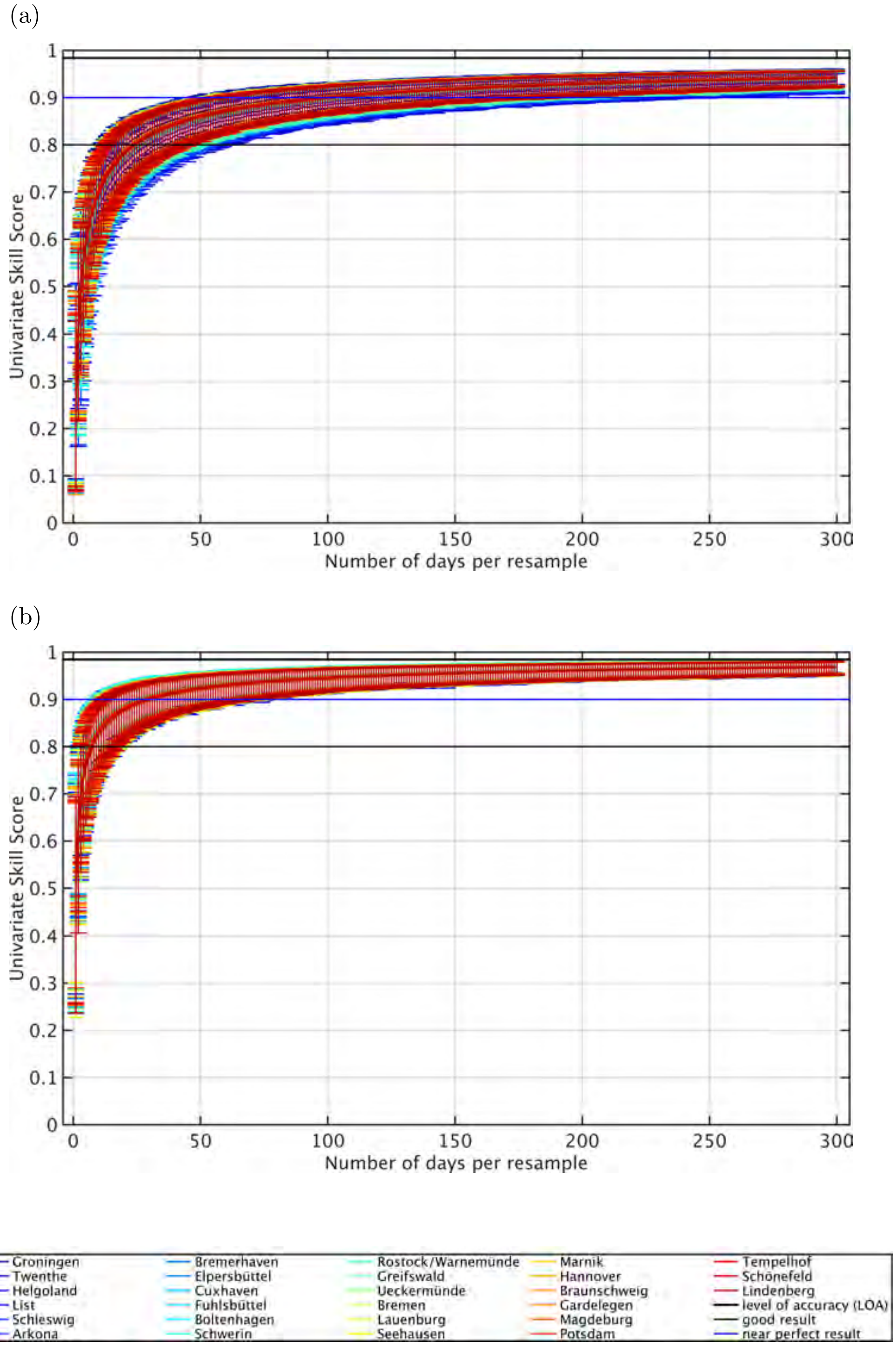

Figure 2.2: Mean of the skill score following Perkins et al. (2007) (SSP) for the whole year for (a) TC and (b) RH for each weather station with its 5th and 95th percentile shown by horizontal bars as a function of the number of randomly chosen days. The thick black line marks the level of accuracy (LOA); the thin black (blue) line marks the good (near-perfect) agreement.

(a)

(b)

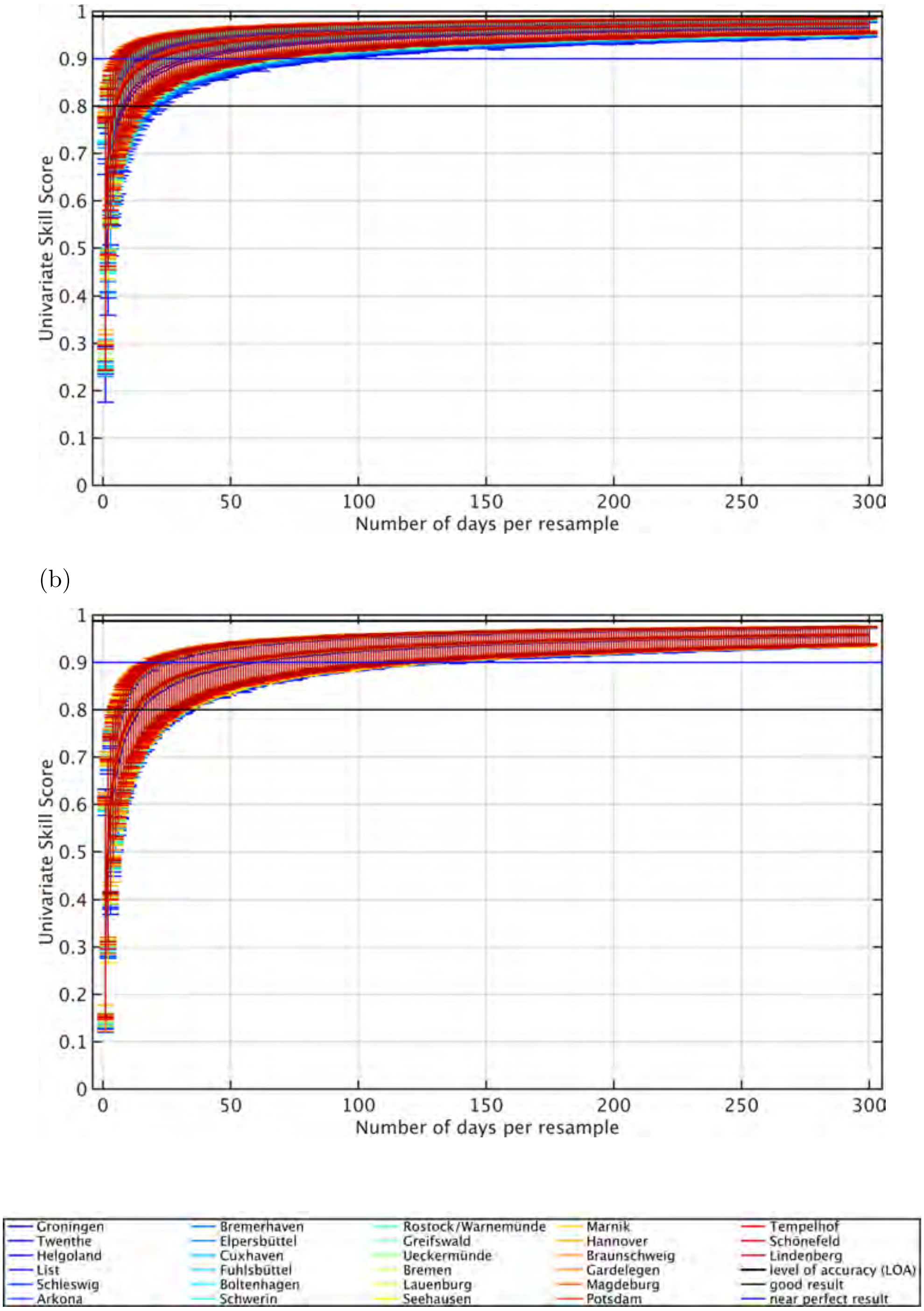

Figure 2.3: Same as Figure 2.2 but for (a) FF and (b) DD.

from the 5^{th} to the 95^{th} percentiles, is smaller for the continental weather stations and the diurnal cycle of these stations is more intensely developed (Figure 2.2, Figure 2.3 and Appendix C). Thus, fewer days are needed to represent the full temperature range. This effect is larger than the differences in temperatures from meteorological situations.

For relative humidity, the SSPs for more maritime weather stations are higher than for more continental weather stations for a given number of days per resample. The relative humidity at the maritime weather stations is strongly impacted from the humidity supply from the water surfaces. Therefore, the PDFs can be constructed using a lower number of days. For wind speed and wind direction, no such dependencies are found.

As well as the SSP convergence criteria discussed above, the number of days required to simulate the climate with SDD depends on the climate scale to be simulated as well as the season and the dependency of the meteorological variable. This means that the meteorological variables considered must be selected for the particular application.

2.3.2 Method for combined meteorological parameters

The above assessment of PDF's agreement focused on single and independent meteorological variables. Climate adaptation measures, however, often affect more than one meteorological variable. For example, urban greening by irrigated parks or irrigated green roofs increases the evaporation in urban areas. Thus, heat energy is used for evaporation and the temperature (TC) decreases. The evaporation is only possible for water vapour pressure below saturation. The saturation vapour pressure of water in the atmosphere increases exponentially with temperature. Therefore, the evaporation rate and also the cooling effect of urban greening is strongly linked to the relative humidity (RH) at a given temperature and is a non-linear effect. Consequentially, it is important to capture the distribution of the relative humidity and the corresponding temperature at the time with the statistical method. Relationships like the one between TC and RH and similar ones between other meteorological variables need to be taken into account in the formulation of the SSP. The newly developed bivariate skill score (BSS) accounts for combined variables.

The calculation of the bivariate skill score (BSS) is based on two two-dimensional probability density functions (2D-PDFs), Z_M and Z_O. For one of these 2D-PDFs, the PDF of the first variable, e.g., temperature, is calculated. For each bin of the first PDF, the PDFs of the values of the second variable at corresponding time, e.g. relative humidity, are calculated. The BSS is defined as sum of the corresponding minima of two 2D-PDFs (Equation 2.37). The number of bins for each dimension is given with n and m and $Z_{M_{ik}}$ and $Z_{O_{ik}}$ are the bins of the 2D-PDFs. Both 2D-PDFs agree perfectly if the BSS is equal to one and have no intersection if the BSS is equal to zero.

$$\mathrm{BSS} = \sum_{i=1}^{m} \sum_{k=1}^{n} \mathrm{minimum}(Z_{M_{ik}}, Z_{O_{ik}}) \tag{2.37}$$

The data described in Section 2.2.3 are analysed with the BSS. The 2D-PDFs are built with the same bin size as the PDFs for the SSPs: 1 K bins for temperature, 1 m/s bins for wind speed, 5 % bins for relative humidity and 30° bins for wind direction with the first bin for a wind direction from 345° to 15°.

Just as for the SSP, the LOA of the BSS is a measure of the consistency, robustness and completeness of the dataset investigated. The LOAs are calculated as the mean from bootstrapping a thousand resamples of the BSSs foreach of the 27 weather stations used and each combination of the meteorological variables from the full dataset. This is done for the 30-year time series as well as for each season (Table 2.4). The LOAs of the BSSs have values of 0.94 to 0.98. These are lower than the LOAs of the single variable (Table 2.1), since the BSSs are built from combinations of two non-identical PDFs. However, the results of the LOAs based on the BSSs are still high and the datasets are consistent and robust against the test. Nevertheless, the assessment criteria have been adapted to the lower consistency of the data against the same dataset. To do this, the assessment criteria given by Perkins et al. (2007) are multiplied by the LOAs derived here from the analysed time series. The assessment criteria needed to reach a good agreement are given in Table 2.5 while the BSSs needed to reach a near-perfect agreement are given in Table 2.6 for the 30-year time series and separate seasons for all combinations of meteorological variables.

The dependency of the BSSs on the size of the reduced dataset is tested with bootstrapping of a thousand resamples for each number of randomly chosen days between one and 300 from the full dataset. The mean from bootstrapping, built for each variable at each weather station for a whole year, is shown against the number of days per resample in Figure 2.4 and Figure 2.5. The figures are given per seasons in Appendix D. The BSSs from bootstrapping are asymptotic solutions and converge against the LOAs but do not reach the LOAs within 300 days. The convergence is strongest for the BSS values of RH/FF

Table 2.4: Level of accuracy (LOA) for the BSSs for 30 years of data per season and for full years.

BSS	LOA TC/FF	LOA TC/RH	LOA RH/FF	LOA DD/TC	LOA DD/FF	LOA DD/RH
MAM	0.96	0.95	0.97	0.95	0.97	0.96
JJA	0.96	0.96	0.97	0.96	0.97	0.96
SON	0.95	0.95	0.96	0.94	0.96	0.96
DJF	0.95	0.94	0.96	0.94	0.95	0.96
year	0.97	0.96	0.98	0.96	0.98	0.98

(Figure 2.4c). This is the combination of the two meteorological variables that have the strongest convergence in SSPs. The BSS of both variables with the weakest convergence in SSPs, wind direction and temperature, increases less than all other combination with increasing number of randomly chosen days (Figure 2.5c). This different behaviour in the convergence results in different numbers of days needed to reach the assessment criteria (Table 2.7 and Table 2.8). The minimum numbers of randomly chosen days needed to reach a good (Table 2.7) and a near-perfect (Table 2.8) agreement are much larger than the numbers found for the single variables (Table 2.2 and Table 2.3).

The convergence of the BSSs against the LOAs (Figure 2.4, Figure 2.5 and Appendix D) again shows a different behaviour for weather stations with more maritime (marked with blue) and more continental (marked with red) climates. All BSSs built by a combination of wind speed with another meteorological variable require a higher number of days per resample for a more maritime weather station than for a weather station with more continental climate to meet the assessment criteria. The range of these BSSs given from the 5th to the 95th percentile from bootstrapping is larger for weather stations with more maritime climate. The effect is largest during autumn and winter months and results from the larger variability of wind speed near the coast during these months.

The range of the BSSs of temperature and relative humidity is expanded towards higher values for the weather stations with more maritime climate. This is in agreement with the result of the SSPs for relative humidity but in contrast to the result of the SSPs for temperature. For the BSSs of wind direction combined with temperature or relative humidity, respectively, no such dependencies are found.

Table 2.5: Minimum BSS needed to reach a good agreement.

BSS	TC/FF	TC/RH	RH/FF	DD/TC	DD/FF	DD/RH
MAM	0.77	0.76	0.78	0.76	0.78	0.77
JJA	0.77	0.77	0.78	0.77	0.78	0.77
SON	0.76	0.76	0.77	0.75	0.77	0.77
DJF	0.76	0.75	0.77	0.75	0.76	0.77
year	0.78	0.77	0.78	0.77	0.78	0.78

Table 2.6: Minimum BSS needed to reach a near-perfect agreement.

BSS	TC/FF	TC/RH	RH/FF	DD/TC	DD/FF	DD/RH
MAM	0.86	0.86	0.87	0.86	0.87	0.86
JJA	0.86	0.86	0.87	0.86	0.87	0.86
SON	0.86	0.86	0.86	0.85	0.86	0.86
DJF	0.86	0.85	0.86	0.85	0.86	0.86
year	0.87	0.86	0.88	0.86	0.88	0.88

Table 2.7: Minimum number of days needed to reach a good agreement for BSS.

BSS	TC/FF	TC/RH	RH/FF	DD/TC	DD/FF	DD/RH
MAM	57	71	33	81	38	40
JJA	36	45	26	55	29	34
SON	58	65	26	82	36	36
DJF	64	63	31	79	41	39
year	95	106	34	132	41	45

Table 2.8: Minimum number of days to reach a near-perfect agreement for BSS.

BSS	TC/FF	TC/RH	RH/FF	DD/TC	DD/FF	DD/RH
MAM	159	215	95	242	109	108
JJA	99	124	77	148	82	91
SON	178	196	73	233	98	96
DJF	196	182	86	225	120	107
year	281	296	116	>300	137	150

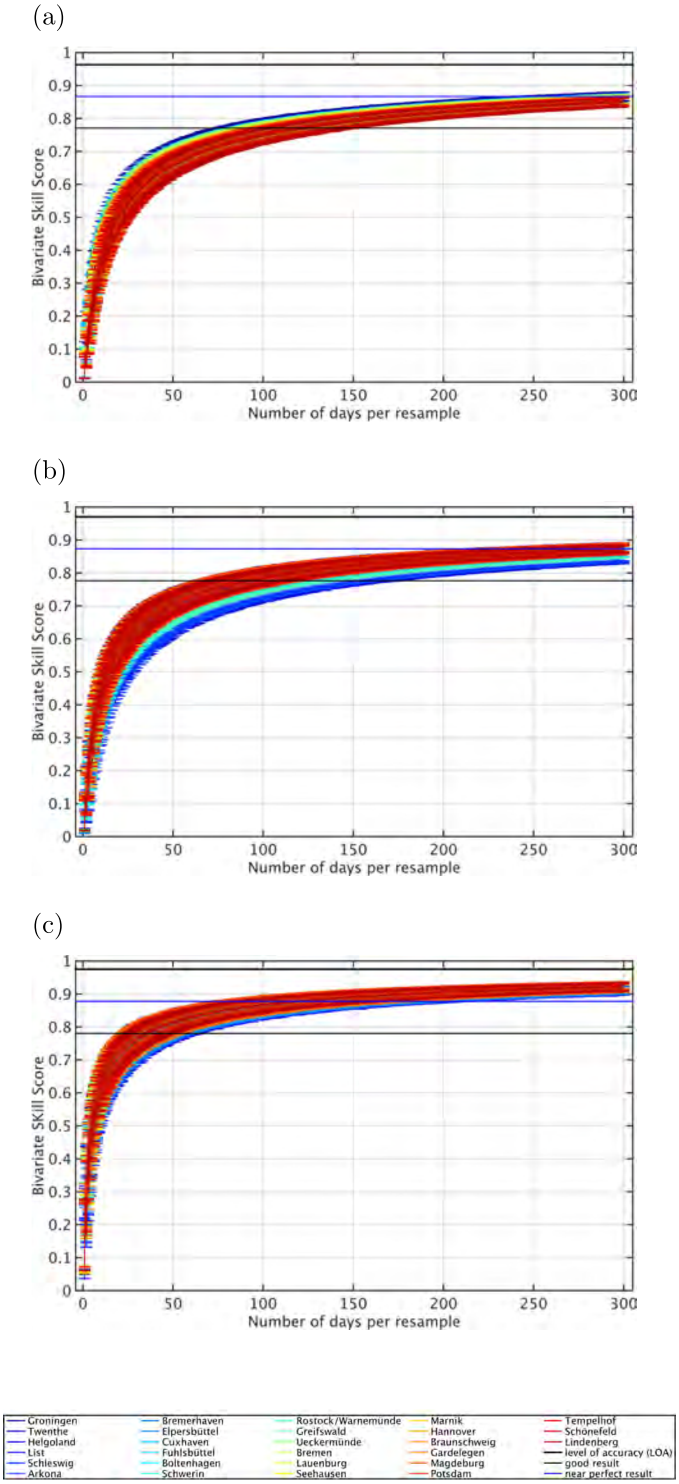

Figure 2.4: Mean of the bivariate skill score (BSS) for the 30 years of data for (a) TC/RH, (b) TC/FF and (c) RH/FF for each weather station with its 5th and 95th percentile shown by horizontal bars as a function of the number of randomly chosen days per resample.

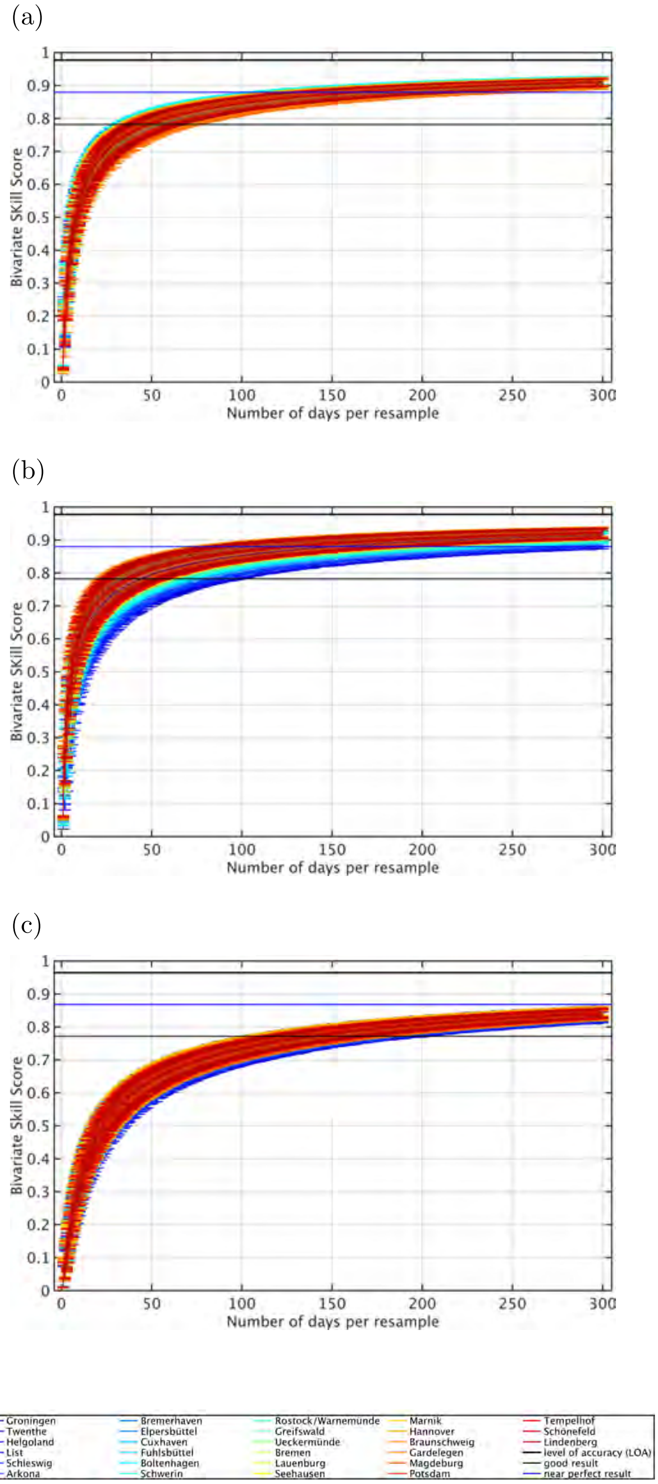

Figure 2.5: Same as Figure 2.4 but for (a) DD/RH, (b) DD/FF and (c) DD/TC.

The results from the statistical tests of the agreement of 2D-PDFs from a reduced dataset against the 2D-PDFs of the full dataset show dependencies in four influencing factors: the variables itself. If the amplitude of the reduced dataset is small compared to the amplitude in the full dataset, a larger reduced dataset is needed to rebuild the statistics of the full dataset. The second influencing factor is the period investigated. An annual cycle of a meteorological variable needs more data to rebuilt the statistics than a season. The strength of this effect depends on the meteorological variable and is most developed for temperature. The third influencing factor is the size of the investigated dataset. A small dataset will probably be less consistent and robust against the BSS than a large dataset. Therefore, the assessment of the size of the reduced dataset has to be handled with care. The fourth influencing factor is the geographic location of the area investigated. More maritime or more continental climate as well as location in, e.g., the trade wind zone or prevailing westerlies influences the number of data of the reduced dataset needed to rebuild the full dataset.

In the present thesis, the BSS is calculated to assess the effectiveness of different climate mitigation and adaptation measures for individual seasons in Chapter 4 and Chapter 5. Results for individual applications are given in the separate chapters.

3 Influence of large offshore wind farms on the North German summer climate

Preface

This chapter has been published by Boettcher, M., P. Hoffmann, H.-J. Lenhart, K. H. Schlünzen, R. Schoetter, 2015: Influence of large offshore wind farms on North German Climate. Meteorologische Zeitschrift, DOI: 10.1127/metz/2015/0652.

For this thesis, the abstract has been left out and the references and acknowledgements are summarised at the end of the thesis. The Appendix of the original publication is given in Appendix E.

The reference simulations for this study have been prepared and executed by Peter Hoffmann. Input for wind farm data were provided by Hermann-J. Lenhart. K. Heinke Schlünzen and Robert Schoetter were involved in discussing simulations.

3.1 Introduction

Wind turbines become more and more important to generate electricity since their CO_2 footprint is small. They extract kinetic energy from the flow and convert it into electric energy. The wind speed is thereby reduced in the wake of a wind turbine and turbulence is increased. The single wakes of several wind turbines in a wind farm interact and cause a large single wake for one wind farm through superposition. The length of the wake depends on the atmospheric stability and therefore the temperature profile, the ambient turbulence and the surface roughness, because these quantities affect the vertical mixing (Emeis, 2010). The smooth surface and reduced atmospheric turbulence around offshore wind farms lead to a wake which is in neutral cases about three times longer than for onshore wind farms (Emeis, 2010). Analyses of wakes resulting from wind farms located in the North Sea and the Baltic Sea show a measurable downwind influence on the wind field up to distances of several tens of kilometres (Christiansen and Hasager, 2005). For onshore wind farms, Fitch et al. (2013) found a 10 % deficit in wind speed 60 km downwind of the wind farms during nighttime.

The reduced wind speed and the associated wind shear in the wake induces atmospheric mixing. As a result, air from aloft is entrained increasing the lower wind speed in the wake. Due to the turbulent exchange, the area of reduced wind speed is vertically extended. This leads to lower wind speeds in levels well above the wind farm (Baidya Roy et al., 2004). Furthermore, the dynamic pressure in front of each rotor leads to an increase of the wind speed below the rotor, close to the surface (Baidya Roy et al., 2004). Through this, the vertical mixing is increased and this also affects the surface fluxes and mixes the vertical temperature profile (Baidya Roy and Traiteur, 2010). Because of these effects on the vertical exchange, a multitude of very large wind farms is able to change the global mean temperature as found from global model simulations whereby a cooling is found for offshore and a warming for onshore installations (Wang and Prinn, 2010). Regional changes generated by such very large wind farms can be in the order of up to ± 2 K (Keith et al., 2004). In addition, the global distribution of rainfall and clouds may be changed (Wang and Prinn, 2010). In very extreme cases with energy extraction in the range of terawatts, the global atmospheric motion can be affected and may result in global climate effects (Miller et al., 2011).

In the present study, the impact of large offshore wind farms in the German Bight on regional summer climate is investigated using the meteorological model METRAS. The changes in the climate caused by the proposed wind farms are determined for North-Western Germany and with respect to Hamburg. Hamburg is located in the centre of the model domain (Figure 3.1).

Hamburg has a maritime climate with moderately warm and moist weather conditions. With climate change, a warmer climate can be expected (Daschkeit, 2011). Therefore, adaptation measures for reduction of heat stress and the urban heat island become more important also for Hamburg. Schlünzen et al. (2010) showed that the urban heat island of Hamburg is most relevant during the summer months, and it will probably not change in future climate (Hoffmann and Schlünzen, 2013) if the urban morphology is not changed. The present study investigates, if one of the possible CO_2 mitigation measures, namely energy production by offshore wind farms in the German Bight, impacts the summer climate of Hamburg. As a consequence of the changed flow field over the German Bight, changes in the development of mesoscale meteorological systems such as the land sea breeze or the track of a cyclone may be possible. This may cause changes not only in the wake of the wind farms up to a distance of several tens of kilometres downwind, but also in a much larger area up to several hundreds of kilometres. In the focus of the

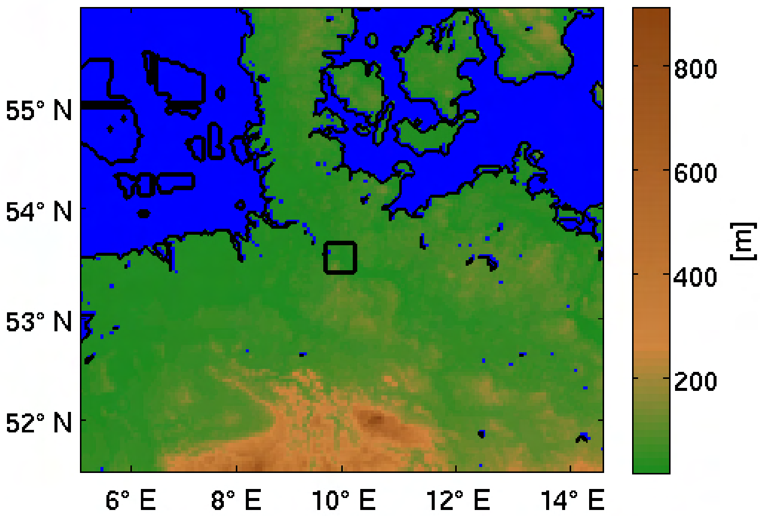

Figure 3.1: Orography of the model domain. Hamburg is located in the domain centre and marked with a black frame. The wind farms in the German Bight are also outlined with black frames and located in the North-West quadrant of the model domain.

current study is if the urban climate of Hamburg, a city situated about 100 kilometres inland from the coast, could be influenced by the wind farms in the German Bight.

To represent the climatological mean, simulations of typical weather situations are performed and the results are averaged. The methods, data and model used in the present study are described in Section 3.2. The results are discussed in Section 3.3. Conclusions are drawn in Section 3.4.

3.2 Methods and data

In the present study, different weather situations are simulated using the numerical mesoscale model METRAS (Section 3.2.1). The model is extended to account for wind farm effects (Section 3.2.2). The model domain and wind farm data are described in Section 3.2.3. The weather situations are the same as introduced in the weather pattern classification of Hoffmann and Schlünzen (2013). A statistical skill score is used in the present study to determine, if the climatological frequency distributions of the selected meteorological variables are represented (Section 3.2.4) and thus the selected cases do indeed represent climatological data of the summer. Section 3.2.5 shows that the simulated sensible and latent heat fluxes resemble the measurements of the fluxes in the German Bight.

3.2.1 Mesoscale atmospheric model METRAS

METRAS (Schlünzen, 1990; Schlünzen et al., 2012) is a non-hydrostatic, three-dimensional, numerical model of the atmosphere, used in the present study to determine the influence of large offshore wind farms on meteorology. The relevant model characteristics are shortly summarised below.

The basic equations for momentum, temperature and humidity are solved in flux form on a terrain following Arakawa-C grid. The equations are Reynolds averaged, and the anelastic and the Boussinesq approximations are used (Schlünzen, 1990). The turbulent fluxes resulting from Reynolds averaging are parametrised with a first order closure. The turbulent exchange coefficients are calculated with a mixing length approach for stable stratification and consider a counter gradient term for unstable stratification (Lüpkes and Schlünzen, 1996). The momentum advection is solved using the Adams-Bashfort scheme with second order central differences in space. A seven point filter is used to smooth the short waves resulting from this numerical scheme. The advection of scalars is solved with a first order upstream scheme. Depending on the time step needed for the different processes in the model, the vertical diffusion is solved either explicit or with the semi-implicit Crank-Nicholson scheme. For taking account of sub-grid scale surface cover effects, each grid cell may include up to ten surface cover classes. A flux aggregation method is used to determine the vertical fluxes close to the surface (Von Salzen et al., 1996). Due to the 4 km horizontal grid resolution used in this study, sub-grid scale surface cover effects and the connected surface fluxes are important. Therefore, the flux aggregation method is used in the hole domain, also in the urban areas, instead of the coupled urban parametrisation scheme (building effect parametrisation) (BEP) (Grawe et al., 2013). The different surface cover classes differ in albedo, thermal diffusivity, thermal conductivity, water availability, water saturation values and roughness lengths; typical initial values are given in Schlünzen and Katzfey (2003).

For the present simulations, METRAS is forced with ECMWF analysis data (ECMWF, 2009, 2010) using the nudging approach. Simulations with initialisation date after 26$^{\text{th}}$ January 2010 are nudged with 16 km resolution data, before with 25 km resolution data.

Nudging is done at the lateral boundaries. The variables that are nudged are the horizontal wind components, the temperature and the humidity. A nudging term is added to these equations. The nudging term is larger at the lateral boundaries and decreases towards the inner model domain. It becomes nearly zero five grid cells away from the lateral boundaries.

Cloud water and rain water are not forced, but the ECMWF data of these are added to the specific humidity values at the lateral boundaries to allow for smaller scale cloud developments in the nudged model METRAS. At the surface, the budget equations for temperature and humidity are solved. For the wind components a no slip condition is applied. The falling of rain water is explicitly calculated (including evaporation). Rain at the first grid level is assumed to reach the ground. Clouds close to the ground are also assumed to reach the ground. At the model top, the horizontal wind components are nudged while the vertical wind component is set to zero. For the other variables mentioned before, zero gradient boundary conditions are applied.

The water temperatures are prescribed from the NOAA Optimum Interpolation Sea Surface Temperature V2 (Reynolds et al., 2002) and interpolated to the METRAS grid. The water temperatures are corrected for the local altitude to determine the water temperature for inland water bodies. For the soil temperatures, the same values are taken. Initial surface temperatures are taken and interpolated from ECMWF analysis data (ECMWF, 2009, 2010).

The three-dimensional version of METRAS employs a balanced basic state profile that is consistent with the averaged profile of the ECMWF analysis data. This basic state is also the initial profile and extended to the whole model domain assuming horizontal homogeneity. The diastrophy method with orography growing is used (Pielke, 1984). Within the first 1.5 hours of integration intense nudging imposes the heterogeneous large scale situation. The initialisation phase takes about 3 hours to ensure a heterogeneous meteorology consistent with the forcing data.

The model simulations start for 2000 local time (LT) of the initialisation day. The first update of the forcing data takes place 4 hours later. After that, the forcing data are updated every six hours. Between two updating times, forcing data are linearly interpolated (Schlünzen et al., 2011). The model is integrated for a period of three days and four hours for each simulation.

METRAS has successfully been applied to the German Bight and the northern part of Germany before (Schlünzen, 1990, 1997; Schlünzen et al., 1997; von Salzen and Schlünzen, 1999; Meyer and Schlünzen, 2011). The model applied here has been extended with the actuator disc concept to represent the effects of wind turbines.

3.2.2 Parametrisation of wind turbines

Wind turbines are not resolved in mesoscale models but its effects are parametrised. Several approaches to consider the impact of wind turbines in atmospheric models are discussed in the literature. High resolution models designed for wind turbine load and interactions between wind turbines use an explicit consideration of the forces acting on the rotor (Fitch et al., 2012; Gross, 2010) while regional and global models with a coarse resolution parametrise wind farms trough enlarged roughness length (Keith et al., 2004; Fitch et al., 2012; Wang and Prinn, 2010). An intermediate parametrisation between these two approaches is to consider wind turbines or wind farms by a sink of kinetic energy, done by an additional term to the momentum equations (El Kasmi and Masson, 2008; Fitch et al., 2012, 2013; Linde, 2011). In this parametrisation, the effects of wind turbines and wind farms are modelled at hub hight, which permit a flow around the wind turbines and wind farms. Hence, the parametrisation is more realistic than the roughness length approach but less computational expensive than explicit consideration of the forces. The intermediate parametrisation is used for this study. The parametrisation is realised with the actuator disc concept (ADC). In the ADC, a wind turbine rotor is described as an infinitesimal thin disc with the size and position of the rotor. Betz published in 1926 the concept based on the conservation law for momentum and mass for a laminar and frictionless flow (Hau, 2002; Molly, 1978). This concept is used here.

Figure 3.2 shows a schematic diagram of the ADC. The kinetic energy of the air depends on the velocity. Far upwind of a wind turbine, the air flow is not influenced by the wind turbine and has the mean speed v_1. Due to the extraction of kinetic energy, the mean flow speed v_2 downwind of a wind turbine is reduced. The wind speeds v_1 and v_2 are averaged for the rotor parallel areas A_1 and A_2 up- and downwind of the rotor (area A'). The pressure in front of the rotor increases because of the wind speed reduction. The parallel streamlines of the laminar flow spread. The air which passed the small area A_1 far upwind of the wind turbine passes a larger area A_2 far downwind of the wind turbine. The maximal thrust T_{max} is reached for $v_2 = 0$. Within this conceptual model the dimensionless thrust coefficient c_T only depends on mean wind speed and can be formulated as the percentage of rotor thrust T' to maximum thrust T_{max} for an air density ρ (Equation 3.1).

$$c_T = \frac{T'}{T_{max}} = \frac{\frac{1}{2}\rho A' \left(v_1^2 - v_2^2\right)}{\frac{1}{2}\rho A' v_1^2} = 1 - \frac{v_2^2}{v_1^2} \tag{3.1}$$

The thrust coefficient c_T is a parameter for a given wind turbine type. It is provided by the wind turbine manufacturers or can be determined from field measurements by applying Equation (3.1). The thrust coefficient varies with mean wind speed. According to the definition of the thrust coefficient by Mikkelsen (2003), the rotor thrust in Equation (3.2) only depends on the mean wind speed of the undisturbed flow, the thrust coefficient and the rotor area. Since the rotor area can be easily calculated by using the given rotor diameter D, only the mean undisturbed wind speed has to be determined to apply Equation (3.2). This equation is used in the numerical model.

$$T' = \frac{1}{2}\rho A' \left(v_1^2 - v_2^2\right) = c_T T_{max} = \frac{1}{2} c_T \rho A' v_1^2 \tag{3.2}$$

The undisturbed wind speed is calculated using a so named reference rotor in some distance upwind of the actual rotor. Prospathopoulos (2010) and Linde (2011) showed that the best results are achieved when choosing a distance d of 1.0 or 0.1 times rotor diameter D upwind of the wind turbine, respectively. In this area, the wind speed and the wind direction are already slightly disturbed. However, choosing a position further

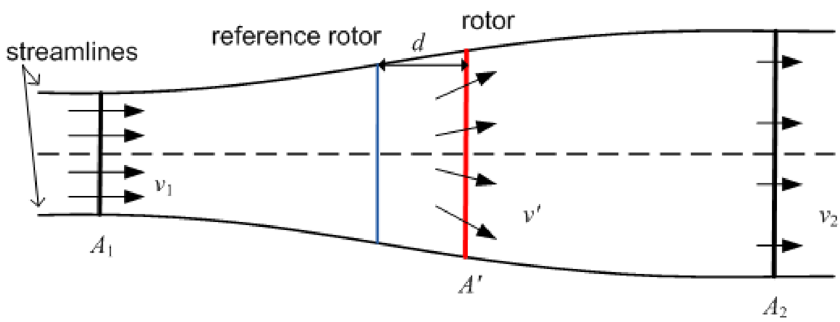

Figure 3.2: Schematic diagram of the actuator disc concept. The mean wind speed upwind, at and downwind of a wind turbine rotor is denoted with v_1, v' and v_2. The corresponding areas are given with A_1, A' and A_2. The distance between the rotor and the reference rotor is given with d.

upwind decouples the wind speed and direction at rotor and reference rotor position, especially in complex terrain. The choice of the reference rotor position $d = 0.1D$ produces a smaller error than the position $d = 1.0D$ as shown by LINDE (2011) using an obstacle resolving microscale model.

In a mesoscale model, horizontal grid sizes are typically large compared to the size of a wind turbine rotor. Therefore, the rotor and the reference rotor are in general in the same grid cell for a single wind turbine. Furthermore, several wind turbines might be located within one grid cell in the horizontal and then wakes are superposed to one large wake. The vertical grid size is typically less coarse. Therefore, a rotor is represented at its real hub height, usually within several vertical grid cells. A whole wind farm is located in just a few adjacent grid cells. Therefore, to determine the average reference wind speed in METRAS for each wind farm, the wind speed of all grid cells containing the same wind farm are averaged. This averaged value is then used to be the undisturbed upwind wind speed.

The part of the grid cell that is covered by a rotor is defined by a wind turbine mask. Multiplying Equation (3.2) with the wind turbine mask and subtracting this term from the basic equation of momentum leads to the parametrisation for wind turbines. Since the thrust coefficient c_T depends on mean wind speed v_1, the wind turbines switch on and off autonomously, if the wind speed becomes higher or lower then the cut-in or cut-off velocity.

Compared to the coarse grid of a mesoscale model, the tower of a wind turbine is small. More than three rotor diameters downwind, the shape of the wake is mainly determined by the influence of the rotor. The influence of the tower on the wake is negligible in this area (LINDE, 2011). Therefore, the towers of the wind turbines are neglected in the present study. With these assumptions and by using the ADC, several large wind farms can be represented in the model domain.

Due to a lack of ground based measurements in the wake of large offshore wind farms, the model is verified against other models and satellite data. Simulations with this parametrisation give plausible results of the offshore wind farm Horns Rev (not shown) against the satellite data in CHRISTIANSEN and HASAGER (2005). The model also archived plausible results redoing the idealised simulations of the model COSMO of an offshore wind farm from STÜTZ et al. (2012) and the single onshore wind turbine Nibe B with the model MITRAS of LINDE (2011).

3.2.3 Model domain

The model covers a domain from about 50°47′ N to 56°25′ N and from about 4°26′ E to 15°40′ E, which corresponds to an area of 700×628 km^2 (Figure 3.1). This includes Northern Germany and the German Bight as well as parts of The Netherlands, Denmark, Sweden, Poland and the Baltic Sea. Hamburg is located in the centre of the model domain (marked with a black frame in Figure 3.1). The wind farms planned in the German Bight are projected to be found in the North-West part of the domain and cover a considerable part of the area. The horizontal grid size is 4 km. The vertical grid resolution in the lowest 100 m is 20 m, with the lowest grid level at 10 m above ground. Above, the vertical grid size increases with an increasing factor of 1.175 per grid cell. The maximum grid size is 1000 m above 5000 m. The domain includes 34 model levels with 19 levels located within the lowest 2000 m. The model top is at 12000 m. Due to the high vertical grid resolution, the momentum absorption of the wind turbines is considered in their corresponding hub height.

Data describing the position of the proposed wind farms are taken from the "Zukunft Küste - Coastal Futures" project (Burkhard, 2006; Lange et al., 2010). Following the extreme scenario "B1 - the North Sea is primarily used as energy park" 90 GW installed power are proposed to be installed in the German Bight until the year 2055. The average power of a single wind turbine is assumed to be 10 MW. This leads to a total number of 9000 wind turbines located in 25 wind farms. For the simulations discussed in the present work, the wind turbines are placed in a distance of 1990 m from each other in each direction without considering the main wind direction. This leads to exactly 9000 wind turbines in the proposed area (Figure 3.1). To avoid effects from the model boundaries, the wind farms are placed at least four grid cells away from the lateral boundaries.

The technical specification for wind turbines that produce 10 MW is yet not clear. Therefore, the thrust coefficient is deduced from accessible measurements of a Nordex N80 / 2500 wind turbine for a standard density of the air (Machielse et al., 2007). The determination of the thrust coefficient is given in the Appendix E. A hub height of 80 m is assumed.

3.2.4 Simulated weather situations

For quantification of the impact of large wind farms in the German Bight on the summer climate, the climate mean needs to be simulated. The computational costs to simulate 30 years on a 4×4 km^2 grid would be too large, therefore only a selection of typical weather situations occurring in the summer season are simulated. The statistic-dynamical downscaling method for simulating the UHI of Hamburg of Hoffmann and Schlünzen (2013) is used as a base. The simulations from this study are extended to represent the climate summer mean of Northern Germany by a number of additional simulations. The number of necessary additional simulations is determined by a SSP. The SSP is also used to evaluate the simulated frequency distributions of hourly values.

Hoffmann and Schlünzen (2013) developed the statistical-dynamical downscaling method for simulating the UHI of Hamburg with METRAS. There are several comparison studies showing that there is no best weather pattern classification (WPC) and that WPC should be "viewed as purpose-made" (Huth et al., 2008). Therefore, each target parameter requires the construction of its own optimal classification. The WPC used here is especially developed for representing the mean strong UHI of Hamburg. A detailed discussion about the choice of the classification is given in Hoffmann and Schlünzen (2013).

Seven weather pattern (WP), important for the UHI, were found through the WPC by clustering 700 hPa fields from the ERA40-reanalysis using the k-means based clustering method SANDRA (simulated annealing and diversified randomization, Philipp et al. (2007)). Due to the low number of WP, the explained UHI variance was not high enough if only days close to the cluster centre were simulated (Hoffmann, 2012). Therefore, Hoffmann (2012) subdivided the WP according to the strength of the UHI within each WP. Consequential, two weather situations are simulated for each WP. These represent the maximum and the threshold UHI. The threshold UHI is 3 K and refers to the magnitude of the UHI. For planning adaptation measures only strong UHI days are interesting because these are situations where temperatures can be reduced using such measures. Hence, this method simulates the mean strong UHI of Hamburg (UHI $>$ 3 K). The seven weather situations representing the maximum UHI inside each WP are denoted with WP1M to WP7M. The seven threshold weather situations are named WP1T to WP7T. WP7M and WP7T refer to the same weather situation. Consequently, the mean strong UHI of Hamburg is calculated from thirteen different simulations by statistical recombination (Hoffmann, 2012).

To extend the thirteen simulations of HOFFMANN (2012) to represent the climatological summer mean for Northern Germany additional to the mean strong UHI of Hamburg, preferably more than thirteen simulations are used. Therefore, the simulations of HOFFMANN (2012) are completed by simulations for the meteorological situation closest to the seven cluster centres (WP1C to WP7C) and used as the reference simulations for the current condition without wind farms in the German Bight. For each simulated situation a two day period is evaluated, therefore 40 days are available in total to represent the climatological summer mean. To ensure that these 40 days are sufficient, a test with a statistical skill score following PERKINS et al. (2007) is applied. The SSP compares two frequency distributions and is equal one if both distributions are the same and is equal zero if both distributions have no overlap. PERKINS et al. (2007) state that for SSP > 0.8 the agreement is "considerable" and for SSP $= 0.9$ the agreement is "near perfect". Therefore, the frequency distributions are defined to be represented reasonable well in the present study if the SSP is larger than 0.8. This means that more than 80 % of the frequency distributions overlap.

The data from 27 weather stations in Germany and The Netherlands include hourly observations over 30 years from 1981 to 2010. The investigations have been done for each weather station separately. Analysis is done for the frequency distributions of wind speed and temperature because they are most important to quantify the impact of wind farms on climate. The frequency distributions are build using 1 m/s bins for wind speed and 1 K bins for the temperature. The number of days needed to represent these frequency distributions is the required number of days for representing the summer climate. The bootstrap resampling method is used in order to create thousand pairs of frequency distributions from which the SSP is calculated.

The mean SSP for 40 randomly chosen days from measurements is in the range of 0.91 to 0.95 for wind speed with a mean of 0.94 (Figure 3.3a). For temperature, the mean SSP is 0.91 with the range of 0.89 to 0.91 (Figure 3.3b). Therefore, the SSP for 40 days is clearly higher than 0.8 and thus close to a "near perfect" agreement as defined by PERKINS et al. (2007).

In contrast to the SSP test, the simulated 40 days are not independent from each other, but always two consecutive days are simulated. Furthermore, the situations are chosen by a WPC involving the occurrence of the WP, even if the SSP expects randomly chosen days. For wind speed, the mean SSP is 0.87 which is slightly below the range for wind

(a)

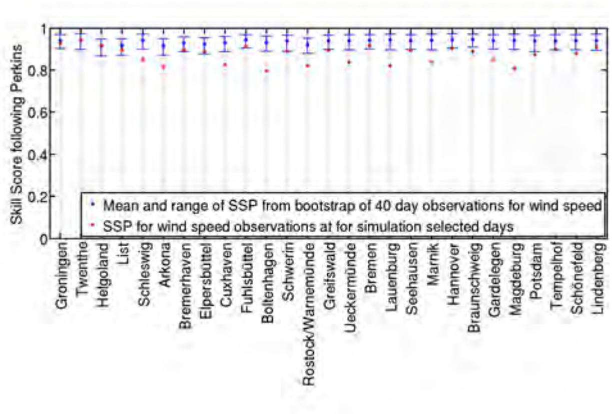

(b)

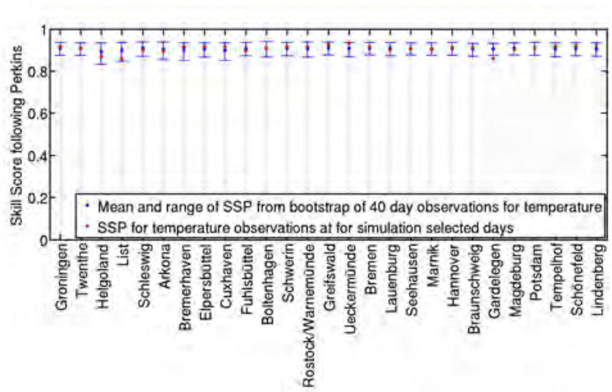

(c)

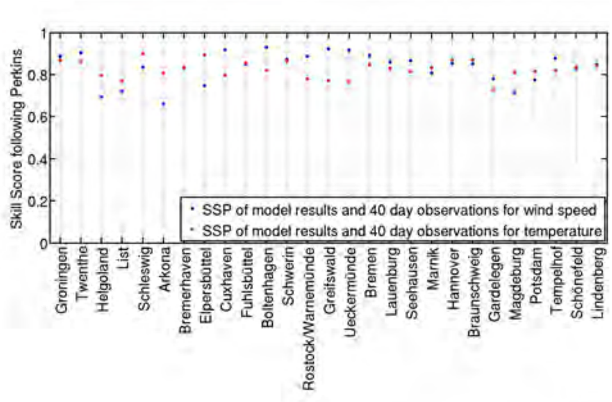

Figure 3.3: Skill Score following Perkins for individual meteorological sites for (a) wind speed and (b) temperature based on 30 years of hourly data. (c) Skill Score following Perkins for individual meteorological sites for wind speed and temperature based on model results and the chosen 40 days.

speed of 40 randomly chosen days. For temperature, the mean SSP is 0.90 and thus similar to the SSP for temperature of 40 randomly chosen days. The SSPs are shown in Figure 3.3a for wind speed and in Figure 3.3b for temperature for all 27 weather stations. For wind speed the SSP is lower for the chosen 40 days than for randomly selected 40 days at 13 out of the 27 sites, but only one of these stations (Cuxhaven) is close to the German Bight. Thus, the representation of the summer climate is estimated to be at least sufficient. For temperature, the SSP of the chosen 40 days fits the range of the randomly chosen 40 days except for Gardelegen, again one site not close to the German Bight. The SSPs for wind speed and temperature are both higher than 0.8.

Figure 3.3c shows the SSP of the model results against the chosen 40 days. The SSP for wind speed is in the range of 0.66 to 0.90 and for temperature from 0.73 to 0.90. The mean SSP is 0.83 for both and therefore a good result (Perkins et al., 2007). Thus, the 40 chosen weather situations and the following model results represent the climate summer mean for Northern Germany. Calculating the mean strong UHI following Hoffmann (2012), the results of these simulations are also usable to investigate in the impact of large offshore wind farm to the UHI of Hamburg.

3.2.5 Simulated sensible and latent heat fluxes in the German Bight

The air temperature in Northern Germany is impacted by the sea surface temperature of the German Bight. Therefore, the simulated sensible heat flux between water and atmosphere is important for correctly simulating the summer climate. For the German Bight during summer months (June, July and August) the monthly mean sensible heat flux is slightly positive, means warming the atmosphere, in the range of 2 W/m^2 to 12 W/m^2 with higher values at the coast and lower values at the open sea (Becker, 1981; Michaelsen et al., 1998; Schlünzen and Krell, 2004). In Figure 3.4a, the simulated mean sensible heat flux averaged for the reference simulations is shown. The result fits very well with the data from Michaelsen et al. (1998).

The air temperature is highly impacted by the cloud development and therefore the total air mass water content. Thus, to simulate the mean latent heat flux for the German Bight is important. The mean latent heat flux shows the same pattern as the sensible heat flux but in the range of 35 W/m^2 to 60 W/m^2. Figure 3.4c shows the simulated mean latent heat flux for the reference simulations. The result fits with the data from Michaelsen

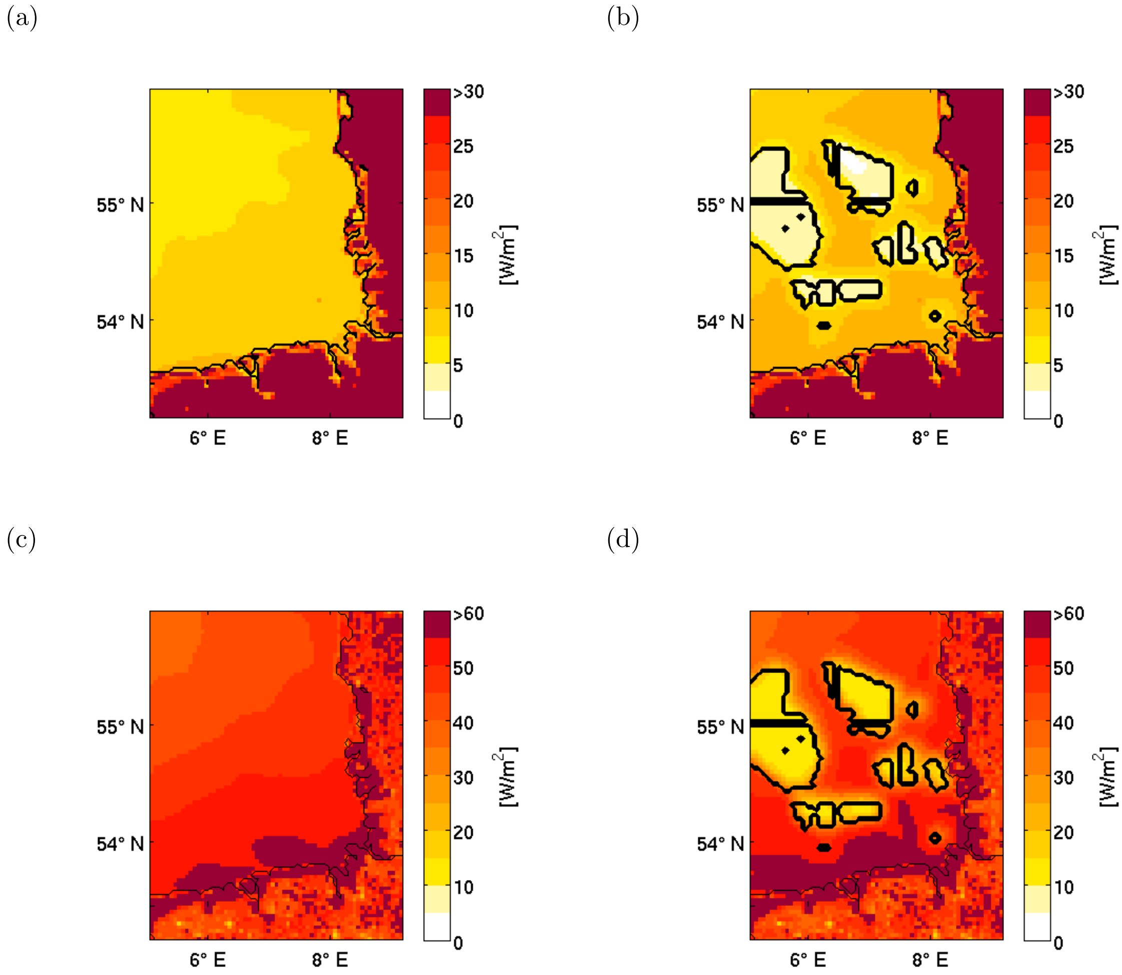

Figure 3.4: Mean sensible heat flux (a), (b) and mean latent heat flux (c), (d) between sea surface and atmosphere for averaged summer climate in the German Bight from (a), (c) reference simulations and (b), (d) scenario simulations. Positive values are defining fluxes from the ocean to the atmosphere.

et al. (1998). Therefore, the chosen 40 days are representative for the mean sensible and latent heat flux in the German Bight during summer months as well as for wind speed and temperature frequency distribution.

3.3 Results

To determine the influence of the wind farms, each weather situation is simulated twice, with and without wind farms in the German Bight. The latter is here denominated as "reference case", while the case that considers wind farms is named "scenario". The model simulations are evaluated with focus on simulation results in 10 m above ground to estimate the impact of the offshore wind farms on close to surface meteorology. The main target variable is the temperature in 10 m above ground. Other variables are studied to determine the reasons for changes in the temperature. The model results are stored every 30 minutes and results from midnight to midnight of the last 48 hours of each model simulation are used. Only those results are considered that are at least ten grid cells from the lateral boundaries. This shall avoid direct effects from nudging. The impact of the wind farms on different weather situations in the German Bight area is analysed in Section 3.3.1. The impact on the regional climate is investigated in Section 3.3.2. The impact on the climate of Hamburg is analysed in Section 3.3.3.

3.3.1 Impact of the wind farms on the meteorology for the different weather situations

Differences in temperature between the scenario and the corresponding reference case appear in all simulated weather situations and also in the summer climate average (Figure 3.5b). The changes in the temperature are, however, not restricted to the area of the wind farms but in average and in most weather situations simulated in a much larger area. In most cases, the flow upwind and lateral to the wind farms is also affected, not only the flow downwind. In some cases, the wind speed in the wind farm areas is temporarily lower than the cut-in wind speed of 2.5 m/s and the wind farms switch off. Then the differences in the temperature between scenario and the corresponding reference case decrease. Some hours after cut-off, the impact inside the model domain has nearly disappeared (Figure 3.6a, 3.6b). In the simulations used in this study, the wind speed is lower than the cut-in velocity for only few hours. Additional simulations not used in this study, have lower wind speed and show no effect of wind turbines, neither at instant time nor in few hours mean (not shown).

If the wind speed is higher than the cut-in velocity, the impact of the wind farms is found in a large area. The effects depend on the weather situation. The impact differs from local effects to large scale temperature changes or from large scale cloud development to local cloud dispersal. In most but not in all cases, the effects are scattered and only local and not uniformly distributed.

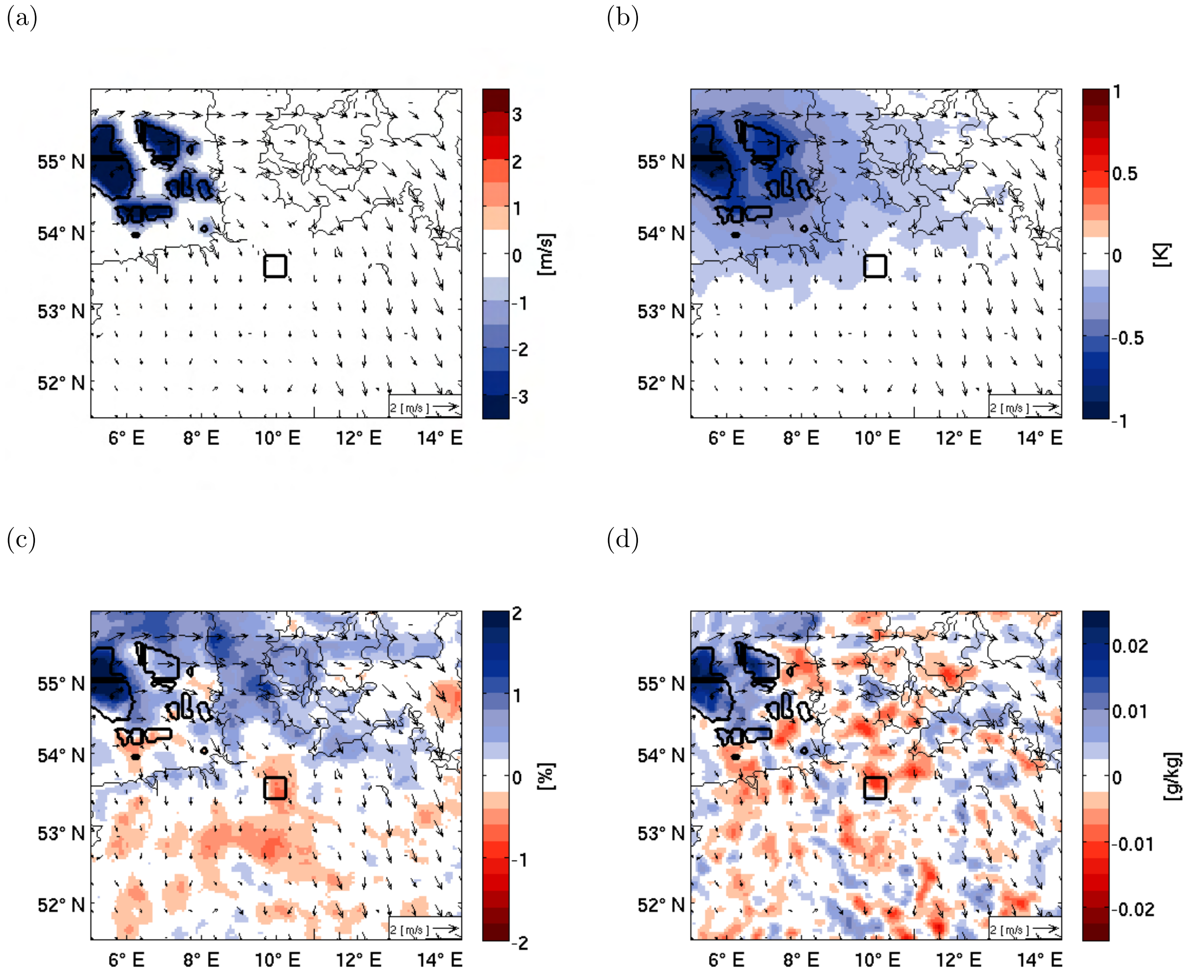

Figure 3.5: Mean differences in (a) wind speed, (b) temperature and (c) relative humidity at 10 m above surface and (d) integral cloud water content between scenario and reference simulations for averaged summer climate. Hamburg is located in the domain centre and marked with a black frame. The wind farms in the German Bight are also outlined with black frames and located in the North-West quadrant of the model domain. The vectors illustrate the mean wind velocity for the reference simulations, every 11^{th} vector is shown.

As a result of the changed temperature and relative humidity, the cloud cover over the German Bight changes as well. Depending on the weather situation, sometimes sea fog is generated or existing sea fog is extended in the horizontal and vertical dimension. In other weather situations, convective clouds are shifted in space and time. In some weather situations, new clouds are generated and change the temperature field in such a way that clouds in other areas disappear. As an example, the pattern of convective cloud development is changed in WP1C, therefore local warming and cooling alternates (Figure

(a) (b) (c) (d)

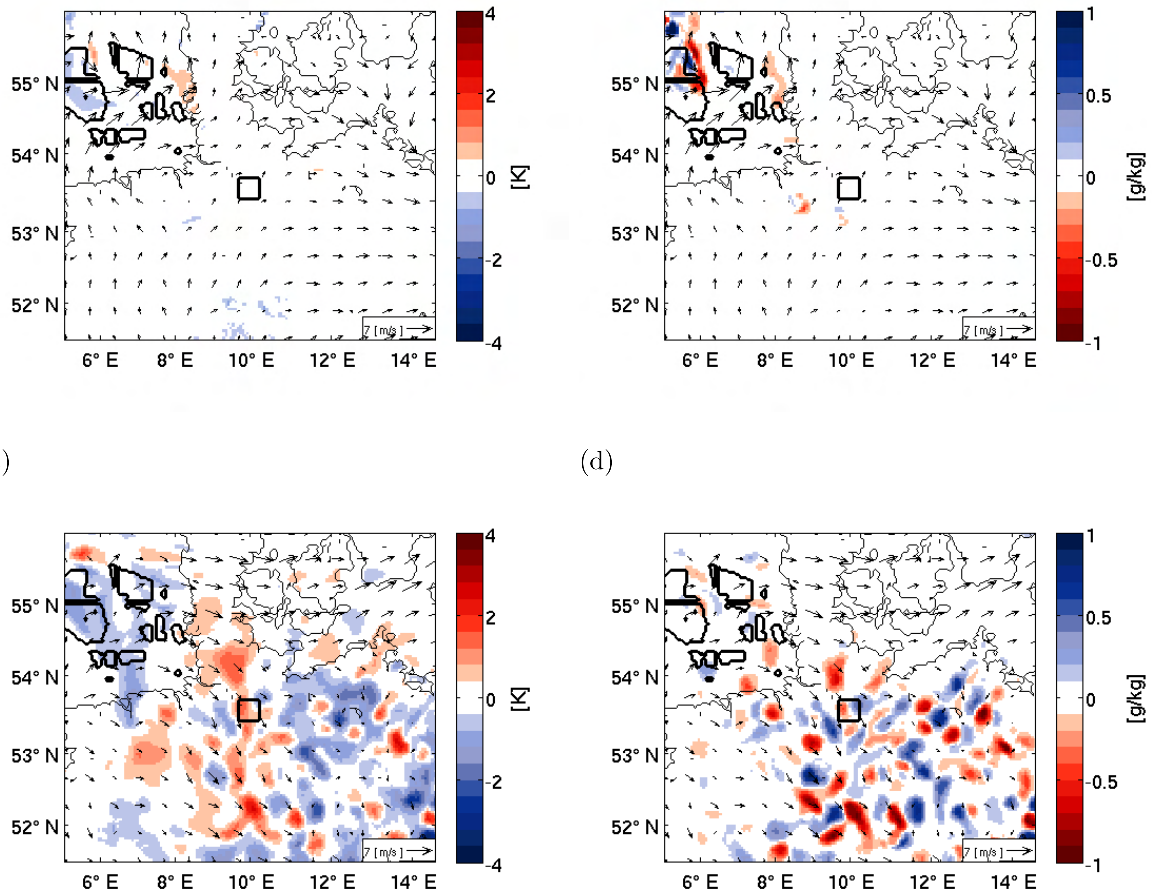

Figure 3.6: Differences in (a), (c) temperature at 10 m above surface and (b), (d) integral cloud water content between scenario and reference simulations for (a), (b) WP6C at 0000 LT and (c), (d) WP1C at 1800 LT of the last day of simulation. Hamburg is located in the domain centre and marked with a black frame. The wind farms in the German Bight are also outlined with black frames and located in the North-West quadrant of the model domain. The vectors illustrate the instantaneous wind velocity for the reference situations, every 11$^{\mathrm{th}}$ vector is shown.

3.6c, 3.6d). Thus, not only cooling but in some weather situation also local warming is possible as a result of wind farms in the German Bight. Some further examples of the effects of wind turbines in different WPs are shown in Eichhorn (2013).

3.3.2 Impact of wind farms on regional climate

For analysing the impact of large wind farms on regional climate, the differences between each scenario and its corresponding reference case are averaged over all weather situations. As shown in Section 3.2.4, the regional summer climate is sufficiently represented by the averaging approach.

The largest differences in wind speed between the scenario and reference cases were found within and close to the wind farms (Figure 3.5a). Here the largest decrease in wind speed is simulated reaching up to 3 m/s in the summer climate average. An underflow with high wind speed close to the ground in the near wake is not obtained in this study, because the grid resolution of 4×4 km^2 do not represent the near wake. In the far wake, the underflow is eliminated by the vertical exchange. The decreases in wind speed in the areas around the wind farms are small and within ± 0.5 m/s.

As shown in Figure 3.4a, the mean sensible heat flux is slightly positive, meaning the atmosphere gets warmed by the sea surface in the German Bight. The reduced wind speed in the wind farm area results in a decrease of the mean sensible heat flux in the same area (Figure 3.4b). This leads to lower air temperatures in 10 m above sea level in all scenario cases in the wind farm region and therefore in the summer mean in that area (Figure 3.5b). Based on the air temperature reduction, the temperature gradient between sea surface and air increases and counteract the reduction of the sensible heat flux. This effect is weaker than the effect of the reduced wind speed but becomes important in the area around the wind farms. Due to the in average lower temperature, the mean sensible heat flux around the wind farms becomes slightly higher but this can not counteract completely the decrease in temperature. The major effect in temperature is found inside the wind farm area but a large area over Northern Germany and Southern Denmark is affected (Figure 3.5b). As mentioned in Section 3.3.1, dependent on the weather situation, local warming and cooling occur due to changes in the cloud development. Even if the local warming in some weather situations may have the same magnitude as the cooling, on average the warming effect is small compared to the cooling (Figure 3.5b). In the climatological summer mean, the warming (below 0.1 K) is one order of magnitude smaller than the cooling (up to 1.0 K) and very local.

The changes in the latent heat flux between scenario (Figure 3.4d) and reference (Figure 3.4c) simulations are similar to the changes in the sensible heat flux (Figure 3.4).

In climate summer average, the relative humidity is increased in the area of decreased temperature and decreased due to decreases in the total air mass water content in the remaining areas (Figure 3.5c). The differences in temperature and relative humidity are strongest within and close to the wind farm area. But unlike the changes in the wind speed, these effects are scattered over a larger area. The changes in temperature and total air mass water content cause also changes in the cloud development and therefore generate changes in temperature again. The differences of the mean integral cloud water content show cloud development in the wind farm area but scattered effects of cloud development and dispersal in the areas far away (Figure 3.5d). Thus, the changes in temperature, relative humidity and cloud development are more long-range than the changes in the wind speed. Because of the mean wind direction and the position of the wind farms, often large parts of the downwind area are located over land.

To determine the upwind and downwind as well as the lateral effects the wind farms have on the regional summer climate, the model domain around the wind farms is split into four regions. The first region is the wind farm area itself, which is the same for every weather situation. The wind farm area is extended about 200×200 km^2. The other three regions are determined for each half-hourly output time separately with respect to the instantaneous wind direction in the wind farm area. Their size is chosen to be the same as that of the wind farm region. This leads to areas up to 200 km upwind and 200 km downwind of the wind farm area for the upwind and downwind regions, respectively. The region lateral of the wind farm area is determined to extend 100 km towards each side of the wind farms. Some of the model domain boundaries are very close to the wind farm areas. Therefore, not every region is evaluated for each output time and sometimes the regions are evaluated in a smaller domain. This is considered in the space and time averaging. Analyses are separately done for nighttime and daytime. The nighttime is chosen from 1800 LT to 0530 LT and the daytime accordingly from 0600 LT to 1730 LT.

The space averaged time series are calculated for every region. For wind speed no diurnal cycle is found (not shown). The decrease in temperature between scenario and reference climate shows changes in the areas around the wind farms and the changes are time dependent. On average, a cooling with the magnitude of -0.23 K is found, values for day and night time do not differ (Table 3.1). Splitting the changes in temperature with respect to the different regions, the major mean cooling effect is found within the wind farm region (-0.55 K). The regions lateral and downwind are cooled with the magnitude of -0.16 K and -0.17 K respectively. The effect upwind of the wind farm area is small (-0.01 K).

Separating the changes in night- and daytime averages for the different regions highlights different behaviours during time of day. The largest differences are found again in the wind farm region, with cooling of -0.61 K during the night and -0.48 K during the day. The region lateral show slightly larger temperature decreases (-0.17 K) during night than during the day (-0.15 K). In the region downwind, the decrease of temperature is smaller during the night (-0.16 K) than during the day (-0.18 K). These diurnal effects are also apparent at night (Figure 3.7a) and day (Figure 3.7c) in the whole domain. The night-time patterns show a high magnitude inside and close to the wind farm area while the effect is only scattered for the distance. Even though the maximum magnitude of temperature reduction is smaller during day, the area of strong influence is larger. It is more than 0.3 K over Schleswig-Holstein which is very often in the downwind area due to the frequency of the weather situations with westerly winds. Consequently, the pattern of the daily mean (Figure 3.5b) is a superposition of both patterns. Even if the mean changes in the temperature are small, the simulations show that wind farms have an impact on regional climate. Hence the statistics for the summer climate are satisfied, the mean influence is real. In single situations, the impact can be much larger or nearly vanish.

The changes in the integral cloud water content show no diurnal cycle. The night- (Figure 3.7b) and daytime (Figure 3.7d) averages of the integral cloud water content are similar to the daily mean (Figure 3.5d).

Table 3.1: Space and time averaged temperature differences between scenario and reference cases for the regions "wind farm", "upwind", "downwind", "lateral", "total" and "Hamburg" as mean values and separated for night (1800 LT - 0530 LT) and day (0600 LT - 1730 LT) as summer average.

region	mean [K]	night [K]	day [K]
wind farm	−0.55	−0.61	−0.48
upwind	−0.01	−0.02	−0.01
downwind	−0.17	−0.16	−0.18
lateral	−0.16	−0.17	−0.15
total	−0.23	−0.23	−0.23
Hamburg	−0.05	−0.01	−0.08

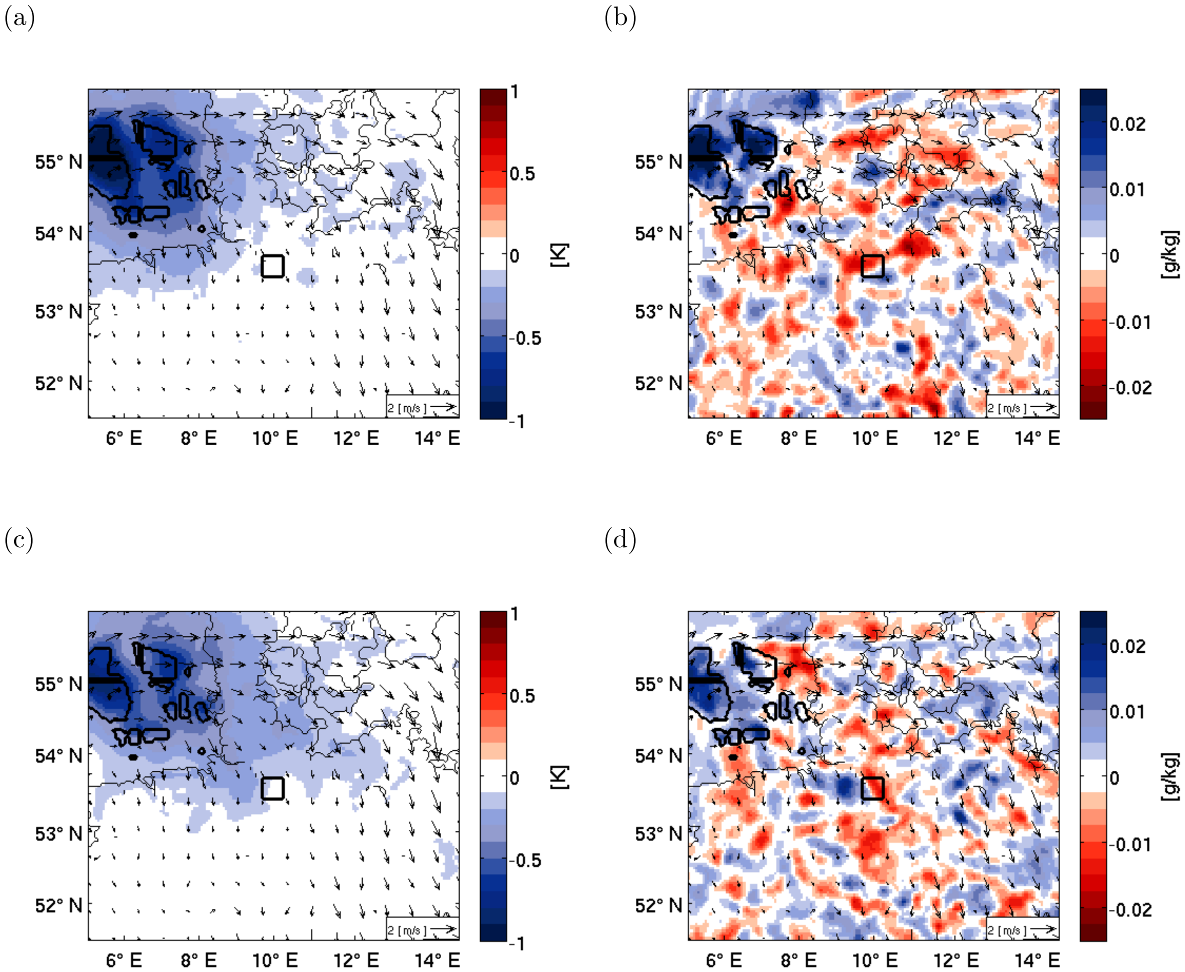

Figure 3.7: Same as Figure 3.5b and 3.5d but for (a), (b) nighttime and (c), (d) daytime temperature and integral cloud water content.

3.3.3 Impact of the wind farms in the German Bight on the summer climate of Hamburg

Hamburg is situated roughly 100 km inland from the German Bight. As shown in Sections 3.3.1 and 3.3.2, the impact of the wind farms is quite long-range. Hamburg is located in the margins of the influenced region.

Analyses of the model results shows that the wind farms in the German Bight lead to in average slightly higher wind speed in the western part of Hamburg and to lower wind speeds in the southern and north-eastern part (Figure 3.8a). On average, the changes in wind speed are very small ($< \pm 0.1$ m/s) but in single situations, the pattern and the magnitude of the differences can be more pronounced. The regional wind climate as represented by the simulations is only marginally changed in Hamburg by the wind farms in the German Bight.

The changes in temperature are independent of the changes in wind speed (Figure 3.8b). A small cooling of up to -0.1 K is found that decreases from north-west to south-east. The wind farms in the German Bight also influence the relative humidity. In the area of Hamburg, it results in a small drying (≤ -1 %), mainly during the night (Figure 3.8c). In summer mean, Hamburg is located in an area of cloud dispersal. The decrease in the integral cloud water content (Figure 3.8d) counts up to 0.015 g/kg, about 10 % compared to the reference mean.

The changes impact the urban climate. Hoffmann et al. (2012) found a dependency of the UHI on wind speed, relative humidity and cloud cover. These variables are affected by the wind farms. Even if these changes are, except the cloud dispersal, in average and each for itself small, the interaction leads to changes of the UHI. The cloud dispersal increases the incoming solar radiation and therefore intensifies the UHI. The mean strong UHI is built for the evening hours from 2000 LT to 2400 LT as a difference between the city of Hamburg and model results averaged from two measurement sites in the rural surrounding (Hoffmann, 2012).

As discussed by Hoffmann (2012), the UHI pattern of the current conditions reflects the build-up density and the ground sealing of Hamburg but is also influenced by the river Elbe, which results in a slight warming (Figure 3.9a). The harbour areas and the high building density close to the river Elbe create the largest values for the UHI with a magnitude of up to 0.8 K. Note that these values are much smaller than the summer average value of 2.5 K based on Figure 10 of Schlünzen et al. (2010) for the site of St. Pauli from measured data. This site is within the dense build-up part of the city and close to the river. However, it is not very representative and not comparable with a 4×4 km^2 summer average value as derived from the model results. The sub-urban areas in the southern and north-eastern parts of Hamburg show small UHI values with a magnitude of approximately 0.1 K.

To estimate the impact of the wind farms on the UHI, the UHI is calculated from the results of the scenario cases. The resulting UHI is shown in Figure 3.9b. The UHI, especially in the inner city, but also in the western and south-eastern parts of Hamburg is up to 0.2 K higher than for the reference case. In the eastern part of Hamburg the

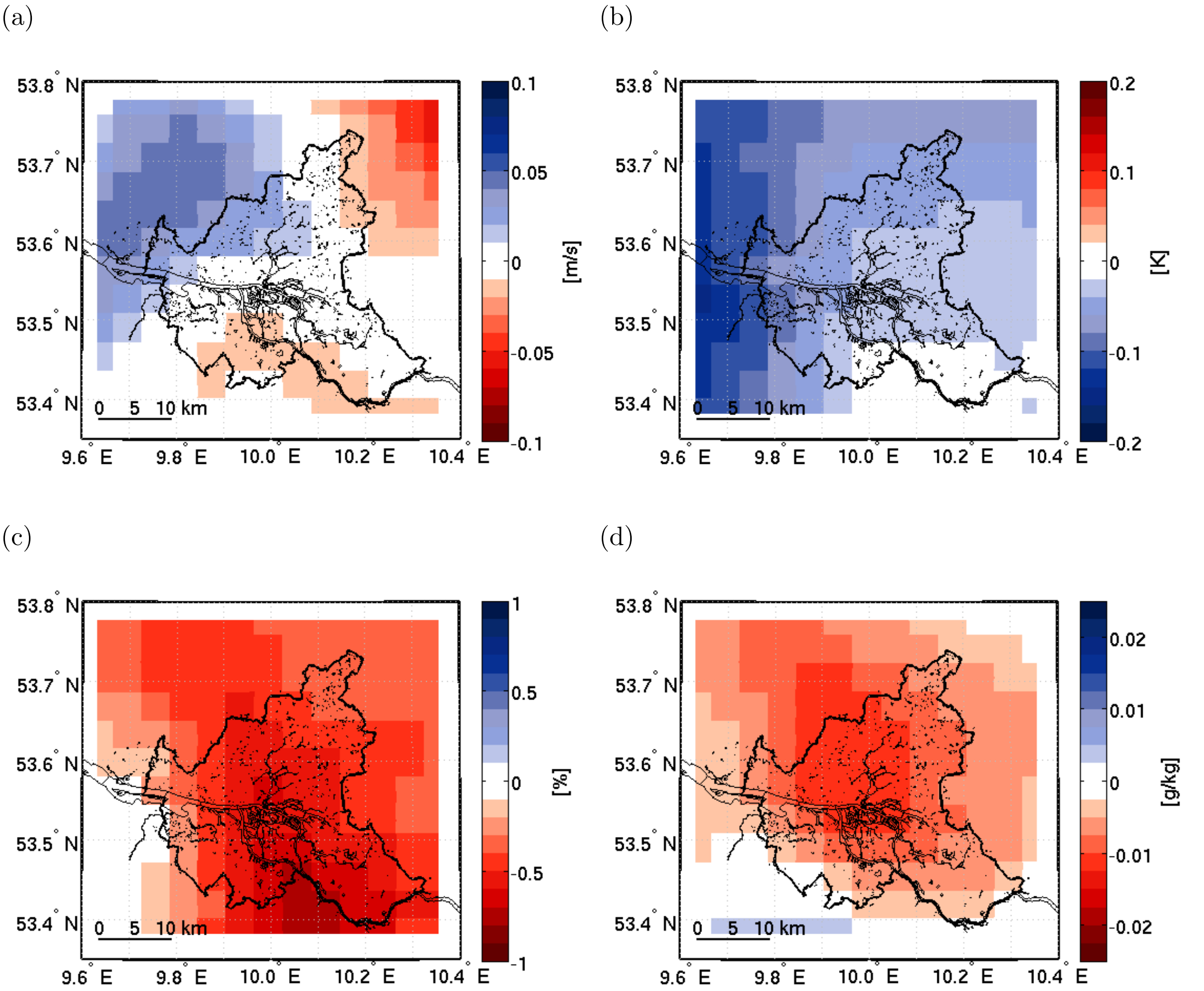

Figure 3.8: Mean differences in (a) wind speed, (b) temperature and (c) relative humidity at 10 m above surface and (d) integral cloud water content between scenario and reference simulations for summer climate average. Hamburg is marked with a thick black line and the thinner lines illustrate the water bodies of Hamburg.

UHI decreases up to -0.1 K (Figure 3.10a). Therefore, even if the temperature in daily or night- or daytime mean decreases, the temperature difference between large areas of the city and the rural surroundings increases in the evening hours.

The changes in the mean strong UHI mainly result from the simulations conducted for the three weather situations WP1T, WP4T and WP6T. This is apparent if only these situations are used to calculate the differences as shown in Figure 3.10b, which is only based on changes resulting from these three cases. Changes of the UHI up to ± 0.2 K in these three WP occur (Figure 3.11) while the changes in the other WP are small ($\leq \pm 0.02$ K).

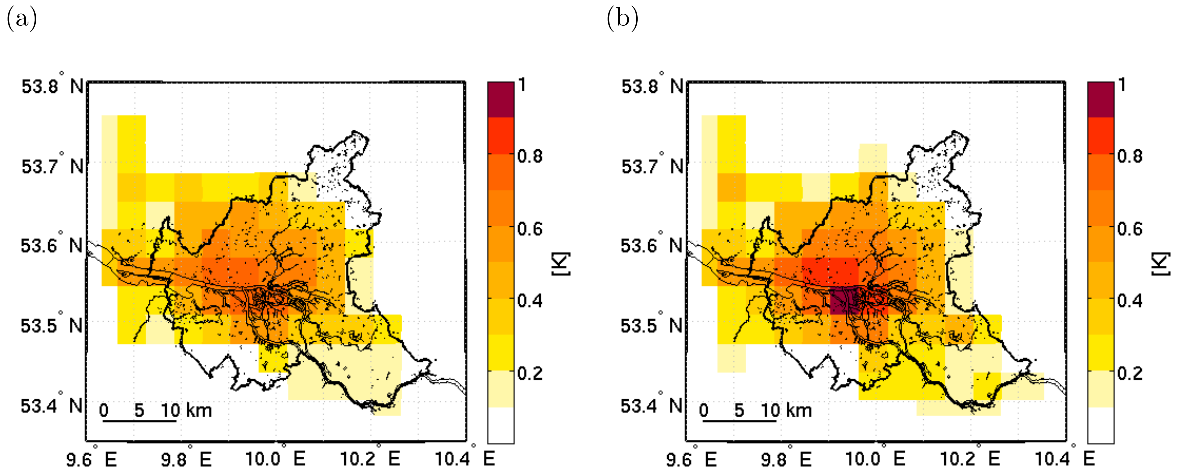

Figure 3.9: Mean strong UHI of Hamburg at 10 m above surface between 2000 LT and 2400 LT based on (a) the reference simulations and (b) the scenario simulations. Hamburg is marked with a thick black line and the thinner lines illustrate the water bodies of Hamburg.

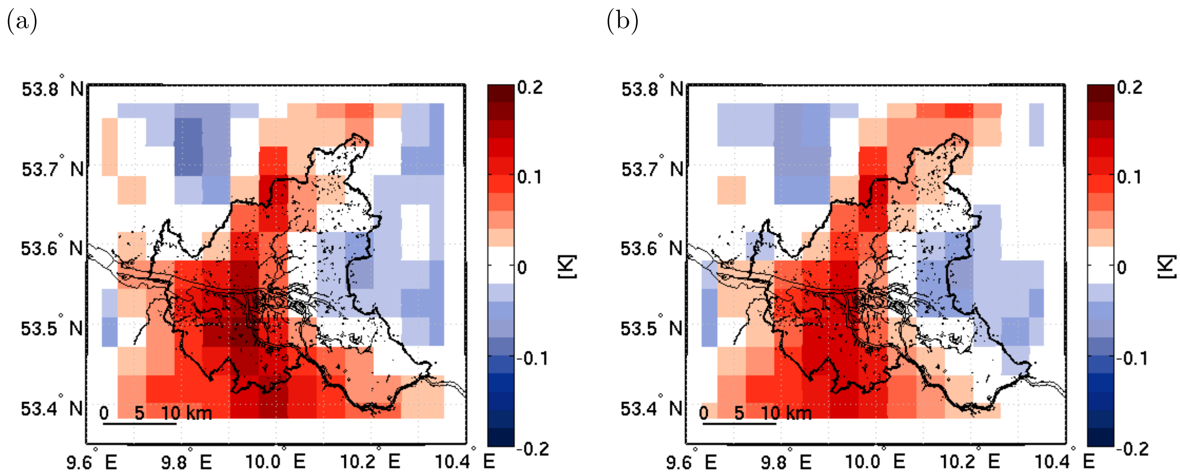

Figure 3.10: Differences of the UHI of Hamburg between (a) all the scenario and all the reference simulations and (b) only the most relevant weather situations WP1T, WP4T and WP6T at 10 m above surface between 2000 LT and 2400 LT. Hamburg is marked with a thick black line and the thinner lines illustrate the water bodies of Hamburg.

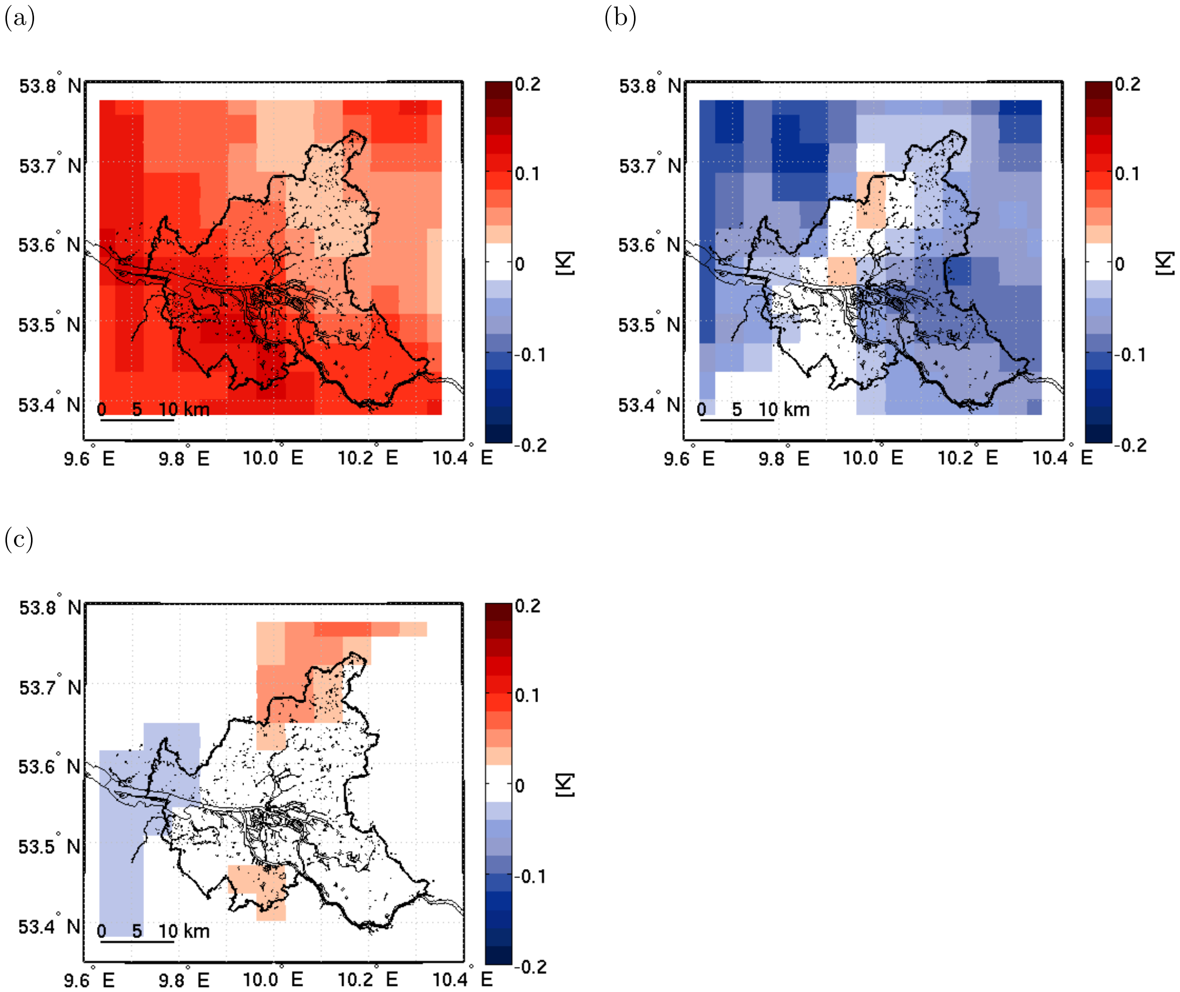

Figure 3.11: Differences of the UHI of Hamburg between the scenario and the reference simulations of the most relevant weather situations (a) WP1T, (b) WP4T and (c) WP6T at 10 m above surface between 2000 LT and 2400 LT. Hamburg is marked with a thick black line and the thinner lines illustrate the water bodies of Hamburg.

Summarising, the average of these three patterns reflects the average changes well. The urban effect becomes more important in the scenarios with large offshore wind farms. In average, the UHI increases because of the cloud dispersal even if the changes in the other meteorological variables are in average small. The urban effects should be reduced, so that the cooling of the wind farms remains noticeable as a slight cooling for Hamburg (Figure 3.8b). All in all, the impact of 100 km away offshore wind farms on the urban climate is not negligible.

3.4 Conclusions

In the present study, the influences of large wind farms in the German Bight on regional and urban climate are investigated using the non-hydrostatic, three-dimensional, numerical model METRAS, which is now extended for the representation of wind turbines with the actuator disc concept. In the present study, simulations are performed for the current situation and for a scenario with large wind farms in the German Bight. The impact is analysed not only in the wind farm area itself or in its direct wake but also for 100 km apart from the wind farms. Hereby, this study closes the gap between several local (Baidya Roy et al., 2004; Baidya Roy and Traiteur, 2010; Baidya Roy, 2011; Christiansen and Hasager, 2005; Zhou et al., 2012) and global studies (Keith et al., 2004; Miller et al., 2011; Wang and Prinn, 2010).

Due to the coarse grid resolution of 4 km used in the present study, several wind turbines are represented in one grid cell by a fraction of rotor area per grid volume. However, the high vertical resolution allows the consideration of the wind turbines in their corresponding height. Therefore, the momentum absorption is simulated in higher model levels and this only interacts with the flow field at the surface.

To represent the summer climate, 40 days from 20 characteristic weather situations are simulated and their results averaged. The selected weather situations represent the summer climate well. This was shown by comparing statistics of 30 years of data from 27 weather stations and determining the skill scores following Perkins et al. (2007).

The wind farms in the German Bight affect a large area inland. Because of changed surface fluxes within the wind farm area, temperature, relative humidity and cloud development change locally and on the regional scale. On average, the wind farms in the German Bight result in a cooling for Schleswig-Holstein, Hamburg, the north-eastern part of Lower-Saxony and the southern part of Denmark. These areas are located in the main wind direction and frequently downwind of the wind farms. The local warming found for some weather situations does not appear in the summer average, because this warming is very local and one order of magnitude smaller than the cooling. The intensity of the cooling, however, changes between night- and daytime. The largest impact is always found within the wind farms itself. Inside the wind farm areas and in the lateral area, the impact of the wind farms is larger during the night then during the day. This is reversed in the area downwind of the wind farms.

Hamburg is located about 100 km from the coast but still inside the area affected by the offshore wind farms. The wind speed and temperature are slightly decreased. Hamburg is located in the area of decreased relative humidity, generated by a decreased total air mass water content. The integral cloud water content decreases about 10 % compared to the reference mean. As shown by Hoffmann et al. (2012), the relevant variables for estimating the UHI of Hamburg are wind speed, cloud cover and relative humidity. All these variables are affected by the wind farms in the German Bight, and the UHI of Hamburg increases during evening hours even if the absolute value of temperature decreases in daily, night- or daytime mean. Therefore, the urban effects of Hamburg become more important when large offshore wind farms are installed in the German Bight. The temperature reduction found in this study supports the global results of Wang and Prinn (2010), who found global cooling caused by large scale wind farms if they are installed over water. The current results show that the same effect is true for the regional and, furthermore, that it might impact the development of summer urban heat islands.

4 Modelling impacts of urban development and climate adaptation measures on the summer climate of Hamburg

Preface

This chapter is intended for publication by Marita Boettcher, David D. Flagg, David Grawe, Peter Hoffmann, Ronny Petrik, K. Heinke Schlünzen, Robert Schoetter and Nora Teichert.

For this thesis, the abstract has been left out and the references and acknowledgements are summarised at the end of the thesis. The Appendix of the original publication is given in Appendix F.

The reference simulations for this study have been prepared and executed by Peter Hoffmann. Perceived Temperature calculation and the contribution of Section 4.2.3.2 and Section 4.4.3 was done by Robert Schoetter. David D. Flagg and David Grawe were involved in preparing the input data for land use. Ronny Petrik, K. Heinke Schlünzen and Nora Teichert were involved in discussing simulations.

4.1 Introduction

In addition to changes due to global climate change, urban areas develop their specific local climate by modifying the regional climate. The heat storage in the urban fabric, e.g., buildings and streets, differs from the rural areas and therefore modifies the local heat fluxes and, as a consequence, the long wave radiation budget. The albedo of urban structures influences the short wave radiation budget. The heat fluxes into the ground are changed by the sealed surfaces. The latter also decrease the latent heat flux. Furthermore, the wind field is impacted by the urban structures. These processes change the regional meteorology within the urban areas and need to be captured in numerical models to simulate the urban environment. As found by Best and Grimmond (2015), it is important to include the albedo of different building materials, the short and long wave trapping in the street canyons and the evaporation from the vegetation. Therefore, the fraction of the buildings, streets and vegetation per grid cell needs to be included. Best and Grimmond (2015) also showed that a simple representation of the processes is sufficient for the application of atmospheric models with a focus on local scale fluxes. Similar results were found by Jänicke et al. (2016) who found that the moderately complex UCM (SLUCM) and the complex UCM (BEP) also did not represent intra-urban and urban and rural differences more accurate than the simple slab scheme.

To reduce the increased urban temperatures, climate adaptation measures might be preferred. These are well investigated and typically account for the importance of urban morphology and city size on the intensity of the UHI. The influence of different urban forms was investigated for Beijing by Yang et al. (2016), who compared the UHI of a compact city to a dispersed city. They showed that a dispersed (compact) city produces a lower (higher) maximum UHI intensity but the affected area is larger (smaller). These results are in agreement with the results found by Georgescu et al. (2013) for Arizona.

Since the UHI develops because of different properties of the urban surfaces and structures (e.g., buildings and streets) compared to the rural surfaces and structures (e.g., natural soil and trees), several adaptation measures were suggested to reduce the UHI by replacing urban surface cover with natural surface cover. One approach for reducing the UHI is to establish green spaces. While street trees affect only small areas (Bowler et al., 2010), urban parks can affect neighbourhoods (Honjo and Takakura, 1991). The cooling effects of a park were measured in a downwind fetch of 20 m (Spronken-Smith et al., 2000) to 1000 m (Bowler et al., 2010; Ca et al., 1998).

Changing the solar radiation budget to reduce urban warming has been investigated by increasing the albedo of roofs, streets and pavements using white and green roofs or by unsealing parking areas and walkways. Greening of roofs and walkways not only affects the sensible heat flux but also increases the latent heat flux (Takebayashi and Moriyama, 2012). As Gross (2012) showed, the maximum surface temperature of a green roof in summer is up to 40 K lower than for a concrete roof. In the summer mean, the surface temperature of a green roof has been 2.8 K lower than for a concrete roof (Gross, 2012). A numerical study by Georgescu et al. (2014) showed a larger impact of white roofs than green roofs on regional temperatures. A combination of white and green roofs indicated the largest cooling effect on the regional climate (Georgescu et al., 2014).

Climate change adaptation measures may be assessed with respect to their potential to lower the air temperature, but to assess the relevance of these reductions to consideration of changes in the urban climate connected to adaptation measures for human thermal comfort, other measures are needed. Human thermal comfort depends on air temperature, humidity, wind speed and radiation; all these parameters influence the heat budget of the human body. A variety of thermal comfort indicators have been developed (De Freitas and Grigorieva, 2015). Their complexity ranges from single-parameter indicators (e.g. dew point temperature), algebraic or statistical models (e.g. Wet Bulb Globe Temperature, WBGT) to physically-based indicators calculating the energy balance of the human body (e.g. the Physiological Equivalent Temperature PET, and the Perceived Temperature PT).

Theeuwes et al. (2013) investigated the influence of urban lakes on the WBGT and found that the increase of humidity due to the lakes cancels out up to $\sim$ 60 percent of their cooling effect due to the lower air temperature. Müller et al. (2014) investigated the influence of various adaptation measures on PET and found that the reduction of air temperature due to construction materials with high albedo is compensated for by the enhanced reflection of solar radiation which increases the radiative temperature. These results show that there is a possibility that adaptation measures which reduce the air temperature during hot weather conditions do not necessarily lead to a large improvement of human thermal comfort since changes in humidity, wind or radiation might act in opposition to the effect of the reduced air temperature. In this study we investigate how the adaptation measures influence the temperature, the UHI and the human thermal comfort. This is evaluated by using the Perceived Temperature.

Hamburg has a maritime climate with moderate warm and moist weather conditions (Schlünzen et al., 2010). An analysis of the observational data from Fuhlsbüttel (the weather station at Hamburg airport) indicated increasing annual temperatures since the observations started in 1891 (Schlünzen et al., 2010). The annual temperatures significantly increased by 0.07 K per decade from 1891 to 2007 (Schlünzen et al., 2010). The future climate conditions of the metropolitan region of Hamburg (MRH) were investigated with two regional climate models (RCMs): REMO (Jacob and Podzun, 1997; Jacob et al., 2008, 2009) and CLM (Hollweg et al., 2008). The models were driven with the A1B projections from the general circulation model ECHAM5-MPIOM (Jungclaus et al., 2006; Roeckner et al., 2003). Results from these RCMs showed an increase of the annual averaged temperature in the range of 0.75 K to 1.75 K by the middle of the 21st century for the A1B Scenario (Daschkeit, 2011; Hollweg et al., 2008; Jacob et al., 2008). In addition, an increase in the number of summer days (daily maximum temperature >= 25 °C) and hot days (daily maximum temperature >= 30 °C) has been projected (Daschkeit, 2011). Thus, events with extreme temperatures are expected to occur more frequently. The RCMs did not include the urban impacts on climate.

In response to the widespread presence of many of the aforementioned physical differences between city and rural environments, Hamburg develops its own urban climate and urban heat island (UHI) where minimum temperatures in the city are higher compared to the rural surroundings (Schlünzen et al., 2010). The UHI of Hamburg is most pronounced during summer at the downtown climate station St. Pauli, with a mean temperature difference of 3 K compared to a rural station (Schlünzen et al., 2010). Stations in the less densely built-up urban areas of Hamburg develop a summer UHI of 0.7 K to 1.5 K (Schlünzen et al., 2010). Hoffmann et al. (2016) investigated the summer UHI of Hamburg using a statistical-dynamical downscaling (SDD) method in combination with the high-resolution numerical model METRAS (Schlünzen et al., 2012). The control experiment for the current climate showed a UHI of up to 1.2 K for the harbour areas and for downtown Hamburg. The simulated spatial pattern corresponded well with the spatial pattern of the UHI of Hamburg found from temperature proxy data by Bechtel and Schmidt (2011). The future summer UHI has been calculated for the middle and the end of the 21st century without changing the urban morphology. The statistic for the SDD method was based on the A1B projections of the two RCMs, REMO and CLM (Hoffmann et al., 2012; Hoffmann and Schlünzen, 2013). The intensity of the summer UHI was expected to change little (< 0.1 K) due to regional climate change by the middle of the 21st century (Hoffmann et al., 2012; Hoffmann and Schlünzen, 2013). Only at the end of the 21st century can larger changes be detected based on the CLM results, while results based on REMO projections showed no changes in the UHI pattern.

Since the intensity of the UHI of Hamburg is of the order of the projected temperature increase based on the A1B scenario for the MRH until the middle of the 21st century, one idea is to counteract the regional warming introduced by the global climate change by reducing the UHI. This approach has been investigated for different urban areas. For Arizona, urban expansion was found to be a strong driver for urban warming until the mid-21st century, especially compared to climate change scenarios with low emission trajectories of greenhouse gases (Georgescu et al., 2013). For the end of the 21st century, the impact of urban expansion on the temperatures is still found to be important (Georgescu et al., 2013). Therefore, Georgescu et al. (2014) suggested urban planning as a measure to offset large parts of the climate change-induced temperature increase. With the same objective in mind, Adachi et al. (2012) calculated for Tokyo a UHI that is about 75 percent of the magnitude of the projected global warming. For Beijing the UHI contributes up to 20 percent of the total warming introduced by global climate change and UHI (Yang et al., 2016).

In this study, impacts of different climate adaptation measures on the UHI are studied. In the scenarios assumed, the urban development is combined with adaptation measures to reduce the urban effects on local climate. The model-aided assessment of these measures shows to what degree future climate changes can be counteracted by adaptation measures, taking Hamburg (Germany) as an example. Adaptation measures are studied for the summer months from June to August (JJA) in order to determine the effect of these adaptation measures on the warmest months of the year where they are most needed. Three urban development scenarios are analysed, ranging from a decreased building density to a “dense city” approach. Climate adaptation measures like green roofs and changing the albedo of building materials are considered in the model input for the different scenarios. This study shall answer the question: Can the effects of climate change be compensated for by climate adaptation measures realised in urban development measures? The methodology of the study is described in Section 4.2. An overview of the urban development scenarios, the adaptation measures investigated and their realisation in a numerical model is given in Section 4.3. The results are presented and discussed in Section 4.4. Conclusions are drawn in Section 4.5.

4.2 Modelling methodology

The present study employs the numerical mesoscale model METRAS, which is briefly introduced in Section 4.2.1. The method of SDD and the meteorological situations selected are presented in Section 4.2.2. The methods for data analysis are given in Section 4.2.3.

4.2.1 Model set-up

METRAS (Schlünzen, 1990; Schlünzen et al., 2012) is a non-hydrostatic, three-dimensional, numerical model of the atmosphere. The model has been extensively used to simulate atmospheric phenomena with horizontal scales between 100 meters and several kilometres (Schlünzen, 1990). It has been applied and evaluated for Northern Germany and the metropolitan region of Hamburg (Chapter 3 and Hoffmann et al. (2016); Schlünzen (1990); Schoetter et al. (2013)). The model settings employed in this study are described in Chapter 3 and Hoffmann et al. (2016) and summarised in the Appendix F. The method of modelling the surface energy balance with its urban specifics is given in Section 4.2.1.1. In Section 4.2.1.2, an overview of the model domain is provided.

4.2.1.1 Subgrid-scale land use and surface energy balance

METRAS is able to consider the heterogeneous land surfaces of urban and rural areas on a subgrid-scale level instead of only one main land use per grid cell. Each grid cell consists of a variable number of surface cover classes (SCCs). The combined effect of these SCCs on the meteorological variables is computed by applying a flux aggregation method with blending height (Von Salzen et al., 1996). The different SCCs are characterised by their albedo, soil water availability, saturation value for soil water content, thermal diffusivity, thermal conductivity, and roughness length. A subset of SCCs and the corresponding parameter values are given in Table 4.1.

The surface temperature is calculated from the surface energy budget equation by using the force-restore method (Deardorff, 1978). The humidity at the surface is calculated from a budget equation following Deardorff (1978). With these methods, the heat storage in urban materials, reduced evaporation, albedo of urban materials and the higher aerodynamical roughness are parameterised. The effects of vegetation and buildings are both considered to be at the ground surface, neglecting details of the vertical structure. Their dynamical effect is considered by an enhanced roughness length (Table 4.1). The turbulence parameterisation and flux aggregation method employed imply that METRAS results are calculated as results at 10 m above displacement height. Values below 10 m are not predictable for a grid cell with these methods. Since obstacles such as building and trees are not explicitly resolved in METRAS, the effects of radiative trapping are not considered. In addition, the effect of anthropogenic heat is not included in the version of METRAS used in this study.

Urban structures as given in land-use datasets are linked to several generic SCCs (Table 4.1). For example, the land-use class “detached house” from a land-use dataset is represented in METRAS by different fractions of SCCs, namely “grass”, “bushes”, “trees”

Table 4.1: Subset of surface cover classes (SCC) used in METRAS. The SCCs developed for representing the three socio-economic scenarios and the corresponding reference surface cover classes (bold letters) are given. The parameters that are unchanged compared to the reference SCC are indicated by “-”.

SCC	Albedo A [.]	Initial soil water availability α [.]	Saturation value for soil water content W $[m]$	Thermal diffusivity κ $[m^2/s]$	Thermal conductivity ν $[J/Km]$	Roughness length z_0 $[m]$
Short, dry grass	**0.20**	**0.35**	**0.05**	**5.2E-07**	**1.33**	**0.01**
Short bushes	**0.20**	**0.35**	**0.09**	**5.2E-07**	**1.33**	**0.10**
Asphalt	**0.09**	**0.50**	**0.0015**	**2.3E-06**	**1.35**	**0.0003**
Asphalt, increased albedo	0.20	-	-	-	-	-
Concrete	**0.15**	**0.50**	**0.0015**	**2.3E-06**	**1.81**	**0.0003**
Concrete, increased albedo	0.35	-	-	-	-	-
Brick/Pavers	**0.30**	**0.02**	**100.00**	**2.3E-06**	**0.90**	**0.0006**
Brick/Pavers, increased albedo	0.40	-	-	-	-	-
Low-buildings with sealed surroundings	**0.18**	**0.50**	**0.0015**	**1.4E-06**	**2.61**	**0.6000**
Low buildings with sealed surroundings, increased albedo	0.60	-	-	-	-	-
Low buildings with sealed surroundings, green roof	0.20	-	100.00	-	-	-
Low buildings with sealed surroundings, grass pavers	0.20	0.05	0.05	-	-	-
Low buildings with sealed surroundings, increased albedo and grass pavers	0.60	0.05	0.05	-	-	-

continued on next page

continued from page before

SCC	Albedo A [.]	Initial soil water availability α [.]	Saturation value for soil water content W $[m]$	Thermal diffusivity $\kappa\ [m^2/s]$	Thermal conductivity $\nu\ [J/Km]$	Roughness length $z_0\ [m]$
Low buildings with sealed surroundings, green roof and grass pavers	0.20	0.55	100.00	-	-	-
High-buildings with sealed surroundings	**0.18**	**0.50**	**0.0015**	**2.3E-06**	**3.44**	**1.2000**
High buildings with sealed surroundings, increased albedo	0.60	-	-	-	-	-
High buildings with sealed surroundings, green roof	0.20	-	100.00	-	-	-
High buildings with sealed surroundings, grass pavers	0.20	0.05	0.05	-	-	-
High buildings with sealed surroundings, increased albedo and grass pavers	0.60	0.05	0.05	-	-	-
High buildings with sealed surroundings, green roof and grass pavers	0.20	0.55	100.00	-	-	-

and “low buildings” while the land-use class “high-rise buildings” from a land-use dataset is represented by other fractions of SCCs including an SCC named “high buildings”. The representation of both of these land-use classes from a land-use dataset by SCCs also accounts for any adjacent sealed surfaces (sealed driveways, sidewalks, footpaths, patios, parking spaces, etc.). Urban development scenarios in land use investigated in this study are mapped to changes of the SCCs and their fractional covers (Section 4.3).

An evaluation study of an earlier version of METRAS indicated that the realistic initialisation of the atmospheric profile and the modelling of the subgrid-scale surface fluxes with flux aggregation improves the model results, especially for the latent heat fluxes (Schlünzen and Katzfey, 2003). The urban canopy parameterisation BEP (Martilli et al., 2002) coupled to METRAS (Grawe et al., 2013) does not include vegetation. Furthermore, simulations with METRAS coupled to BEP show a more intense UHI but also a decrease in the model performance with respect to other meteorological variables, e.g., wind speed and wind direction (Grawe et al., 2013). Therefore, flux aggregation is applied in this study. Schlünzen and Katzfey (2003) showed that METRAS performs well with the flux aggregation method.

4.2.1.2 Model domains

The urban climate of the metropolitan region of Hamburg is investigated with an SDD method. Three refinement steps are made to downscale the ECMWF analysis data to a horizontal resolution of 250 m. The coarsest model grid of METRAS has a 4 km horizontal grid resolution (HH4) and covers Northern Germany, the German Bight and parts of The Netherlands, Denmark, Poland and the Baltic Sea (Figure 4.1). To simulate the metropolitan region of Hamburg in more detail, two additional model grids with horizontal resolutions of 1 km (HH1) and 250 m (HH250) are 1-way nested within HH4. Model domain HH1 covers the area of Hamburg and the surroundings up to a distance of $\sim$ 100 km from the city centre (Figure 4.1). The highest resolving grid, HH250, covers the state of Hamburg (Figure 4.1). The characteristics of the three model domains are summarised in Table 4.2.

All three model domains use the same vertical grid. Close to the surface the vertical grid size is 20 m with the lowest grid level at 10 m above ground. Above 100 m above ground, the vertical grid size increases by 17.5 percent per grid cell to a maximum grid size of 1000 m at 5000 m above ground. The domain includes 34 model levels with 19 levels in

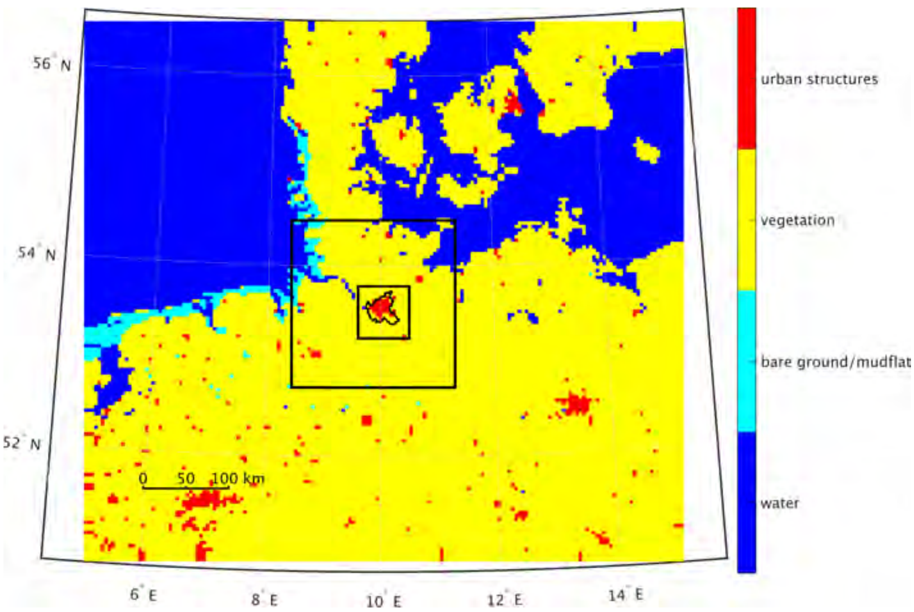

Figure 4.1: Surface cover classes grouped into four main groups for the HH4 model domain. Note that the figure shows only the groups with the highest percentage per grid cell. The numerical model considers subgrid-scale land uses. The black rectangles mark the HH1 and the HH250 model domains. The state boundary of Hamburg is marked with a black line.

the lowest 2000 m. The highest model level is at 12000 m.

4.2.2 Meteorological situations

This study focuses on the summer climate of Hamburg. The objective is to determine average impacts of urban development and adaptation measures on the urban climate; thus the 30-year mean values need to be represented. An SDD method is used to assess the summer climate based on selected weather periods consisting of several days. To determine how many days are required, the hourly data of a 30-year time series of 27 weather stations in Northern Germany and The Netherlands are analysed in Section 4.2.2.1. The selected days are given in Section 4.2.2.2.

4.2.2.1 Selection criterion

The assessed weather stations are selected and the station data are prepared following the method developed by Martens (2012). Probability density functions (PDFs) for the

Table 4.2: Characteristics of the METRAS model domains and the forcing data employed.

Domain	Horizontal grid resolution	Total grid area	Number of horizontal grid cells	Parent grid for forcing	Model start time on initialisation day	Integration period for each simulation	Output interval	First update of forcing data	Forcing interval
HH4	4 km	700 × 628 km^2	175 × 157	ECMWF analysis data	2000 local time	Three days and four hours	30 minutes	0000 local time on the first simulation day	Six hours
HH1	1 km	191 × 194 km^2	191 × 194	HH4	2100 local time	Three days and three hours	30 minutes	0000 local time on the first simulation day	30 minutes
HH250	250 m	59.75 × 60.25 km^2	239 × 241	HH1	2200 local time	Three days and two hours	30 minutes	0000 local time on the first simulation day	30 minutes

summer (JJA) are calculated for meteorological variables for the years 1981 to 2010. The variables selected are relevant to calculate human thermal comfort in urban areas and the UHI. Therefore, temperature (TC), relative humidity (RH), wind speed (FF) and wind direction (DD) are used, since they are linked with UHI (Hoffmann et al., 2012). A bin size of 1 K for temperature, 5 % for relative humidity, 1 m/s for wind speed and 30° for wind direction is used. The wind direction from the north (360°/0°) is used as the centre for the first bin of wind direction, including values from 345° to 15°. A skill score is used for PDF comparison to determine if PDFs of all data (climate average) agree with a PDF based on a limited number of days. This skill score will be used to determine the number of days needed for sufficient representation of the climatological average.

The Skill Score (SSP) introduced by Perkins et al. (2007) assesses the overlap of two PDFs Z_M and Z_O. If n is the number of bins and Z_{M_i} and Z_{O_i} the probability density for the i$^{\text{th}}$ bin of the distributions M and O, the SSP is given by Equation (4.1). An SSP equal to one denotes a perfect agreement while an SSP equal to zero means no overlap of the two PDFs. Perkins et al. (2007) consider an SSP > 0.8 as a good agreement between the two PDFs and SSP $= 0.9$ as near-perfect agreement.

$$\mathrm{SSP} = \sum_{i=1}^{n} \mathrm{minimum}(Z_{M_i}, Z_{O_i}) \tag{4.1}$$

Calculating the SSP per variable does not take into account relationships between different variables. Therefore, the possible dependency of the temperature on, e.g., wind speed or relative humidity is not considered. These relations are, however, of large relevance for determining the UHI, which depends on wind speed and relative humidity (Hoffmann et al., 2012). Furthermore, the number of days required to represent the distribution of temperature is not necessarily sufficient for reflecting the distribution of relative humidity and wind speed at a given temperature. To consider the relationships between the PDFs of the different variables, the SSP is extended to a bivariate Skill Score (BSS).

The BSS is based on a joint PDF. For each bin of the PDF of the first variable, e.g. temperature, the time-corresponding values of the second variable, e.g. relative humidity, are calculated as a dependent second PDF. The result is a joint PDF of the temperature and relative humidity. Similar to the SSP, the BSS (Equation 4.2) is the sum of the minima of the dependent two-dimensional PDFs Z_O and Z_M, where n and m are the number of bins for each dimension. Like SSP the BSS is one if both two-dimensional

PDFs overlap perfectly and zero if they have no overlap at all.

$$\mathrm{BSS} = \sum_{i=1}^{m} \sum_{k=1}^{n} \mathrm{minimum}(Z_{M_{ik}}, Z_{O_{ik}}) \tag{4.2}$$

The bivariate skill score was applied to 27 weather stations using the data of 30 summers from 1981 to 2010. The assessment criteria for BSS cannot be as high as the criteria for the SSP because of the non-perfect consistency of the dataset. One thousand resamples of the full dataset are extracted with the bootstrap method, and the BSS is calculated for each resample of each weather station. The mean BSS determined by this method is a measure of the statistical robustness and completeness of the observational dataset. It is named the level of accuracy (LOA) in the following discussion. The LOA is the value that can be maximally reached by the BSS, calculated with a reduced number of data. The LOA is always below one (Table 4.3). The assessment criteria given by Perkins et al. (2007) are adapted by multiplying the criteria by the LOA. The values of the BSS for a good result (BSS 0.77 to 0.78 for the different variable combinations) and a near-perfect result (BSS 0.86 to 0.87 for the different variable combinations) are given in Table 4.3.

The BSS is calculated with different numbers of days (1 to 300 days) selected out of the full dataset. The BSS for each number of selected days is then calculated as a mean from 1000 resamples built by bootstrapping.

Figure 4.2a shows the BSS of TC/RH as a function of the number of selected days for each weather station, along with the 5$^{\text{th}}$ and 95$^{\text{th}}$ percentiles, which are determined from bootstrapping as measure of uncertainty. The LOA for the BSS is given with a thick black line while the criteria for a good and a near-perfect result are marked with a thin black and a blue line, respectively. An asymptotic solution towards the LOA is noticeable for the BSS TC/RH for a higher number of selected days. The BSSs for the other combinations of the variables show the same behaviour (not shown). The BSSs built with 60 randomly chosen days fit the range between the assessment criteria for each combination of the variables (Table 4.3). The gradient of the BSSs for 60 selected days is small and a higher number of days only slightly increases the BSSs. Therefore, 60 days are selected as the optimal total number of days required for representing the urban summer climate of Hamburg with good accuracy. The numbers of selected days needed to reach the criteria for good/near-perfect results are given in Table 4.3 for all variable combinations.

Table 4.3: Level of accuracy (LOA), assessment criteria and required number of days for reaching the assessment criteria of the bivariate skill score (BSS). The last column gives the BSS for 60 randomly chosen days. TC denotes temperature, RH relative humidity, FF wind speed and DD wind direction.

BSS	LOA	Good result	Near-perfect result	Required number of days for good/near-perfect result	BSS for 60 days
TC/RH	0.96	0.77	0.86	37/100	0.82
TC/FF	0.97	0.78	0.87	33/96	0.83
RH/FF	0.97	0.78	0.87	26/77	0.85
DD/RH	0.96	0.77	0.86	34/91	0.82
DD/FF	0.97	0.78	0.87	29/82	0.84
DD/TC	0.96	0.77	0.86	44/119	0.80

(a) (b)

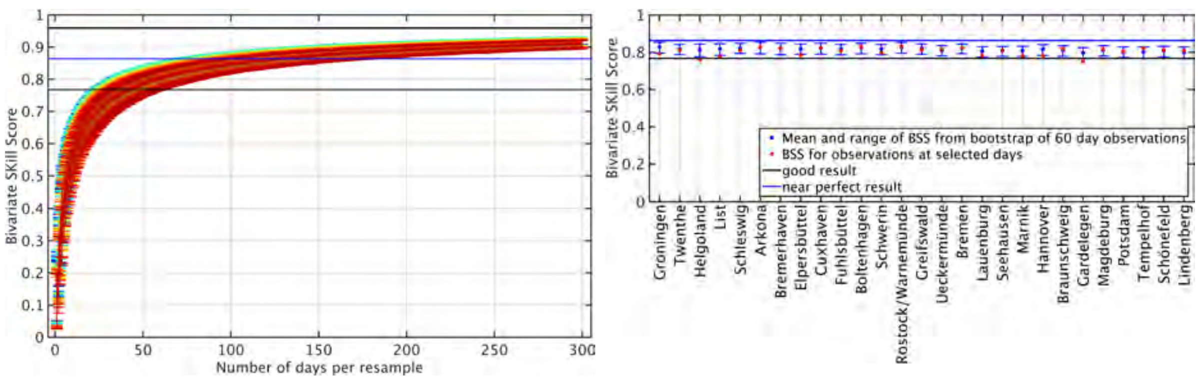

Figure 4.2: Examples of (a) the mean of the bivariate skill score (BSS) for TC/RH for each weather station with its 5th and 95th percentile as a function of the number of randomly chosen days and (b) the BSS for 60 days for each weather station for TC/RH. The blue dots and error bars mark the median and the range of uncertainty of 60 randomly chosen days. The red dots mark the bivariate skill score of the 60 days selected for simulation.

Figure 4.2b shows the mean BSS of TC/RH and the 5th and 95th percentiles for each weather station from bootstrapping of 60 days with blue dots and error bars. The assessment criteria for a good and a near-perfect result are marked with a black and a blue line, respectively. The mean BSS for each weather station and each combination of variables is between a good and a near-perfect result (not shown). For some weather stations the 5th percentile BSS of DD/TC is lower than the mean assessment criteria for a good result. However, the BSS of DD/TC is the only exception. Therefore, 60 days is accepted as representing the full dataset.

4.2.2.2 Selected days for representing the summer climate

As shown in Section 4.2.2.1, the joint PDFs of hourly meteorological variables with relevance for the urban summer climate can be represented well with 60 randomly chosen days out of a 30-year sample. In theory, the days chosen to compute the BSS are independent from each other. In contrast to the theory, the 60 days used in the present study are selected with a weather pattern classification (WPC) (Hoffmann and Schlünzen, 2013) and are not independent from each other but consist of 20 periods of three days each.

Huth et al. (2008) have shown that there is no generally best WPC. The WPC has to be adapted for each target variable and target area. In the study of Hoffmann and Schlünzen (2013), a WPC is developed for the mean strong summer UHI of Hamburg. The k-means based clustering is done using the 700 hPa field from the ERA 40-reanalysis (Uppala et al., 2005). Seven weather patterns (WPs) were determined to be important. Using only the meteorological situations of the cluster centres of each WP leads to a low variance of UHI. Therefore, Hoffmann and Schlünzen (2013) subdivided each WP according to the strength of the UHI. From each WP, three weather situations were selected that characterise the maximum UHI, the cluster centre and the weather situation resulting in a UHI next to a threshold for UHI of 3 K. In one WP the maximum and threshold UHI resulted in the same weather situation; thus 20 unique weather situations consisting of 3 days were found.

This leads to a total number of 60 days. The BSS is used to analyse the PDFs of the 60-day simulated to test whether they adequately represent the summer climate of Hamburg. For most BSSs at most weather stations, the BSSs are in the range of good results. See, for example, the BSS of TC/RH for the selected 20 weather situations, marked with red dots for each weather station in Figure 4.2b. Only very few weather stations show BSS values below "good" and only for some combinations of variables, e.g., Gardelegen and Magdeburg, which are away from the target region of Hamburg. Fuhlsbüttel, the weather station at Hamburg airport, shows good results. This is also the case for weather stations close to Hamburg. Therefore, the 60 selected days based on 20 weather situations are found to represent the summer climate of Hamburg well. Thus, these 20 different weather situations are simulated using METRAS.

4.2.3 Method for model result analysis

In Section 4.2.3.1, the method of assessing the impact of the scenarios on the urban climate is given. In Section 4.2.3.2, the offline calculation of perceived temperature is described.

4.2.3.1 Urban and scenario effects

Each of the 20 selected weather situations (Section 4.2.2) consists of three days, which are simulated with METRAS. The model output is written every 30 minutes. Results are analysed at the lowest model level (10 m above ground). Differences between scenario and reference cases are always calculated as scenario minus reference value. To estimate differences between urban and rural areas, these respective areas need to be defined. The corresponding urban and rural areas are determined by circles with radii of 10 km and 20 km around the centre of Hamburg, located at the town hall. The area with the radius $<=$ 10 km fits well with the highly sealed areas of Hamburg and the area with a radius of 20 km (10 km $<$ radius $<=$ 20 km) fits well with the rural areas close to the city. To enlarge the radius further would force consideration of areas far away from the city, and therefore the results could be influenced by mesoscale weather phenomena interacting with the urban effects. To avoid altitude effects by orography, only grid cells with a surface height between 0 m and 30 m above sea-level are considered in the evaluation. In this study, grid cells are defined to be "urban" if they are at least 50 percent sealed, while rural grid cells are defined as those that have no sealing (zero percent). Grid cells containing water areas are neglected to avoid the damping effects of water bodies on the temperature cycle. Figure 4.3 shows the grid cells defined by this method. The grid cells defined by this method for the reference case are the same as used for the scenario simulations, so differences generated by the scenarios can be estimated. All grid cells considered are at least 10 grid cells from the lateral boundaries to avoid direct effects from nudging.

The mean horizontal pattern of the meteorological variables (e.g. temperature, relative humidity) is assessed at 10 m above ground. The average of the 60 simulated days is calculated for each model output time and each variable. To illustrate the impact of the adaptation measures, the absolute values for the reference simulations are given adjacent to the differences of scenario minus reference simulation. The spatial patterns of the variables are given for daytime (0700 LT to 2000 LT) or nighttime (2200 LT to 0500 LT). The spatial patterns of urban cool island (UCI) and UHI are only calculated for Hamburg. The spatial patterns result from the 10 m temperature at each grid cell in the urban Hamburg minus the mean 10 m temperature at the grid cells determined as rural. For UCI and UHI, morning (0700 LT to 1100 LT) and evening (1900 LT to 2300 LT) mean patterns are calculated.

4.2.3.2 Perceived temperature calculation

Reducing the UHI is one important part of urban climate adaptation measures. Even if the resulting variables themselves are in a range comfortable for humans, the resulting human thermal sensation is not necessarily improved. Thus, one of the goals of climate change adaptation is the improvement of human thermal comfort, which depends not only on air temperature but also on humidity, wind speed and radiation. In this study, we use the perceived temperature (PT) (Staiger et al., 2012) which has been developed by the German Meteorological Service (DWD). PT is a temperature which would be perceived by a reference human body in a reference environment if the mean radiant temperature were equal to the air temperature with a wind speed of 0.1 m/s, and relative humidity of 50 percent. PT is based on a heat budget equation of the human body accounting for metabolic heat production, radiative heat transfer at the skin as well as the sensible and latent heat exchange by respiration and by the skin. The reference human adapts its clothing within certain limits in order to achieve thermal comfort. According to De Freitas and Grigorieva (2015), PT belongs to the group of the most enhanced thermal comfort indicators since it is physically based, solving the heat budget equation of a reference human body. However, a number of simplifications are made when using PT to define human thermal comfort.

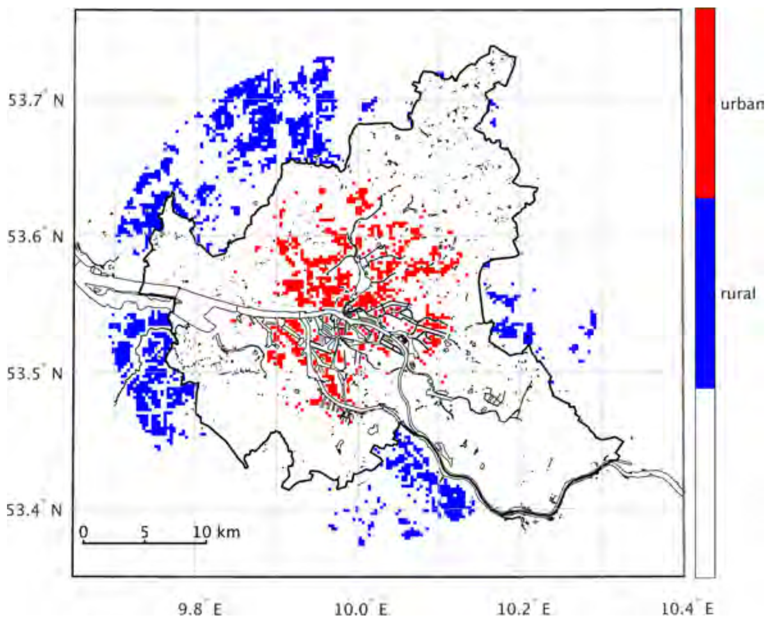

Figure 4.3: Urban (red) and rural (blue) grid cells as defined in Section 4.2.3.1. The state boundaries of Hamburg are marked with a thick black line, water bodies are marked with thin black lines.

- It is assumed that the humans adapt their clothing in order to achieve thermal comfort. If this is not the case (e.g. due to cultural reasons), thermal stress will be more frequent than indicated by PT.
- PT neglects differences between humans. The heat budget is calculated assuming a male person of 35 years, weight of 75 kg and 1.75 m tall, walking on flat ground. Persons deviating from these characteristics will experience a different thermal comfort than indicated by the PT.
- PT depends only on the actual meteorological conditions. That there might be a physiological or psychological adaptation to the prevailing climatic conditions is thus neglected (Cheng et al., 2012; Vanos et al., 2012).
- PT is based on a steady-state and one-node model of the human body. Vanos et al. (2012) point out that such thermal comfort indicators neglect to consider that different parts of the body might experience different levels of heat stress and they neglect effects of rapidly changing atmospheric conditions.

These above simplifications seem acceptable for this study and we use PT, developed by the DWD for application in Germany, to analyse the influence of the adaptation measures on the climatology of human thermal comfort in Hamburg.

Air temperature, water vapour pressure, wind speed and the short- and long wave up- and downwelling radiative fluxes are required for PT calculation. These variables are taken from the METRAS results. PT is calculated for a person standing on asphalt in an open area. We interpolate the values of air temperature, specific humidity and wind speed simulated at 10 m above ground (lowest model level) to 2 m (air temperature and specific humidity) and 1 m (wind speed), assuming an open asphalt area. The stability functions for momentum and scalar quantities implemented in METRAS (Schlünzen et al., 2012) and the friction velocity, friction temperature and friction humidity simulated for the surface cover class "asphalt" are used for this purpose. This class is calculated in each grid cell but might be considered in the averaged values with zero weight due to the subgrid-scale land cover data considered. The simulated long- and shortwave radiation values are used directly. The reflected shortwave radiation is calculated using the albedo of asphalt. The longwave upwelling radiation is calculated based on the surface temperature simulated for asphalt, assuming an emissivity of 0.95.

Based on this method, the results are valid for a male person standing on asphalt in an open area. One has to keep in mind that human thermal comfort is additionally influenced by shading and radiation trapping in narrow street canyons (Schoetter et al., 2013). This is not considered in the present study.

4.3 Scenarios for urban developments and climate adaptation measures

The future structure of the city of Hamburg as well as the climate adaptation measures implemented depends on the socio-economic development of the MRH. For this reason, potential pathways of the future demography, economy, and environmental awareness have been developed by Rottgardt et al. (2014). The adaptation measures suggested in their study are based on socio-economic scenarios, with assumptions about population development, financial circumstances and environmental awareness for the year 2050. In Section 4.3.1, the technical realisation of the scenarios in METRAS is described, while in Section 4.3.2 the three scenarios and their effect on the input parameters for METRAS are illustrated.

4.3.1 Scenarios realised in METRAS

To take into account the adaptation measures included in the three socio-economic scenarios studied in this paper, new SCCs (Section 4.2.1.1) dealing with the parameter values of the adapted areas are developed. By changing the SCCs or the percentage of SCCs within a grid cell compared to the reference situation, the urban development is mapped according to the three socio-economic scenarios. An overview of the new SCCs, their corresponding reference SCCs and the changed parameters is given in Table 4.1.

The albedo describes the reflectivity of surfaces and directly influences the short wave radiation budget. Increasing the albedo leads to a higher reflectivity and reduces the warming of the surfaces. Changes in the albedo of building materials are applied for transport areas (asphalt, concrete and pavers) and for buildings. In the case of buildings, a relevant part of albedo change is the roof. Therefore, the albedo for the SCCs low and high buildings is mainly determined by the roof albedo. Examples of albedo for different materials are given in Gross (2012) and Back (2011). The values used in this study (Table 4.1) are chosen at the upper limit of the given range to yield a clear difference from the reference value while remaining physically plausible.

Green roofs affect their surrounding by two different processes: albedo and evaporation (Gross, 2012). The effect of green roofs depends on the available amount of water. In this study, irrigated green roofs with perpetually sufficient water availability are investigated. Therefore, the water availability for low and high buildings with green roofs is set to a very high value. This approach permits representation of green roofs with a large water reservoir or with irrigation (Table 4.1). The albedo for these SCCs is mainly determined by the albedo of the roofs. Thus, the albedo is set to the albedo used in this model for grass and short bushes (Table 4.1).

Unsealing of parking areas and walkways is represented in the model by using interlocking stone pavers containing grass surfaces, hereafter called grass pavers, for these areas. Therefore, the albedo for these new SCCs is close to the albedo of grass. The water availability is set to the water availability of grass while the water saturation is set close to the value for brick/pavers. As a result of these parameter values, the evaporation for areas with grass pavers is slightly higher after a rainfall event than in the reference SCC but becomes small after a few days without rain, representing the depletion of the water reservoir during a drier period.

In scenario s3 additional SCCs that combine changes of roof albedo and grass pavers or green roofs and grass pavers are considered. The parameter values set for these SCCs are combinations of those set according to the aforementioned adaptation measures.

The thermal diffusivity and conductivity and roughness length parameters in the new SCCs are not different from those of the reference SCC. The reference values are listed in Table 4.1 (bold letters) along with the changed values of SCCs for the new SCCs introduced in the scenarios. The assumed changes of building density and height in the three socio-economic scenarios are realised in the simulations by changing the land use class from low to high-rise buildings. The SCCs low and high buildings differ in the building height and, therefore, in thermal diffusivity and conductivity as well as in roughness length, so the percentage of the mentioned SCCs per grid cell is changed to represent the changes in this land use class. A decrease of building density is realised by decreasing the percentage of low and high buildings and increasing green areas in a grid cell, while an increased building height is realised by an increased fraction of high buildings and a corresponding reduction of low buildings in the corresponding grid cell. Changes in the fraction of different SCCs per grid cell result in changes to the effective thermal diffusivity and conductivity as well as roughness length of a grid cell even if the parameters of the SCCs involved are not changed.

The impacts of the new SCCs on surface and 10 m temperature are tested with a 1-D version of METRAS, which only computes equations in a single vertical column. The results are compared with those from the reference SCCs. For each SCC the model is integrated for three summer weeks when the incoming solar radiation is high. This ensures soil and vegetation drying effects can be seen. The simulations are started for a situation with sufficient soil water and immediately after the end of a rainfall event, meaning the soil is wet with puddles on the sealed surfaces. Results for the surface and the 10 m temperature are given in Figure 4.4.

During the first days of simulation, the maximum temperatures are influenced by the past rainfall and are, therefore, lower than at later days. The longer after the rainfall event, the more the surface dries due to evaporation, and the more the temperature amplitude and the temperature maximum increase. The increase depends on the SCC. After a few days the amplitude, maxima and minima of the surface temperature achieve equilibrium values (Figure 4.4a, Figure 4.4c and Figure 4.4e). The corresponding temperature at 10 m is still increasing (Figure 4.4b, Figure 4.4d and Figure 4.4f). After about 13 days

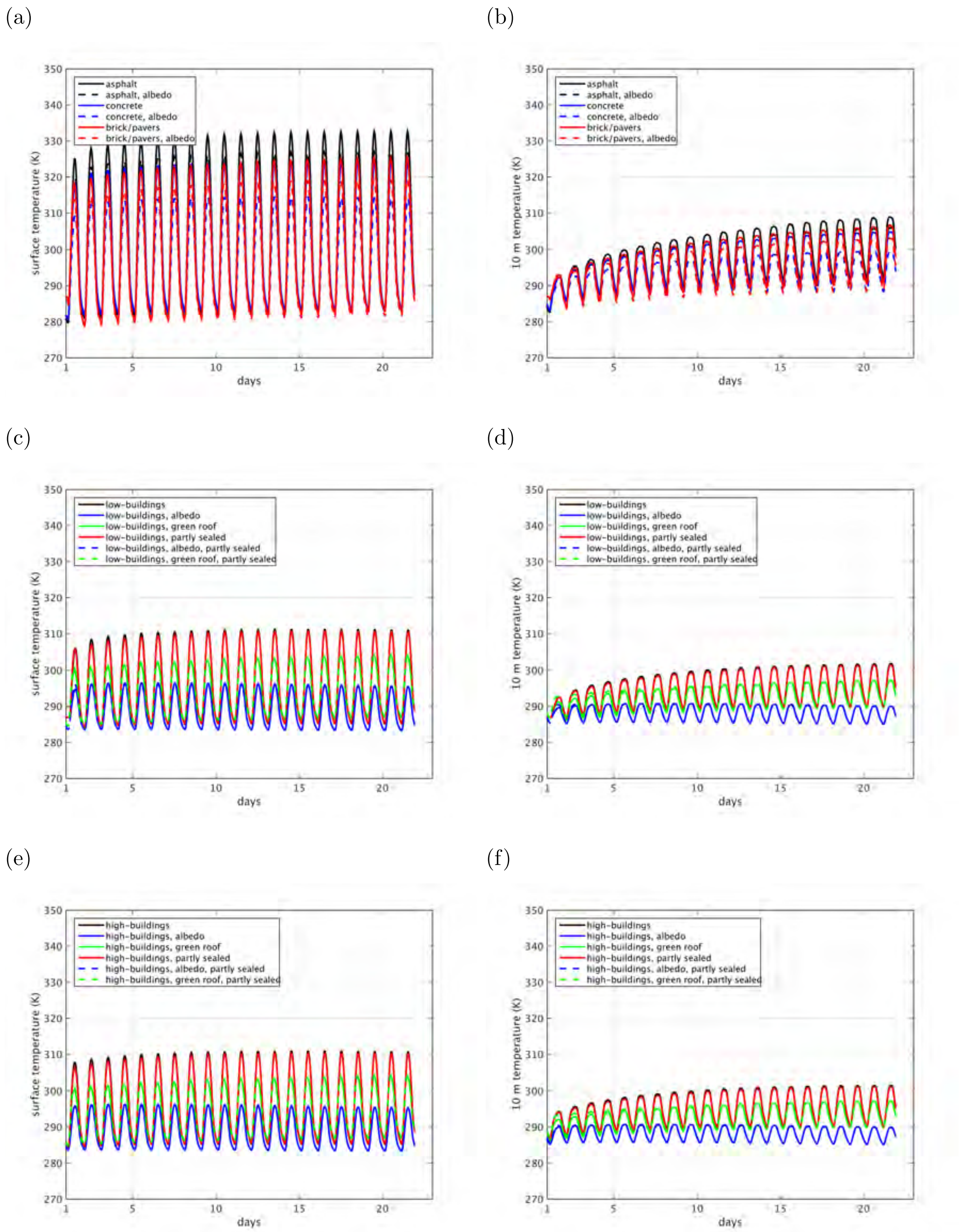

Figure 4.4: Temperature for the SCCs newly developed for the scenarios and the reference SCCs; (a),(c),(e) are surface temperature and (b),(d),(f) are temperature at 10 m above ground.

the diurnal cycle of the 10 m temperature is fully developed over SCCs low and high buildings (Figure 4.4d and Figure 4.4f). The 10 m temperatures over the SCCs asphalt, concrete and brick/pavers still increase despite the constant amplitudes of the diurnal cycle of the surface temperature.

The largest effect of adaptation measures results from albedo changes for SCCs low and high buildings. The surface temperature decreases about 15 K while the 10 m temperature decreases about 10 K (Figure 4.4c to Figure 4.4f). The decrease in 10 m temperature amounts to about 5 K for SCCs asphalt, concrete and brick/pavers (Figure 4.4b). The differences between albedo values for the reference and the new SCCs of asphalt, concrete and brick/pavers are smaller than the differences for low and high buildings. The effect of green roofs for SCCs low and high buildings is in the range of 8 K for surface temperature and 5 K for 10 m temperature (Figure 4.4d and Figure 4.4f). The effect of grass pavers is small compared to the other temperature reductions with $1-2$ K for the surface and less than 1 K for the 10 m temperature (Figure 4.4a and Figure 4.4b).

The 1-D results are valid for homogeneous areas of unlimited size covered with a single SCC. Therefore, they reflect possible upper limits that will not be found in realistic urban morphologies. In a 3-D model with subgrid SCCs and a grid resolution of a few hundred metres or coarser, the impact of any adaptation measure is much smaller, because the contribution of the new SCCs to the total surface cover of a grid cell is small.

4.3.2 Scenario characteristics

Possible urban developments are realised by three socio-economic scenarios within the HH250 domain. All simulations are performed for the reference situation and the three scenarios. The surface cover for the reference situation is derived from current land use. The three socio-economic scenarios, s1, s2 and s3, are based on three different urban development scenarios for the year 2050: Decreasing population size and ageing population with reduced public funds are assumed in scenario s1 (Section 4.3.2.1), a stagnant number of inhabitants with sufficient public funds in scenario s2 (Section 4.3.2.2), and a growing city with good public funds in scenario s3 (Section 4.3.2.3). A varying number of adaptation measures are implemented in each scenario, based in part on the number of inhabitants and the financial circumstances. Adaptation measures and environmental conditions considered in the scenarios include changes in the albedo of building materials, intense greening of roofs, unsealing of urban areas (e.g. parking areas and walkways), heightening of existing buildings and changes in the building density ("compact city" approach). The amounts of changes in the land-use data are given in Kruse et al. (2014). These changes are linked to the SCCs and, therefore, the simulations differ in the SCCs employed.

4.3.2.1 Scenario 1

Scenario s1 assumes a decreasing number of inhabitants and ageing of the population due to low birth rate and conservation and deconstruction as a private responsibility (Rottgardt et al., 2014). Low public funds lead to less support for the urban infrastructure, e.g. public transport. The area covered by buildings is slightly decreased, while sealed surfaces are slightly increased in residential areas because of increased individual transport. Adaptation measures are not implemented because financial support is lacking.

The fractions of sealed surfaces for apartment buildings and industrial areas are slightly decreased (Figure 4.5a), and thus the fraction of evaporative surfaces is increased (Figure 4.5b). The changes are small and therefore no differences are visible in the difference of albedo between the current situation and the scenario (Figure 4.5c). The roughness length slightly decreases in the areas with decreased building density (Figure 4.5d).

4.3.2.2 Scenario 2

In scenario s2, a thriving economy and an increasing demand for land is assumed with a stagnation in the number of inhabitants but with sufficient private funds so the demand for living space increases (Rottgardt et al., 2014). This leads to more dense urban areas (compact city), in both residential as well as commercial areas. Individual transport and sealed surfaces are slightly decreased because of a well-developed public transport system. Adaptation measures are sporadically implemented because of an assumed minimal financial support by public funds.

The fraction of sealed surfaces is increased in the city and the northern suburbs and slightly increased in the southern suburbs compared to the reference situation (Figure 4.6a). Green roofs and grass pavers installed in the inner city and the southern suburbs add to the green spaces within the more compact parts of the city (Figure 4.6b) so that the fraction

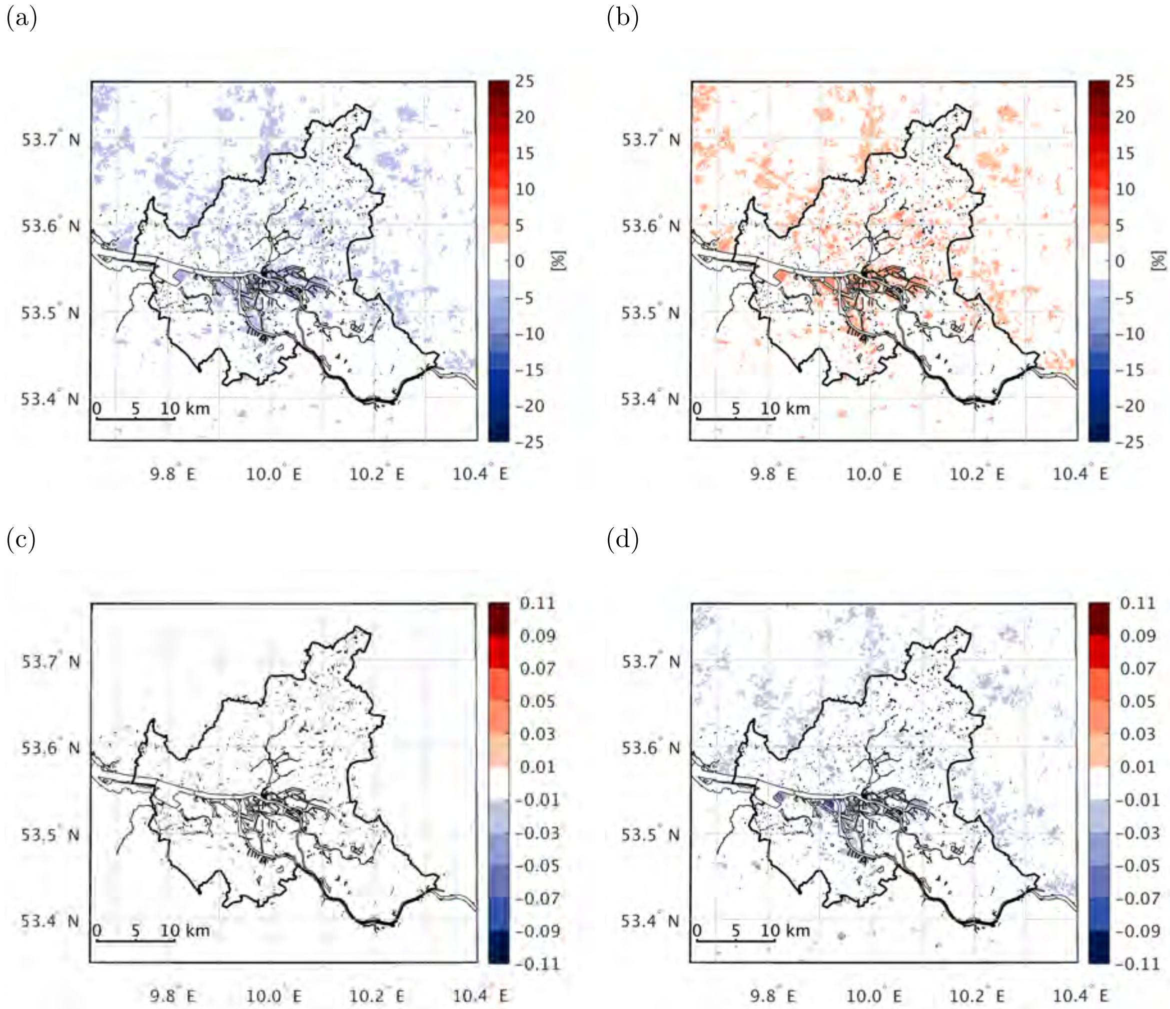

Figure 4.5: Changes in scenario s1 compared to the reference case for (a) fraction of sealed surfaces, (b) fraction of evaporative surfaces, (c) albedo and (d) logarithmic averaged roughness length. Blue (red) denote decrease (increase) in the scenario compared to the reference case. The state boundaries of Hamburg are marked with a thick black line and the thinner lines illustrate the water bodies of Hamburg.

of evaporative surfaces increases. The small amount of green roofs and grass pavers assumed in the northern suburbs does not add sufficient amounts of evaporative surfaces to counteract the larger area of sealed surfaces. The increased fraction of sealed surfaces is also reflected in an increased roughness length (Figure 4.6d). Building materials with high albedo used for private buildings lead to an increased albedo (Figure 4.6c).

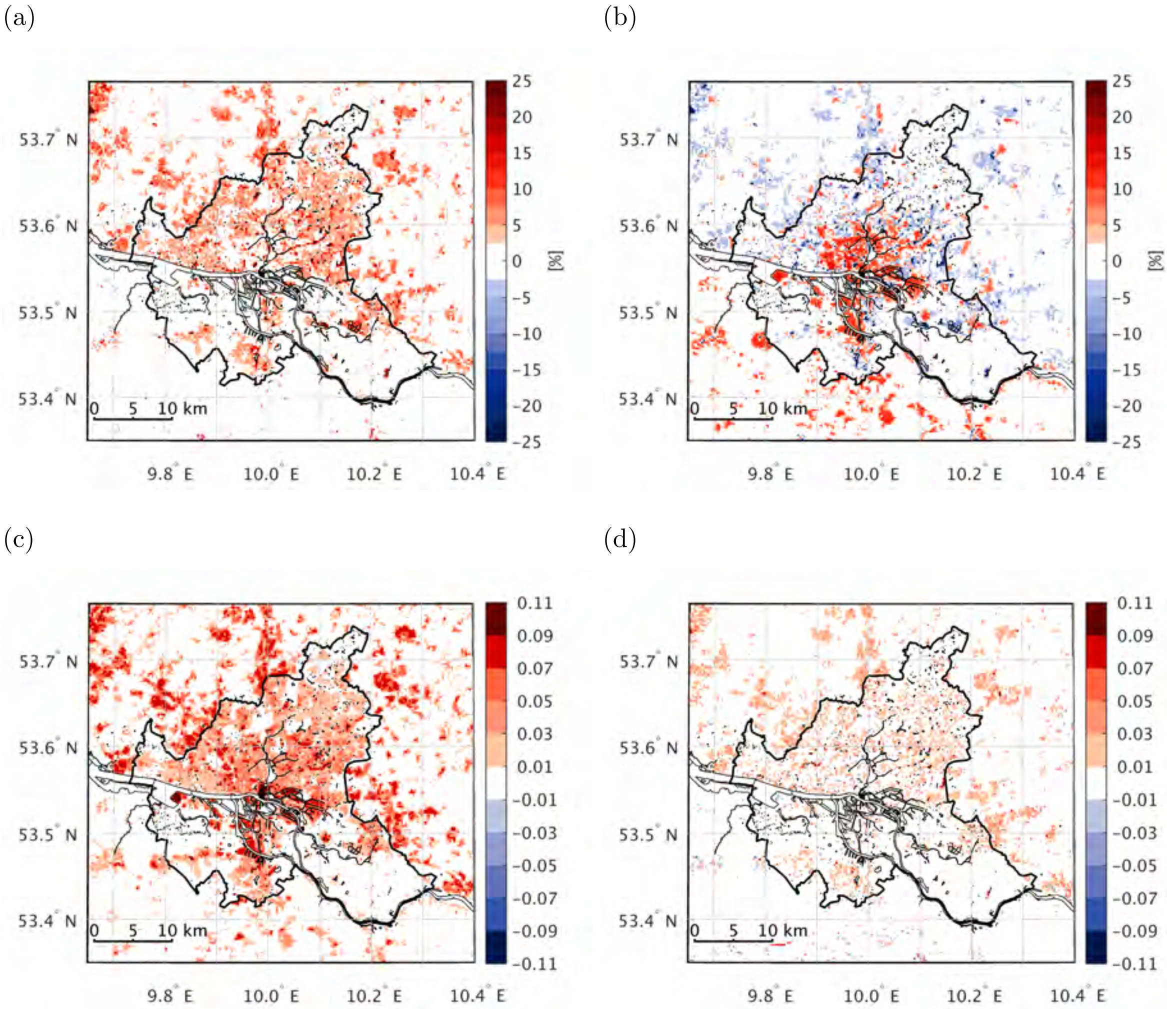

Figure 4.6: Same as Figure 4.5 but for scenario s2.

4.3.2.3 Scenario 3

In scenario s3, a compact city as a centre for environmental innovation is assumed with a growing population (Rottgardt et al., 2014). The building density is assumed to increase by densification and by adding floors onto existing buildings. Individual transport decreases because of a well-developed public transport system supported by public funds. Furthermore, adaptation measures are assumed to be supported by public funds and are therefore substantially implemented.

The building density and height are increased compared to the current situation but the traffic areas are reduced. The sealed surfaces decrease for the inner city of Hamburg and parts of the southern suburbs and increase in the northern suburbs and the outer city (Figure 4.7a). The evaporative surfaces increase in proportion to the widespread implementation of adaptation measures like green roofs and grass pavers (Figure 4.7b). Building materials used in scenario s3 lead to a higher albedo (Figure 4.7c). The changes of the roughness length between the current situation and the scenario reflect the changed sealed surfaces (Figure 4.7d).

4.4 Results and discussion

The simulations for the reference case are evaluated in Section 4.4.1. The scenario results are presented for the meteorological variables in Section 4.4.2. The impact of the scenarios on the perceived temperature is analysed in Section 4.4.3. The results are discussed in Section 4.4.4.

4.4.1 Evaluation of model results

An evaluation of the 4 km and 1 km METRAS results used for the forcing of 250 m simulations has been conducted by Hoffmann et al. (2012) and Hoffmann et al. (2016) for all cases with the exception of the cluster centre simulations. They directly compared results of individual simulations with hourly temperature, humidity and wind observations from DWD stations in and near Hamburg. The statistical measures showed values which are within the range of evaluation studies of other mesoscale models summarised in Schlünzen et al. (2016).

For evaluating the 250 m simulations, the HITRATE, BIAS, root mean square error RMSE and correlation coefficient (R) are calculated comparing model results with hourly observation from the weather station at Fuhlsbüttel. The other weather stations presented in Section 4.2.2 are located outside the HH250 model domain. The statistical measures are calculated following the guidelines of COST728 (Schlünzen and Sokhi, 2008) using the method described in Hoffmann et al. (2016). The uncertainty of the observations used for calculating the HITRATE is accepted as ±2 K for temperature, ±5 % for relative humidity, ±1 m/s for a wind speed lower than 10 m/s, ±2.5 m/s for wind speeds higher than 10 m/s and ±30° for wind direction in case of wind speed higher than 1 m/s. Wind direction is not evaluated for wind speeds lower than 1 m/s. In contrast to Hoffmann et al. (2016), who evaluated only the second simulation day of each simulation, all hourly

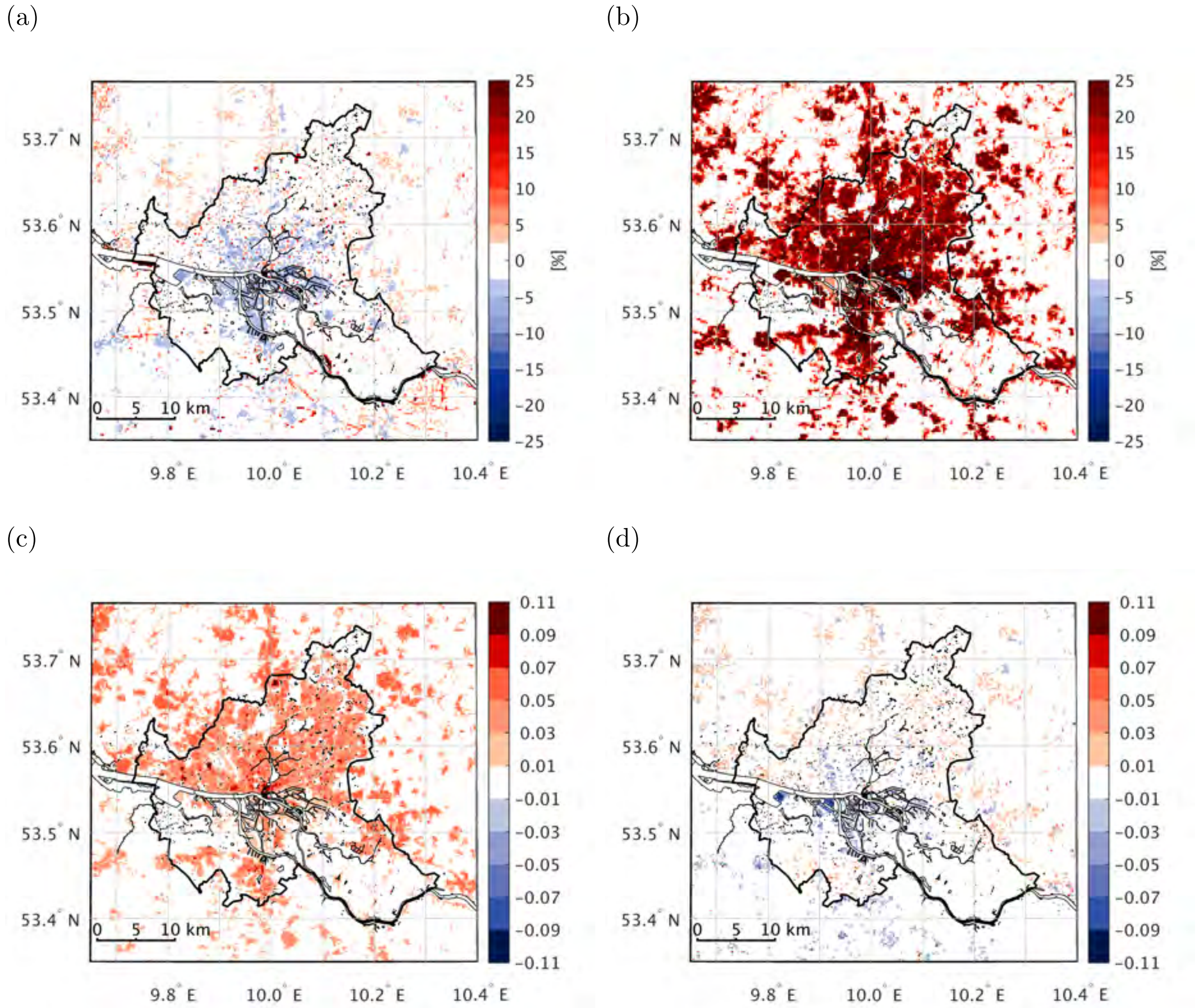

Figure 4.7: Same as Figure 4.5 but for scenario s3.

values are used to compute the values for the statistical measures (Table 4.4). The results of BIAS, RMSE, and R for the temperature as well as RMSE and R for wind direction agree with typical performances of mesoscale meteorological models (Schlünzen et al., 2016). The BIAS of the wind direction is larger than for the best 50 percent of typical meteorological model performances (−13° to 10°, Schlünzen et al. (2016)). For wind speed, the RMSE is close to the median of typical model performances (1.8 m/s) while the BIAS is larger than for the best 50 percent of typical model performances (−0.2 m/s to 0.7 m/s) and R is lower than the median of the performances (0.62) (Schlünzen et al., 2016). For relative humidity, no values for comparison are given in Schlünzen et al. (2016). Given the dependency of two model variables (i.e. temperature and specific humidity) BIAS and RMSE are in an acceptable range. Currently, not many model comparison studies are available that deal with HITRATE because the allowed deviation, which is needed to compute the HITRATE, varies among the evaluation studies (Schlünzen et al., 2016). The values of HH250 are of the same order as the values of the 4 km and 1 km simulations (Hoffmann et al., 2016) for 10 stations in Northern Germany.

Table 4.4: Evaluation measures HITRATE, BIAS, root mean square error (RMSE) and correlation coefficient (R) for evaluation of HH250 simulations. The measures are calculated for the DWD weather station Fuhlsbüttel.

	HITRATE	BIAS	RMSE	R
Temperature	0.56	−0.5 K	2.4 K	0.89
Relative humidity	0.36	+2.2 %	11.4 %	0.80
Wind speed	0.46	−0.9 m/s	1.9 m/s	0.47
Wind direction	0.44	+17°	66°	0.67

Hoffmann et al. (2016) compared the UHI pattern computed from the 1 km METRAS simulations using an SDD method to the observed UHI data from Schlünzen et al. (2010) and to the UHI pattern constructed using Ellenberg indicator values for temperature (UHIE) (Bechtel and Schmidt, 2011). The METRAS-UHI pattern computed by Hoffmann et al. (2016) corresponds to the average (8 pm to 12 am) UHI pattern calculated as the difference of near-surface temperatures for all grid points minus values simulated for the rural DWD station Grambek. For all datasets (observed UHI and UHIE), significant pattern correlations between 0.74 and 0.8 were found, while the UHI intensity was underestimated by METRAS, mainly in the city centre. Hoffmann et al. (2016) attributed the lower intensity mainly to the missing anthropogenic heat and radiative trapping effects. In addition, comparison of simulation results and point observations in urban areas can be error prone because of the small-scale spatial temperature variability, which cannot be fully captured by numerical models on a kilometre scale. It can be expected that the 250 m simulations are able to improve the spatial temperature variability. However, to verify this, more long-term observations within the city of Hamburg are needed. Such data will be available in the next few years from the Hamburg Urban Soil Climate Observatory (HUSCO) (Wiesner et al., 2014).

In summary, METRAS performs sufficiently well for the MRH and for Hamburg and it is able to simulate a realistic UHI. Therefore, METRAS can be used to investigate urban development and climate adaptation scenarios.

4.4.2 Scenario impacts on meteorological variables

The most pronounced changes in the meteorological variables are found in scenario s3 (Table 4.5). For some variables, the results for scenarios s1 and s2 show different spatial patterns or converse behaviour to scenario s3. Therefore, the changes between scenario s3 simulations and the reference case are shown next to the results from the reference case, which represents the summer climate mean. In cases where the behaviour of the scenarios s1 and s2 is different from scenario s3 in a certain variable, the particular figure is shown.

The three socio-economic scenarios include changes in building density and height which introduce changes in the roughness length and wind speed. The latter is an important parameter in urban ventilation, UHI development and human wind comfort. The spatial patterns of the wind speed 10 m above ground during day- and nighttime in the reference case and scenarios are similar (not shown) and differ only slightly in the magnitude of the wind speed (Table 4.5). The differences in wind speed between day- and nighttime result from the more stable stratification close to the surface during nighttime. The higher roughness length in urban areas leads to lower wind speed compared to rural areas. The daytime mean for the reference is shown in Figure 4.8a. Scenario s3 shows decreased wind speed in the areas with increased building density and height (Figure 4.8b). Similar changes are found for scenario s2 (not shown). In scenario s1, the wind speed is slightly increased, aligned to the areas with decreased building height and therefore decreased roughness length (Figure 4.9a). The magnitude of the changes in wind speed in the assessed scenarios implies neither disadvantages for urban ventilation or increased UHI development caused by the wind speed reduction nor discomfort by increased wind speed.

During nighttime, the mean latent heat flux is close to zero (Table 4.5). The highest latent heat fluxes are found above water bodies (not shown). In the daytime mean, the latent heat flux for the reference case reflects the SCCs in the model domain, with latent heat fluxes of up to 250 W/m^2 in the forest areas in the east and south of the domain and lower latent heat fluxes in the urban areas (Figure 4.10a). Thus, the changes in the scenarios are correlated with the fraction of vegetation. The latent heat fluxes increase with the increased evaporative surfaces in s1 (not shown) and s3 (Figure 4.10b) during daytime whereas the magnitude in scenario s1 is less pronounced than in scenario s3. In scenario s2, the latent heat flux increases in the inner city and the southern suburbs while the northern suburbs show a decrease depending on the amount of evaporative surfaces in the model domain (Figure 4.9b).

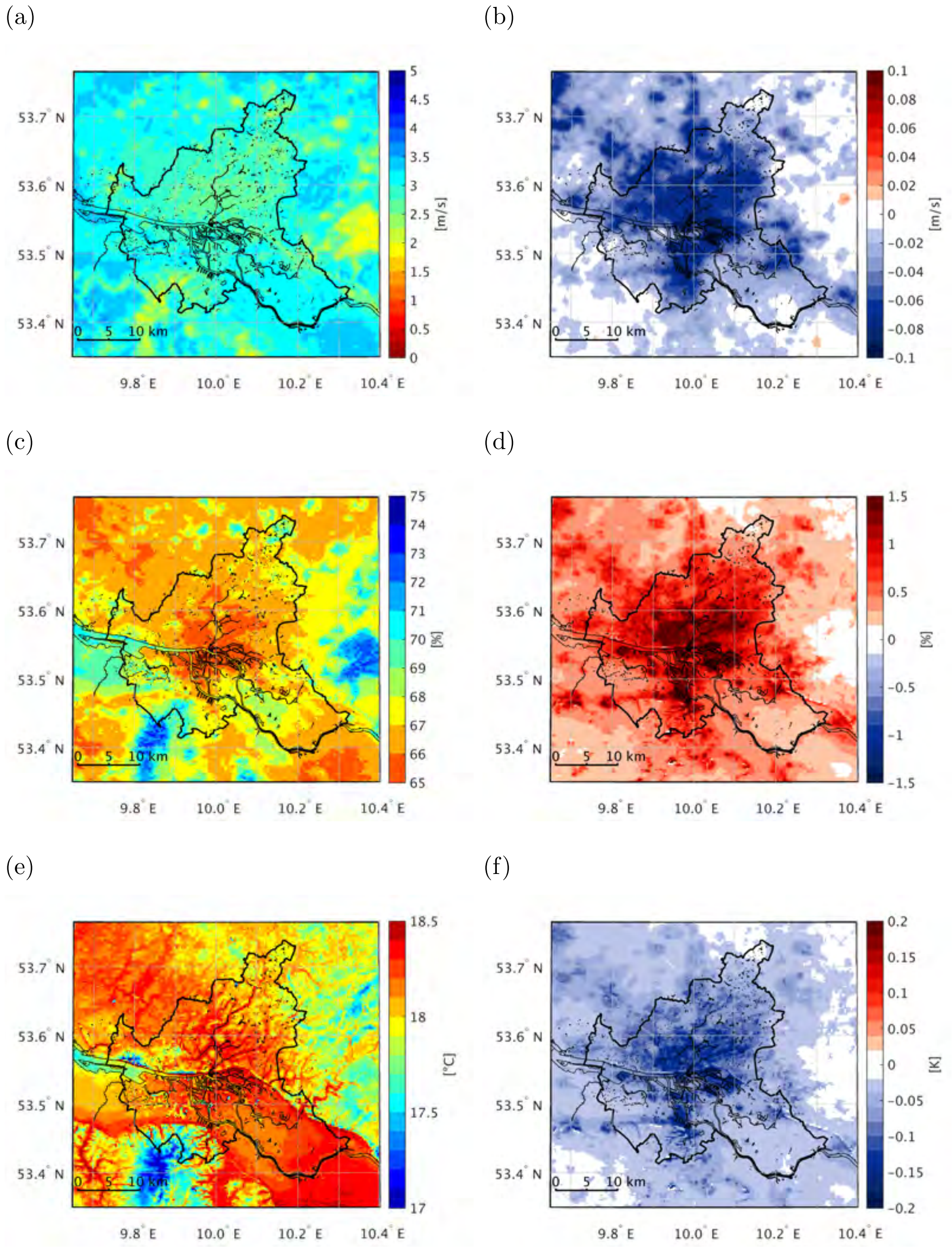

Figure 4.8: Daytime (0700 LT to 2000 LT) mean spatial pattern at 10 m above ground for (a),(b) the wind speed, (c),(d) the relative humidity and (e),(f) the temperature. The left column shows the reference case whereas the right column shows the differences from scenario s3 minus reference case. The state boundaries of Hamburg are marked with a thick black line, water bodies are marked with thin black lines.

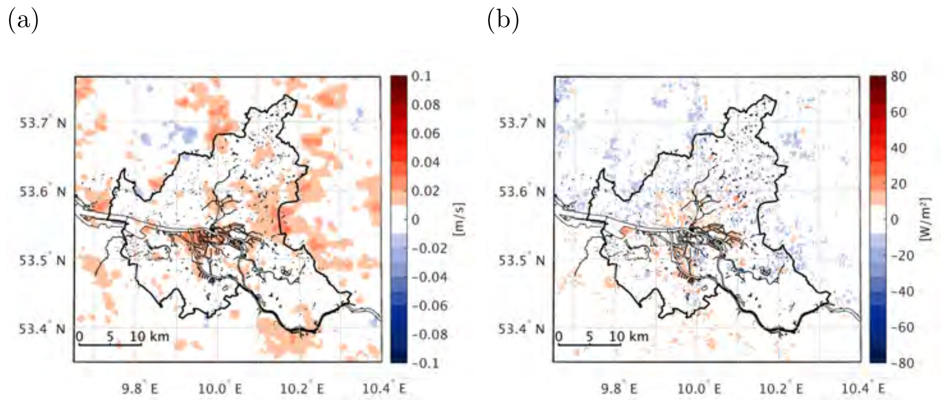

Figure 4.9: Daytime (0700 LT to 2000 LT) mean spatial pattern at 10 m above ground for the differences in (a) wind speed of scenario s1 minus reference case and (b) latent heat flux of scenario s2 minus reference case. The state boundaries of Hamburg are marked with a thick black line, water bodies are marked with thin black lines.

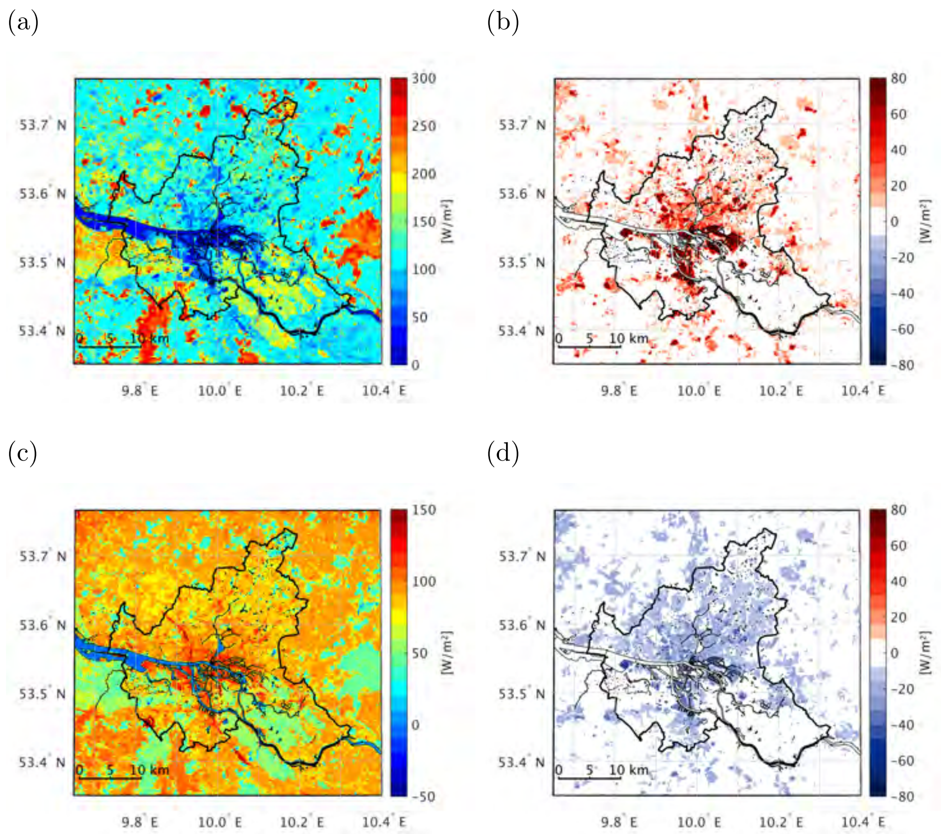

Figure 4.10: Daytime (0700 LT to 2000 LT) mean spatial pattern at 10 m above ground for (a),(b) the latent heat flux and for (c),(d) the sensible heat flux. The left column shows the reference case whereas the right column shows the changes due to the scenario s3. The state boundaries of Hamburg are marked with a thick black line, water bodies are marked with thin black lines.

Table 4.5: Day- (0700 LT to 2000 LT) and nighttime (2200 LT to 0500 LT) mean for urban and rural areas for reference case and scenarios s1, s2, and s3.

	Reference case				Scenario s1				Scenario s2				Scenario s3			
	day		night		day		night		day		night		day		night	
	urban	rural	urban	rural	urban	rural	urban	rural	urban	rural	urban	rural	urban	rural	urban	rural
Wind speed [m/s]	2.8	2.9	2.0	2.1	2.8	2.9	2.0	2.1	2.8	2.9	2.0	2.1	2.7	2.9	2.0	2.1
Latent heat flux [W/m^2]	72.9	156.0	1.6	3.1	77.1	155.9	1.8	3.1	80.2	155.5	2.0	3.1	116.6	155.0	3.3	3.0
Relative humidity [%]	65.8	67.5	86.3	87.9	65.8	67.6	86.4	87.9	66.1	67.7	86.3	87.8	67.1	67.9	87.0	88.1
Integral cloud water content [kg/m^2]	0.058	0.055	0.030	0.027	0.057	0.056	0.030	0.027	0.057	0.055	0.031	0.027	0.058	0.056	0.030	0.027
Sensible heat flux [W/m^2]	106.8	72.0	-8.8	-9.7	105.5	72.0	-8.9	-9.7	92.0	72.4	-9.1	-9.6	81.2	72.7	-9.7	-9.6
Temperature [°C]	18.2	18.2	14.5	14.2	18.2	18.1	14.5	14.2	18.2	18.1	14.5	14.2	18.1	18.1	14.4	14.2

The increased latent heat fluxes change the energy balance at the surface and lead to a reduced air temperature. A combination of increased latent heat fluxes and decreased temperatures leads to an increased relative humidity. The latter might have negative impacts on human comfort during situations with heat stress.

The relative humidity is clearly lower during daytime than during nighttime because of the lower temperatures during the night (Table 4.5). In the inner city, lower values are found compared to the rural areas in the east and the south (Figure 4.8c). The spatial pattern of the relative humidity is correlated with the spatial pattern of the temperature (Figure 4.8e; lower relative humidity in areas with higher temperatures). However, the relative humidity is more large scale decreased than the temperature in the inner city would indicate. This is induced by the sealed surfaces which yield less evaporation in the city. In scenario s3, the strongest increase in relative humidity of 1.3 percent in the spatial-temporal mean is found for urban areas during daytime (Table 4.5). The spatial result shows an increase of relative humidity of more than 1 percent for large areas (Figure 4.8d). During nighttime, the increase of the relative humidity in the urban areas due to s3 is less pronounced but with a similar spatial pattern (not shown). The changes in relative humidity due to adaptation measures of scenario s1 and s2 are negligible in the spatial and temporal average (Table 4.5). The spatial results show a scattered increase of relative humidity up to 0.5 percent for scenario s2 and less increase for scenario s1 (not shown).

An increase of relative humidity may lead to a more frequent cloud development or a greater area of cloud development. Clouds influence the short- and long-wave radiation budget which is directly linked with the energy balance at the surface. For UHI development, cloud cover is an important parameter because of shading of incoming short-wave radiation and absorption and emission of long-wave radiation. The integral cloud water content is used as a proxy for cloud cover, which shows a maximum at 1700 LT in the reference case and the scenarios (not shown). The differences between all scenarios and between urban and rural areas are varied (Table 4.5). A non-distinctive change signal indicates that the UHI development in the scenarios does not induce systematic change in cloud development and cloud cover over the city.

During the night, the sensible heat fluxes of urban and rural areas for the reference case and all scenarios are negative, in the vicinity of about -9 W/m^2 (Table 4.5). This means that the atmosphere gets cooled by the surface. The changes in the scenarios are negligible during nighttime (Table 4.5). In the daytime mean, the sensible heat flux shows negative values for the water bodies of Hamburg and positive values for the other areas. Therefore, the atmosphere gets cooled by the water bodies during the day (Figure 4.10c). The atmosphere in the inner city gets heated up the most, with a sensible heat flux up to 150 W/m^2 while the atmosphere in the forest areas is moderately heated up with a flux of up to 50 W/m^2. During the day, the sensible heat fluxes in all rural areas show similar magnitude, in the order of about 72 W/m^2 (Table 4.5). In the urban areas, the sensible heat flux shows different magnitudes, depending on the scenario and the adaptation measures included. Scenario s3 shows a reduction of the sensible heat fluxes towards the atmosphere (Figure 4.10d). This is mainly caused by changes in the albedo, but the cooling of the surface due to the increased latent heat flux also leads to a reduction of the sensible heat flux. The decrease in scenario s2 is less pronounced than in scenario s3 and is linked to the increased albedo (not shown). For scenario s1, no changes in the sensible heat flux are found in the spatial pattern (not shown).

As a result of the changed processes discussed above, the 10 m temperature is affected in the scenarios. In the reference case, the 10 m temperature is clearly higher during daytime than during nighttime (Table 4.5). Higher temperatures are found in the urban areas and the river valleys than in the rural areas during day and nighttime (shown for daytime in Figure 4.8e, not shown for nighttime). During daytime, forest areas in the east and south of the model domain also show lower temperatures than the urban areas and the river valleys (Figure 4.8e). The largest decrease of the temperature is found in scenario s3 during daytime, with a reduction in magnitude of about -0.2 K for the inner city in the areas with increased albedo and increased latent heat flux and decreased sensible heat flux (Figure 4.8f). During nighttime, this decrease in temperature is less pronounced but the temperatures are still reduced by -0.1 K (not shown). In scenario s2, a decrease in temperature in the areas with increased albedo and reduced sensible heat flux is found for daytime (not shown). During nighttime, small local increases of temperature are found for scenario s2 (not shown). For scenario s1, almost no changes occur (not shown). These results show that the largest temperature reduction during daytime is induced by the increased albedo and is supported by the increased evaporation introduced by urban greening. The decreased heat storage during daytime caused by the increased albedo is, together with the slightly increased evaporation during nighttime, the cause of nighttime cooling.

The temperatures of the urban areas are higher than the temperatures for the rural areas

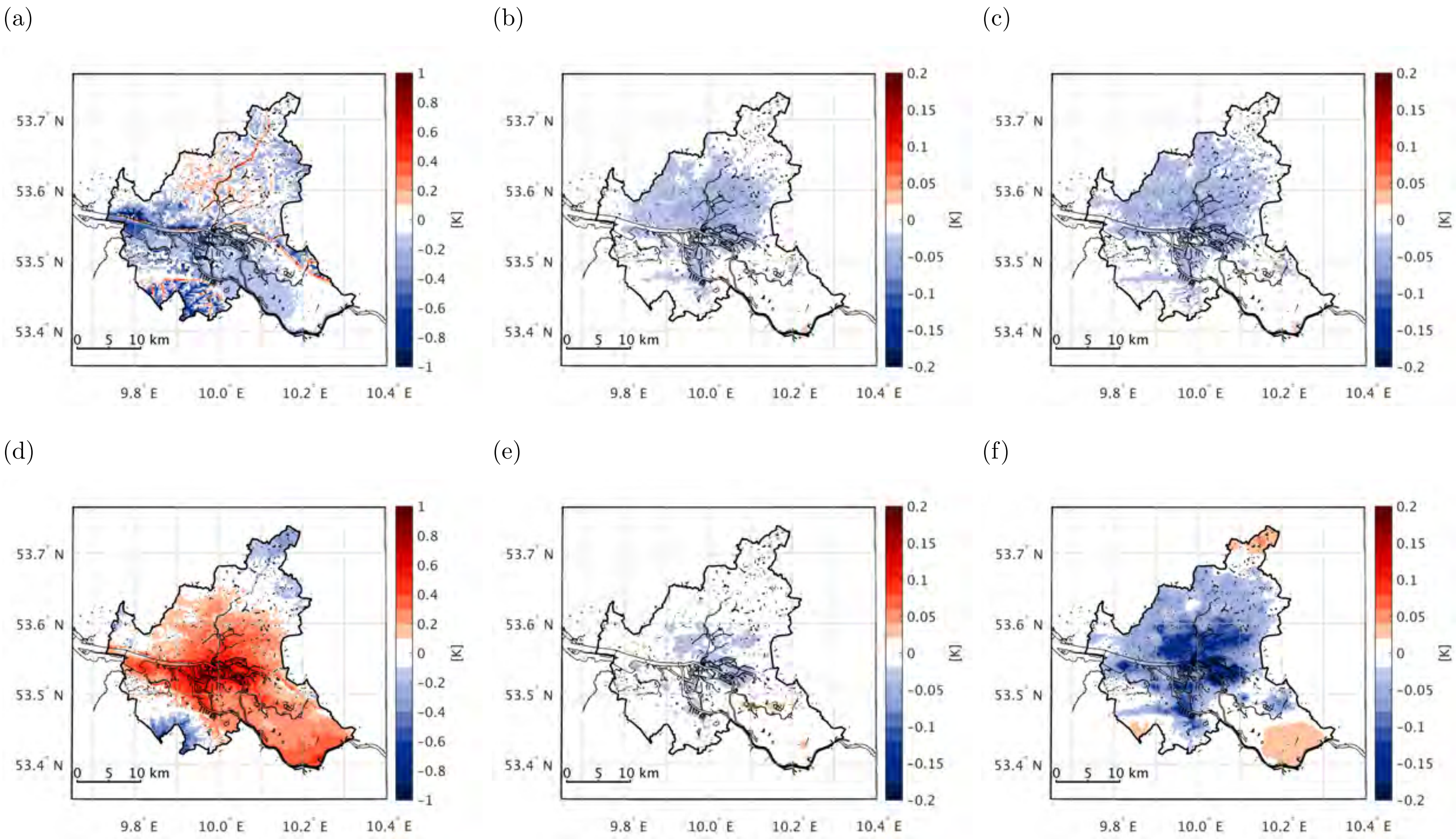

Figure 4.11: Mean spatial pattern at 10 m above ground for the (a),(b),(c) UCI of Hamburg during morning hours (0700 LT to 1100 LT) and (d),(e),(f) UHI of Hamburg during evening hours (1900 LT to 2300 LT) for (a),(d) reference case, (b),(e) scenario s2 minus reference case and (c),(f) scenario s3 minus reference case. Only areas within Hamburg are considered. The state boundaries of Hamburg are marked with a thick black line, water bodies are marked with thin black lines.

for most of the day. The resulting urban cool island (UCI) and UHI patterns are assessed for morning (Figure 4.11a) and evening hours (Figure 4.11d), respectively. Only from 0700 LT to 1100 LT is the temperature in the urban areas lower than in the rural areas so that Hamburg develops a UCI (Figure 4.11a). Large parts of the city are cooler than the mean rural temperature because of the large heat storage capacity of buildings and urban surfaces. Areas warmer than the rural mean are linked to river valleys and orographic effects like south-facing slopes. For scenarios s2 and s3, the UCI is intensified by −0.1 K compared to the reference (Figure 4.11b and Figure 4.11c). Those areas are linked with the areas of increased albedo and therefore increased reflection of short-wave radiation and decreased surface heating. For scenario s1, the changes in UHI during morning hours are negligible (not shown).

During evening hours, the inner city shows higher temperature than the rural areas for large parts of the city so that the city of Hamburg develops a UHI (Figure 4.11d) because of the heat stored in the urban materials. Those limited urban areas found to be cooler than the rural areas are subjected to effects from either orography and/or forested areas. Scenario s3 shows a decrease of UHI of as much as −0.2 K for the inner city but also a slight increase in the outer areas (Figure 4.11f). The decrease in the UHI results from the reduced heat storage during daytime. The outer areas become relatively warmer compared to the rural areas because of missing adaptation measures in these areas, while large rural areas are affected by the comprehensively implemented adaptation measures. For scenario s2, a slight decrease of UHI is found for the inner city (Figure 4.11e). The changes are again negligible for scenario s1 (not shown).

4.4.3 Scenario impacts on perceived temperature

The analysis is split into the time periods 1000 to 1600 LT (NOON) and 2100 to 2400 LT (LATE). The motivation for using the NOON time period is that outdoor heat stress occurs mainly around noon and in the early afternoon around the time of maximum solar radiation (Section 4.4.3.1). The LATE time period has been chosen in order to assess the changes of perceived temperature (PT) after sunset, when the shortwave radiation does not influence PT (Section 4.4.3.2).

4.4.3.1 NOON

NOON PT values (Section 4.2.3.2) are highest in the centre of the city (Figure 4.12), due to the lower wind speed in these areas. High values of PT are also simulated in the Sachsenwald forest. This is due to the higher values of humidity and lower values of wind speed there. However, PT has been calculated for a person standing in an open area. Shading due to the presence of buildings and trees is not considered. The average values of PT in the urbanised areas are slightly above 20 °C, which is above the range for which thermal comfort is achievable by appropriate clothing (0 °C to 20 °C; Staiger et al. (2012)).

The PT changes simulated for scenario s1 are negligible, which is consistent with the very small changes simulated for the different input variables for PT for this scenario.

For scenario s2, PT increases between 0.1 K and 0.3 K within the urban area of Hamburg. Note that this means the daytime average in the summer. Thus, this is a notable increase and in contrast to the decrease in air temperature simulated for this scenario. The physical reasons for this result are the decreasing wind speed due to the higher and more densely spaced buildings, the increase of specific humidity due to greening of the city and the increase of the mean radiant temperature due to increased reflected short wave radiation resulting from the use of asphalt with higher albedo.

For scenario s3, PT is not systematically changed in the Hamburg area, despite the decreasing air temperature. The physical reasons are the same as for s2. However, the air temperature decreases more and the wind speed less for scenario s3 compared to scenario s2. Therefore, PT is not increasing as in scenario s2, but changes remain between −0.15 K and +0.15 K, with many areas of unchanged PT.

The results for NOON indicate that adaptation measures leading to a decrease of the air temperature can lead to an increase in the perceived temperature, PT. Since the average summer NOON PT in the reference scenario is above the limit where thermal comfort is achievable, the increase of PT for s2 leads to increasing heat stress during NOON. PT does not consider direct radiative effects (e.g., shading, long-wave radiation of buildings and vegetation). Therefore, PT could be smaller for increased building heights if the street canyons are narrow enough (Schoetter et al., 2013).

4.4.3.2 LATE

For LATE, PT is highest in the centre of Hamburg, in the harbour area and in the south-east (Figure 4.13). This is due to higher values of air temperature and lower values of wind speed in these areas. The PT values are in the range where thermal comfort is achievable. Note that these values reflect the summer average.

Negligible changes of PT are found for scenario s1 and scenario s2 (not shown). This is reasonable since the PT input variables do not change much.

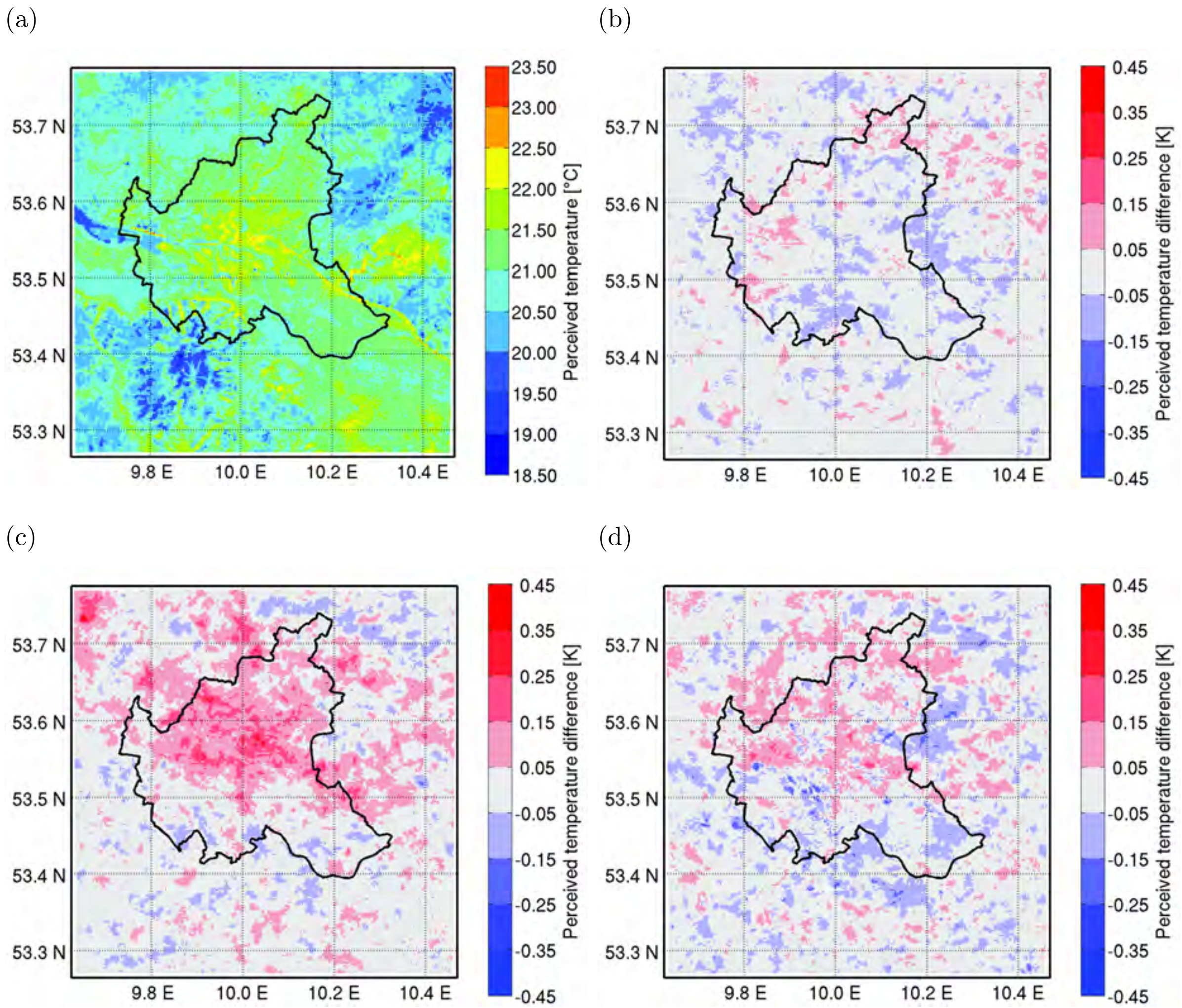

Figure 4.12: NOON values for perceived temperature at 10 m above ground for (a) reference, (b) scenario s1 minus reference case, (c) scenario s2 minus reference case and (d) scenario s3 minus reference case. The state boundaries of Hamburg are marked with a black line. All values are for summer average.

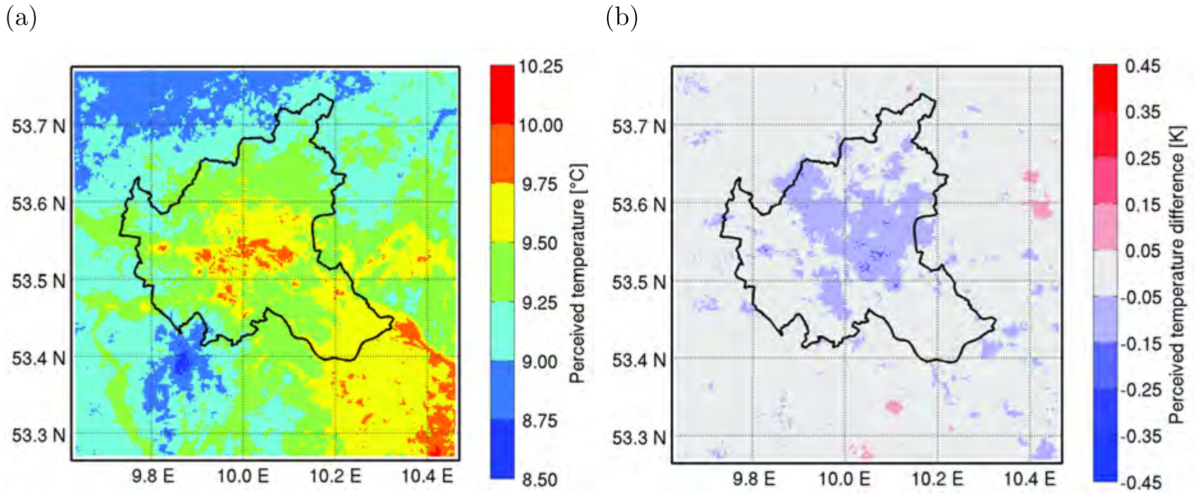

Figure 4.13: LATE values for perceived temperature at 10 m above ground for (a) reference and (b) scenario s3 minus reference case. The state boundaries of Hamburg are marked with a black line. All values are for summer average.

For scenario s3, the perceived temperature PT is reduced by about 0.1 K near the centre of the city. This is about the same reduction as simulated for the air temperature. The physical reason is that wind speed and mean radiant temperature are nearly unchanged. The specific humidity increases for scenario s3. However, the sensitivity of PT to specific humidity is small for situations with thermal comfort (Schoetter et al., 2013) since there is not much transpiration of humans in this case. For this reason the increasing humidity does not counteract the effect of the decreasing air temperature. This is in contrast to the result obtained for NOON.

4.4.4 Discussion

Scenario s1 assumes a decreasing number of inhabitants for Hamburg without implementation of adaptation measures. As a result, the fraction of sealed surfaces is slightly reduced. The increased evaporative surfaces increase the latent heat flux during daytime. Consequently, the relative humidity slightly increases during the day but with negligible change in temperature. Without change to the albedo, the impact on the surface energy budget is negligible. As a result, the temperature, the sensible heat flux and the UCI and UHI change little in scenario s1 compared to the reference case. The changes in PT are also small. This means for Hamburg that with only a slight renaturisation without further adaptation measures, there is no benefit to human thermal comfort.

In scenario s2 a stagnant number of inhabitants and sporadically implemented adaptation measures are assumed. The building density is increased. Adaptation measures counteract the increased sealed surfaces by greening urban areas. The latent heat fluxes for the inner city and the southern suburbs slightly increase during the day and decrease for the outer city and the northern suburbs. The increased albedo leads to a decreased 10 m temperature during daytime. During nighttime the changes are negligible. Only in areas with large increases of sealed surfaces does the temperature increase slightly during nighttime. The weak signal for latent heat flux combined with decreased temperature leads to higher relative humidity during daytime. The increased sealed surfaces and therefore changed heat storage are responsible for the larger impact of urban development on the UCI during morning hours (0700 LT to 1100 LT) compared to the UHI during evening hours (1900 LT to 2300 LT). During morning hours the albedo and the heat storage increase; both cause urban cooling. During the evening hours, the structures and sealed surfaces release the stored heat. Only a slight decrease in the UHI magnitude persists from daytime cooling. Consequently, the changes in PT are negligible for LATE. For NOON, the PT increases due to an unfavourable combination of meteorological variables. For Hamburg these results imply that a decrease in temperature does not necessarily improve human thermal comfort and that the implementation of adaptation measures has to be reviewed very carefully.

For scenario s3 an increasing number of inhabitants and substantial implementation of adaptation measures are assumed. The widespread implementation of adaptation measures leads to a large increase of evaporative surfaces. Thus, the latent heat flux increases in the urban areas during daytime. Combined with decreased temperatures this leads to increased relative humidity for day- and nighttime. The broad implementation of more evaporative surfaces counteracts the increased sealed surfaces caused by the increase in population. Together with an increased albedo, the adaptation measures cause a decrease in temperature during daytime and also a decrease during nighttime. The UCI intensifies during morning hours because of the changed albedo. The decreased amounts of sealed surfaces counteract this effect because of the decreased heat storage but do not balance it. During evening hours, the effect of the decreased heat storage is the main effect that produces changes in the UHI. Thus, the UHI intensity is clearly reduced for large parts of the city. Depending on the changes in the meteorological variables, the PT remains nearly unchanged during NOON. For the LATE hours, the PT decreases as much as the temperature. The results imply for Hamburg that the “compact city” scenario reduces the urban impact on local temperature sufficiently to offset the anticipated short term effect of climate change on local temperature. Using this strategy, there are beneficial effects that help counteract the temperature increase by climate change in Hamburg and therefore to offset the effect of climate change on the local temperatures at least for a few decades.

4.5 Conclusions

The impact of urban development and climate adaptation measures on the urban climate of Hamburg is analysed for three socio-economic scenarios with different possible urban development strategies and adaptation measures. The adaptation measures in the scenarios are based on assumptions about population development and financial circumstances, and are realised by applying different surface covers to represent land use in the numerical model METRAS. The high-resolution urban climate simulations necessary for the analysis are produced by statistical-dynamical downscaling. The three scenarios show different results regarding the question of whether urban development and climate adaptation measures can compensate for the effects of climate change.

The results of the three scenarios imply that the changes in the mean wind speed, introduced by the changed roughness length through changed building density and height, are not relevant to human thermal comfort. In this study the effect of possible increased turbulence due to the changed building density and height is neglected. However, for planning detailed changes in building density and height, the effect of turbulence on local wind comfort and urban ventilation should be considered.

As found by Georgescu et al. (2014), the scenarios assessed in this study show that the largest reduction of temperature was generated by using higher albedo for roofs. The use of green roofs and urban greening supports the temperature reduction in these scenarios by increasing the latent heat fluxes. Therefore, the largest temperature reduction is found with a combination of green roofs and increased albedo.

In this study, no systematic influence of climate adaptation measures on cloud development is found and the systematic changes in the mean wind speed are sufficiently small so that they do not change the UCI and UHI development in the mean summer climate. The changes in UCI and UHI are correlated with the changes in the latent and sensible heat flux and therefore with the number of white and green roofs.

The impact of the three socio-economic scenarios on human thermal comfort is assessed with the calculation of PT. The PT found for Hamburg for the three scenarios is within the computed range of human thermal comfort. In this range, the reaction of PT to changes in relative humidity is less sensitive than for higher PT (Schoetter et al., 2013). When applying these scenario results to other urban areas with higher PT, the non-linear response of PT to relative humidity needs to be considered.

For evaluating the impact of adaptation measures, scenario simulations as well as reference simulations representing the current state of Hamburg are performed. Through statistical combination of the reference simulations, the 30-year mean summer climate of Hamburg is represented with a high-resolution model (250 m horizontal grid resolution) for the period from 1981 to 2010. The evaluation of the model simulations showed that the BIAS, root mean square error and the correlation coefficient are in the range of typical model performances for temperature. For the wind speed and wind direction, the model performance is not in the best 50 percent of the typical model performances (Schlünzen et al., 2016). The statistical measures for model performance in simulating relative humidity seem to be in a reasonable range but no values for comparison are given in Schlünzen et al. (2016). Due to the positive evaluation results, the reference simulation can be treated as the 30-year summer climate of Hamburg.

The dynamical part of the SDD method is performed with three refinement steps from the ECMWF analysis data. This method needs a lot of computing time and also needs time to process the refinement steps consecutively. Additionally, each refinement step increases the uncertainty and may also increase the BIAS of the model results. Another method to refine the grid size from the coarse grid resolution of a global or regional model to high-resolution simulations may be the use of a horizontal non-uniform grid with a high grid resolution in the area of interest and a coarser grid resolution around for nesting into the coarser model.

For the statistical part of the SDD method, a bivariate skill score is developed to estimate if the 30-year summer climate of Hamburg can be sufficiently reproduced by simulating only a few days. The bivariate skill score takes into account the interdependency of different meteorological variables. For this study, the bivariate skill score indicates that the 30-year mean summer climate of Hamburg is well represented with 60 simulated days. The bivariate skill score is easily applicable to other regions or datasets because of its basic statistical methods. The results will depend on the variables assessed and the development of a periodic cycle of the variable in the time series considered. The ratio of the amplitude of the variables in the full dataset compared to the amplitude of the variables in the reduced dataset will influence the result as well as the time period that is investigated. A small dataset will probably be less consistent and robust to the test with the bivariate skill score and therefore should be handled with care. The method is well suited to reduce the number of days needed to represent the statistics while considering the interdependency between different meteorological variables.

The present study showed that the urban climate can be simulated with a high-resolution model using statistical-dynamical downscaling. Use of statistical-dynamical downscaling reduces computational expense and enables investigation of one or more seasons and scenarios or an entire year.

5 Modelling impacts of urban development and climate adaptation measures on the winter climate of Hamburg

5.1 Introduction

In the frame of global climate change, climate adaptation measures become important for urban regions to reduce the regional warming through their ability to reduce the thermal heat stress introduced by the urban climate (Georgescu et al., 2013, 2014; Adachi et al., 2012; Yang et al., 2016). The impact of climate adaptation measures is well investigated for the summer months (e.g. Chapter 4) when the thermal heat stress is largest. Only a few studies have investigated the impact of climate adaptation measures for a whole year (Jacobson and Ten Hoeve, 2012). Climate adaptation measures are mostly introduced for reducing high temperatures and their effects are not investigated for cold seasons when the thermal heat stress is negligible or even thermal cold stress exists. Therefore, the impact of the climate adaptation measures during the cold seasons is largely unknown.

An often-applied climate adaptation measure for cooling urban areas by evaporation is the greening of urban areas, e.g., of roofs, walkways and parking areas (Takebayashi and Moriyama, 2012; Georgescu et al., 2014). The cooling effects of green spaces like parks are well investigated for summer (Honjo and Takakura, 1991; Spronken-Smith et al., 2000; Bowler et al., 2010; Ca et al., 1998) and have a downwind cooling effect of 20 m to 1000 m in warm to hot climates. Another climate adaptation measure is the use of building materials with a higher albedo to modify the surface energy balance and thereby cool the urban areas during warm or hot seasons (Takebayashi and Moriyama, 2012; Georgescu et al., 2013; Gross, 2012; Jacobson and Ten Hoeve, 2012). The size of the city and the urban morphology are important factors for the urban climate (Georgescu et al., 2013; Yang et al., 2016). All these effects are well investigated but usually for the warmest season when their impact is most important without regarding the impact during winter months.

The average winter temperature of Hamburg, Germany, is 0.1 °C to 2.0 °C in the current climate based on regional climate models (RCMs) results (Daschkeit, 2011). Using the same RCMs (Daschkeit, 2011) average winter temperatures for Hamburg are projected to increase for the A1B Scenario by 1.00 K to 2.00 K by the middle of the 21st century with a change in precipitation in the range of −5% to +15%. In the current climate, days with snow cover occur for Hamburg and, especially, the surrounding rural areas. In the future climate, the number of ice days (maximum temperature ≤ 0 °C) is projected to decrease (Daschkeit, 2011) but will be still in the range of 10 ice days per year until the end of the 21st century (Daschkeit, 2011). Modelling the winter climate of Hamburg therefore needs to consider the effects of snow cover.

A numerical model of the atmosphere is used for calculating the winter season in Hamburg with occasional snow cover. The snow cover modifies the atmosphere primarily through changes of the surface albedo, the roughness length and the isolating capacity at the surface (Boone and Etchevers, 2001). The snow cover-connected processes need to be calculated with a snow scheme. Following Boone and Etchevers (2001), there are three classes of schemes with different complexity that can be used to simulate the snow-related processes. The first type contains the relatively simple schemes with one layer of snow or a mixed layer of snow and soil. These schemes are the ones most commonly used in atmospheric models. The second type includes very complex schemes with multiple layers of snow and a detailed description of the snow internal processes. Schemes of this type are mostly employed for avalanche forecasts. The third type deals with schemes of intermediate complexity which have more simplified physical parametrisations than the class two schemes and a lower number of layers to resolve the thermal gradient and the snow density gradient inside the snow cover.

For a regional atmospheric model, the most important processes to model are those of the surface layer and the exchange to the atmosphere (Jin et al., 1999). While modelling snow cover with only one layer, the system is described with two prognostic equations for heat and mass content (Lynch-Stieglitz, 1994). For a scheme with more layers, more prognostic equations are needed (Lynch-Stieglitz, 1994). METRAS, the model applied here, uses the force-restore method to calculate the surface temperature. This is a simple approach using one layer to parametrise the total effects of soil, vegetation and buildings. The extension for snow cover-related processes should fit to the relatively simple representation of the surface effects. Additionally, a snow scheme including several layers of snow needs input data for snow morphology and the thermal snow parameters in high horizontal and vertical resolution. These data are rarely available for most areas. Therefore, in this study METRAS uses a snow scheme of the first type with one layer of snow above the existing layer of soil, vegetation and buildings.

In this Chapter, the impacts of urban development and climate adaptation measures on the winter climate of Hamburg are investigated for one socio-economic scenario (see Chapter 4 for discussing of the impacts of urban developments and climate adaptation measures on the summer climate of Hamburg). Due to the results from summer, where the largest impacts on the summer climate of Hamburg are found for scenario s3, scenario s3 (Section 4.3.2.3) is chosen for assessing the impacts of climate adaptation measures on the winter climate. Scenario s3 includes substantial implementation of climate adaptation measures and considers urban growing.

In order to assess the impact of urban development and climate adaptation measures on the winter climate of Hamburg, SDD is applied to simulate the mean winter climate of Hamburg for December to February from 1981 to 2010. The simulations are preformed three times, two times as reference cases for the current situation with the current SCCs and once for scenario s3. The reference cases are completed first as reference case with using the snow scheme (REF_WITH_SNOW) and then as reference case without using the snow scheme (REF_NO_SNOW) while scenario s3 uses the snow scheme. Hence, the changes resulting from the snow scheme are evaluable using differences of both reference cases. The impacts of scenario s3 are assessable by comparing REF_WITH_SNOW and scenario s3 simulations. REF_WITH_SNOW provides data on the mean current winter climate of Hamburg at a high horizontal resolution (250 m). The modelling methodology is given in Section 5.2. The results are discussed in Section 5.3. The conclusions are drawn in Section 5.4.

5.2 Modelling methodology

The numerical model METRAS is used for estimating the impact of urban development and climate adaptation measures on the winter climate of Hamburg using SDD. The model set-up and the model extension with a snow scheme are described in Section 5.2.1. The forcing methodology with SDD and the benefit of a non-uniform grid are described in Section 5.2.2. The model input from the socio-economic scenario, the land-use data and the meteorology are given in Section 5.2.3. The methods used to analyse the model results are given in Section 5.2.4.

5.2.1 Extensions of METRAS for snow cover-related processes

METRAS is a non-hydrostatic, three-dimensional numerical model of the atmosphere. The model is described in some detail in Section 2.1. The model has been applied and evaluated for Northern Germany and MRH for the summer months (Chapter 3, Chapter 4 and Hoffmann et al. (2016); Schoetter et al. (2013); Schlünzen (1990); Schoetter et al. (2013)).

To simulate the winter months with occasional snow cover, METRAS is extended with a scheme that considers snow processes at the surface. The processes of snowfall, evaporation and snow melt are considered. The snow scheme is realised with a snow water equivalent for snow mass. A single snow layer is assumed for calculating the surface temperature. Snow melt between the soil surface and the snow base is neglected. The snow melt at the lateral boundaries of a snow pack is implicitly considered by the change of snow cover for each SCC depending on changes in snow mass. Snow banks are small compared to the grid resolution, therefore the advection of once-settled snow is not considered. The process of the actual snowfall is also neglected in the snow scheme. Rainfall is kept as it is by using the Kessler scheme (Kessler, 1969) for parametrisation of cloud and rain physics. The development of snow and its slower fall compared to that of rain is not calculated. Therefore, rain reaching close to the ground is treated as snow if the temperature is lower than 273.15 K. This may lead to small errors in the time development of the snowfall and the drift of snow during its fall.

The snow cover modifies the surface energy budget primarily by three different processes: the increased surface albedo, the decreased roughness length and the isolating capacity (Boone and Etchevers, 2001). The already existing calculation of the surface energy budget and the corresponding processes needs to be extended to account for these processes, especially the soil heat flux.

The existing surface energy budget uses the force-restore method (Deardorff, 1978) for calculating the soil heat flux, assuming a harmonic wave as forcing for heat transfer into the ground. The force-restore method neglects the horizontal heat transfer from a soil column to a neighbouring soil column. The new scheme for calculating the snow surface temperature follows this approach and does not consider a horizontal heat transfer in snow and soil.

A snow scheme with a single layer of snow solves the prognostic equations for heat and mass content (Lynch-Stieglitz, 1994). Therefore, the snow mass is needed as input data, as well as information about the albedo, thermal conductivity and diffusivity of the snow. For the thermal conductivity and diffusivity, values from literature are found (Section 5.2.1.6). The data about the snow mass and the albedo are taken from ECMWF analysis data (Section 2.2.1) using the albedo, the snow water equivalent (SWE) and the snow density from the ECMWF data set (Section 2.2.1 and Appendix A).

In the following sections, the snow scheme is described in detail. The calculation of the SWE is given in Section 5.2.1.1. The snow melt calculation is given in Section 5.2.1.2. The calculation of the snow density is given in Section 5.2.1.3. The albedo is calculated as described in Section 5.2.1.4. The roughness length calculation is described in Section 5.2.1.5. The calculation of the surface temperature using the force-restore method with an overlying snow cover is given in Section 5.2.1.6.

5.2.1.1 Snow Water Equivalent

The mass of snow per grid cell is represented by the snow water equivalent (SWE), with the unit of meters (Equation 5.1) as used in many atmospheric models from global to local scale (Douville et al., 1995; Boone and Etchevers, 2001; Drusch et al., 2004; Lemonsu et al., 2010) The mass budget of the SWE changes by the rate of snow fall, P_{snow}, the rate of evaporation, E_{snow}, and the rate of melting, M_{snow}. Only processes at the snow surface are considered in METRAS. The melting and refreezing between the snow pack and the soil are not considered. The lateral snow melt is implicitly considered by the calculation of the snow cover for each SCC.

$$\frac{\partial \text{SWE}}{\partial t} = P_{snow} - E_{snow} - M_{snow} \tag{5.1}$$

5.2.1.2 Melting of snow

Multiplying M_{snow} by the density of water, $\rho_{water} = 1000$ kg/m^3, and the latent heat of fusion, $L_f = 33400$ J/kg, leads to the energy, E_{melt}, per square meter necessary for melting (Equation 5.2). The energy needed for melting is proportional to the difference of the surface temperature, T_S, and the melting point $T_0 = 273.15$ K multiplied by the heat transfer coefficient, $c_{surface}$, from the surface into the snow pack.

$$E_{melt} = M_{snow}\rho_{water}L_f = c_{surface}\left(T_S - 273.15 \text{ K}\right) \tag{5.2}$$

Equation (5.2) implies the rate of melting as given in Equation (5.3). The heat transfer coefficient, $c_{surface}$, from the surface into the snow pack is calculated from the thermal conductivity of snow, c_{snow}, the depth of snow, z_{snow}, and an empirical scaling factor, λ (Equation 5.4).

$$M_{snow} = \frac{c_{surface}}{\rho_{water}L_f}(T_S - 273.15 \text{ K}) \tag{5.3}$$

$$c_{surface} = \lambda\frac{c_{snow}}{z_{snow}} \tag{5.4}$$

The empirical scaling factor, λ, is set to one, which denotes a perfect heat transfer from the air above the snow pack into the snow pack. By assuming this, surface processes like heating of puddles of melt water are neglected. The thermal conductivity of snow, c_{snow}, is calculated following Douville et al. (1995) with Equation (5.5) using the thermal conductivity of ice, c_{ice} = 2.22 W/Km, and the density of the snow pack, ρ_{snow}.

$$c_{snow} = c_{ice}\left(\frac{\rho_{snow}}{\rho_{water}}\right)^{1.88} \tag{5.5}$$

5.2.1.3 Snow density

The density of a snow pack, ρ_{snow}, is very dependent on its age. Following Douville et al. (1995), the exponential increase of the density is given by Verseghy (1991) by Equation (5.6). The minimum and maximum snow density ρ_{min} = 100 kg/m^3 and ρ_{max} = 300 kg/m^3 are the limits for fresh and old snow, respectively. Δt denotes the length of the time-step in seconds, t denotes the time, and τ_1 = 86400 s and τ_f = 0.24 are empirical factors. In case of snow fall, the snow density is given as a mass-weighted density between fresh and old snow.

$$\rho_{snow}\left(t+\Delta t\right) = \left(\rho_{snow}\left(t\right) - \rho_{max}\right)\exp\left(-\tau_f\frac{\Delta t}{\tau_1}\right) + \rho_{max} \tag{5.6}$$

5.2.1.4 Albedo of a snow pack

The albedo, α, of a snow pack varies with the shape of the snow flake, the age of the snow pack and the sedimented particles that are covering the surface. The impact of the different shapes of the snow flakes is neglected in most global circulation models as well as in METRAS. In METRAS, the changes in the albedo by accumulated airborne particles may be calculated explicitly by employing the chemistry module (Spensberger, 2010). This approach is not used to avoid additional complications by the need to include anthropogenic and natural emissions to the atmosphere for the current and future urban morphology and, last but not least, avoid the additional computational resources needed. Therefore, the dependency of the albedo on the age of the snow pack is calculated more simply following Douville et al. (1995) according to the observations of Baker et al. (1990). A weak linear decrease is assumed if the temperature is lower than the melting point (Equation 5.7), an exponential decrease is considered if the temperature is higher than the melting point (Equation 5.8) (Verseghy, 1991).

$$\alpha\left(t+\Delta t\right) = \alpha\left(t\right) - \tau_a \frac{\Delta t}{\tau_1} \qquad for\ T_S < 273.15\ \mathrm{K} \tag{5.7}$$

$$\alpha\left(t+\Delta t\right) = \left(\alpha\left(t\right) - \alpha_{min}\right) \exp\left(\tau_f \frac{\Delta t}{\tau_1}\right) + \alpha_{min} \qquad for\ T_S > 273.15\ \mathrm{K} \tag{5.8}$$

The empirical factor $\tau_a = 0.008$ is used in Equation (5.7) following Baker et al. (1990) and Douville et al. (1995). METRAS uses $\alpha_{min} = 0.85$ and $\alpha_{min} = 0.50$ as maximum and minimum values for the snow albedo like most of the current global circulation models (Douville et al., 1995).

Douville et al. (1995) suggest resetting the snow albedo to 0.85 in the case of snowfall of more than 10 mm. This has been modified by Dutra et al. (2010) who employ a continuous reset to reduce the impact of a threshold. In that modification, the maximum albedo is reached by snow fall greater than 10 kg/m^2 (Dutra et al., 2010). In METRAS, the method of Dutra et al. (2010) is modified as in Equation (5.9). This resets the albedo continuously during snowfall, depending on its magnitude. One hour of snow fall with the magnitude of 0.01 m/h or its equivalent with a higher magnitude in a shorter time completely resets the snow albedo to the maximum. Snow fall with a magnitude lower than 0.01 m/h takes longer to completely reset the albedo because the ageing of the snow pack decreases the albedo meanwhile.

$$\alpha\left(t+\Delta t\right)=\alpha\left(t\right)+min\left(1,\frac{3600\Delta\mathrm{SWE}}{0.01\Delta t}\right)\left(\alpha_{max}-\alpha\left(t\right)\right) \tag{5.9}$$

5.2.1.5 Roughness length of snow-covered areas

The roughness length of snow-covered areas is smaller than the roughness length z_0 of most areas without snow cover because a snow pack smooths the surface. The roughness length for the partly snow-covered surface, $z_{0_{psnow}}$, thereby depends on the ratio of the snow depth and the original roughness length without snow cover. This is taken into account by calculating the roughness length of the snow/surface combination following Douville et al. (1995) with Equation (5.10).

$$z_{0_{psnow}}=\left(1-p_{snow_{z_0}}\right)z_0+p_{snow_{z_0}}z_{0_{snow}} \tag{5.10}$$

The snow roughness length is set to $z_{0_{snow}}=10^{-3}$ m. The snow cover fraction, $p_{snow_{z0}}$, is a weighing factor for calculating the roughness length of the snow-covered surface from the roughness length of the original SCC and the snow roughness length and is calculated following Douville et al. (1995) by Equation (5.11). The empirical factor $\beta=0.408$ is given by Douville et al. (1995).

$$p_{snow_{z_0}}=\frac{\mathrm{SWE}}{\mathrm{SWE}+\beta z_0}=1-\frac{\beta z_0}{\mathrm{SWE}+\beta z_0} \tag{5.11}$$

5.2.1.6 Surface temperature of a snow pack

The exchange of energy between the atmosphere and the surface depends on the surface temperature. It influences the outgoing long-wave radiation, the sensible heat flux and the stratification of the atmosphere close to the surface and therefore all turbulent processes. In the standard version of METRAS the surface temperature is determined by the force-restore method. The sub-grid scale surface cover effects are considered using the flux aggregation method (Section 2.1). Several solutions for calculating the surface temperature of a snow-soil system with the force-restore method are found in literature (Douville et al., 1995; Luce and Tarboton, 2001; Hirota et al., 2002; You et al., 2014). The models use the parameter averaging method, but no solutions for the flux aggregation method are described. Therefore, the surface temperature equation for a snow pack in METRAS has been developed as described below.

In METRAS, each grid cell is covered with a different number of SCCs. For each grid cell, the sub-grid scale surface fluxes are calculated for each SCC. In addition, the surface temperature needs to be calculated for each SCC and each grid cell separately. In the case of a snow-covered surface, METRAS is extended to consider an additional snow layer on top of the surface (Figure 5.1). Therefore, the surface temperature of the snow has to be determined by a more complex system that combines snow surface cover and soil for calculating the exchange between the atmosphere and the surface.

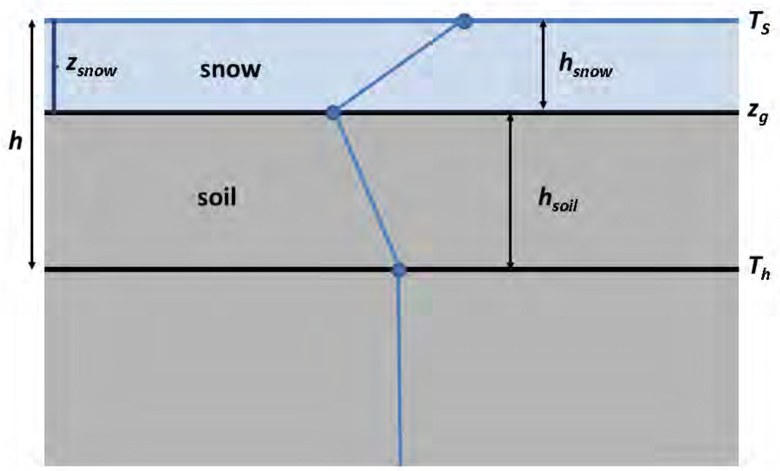

Figure 5.1: Schematic diagram of the snow scheme for considering a subgrid scale land use j.

In the force-restore method, a solution of the heat conduction equation is given with a sinusoidal wave as forcing at the surface. The propagation of the temperature wave into the soil is given by Equation (5.12) by HIROTA et al. (2002). The mean temperature at the surface is denoted by $T_{0_{mean}}$, the amplitude of the temperature wave at the surface by A_0, the frequency of the temperature wave by ω and the damping depth of the temperature wave for a given frequency by d. The derivatives with respect to time t and with respect to depth z are given by Equation (5.13) and Equation (5.14), respectively.

$$T\left(z,t\right)=T_{0_{mean}}+A_0\exp\left(-\frac{z}{d}\right)\sin\left(\omega t-\frac{z}{d}\right) \tag{5.12}$$

$$\frac{\partial T\left(z,t\right)}{\partial t}=\omega A_0\exp\left(-\frac{z}{d}\right)\cos\left(\omega t-\frac{z}{d}\right) \tag{5.13}$$

$$\frac{\partial T\left(z,t\right)}{\partial z}=-\frac{1}{d}A_0\exp\left(-\frac{z}{d}\right)\left(sin\left(\omega t-\frac{z}{d}\right)+\cos\left(\omega t-\frac{z}{d}\right)\right) \tag{5.14}$$

The heat flux through a layer, G, is given by Equation (5.15) (Hirota et al., 2002) with the thermal conductivity ν_g. The index g denotes the system of combined snow surface cover and soil. The specific layers of snow surface cover and soil are denoted with the indices *snow* and *soil*, respectively.

$$G_g(z,t)=-\nu_g\left(\frac{\partial T(z,t)}{\partial z}\right)_g \tag{5.15}$$

For calculating the surface temperature using force-restore method with flux aggregation method, Equation (5.15) is solved in this thesis by using Equation (5.14) for each SCC, denoted by j. The heat fluxes through the layers of snow, $G_{snow,j}$, and soil, $G_{soil,j}$, at the snow-soil-interface in the depth, $z_{g,j}$, are determined by Equation (5.16) and Equation (5.17).

$$\begin{aligned}
&G_{snow,j}\left(z_{g,j},t\right)\\
&=\frac{\nu_{snow,j}}{d_{snow,j}}A_{0_{snow,j}}\exp\left(-\frac{z_{g,j}}{d_{snow,j}}\right)\left(\sin\left(\omega_j t-\frac{z_{g,j}}{d_{snow,j}}\right)+\cos\left(\omega_j t-\frac{z_{g,j}}{d_{snow,j}}\right)\right)\\
&=\frac{\nu_{snow,j}}{d_{snow,j}}\left(\frac{1}{\omega_j}\frac{\partial T_{snow,j}\left(z_{g,j},t\right)}{\partial t}+T_{snow,j}\left(z_{g,j},t\right)-T_{0_{snow,j}}\right)
\end{aligned} \tag{5.16}$$

$$\begin{aligned}
&G_{soil,j}\left(z_{g,j},t\right)\\
&=\frac{\nu_{soil,j}}{d_{soil,j}}A_{0_{soil,j}}\exp\left(-\frac{z_{g,j}}{d_{soil,j}}\right)\left(\sin\left(\omega_j t-\frac{z_{g,j}}{d_{soil,j}}\right)+\cos\left(\omega_j t-\frac{z_{g,j}}{d_{soil,j}}\right)\right)\\
&=\frac{\nu_{soil,j}}{d_{soil,j}}\left(\frac{1}{\omega_j}\frac{\partial T_{soil,j}\left(z_{g,j},t\right)}{\partial t}+T_{soil,j}\left(z_{g,j},t\right)-T_{0_{soil,j}}\right)
\end{aligned} \tag{5.17}$$

The thermal conductivities of snow and soil for a certain SCC are denoted by $\nu_{snow,j}$ and $\nu_{soil,j}$. The damping depths for given frequencies $d_{snow,j}$ and $d_{soil,j}$ are given by Equation (5.18) and Equation (5.19), where $h_{snow,j}$ and $h_{soil,j}$ denote the depth of the daily temperature wave into the snow and soil layers.

$$d_{snow,j} = \frac{h_{snow,j}}{\sqrt{\pi}} = \sqrt{\frac{k_{snow,j}\tau}{\pi}} \tag{5.18}$$

$$d_{soil,j} = \frac{h_{soil,j}}{\sqrt{\pi}} = \sqrt{\frac{k_{soil,j}\tau}{\pi}} \tag{5.19}$$

The thermal diffusivities for snow and soil are given by $k_{snow,j}$ and $k_{soil,j}$, respectively. The period of the temperature wave is given by $\tau = 1$ day $= 86400$ s. Solving Equation (5.17) for the time derivative of $T_{soil,j}(z_{g,j}, t)$ leads to Equation (5.20).

$$\frac{\partial T_{soil,j}\left(z_{g,j}, t\right)}{\partial t} = \frac{\omega_j d_{soil,j}}{\nu_{soil,j}} G_{soil,j}(z_{g,j}, t) - \omega_j T_{soil,j}(z_{g,j}, t) + \omega_j T_{0_{soil,j}} \tag{5.20}$$

No physical processes are considered at the snow-soil interface except the heat conduction. Assuming thermal equilibrium at the snow-soil-interface at the depth $z_{g,j}$, the temperatures $T_{snow,j}(z_{g,j}, t)$ and $T_{soil,j}(z_{g,j}, t)$ are equal all the time and therefore their time derivatives are equal, too. The mean temperature of the snow layer, $T_{0_{snow}}$, is approximated as the surface temperature $T_{0_{snow,j}} \approx T_{S,j}$. The soil temperature, $T_{0_{soil}}$, is approximated as the temperature T_h at depth, h, where the temperature is assumed to be constant during a few days of model simulation in the same way as is done in the standard version of METRAS. The heat fluxes at the snow-soil interface at the depth $z_{g,j}$ are defined as $G_{snow,j}(z_{g,j}, t) \stackrel{!}{=} -G_{soil,j}(z_{g,j}, t)$. Solving Equation (5.16) by using Equation (5.20) leads to Equation (5.21).

$$\begin{aligned} G_j(z_{g,j}, t) &= -\frac{1}{\frac{d_{snow,j}}{\nu_{snow,j}} + \frac{d_{soil,j}}{\nu_{soil,j}}} \left(T_{0_{snow,j}} - T_{0_{soil,j}}\right) \\ &\approx -\frac{\sqrt{\pi}}{\frac{h_{snow,j}}{\nu_{snow,j}} + \frac{h_{soil,j}}{\nu_{soil,j}}} \left(T_{S,j}(t) - T_h\right) \end{aligned} \tag{5.21}$$

The heat conduction equation for a layer with the depth z is given by Equation (5.22), where k_g denotes the thermal diffusivity of the layer.

$$\frac{\partial T}{\partial t} = k_g \frac{\partial^2 T}{\partial z^2} \tag{5.22}$$

Solving Equation (5.22) at the surface by using Equation (5.15) at the surface ($z = 0$) and at the snow-soil interface ($z = z_g$) leads to Equation (5.23). $G\left(0, t\right)$ and $G\left(z_g, t\right)$ are given by Equation (2.29) and Equation (5.21), respectively.

$$\begin{aligned}\frac{\partial T_{S,j}(t)}{\partial t} &= \frac{k_{g,j}}{\nu_{g,j}}\left(\frac{-G_j(0,t) + G_j(z_{g,j},t)}{\frac{d_{g,j}}{2}}\right)\\ &= \frac{2\sqrt{\pi}k_{g,j}}{h_{g,j}\nu_{g,j}}\left(-G_j\left(0,t\right) - \frac{\sqrt{\pi}}{\frac{h_{snow,j}}{\nu_{snow,j}} + \frac{h_{soil,j}}{\nu_{soil,j}}}\left(T_{S,j}(t) - T_h\right)\right)\end{aligned} \tag{5.23}$$

In the case where there is a snow surface, Equation (5.23) becomes Equation (5.24).

$$\frac{\partial T_{S,j}(t)}{\partial t} = \frac{2\sqrt{\pi}k_{snow,j}}{h_{snow,j}\nu_{snow,j}}\left(-G_j\left(0,t\right) - \frac{\sqrt{\pi}}{\frac{h_{snow,j}}{\nu_{snow,j}} + \frac{h_{soil,j}}{\nu_{soil,j}}}\left(T_{S,j}(t) - T_h\right)\right) \tag{5.24}$$

Equation (5.24) is true for a snow cover with a deep $z_{g,j}$ smaller than the depth of the daily temperature wave, h_{snow}. For the extreme case with a snow cover deeper than h_{snow}, h_{soil} becomes zero. Therefore, Equation (5.24) is simplified to Equation (5.25) for a deep snow pack. This equation is equal to the surface temperature equation of the standard version of METRAS (Equation 2.35), but adapted to the thermal parameters of snow instead of soil.

$$\frac{\partial T_{S,j}(t)}{\partial t} = \frac{2\sqrt{\pi}k_{snow,j}}{h_{snow,j}\nu_{snow,j}}\left(-G_j\left(0,t\right) - \frac{\nu_{snow,j}\sqrt{\pi}}{h_{snow,j}}\left(T_{S,j}(t) - T_h\right)\right) \tag{5.25}$$

If the snow melts, h_{snow} becomes zero. Then the remaining type of the surface layer is soil. Equation (5.23) simplifies to Equation (5.26), which is exactly the surface temperature equation of the standard version of METRAS (Equation 2.35).

$$\frac{\partial T_{S,j}(t)}{\partial t} = \frac{2\sqrt{\pi}k_{soil,j}}{h_{soil,j}\nu_{soil,j}}\left(-G_j\left(0,t\right) - \frac{\nu_{soil,j}\sqrt{\pi}}{h_{soil,j}}\left(T_{S,j}(t) - T_h\right)\right) \tag{5.26}$$

5.2.2 Downscaling methodology with non-uniform grids

As discussed in Chapter 2, dynamical downscaling and statistical-dynamical downscaling often need several refinement steps to localise GCM results because with the nudging approach a refinement can be at most a factor of four in the grid resolution (Schroeder and Schlünzen, 2009). For the SDD three refinement steps with one-way nesting are needed to downscale the GCM results to a high enough resolution (Chapter 4). This takes a long computing time for two reasons. First, the refinement steps need to be sequential, and second, the data for the area of interest are computed each time the refinement is done, just with increasing resolution.

One method to reduce the computing time is the use of a non-uniform horizontal grid (Bungert, 2008). The non-uniform grid applies a continuous refinement from the boundaries of the domain to the inner domain which is the area of interest (focus domain). The restriction to a refinement of the grid size of one quarter in one refinement step is met at the boundaries, but inside the model domain, the horizontal resolution can be further refined.

A non-uniform grid contains the focus domain with a high horizontal resolution wherein the results of the numerical simulation will be analysed. Outside of the focus domain, the horizontal grid size increases to a coarser horizontal grid. The non-uniform grid is nested into the GCM result. The whole domain including the focus domain and the area with the coarser horizontal resolution is named the model domain in the following sections.

The non-uniform grid contains asymmetric grid cells with a high horizontal resolution in one direction and a coarse horizontal grid resolution in the other. Gravity waves and their reflections have a different dispersion for grids with high and coarse grid resolutions (Schroeder and Schlünzen, 2009). Therefore, the use of a non-uniform grid may introduce numerical instabilities. Bungert (2008) showed that the numerical methods used in METRAS are able to deal with the effects of the non-uniform grid. However, she noted that the asymmetric grid cells had generated artificial circulations due to the asymmetric orography and land use (Bungert, 2008). Several tests with filtered orography and land use performed by Bungert (2008) showed that at least the influence of the asymmetric surface cover is small when using the flux aggregation method to calculate the effects of the subgrid-scale land use.

To avoid the effects of an asymmetric orography, the preparation of the orography on the non-uniform grid is investigated. The objective is to reduce the asymmetry of the orography as much as needed and keep as much of the orography structure as possible. Seven different ways to prepare the orography of the non-uniform grid are analysed (experiments A - G, Table 5.1).

The orography and the land use of all experiments are filtered with a 3-point filter for the model domain to avoid creation of $2\Delta x$-waves from small-scale orography and land use. For Experiments A, C and E, boundary smoothing following the guidelines of VDI 3783 Blatt 16 (2015) is applied. This means the outer ten rows of grid cells parallel to the boundary are smoothed with a 3-point filter ten times, with a linear decreasing weight of the filter with increasing distance from the boundary.

The result of experiment A is a smooth orography in the boundary zone for the non-uniform grid, while the resulting orography is still asymmetric. To avoid the asymmetric orography, a uniform grid with the coarsest resolution is created. On this the orography is symmetric. The orography of this uniform grid is interpolated to the non-uniform grid using the nearest neighbour method (experiments B - F). The orography of the uniform grid is merged with the non-uniform grid with different weighting methods. All orographies are only modified outside the focus domain. The weighting of the orography from the uniform grid decreases with increasing distance from the lateral boundary linearly (experiment B and C), or squared (experiment D and E) or depending on the aspect ratio of the grid cell (experiment F). The resulting orography in experiments B to F is smooth to very smooth in the boundary zone with missing small-scale orographic information. The filtered and smoothed orography is still asymmetric on the non-uniform grid. A comparison between the different weighting methods showed for the squared method a large decrease of the effect of the coarse orography in the filtered and smoothed orography as well as the method using the aspect ratio of the grid cell. Both do not fit with the linear change of the horizontal grid resolution.

In experiment G, the orography of the uniform grid is interpolated to the non-uniform grid using a bilinear interpolation with the linear weighting method. The asymmetry of the resulting orography of experiment G is reduced. The filtered and smoothed orography

Table 5.1: Test for characteristics of the METRAS model domain with non-uniform grids.

Experiment	Boundary Smoothing	Interpolation method: Nearest neighbour	Interpolation method: Bilinear	Weighting method: Linear	Weighting method: Squared	Weighting method: Aspect
A	x	-	-	-	-	-
B	-	x	-	x	-	-
C	x	x	-	x	-	-
D	-	x	-	-	x	-
E	x	x	-	-	x	-
F	-	x	-	-	-	x
G	-	-	x	x	-	-

is less smooth than that from the experiments A to F. Coarse orography structures at the boundaries remain and become smaller scale towards the inner of the model domain. This fits well with the linearly increasing horizontal resolution of the non-uniform grid.

5.2.3 Model input

The preparation of the model grid is given in Section 5.2.3.1. The urban development scenario is described in Section 5.2.3.2. The simulated meteorological situations are given in Section 5.2.3.3.

5.2.3.1 Selected domain

A non-uniform grid is used that is prepared as described for experiment G (Section 5.2.2). The total area of the model domain measures about 246×248 km^2 and covers large parts of Northern Germany with 247×245 horizontal grid cells (Figure 5.2). The focus domain which includes Hamburg, covers an area of 42.25×41.75 km^2 with 169×167 horizontal grid cells and a horizontal resolution of 250 m.

The model domain includes three areas around the focus domain, namely an area with a constant coarse horizontal grid resolution (coarse grid resolution), an area with a refinement of the horizontal grid size (refinement area) and an area with a constant high

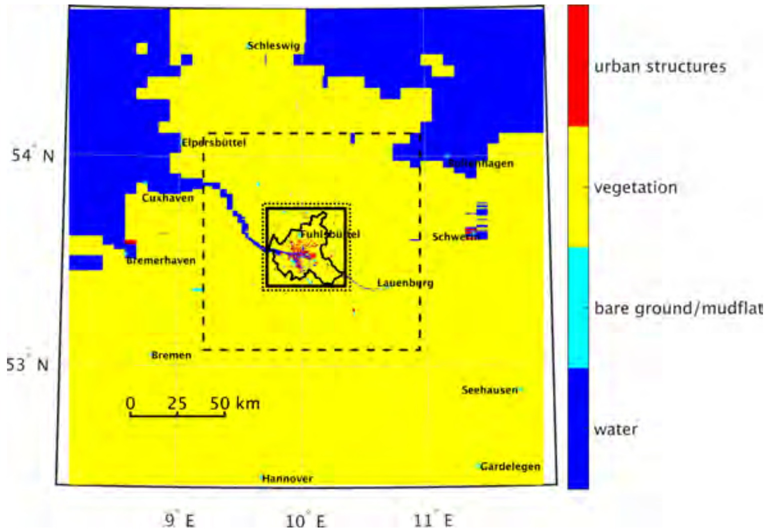

Figure 5.2: Surface cover classes compiled in four main groups for the whole model domain. Note that the figure only shows the group with the highest percentage per grid cell, although the numerical model considers subgrid-scale land uses. The state boundary of Hamburg is marked with an irregular black line. The black rectangle marks the focus domain. The dotted rectangle marks the grid cells with 250×250 m^2 horizontal grid resolution. Between the dotted rectangle and the dashed rectangle the horizontal grid resolution increases from 250 m to 6000 m. Outside of the dashed rectangle, the grid cells have a constant grid size.

horizontal grid resolution, which is somewhat larger than the focus area. The coarse grid area includes the outer ten rows of grid cells at the lateral boundaries of the model domain, with the largest horizontal grid size of 6 km normal to the lateral boundaries. In Figure 5.2, this area is located outside the black dashed rectangle. This area is most affected by nudging. The horizontal grid size is matched to the horizontal grid resolution of 16 km to 25 km of the forcing data from the European Centre for Medium-Range Weather Forecasts (ECMWF) and is the finest horizontal grid resolution that is suitable for nudging. The refinement area, which extends from the coarse horizontal grid at the lateral boundaries to the inner domain, consists of 20 grid cells parallel to the lateral boundaries and is located in between the black dashed and dotted rectangle in Figure 5.2. The increase in horizontal grid resolution refinement from one grid cell to the next is 17.5%. The high resolution area is inside the black dotted rectangle, where the horizontal grid size is constant with a 250 m grid resolution for horizontal direction. This inner area with the fine constant horizontal grid size contains the focus domain and ten grid cells around it which are neglected in the analyses of the model results to avoid structures resulting from the transient change of the refinement area. The focus area is marked with a black rectangle in Figure 5.2.

The vertical grid includes 34 levels with the lowest grid level at 10 m above ground. Close to the surface, the vertical grid size is 20 m. Above 100 m above ground, the vertical grid size increases by 17.5% per grid cell to a maximum vertical grid size of 1000 m. The highest model level is at about 12000 m.

5.2.3.2 Urban development scenario

For estimating the impact of urban development and climate adaptation measures on the winter climate of Hamburg, the socio-economic scenario s3 (Section 4.3.2.3) is applied. The scenario s3 is represented in the METRAS model by changes in the SCC compared to the SCC from the current situation. In scenario s3, a growing population is assumed with decreased individual transport. Therefore, the building density is increased compared to the reference case but the traffic areas decrease. In total, this leads to a decrease in sealed surfaces for the inner city of Hamburg and in the southern suburbs and an increase for the northern suburbs and the outer city (Figure 5.3a). This is reflected in the changes of the roughness length (Figure 5.3d). The widespread implementation of green roofs and grass pavers leads to a strong increase of evaporative surfaces (Figure 5.3b). The use of building materials with higher albedo leads to an increase of the albedo (Figure 5.3c).

5.2.3.3 Selected meteorological situations

To assess the impact of the climate adaptation measures on the winter climate of Hamburg, as many as necessary and as few as possible days are calculated for representing the climate average. The statistics of temperature, relative humidity,wind speed and wind direction for the winter months DJF from 1981 to 2010 are calculated for 27 weather stations in Northern Germany and The Netherlands. The BSS (Section 2.3.2) was used to determine the number of days to be simulated.

Figure C.7 and Figure C.7 show that the BSSs increases with an increasing number of days needed to simulate the PDFs of the four investigated meteorological variables. The BSSs converge towards the LOAs. This behaviour is strongest for the BSS RH/FF. Therefore, for the BSS RH/FF only 86 days are needed to achieve a near-perfect agreement (Table 2.8 and Table 5.2). For BSS DD/TC (weakest convergence) 225 days are required to reach a near perfect result (Table 2.8 and Table 5.2). To reach a good result, 31 and 79 days are required for BSS RH/FF and BSS DD/TC, respectively.

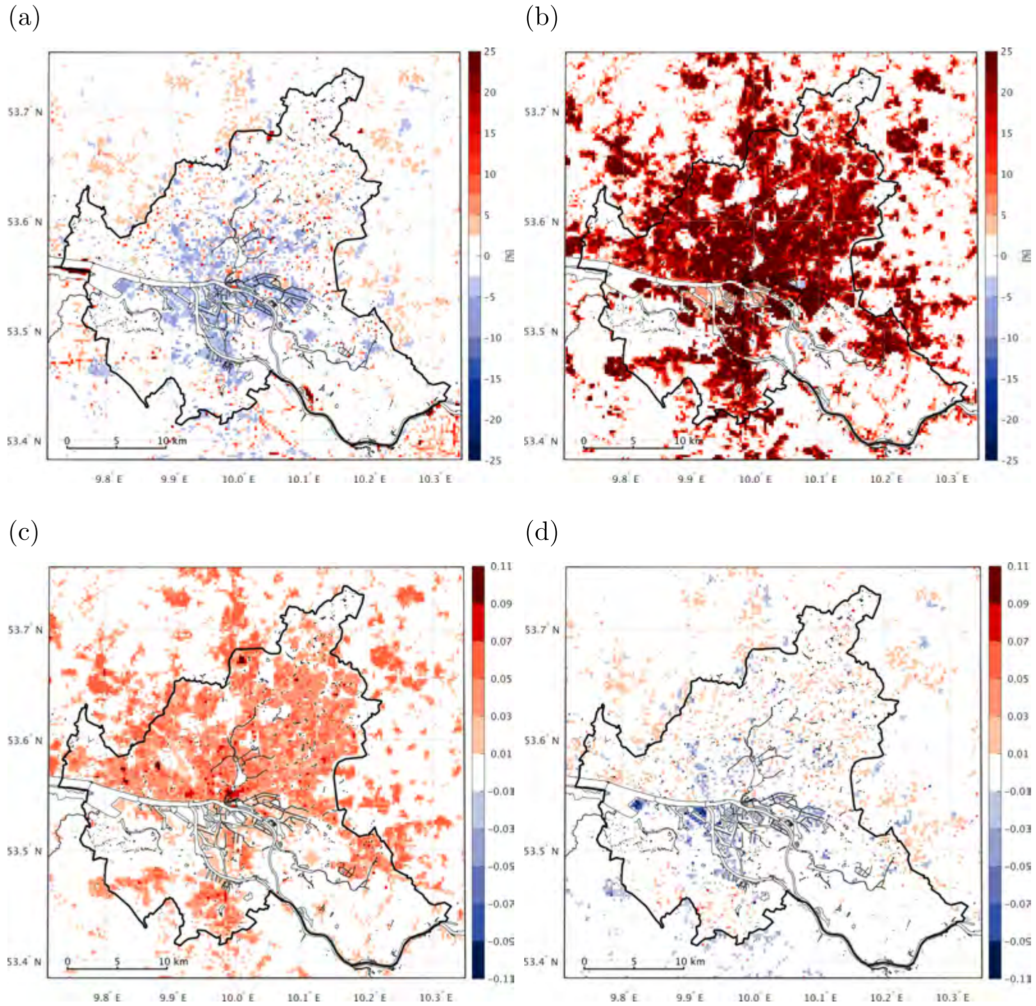

Figure 5.3: Changes in scenario s3 compared to the reference case for (a) fraction of sealed surfaces, (b) fraction of evaporative surfaces, (c) albedo and (d) logarithmic averaged roughness length. Blue (red) denote decrease (increase) in the scenario compared to the reference case. The state boundaries of Hamburg are marked with a thick black line and the thinner lines illustrate the water bodies of Hamburg. This figure shows the same changes from scenario s3 as Figure 4.7 but for the focus area of the non-uniform grid applied for winter climate simulations.

The statistics are calculated for independent, randomly chosen days. The simulations with the numerical model consist of three continuous days. This restriction leads to lower values for the BSSs than to be expected for a given number of randomly chosen days. To avoid low accuracy from the restrictions, the number of days used for the simulations in this study is much higher than the number of days needed to reach a good agreement determined in Section 2.3.2. To simulate the winter climate of Hamburg, 129 days are chosen, consisting of 43 numerical simulations of periods of three days each. The dates of

Table 5.2: Level of accuracy (LOA) and BSS for randomly chosen 129 days in the winter season. The assessment criteria for good and near-perfect agreements are given in Table 2.5 and Table 2.6, respectively.

BSS	LOA	Required number of days for good result	Required number of days for near perfect result	BSS for 129 randomly chosen days	BSS for 129 selected days
TC/FF	0.95	64	196	0.82	0.77
TC/RH	0.94	63	182	0.82	0.78
RH/FF	0.96	31	86	0.88	0.83
DD/TC	0.94	79	225	0.80	0.78
DD/FF	0.95	41	120	0.86	0.82
DD/RH	0.96	39	107	0.87	0.85

the days calculated in the 43 simulations are given in Appendix G.

The BSS is calculated as a mean from 1000 resamples built by bootstrapping for all combinations of the four meteorological parameters for 129 randomly chosen days for each of the 27 weather stations. The mean BSS for each weather station is marked with a blue dot in Figure 5.4 and Figure 5.5. The error bars mark the 5$^{\text{th}}$ and 95$^{\text{th}}$ percentile. The good and near-perfect agreements as a mean of all weather stations are given in Figure 5.4 and Figure 5.5 with a black and a blue line, respectively. The BSS values for the selected 129 days are marked with red dots.

The mean BSS for each weather station and each combination of the meteorological parameters is in the range determined for a good agreement for the 129 randomly chosen days (Table 2.5 and Table 5.2). BSS TC/FF shows the lowest performance for the 129 selected days. The BSSs TC/FF of 129 selected days for the single weather stations approximate the assessment criteria for a good agreement (Figure 5.4a). For some weather stations, the BSS TC/FF is less than the assessment criterion for a good agreement. However, the BSS averaged over all weather stations is within the range for a good agreement (Table 2.5 and Table 5.2). The best result is found for BSS DD/RH, with near-perfect agreement for some weather stations (Figure 5.4d). The mean value of BSS DD/RH, averaged over all weather stations, nearly agrees with the demands for a near-perfect agreement (Table 2.6 and Table 5.2). Therefore, a selection of 129 days sufficiently

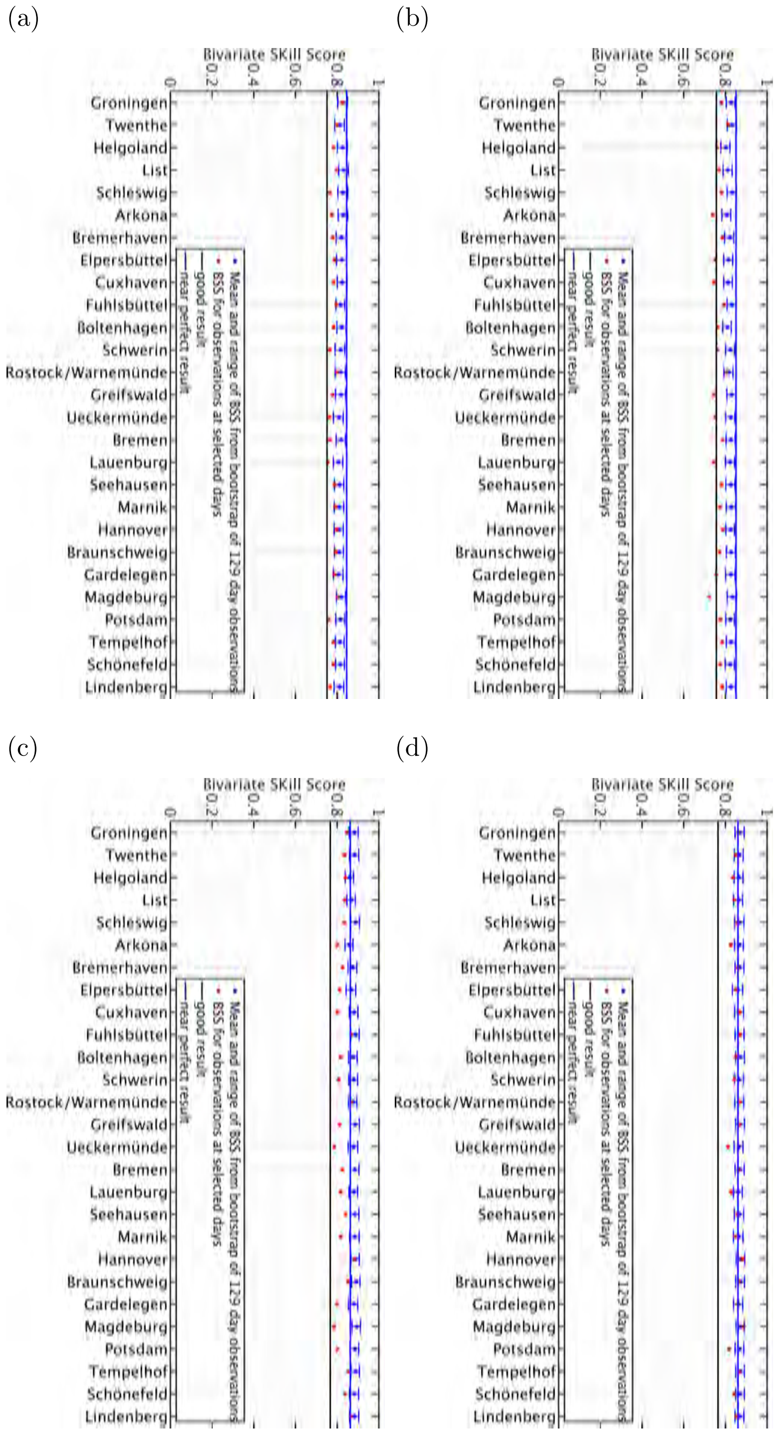

Figure 5.4: Bivariate Skill Score (BSS) for individual meteorological sites for (a) TC/RH, (b) TC/FF, (c) RH/FF and (d) DD/RH based on 30 years of hourly winter data. The mean BSS for each weather station is marked with a blue dot. The error bars mark the 5$^{\text{th}}$ and 95$^{\text{th}}$ percentile. The good and near-perfect agreements as a mean of all weather stations are given with a black and a blue line, respectively. The BSSs for the selected 129 days are marked with red dots.

(a) (b)

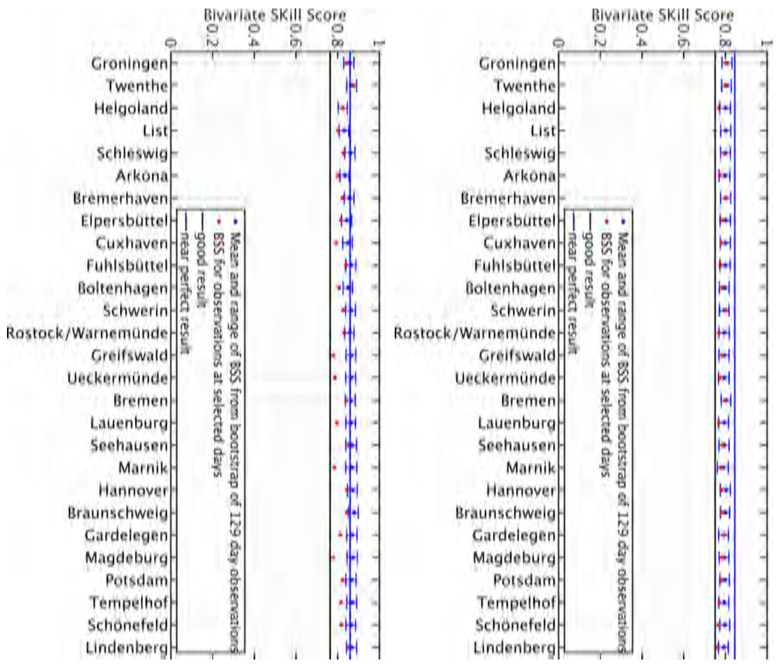

Figure 5.5: Same as Figure 5.4 but for (a) DD/FF and (b) DD/TC.

represents the winter climate of the MRH.

The 129 selected days are used in calculations three times for different scenarios: the two reference simulations for the current situation both without using the snow scheme (REF_NO_SNOW) and with the snow scheme (REF_WITH_SNOW), as well as for scenario s3 using the snow scheme.

5.2.4 Method for model result analysis

In Section 5.2.4.1, the method of evaluation of the model simulations is described. The method of assessing the impact of the socio- economic scenario on the urban climate is given in Section 5.2.4.2.

5.2.4.1 Evaluation method

The evaluation of REF_NO_SNOW is discussed in Section 5.3.1. The results of the evaluation of REF_WITH_SNOW are analysed and discussed in Section 5.3.2. The results of the model simulations are evaluated against the observational data from weather stations in the model domain. Twelve of the 27 weather stations used for calculating the statistics are located in the model domain whereas only the weather station Fuhlsbüttel is located in the focus domain. The weather stations located in the model domain are written in bold letters in Table B.1. The model results are horizontally interpolated to the weather stations using the nearest neighbour method. The evaluation is performed for temperature, relative humidity, wind speed and wind direction. These variables are chosen because they are important for assessing the impact of climate adaptation measures. The model results from the first level at 10 m above ground are used, because the corresponding values at 2 m above ground can not be determined as average value for a grid cell in a physical-sound way. The reason is the use of the flux aggregation method which would lead to different 2 m temperatures above the different SCC.

For evaluation of the model results, the HITRATE, the BIAS, the root mean square error (RMSE) and the correlation coefficient (R) are calculated following the model evaluation guidelines of COST728 (Schlünzen and Sokhi, 2008). The BIAS gives the systematic error of a model simulation and should ideally be zero. The RMSE is a combination of the systematic and non-systematic error and gives the total error of a model simulation and should ideally be zero. The dimensionless error R evaluates the non-systematic error and should ideally be one. The HITRATE indicates how often the model result lies within the forecast with a given accuracy D and should ideally be one. The evaluation measures are given by Equation (5.27) to Equation (5.30), where M_i and O_i denote the model results and the corresponding observation, respectively, $\bar{M}$ and $\bar{O}$ are the corresponding means and N the sample size. D is chosen as in Hoffmann et al. (2016) with 2 K for temperature, 5 % for relative humidity, 1 m/s for wind speeds between 1 m/s and 10 m/s and 2.5 m/s for wind speeds higher than 10 m/s. 30° are used for wind direction during wind speeds larger than 1 m/s. The mean wind direction is only calculated for wind speeds higher than 1 m/s using the normalised u- and v-components. The resulting vector gives the averaged wind direction.

$$HITRATE = \frac{1}{N}\sum_{i=1}^{N} n_i \; with \; n_i \; = \begin{cases} 1 \; for \; |M_i - O_i| \leq D \\ 0 \; else \end{cases} \tag{5.27}$$

$$BIAS = \bar{M} - \bar{O} \tag{5.28}$$

$$RMSE = \sqrt{\frac{1}{N}\sum_{i=1}^{N}(M_i - O_i)^2} \tag{5.29}$$

$$R = \left[\frac{\frac{1}{N}\sum_{i=1}^{N}\left(O_i - \bar{O}\right)\left(M_i - \bar{M}\right)}{\sqrt{\frac{1}{N}\sum_{i=1}^{N}\left(O_i - \bar{O}\right)^2}\sqrt{\frac{1}{N}\sum_{i=1}^{N}\left(M_i - \bar{M}\right)^2}}\right] \tag{5.30}$$

The evaluation measures are calculated as one value using all hourly data calculated for the 12 weather stations in the model domain. Furthermore, the same measures are evaluated for Fuhlsbüttel.

5.2.4.2 Urban and scenario effects

The model output is written every 30 minutes and analysed for the 129 days. Only the results from the focus area are considered for the scenario impact analysis. For each output time and each variable, the average of the 129 simulated days is calculated. The variables are given either as a 24-hour mean or as a day- and nighttime mean. To account for the winter situation, daytime is chosen from 1100 LT to 1500 LT whereas the nighttime is defined as 1800 LT to 0700 LT.

As mentioned in Section 5.2.4.1, the results are assessed at 10 m above ground, which is the lowest model level. The effects of scenario s3 are determined by subtracting the values of REF_WITH_SNOW from those of scenario s3. For estimating the differences between urban and rural areas, the corresponding grid cells are identified from the input data of the reference simulations as described in Section 4.2.3.1. The grid cells found by this method are utilised in the scenario simulation, too, so that the differences generated by the scenario s3 can be determined. The resulting urban and rural grid cells are shown in Figure 5.6.

The urban cool island (UCI) and UHI are calculated only for Hamburg. The spatial pattern is calculated from the values of the temperature at 10 m above ground in Hamburg minus the averaged temperature at 10 m above ground from all rural grid cells.

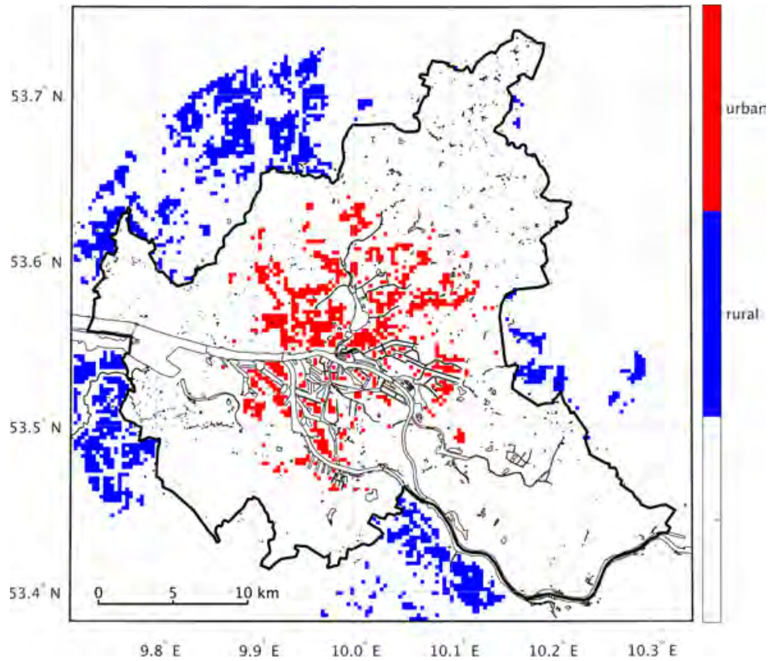

Figure 5.6: Urban (red) and rural (blue) grid cells for the focus domain as defined in Section 5.2.4.2. The state boundaries of Hamburg are marked with a thick black line, water bodies are marked with thin black lines. This figure shows the same urban and rural grid cells as Figure 4.3 but for the focus area of the non-uniform grid applied for winter climate simulations.

5.3 Discussion of results

The evaluation of REF_NO_SNOW is given in Section 5.3.1. REF_WITH_SNOW is evaluated in Section 5.3.2. The scenario s3 results are analysed and discussed in Section 5.3.3. The impact of urban development and climate adaptation measures on winter and summer climate are compared in Section 5.3.4.

5.3.1 Evaluation of winter climate without snow cover

The HITRATE, BIAS, root mean square error (RMSE) and correlation coefficient (R) for REF_NO_SNOW are given as a mean over 12 weather stations in Table 5.3 and separately for Fuhlsbüttel in Table 5.4. Schlünzen et al. (2016) has made a statistical analyses of model evaluations. The results from there are used as measure to assess the current results. BIAS, RMSE and R for temperature and wind direction as a mean over the 12 weather stations are in the better 50 percent of model results summarised by Schlünzen et al. (2016) (Table 5.3). For wind speed, R is in the better 50 percent of model results as well (Schlünzen et al., 2016), although the BIAS and the RMSE for wind speed are worse. The HITRATE is reflecting these results (Table 5.3). Due to a lack of data in Schlünzen et al. (2016), the HITRATEs are not comparable to other values as well as the evaluation measures received for the relative humidity. Compared to the values of the evaluation measures of the reference simulations for the summer climate of Hamburg (Table 4.4), the HITRATEs for temperature, relative humidity and wind direction are improved for the winter climate. R for relative humidity and all evaluation measures for wind speed (except R) are worse for the winter climate than for the summer climate.

The evaluation for Fuhlsbüttel shows results similar to the mean of the 12 weather stations, but mostly with a lower performance (Table 5.4). The BIAS of temperature is larger than the BIAS over the 12 weather stations but still inside the range of the best 50 percent of the model results found in Schlünzen et al. (2016). R for temperature is lower than for the 12-weather station mean, too. The BIAS and R of the relative humidity are lower than for the mean of 12 weather stations because the relative humidity is directly linked to the temperature. An analysis of the model input shows that for Hamburg airport, at the place where the weather station Fuhlsbüttel is located, the SCC implies more buildings than found in reality. This results in larger BIASs in temperature and wind speed for this area.

The wind speed is systematically underestimated in ref_no_snow in the mean over the 12 weather stations and for Fuhlsbüttel alone but the diurnal cycle in wind speed is still intact (large R), which means the stratification of the atmosphere is represented well. The performance of the other variables is good.

5.3.2 Evaluation of winter climate with snow cover

The HITRATE, BIAS, RMSE and R are given for ref_with_snow as a mean over 12 weather station in Table 5.5 and for Fuhlsbüttel in Table 5.6. The evaluation measures for ref_with_snow are very similar to those determined for ref_no_snow, and are in the range of those found for the better 50 percent of model results analysed by

Table 5.3: Evaluation measures HITRATE, BIAS, root mean square error (RMSE) and correlation coefficient (R) for REF_NO_SNOW. The measures are calculated as an average of 12 DWD weather stations in the model domain.

	HITRATE	BIAS	RMSE	R
Temperature	0.81	−0.4 K	1.6 K	0.91
Relative humidity	0.59	0.0 %	7.1 %	0.69
Wind speed	0.35	−1.8 m/s	2.5 m/s	0.78
Wind direction	0.78	8°	38°	0.97

Table 5.4: Evaluation measures HITRATE, BIAS, root mean square error (RMSE) and correlation coefficient (R) for REF_NO_SNOW. The measures are calculated for the DWD weather station Fuhlsbüttel, which is the only weather station inside the focus domain.

	HITRATE	BIAS	RMSE	R
Temperature	0.65	−1.1 K	2.3 K	0.85
Relative humidity	0.51	3.7 %	8.2 %	0.66
Wind speed	0.29	−2.0 m/s	2.7 m/s	0.69
Wind direction	0.65	−9°	47°	0.95

SCHLÜNZEN et al. (2016), with the exception of the values for BIAS and RMSE of wind speed. Therefore, REF_WITH_SNOW represents the winter climate of Hamburg. Comparing the evaluation measures from REF_WITH_SNOW and REF_NO_SNOW, HITRATE is mostly the same except temperature for 12 weather stations. BIAS and RMSE are slightly lower for temperature in REF_WITH_SNOW. This is caused by a reduction of the air temperature at 10 m above ground in REF_WITH_SNOW compared to REF_NO_SNOW and a negative BIAS for temperature in REF_NO_SNOW. The correlation of the diurnal cycle for temperature is not influenced by the snow cover. The BIAS of the relative humidity of REF_WITH_SNOW is increased compared to REF_NO_SNOW. The RMSE of the relative humidity is slightly decreased and R is slightly increased for REF_WITH_SNOW compared to REF_NO_SNOW (Table 5.3 and Table 5.5). The evaluation measures for wind speed and wind direction are almost unaffected by the introduction of the snow cover, however, the diurnal cycle of the wind speed is better simulated in REF_WITH_SNOW (larger R). This is caused by the changed stability due to the changed temperature resulting from snow cover.

Table 5.5: Evaluation measures HITRATE, BIAS, root mean square error (RMSE) and correlation coefficient (R) for REF_WITH_SNOW. The measures are calculated as an average of 12 DWD weather stations in the model domain.

	HITRATE	BIAS	RMSE	R
Temperature	0.80	−0.5 K	1.7 K	0.91
Relative humidity	0.59	0.1 %	7.0 %	0.70
Wind speed	0.35	−1.8 m/s	2.5 m/s	0.79
Wind direction	0.78	8°	38°	0.97

Table 5.6: Evaluation measures HITRATE, BIAS, root mean square error (RMSE) and correlation coefficient (R) forREF_WITH_SNOW. The measures are calculated for the DWD weather station Fuhlsbüttel, which is the only weather station inside the focus domain.

	HITRATE	BIAS	RMSE	R
Temperature	0.61	−1.4 K	2.5 K	0.84
Relative humidity	0.51	4.2 %	8.4 %	0.66
Wind speed	0.28	−2.1 m/s	2.7 m/s	0.70
Wind direction	0.64	−9°	47°	0.95

In Table 5.6 the evaluation measures for REF_WITH_SNOW for Fuhlsbüttel are given. As already seen for REF_NO_SNOW, the model performance for Fuhlsbüttel is somewhat lower than for the mean of the 12 weather stations. For temperature, the four evaluation measures are slightly lower than for REF_NO_SNOW, and the BIAS and R are not in the better 50 percent of model results any more (Schlünzen et al., 2016). Linked to the performance for the temperature, the relative humidity shows higher values for BIAS and RMSE than for REF_NO_SNOW. The HITRATE for wind speed and wind direction is 1 % lower and the BIAS of the wind speed is increased by 0.1 m/s. Nevertheless, R as a measure of the diurnal cycle of the wind speed is slightly increased. The diurnal cycle of the wind speed is mainly determined by the stability of the atmosphere, so that the larger BIAS of the temperature results in a better represented stratification of the atmosphere (Table 5.4 and Table 5.6).

The simulations of REF_WITH_SNOW do not consider snow cover in each case. There were only very few days that actually had a snow cover anywhere in the model domain.

They are marked in Table G.1 with italic letters, where the simulations which include snow cover in the focus domain (11 simulations out of 43 simulations) are marked with bold italic letters. The simulations highlighted with a star in Table G.1 include snow cover at Fuhlsbüttel (8 simulations out of 43 simulations). The evaluation measures are calculated for only those eight simulations which include snow cover at Fuhlsbüttel for REF_WITH_SNOW and REF_NO_SNOW. The values are given for REF_NO_SNOW before and for REF_WITH_SNOW behind the slash in Table 5.7.

Table 5.7: Evaluation measures HITRATE, BIAS, root mean square error (RMSE) and correlation coefficient (R) for simulations having snow at the DWD weather station Fuhlsbüttel, which is the only weather station inside the focus domain. The values are given for REF_NO_SNOW before and for REF_WITH_SNOW behind the slash.

	HITRATE	BIAS	RMSE	R
Temperature	0.67 / 0.48	−1.4 K / −2.6 K	2.4 K / 3.3 K	0.68 / 0.60
Relative humidity	0.46 / 0.49	2.4 % / 3.6 %	8.1 % / 8.0 %	0.59 / 0.58
Wind speed	0.27 / 0.23	−2.0 m/s / −2.2 m/s	2.5 m/s / 2.7 m/s	0.61 / 0.55
Wind direction	0.70 / 0.68	−8° / −9°	39° / 39°	0.51 / 0.54

Most of the evaluation measures are worse for REF_WITH_SNOW compared to REF_NO_SNOW (reddish colour in Table 5.7). Only HITRATE and RMSE of the relative humidity and R for the wind direction are slightly improved (green in Table 5.7). No influence of the snow cover is found for RMSE of the wind direction (Table 5.7).

The evaluation for Fuhlsbüttel shows no improvement by using the snow scheme whereas the evaluation of 12 weather stations shows a worsening for the HITRATE, BIAS and RMSE of the temperature and the BIAS of the relative humidity, but also an improvement for RMSE and R of the relative humidity and R of wind speed. The results of the evaluation measures are still within an acceptable range. Overall, the evaluation at the 12 weather stations showed, that the climate is sufficiently represented by REF_WITH_SNOW.

5.3.3 Scenario impacts

In Schlünzen et al. (2010), a mean winter temperature at 2 m above ground of 1.8 °C is found for Fuhlsbüttel from measurements for the period from 1978 to 2007. The simulated mean winter climate temperature at 10 m above ground for the period from 1981 to 2010 is 1.4 °C for the urban and rural areas in REF_WITH_SNOW. Concerning the accuracy

$D = 2$ K from the estimation of the HITRATE (Section 5.2.4.1) between measurements and simulations, the simulated mean winter climate temperature hits the value from measurements. The mean spatial pattern of the temperature is given for daytime in Figure 5.7a and for nighttime in Figure 5.7c. The temperature at 10 m above ground has a gradient from north-east to south-west. Temperatures are about 0.5 K lower in the north-east for day- and nighttime in REF_WITH_SNOW (Figure 5.7a and Figure 5.7c). The mean day- and nighttime temperatures for urban and rural areas are given in Table 5.8.

During the winter months, the soil is warmer than the atmosphere in the MRH. The winter climate mean deep soil temperature used for simulations is 4.9 °C in a depth where the temperature is not changed by the diurnal cycle (≈ 0.2 m). Higher deep soil temperatures are used for the valley of the river Elbe (5.0 °C to 5.1 °C) and lower deep soil temperatures for the other parts of the city (4.7 °C to 4.9 °C). This is in good agreement with the mean soil temperatures found from measurements in the project HUSCO (Wiesner, 2017) for the winter months from December 2011 to February 2016. The mean soil temperatures measured in HUSCO were 4.3 °C at the depth of 0.1 m and 5.2 °C at the depth of 0.4 m for residential areas and 4.2 °C (0.1 m) and 5.4 °C (0.4 m) for urban green areas (Wiesner, 2017).

The socio-economic scenario s3 includes changes in the building density and therefore in the thermal diffusivity and thermal conductivity as well as in the evaporative areas, the roughness length and the albedo (Section 4.3). The changed thermal parameters increase the coefficient of the restore term in Equation (5.24). In the case of soil without snow cover, the equation simplifies to Equation (5.26) and the coefficient of the restore term increases by about one percent for the city of Hamburg and nearly half a percent for the suburbs in scenario s3. For snow-covered surfaces, the changes are smaller, depending on the density of snow and therefore the thermal characteristics of snow. The increased coefficient of the restore term increases exchange of energy between the surface and the atmosphere. Due to the mean soil temperatures being higher than the mean air temperature and the increased energy exchange between soil and atmosphere, the mean temperature at 10 m above ground is increased in scenario s3 compared to REF_WITH_SNOW (Table 5.8).

The magnitude of the increased energy exchange between soil and atmosphere is different for surfaces without snow-cover and snow covered surfaces. In the case of surfaces without snow cover, the increased albedo in scenario s3 leads to a higher reflection of the incoming short wave radiation. Therefore, the net short wave radiation budget is reduced compared

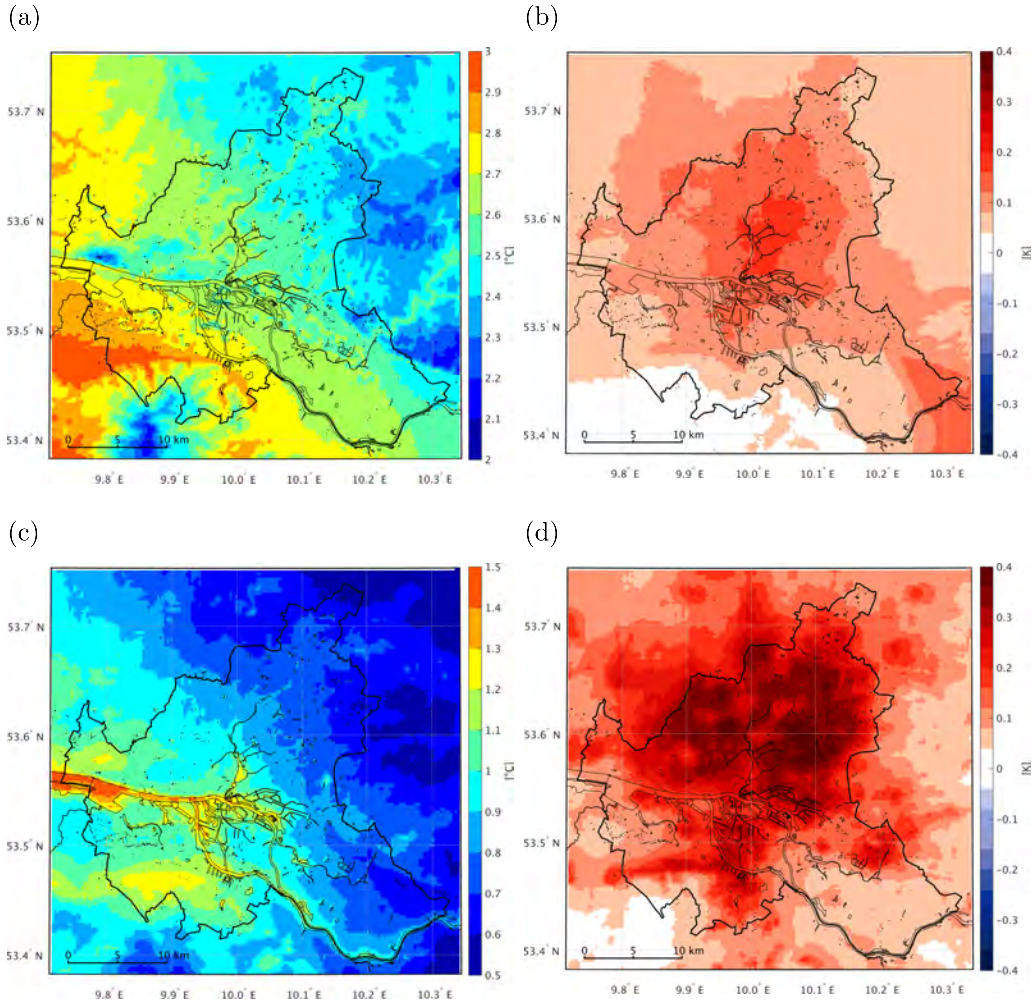

Figure 5.7: Mean spatial pattern for temperature at 10 m above ground for (a),(b) daytime (1100 LT to 1500 LT) and (c),(d) nighttime (1800 LT to 0700 LT). (a), (c) correspond to REF_WITH_SNOW, (b), (d) show differences of scenario s3 minus REF_WITH_SNOW. The boundaries of the state of Hamburg are marked with a thick black line, water bodies are outlined with thin black lines.

to REF_WITH_SNOW and decreases the surface temperature. In addition, the increased latent heat flux (Table 5.8) due to the increased evaporative areas induces a cooling effect in scenario s3 compared to REF_WITH_SNOW. Both effects are smaller than the temperature increase from the increased exchange of energy between soil and atmosphere. Therefore, the changes in temperature at 10 m above ground are a warming of 0.12 K for the urban areas during daytime and a warming of 0.27 K during nighttime for situations without snow cover. For rural areas, the increase in temperature at 10 m above ground is 0.06 K and 0.11 K for day- and nighttime, respectively. These values are for simulations

Table 5.8: Daytime (1100 LT to 1500 LT) and nighttime (1800 LT to 0700 LT) climate means of meteorological variables for urban and rural areas for REF_WITH_SNOW and scenario s3 for the winter months.

	REF_WITH_SNOW				Scenario s3			
	day		night		day		night	
	urban	rural	urban	rural	urban	rural	urban	rural
Temperature [°C]	2.6	2.7	1.0	0.9	2.7	2.8	1.3	1.0
Latent heat flux [W/m^2]	24	28	1	1	26	29	4	1
Relative humidity [%]	86	86	92	93	86	86	92	93
Integral cloud water content [kg/m^2]	0.04	0.04	0.03	0.03	0.04	0.04	0.03	0.03
Wind speed [m/s]	2.3	2.6	2.0	2.2	2.7	2.7	2.4	2.3

without snow cover in the focus area (Table G.1) while the value given in Table 5.8 are climate means.

For situations with snow-covered soil, the impact of the changed albedo in scenario s3 is less important because the surface is covered by snow with a high albedo anyway. The effect of the increased evaporative areas is overlaid by the sublimation from snow to the atmosphere. The higher exchange of energy between surfaces and the atmospheric layer above leads to snow melt in scenario s3. The snow mass is reduced up to 50 percent for the inner city of Hamburg and around 15 percent for large parts of the city. The reduced isolating capacity due to the reduced snow mass leads to a larger exchange of energy between the warmer soil and the colder atmosphere and increases the temperatures at 10 m above ground. The higher temperatures increase the snow melt and therefore give a positive feedback to the exchange of energy between the soil and the atmosphere. Therefore, the temperatures at 10 m above ground show increases for the urban areas about 0.2 K during daytime and about 0.4 K during nighttime (not shown). The effect in the rural areas is less developed, with values of 0.11 K and 0.18 K for day- and nighttime temperature, respectively. Based on scenario s3 results for surfaces with and without snow cover, the winter climate mean temperature at 10 m above ground increases more during nighttime (0.3 K for urban areas, Table 5.8 and Figure 5.7d) than during daytime (0.14 K for urban areas, Table 5.8 and Figure 5.7b). For rural areas, the temperature increases 0.07 K during daytime and 0.13 K during nighttime (Table 5.8).

Due to the different magnitude of changes in the temperature for urban and rural areas (Table 5.8), temperature differences between urban and rural also change. Lower temperatures are found for the urban areas during daytime and higher temperatures are found for the urban areas during nighttime (Table 5.9). The spatial pattern of the temperature differences between urban and rural areas shows for REF_WITH_SNOW that the MRH does not develop a pronounced UCI or UHI, but a gradient in regional scale in the winter climate mean temperature at 10 m above ground (Figure 5.7a and Figure 5.7c) accounts for the differences in temperature between urban and rural areas. Large parts of Hamburg have lower temperatures than the grid cells defined as rural (Figure 5.8a) during daytime. Those parts of Hamburg that are warmer than the rural surroundings during nighttime are either close to the water bodies or have a low altitude (Figure 5.8d). The effect of water bodies is in agreement with results of idealised studies performed by STUBBENHAGEN (2017). She showed that the influence of the relatively warm water bodies on the temperature at 10 m above ground is larger than the effect of the UHI of Hamburg.

Table 5.9: Daytime (1100 LT to 1500 LT) and nighttime (1800 LT to 0700 LT) mean temperature difference for urban and rural areas for REF_WITH_SNOW and scenario s3 for winter.

	REF_WITH_SNOW		Scenario s3	
	day	night	day	night
Temperature difference urban minus rural [K]	-0.09	0.09	-0.03	0.27

Due to the increased temperatures at 10 m above ground in scenario s3, especially in the urban areas north of the river Elbe compared to the rural surroundings (Figure 5.8f), Hamburg develops a widespread UHI in scenario s3 during nighttime (Figure 5.8e). During daytime, scenario s3 leads to a slight warming of the urban areas north of the river Elbe compared to the rural surrounding (Figure 5.8c) and therefore decreases the gradient of temperature and changes the pattern of the temperature difference of urban areas minus

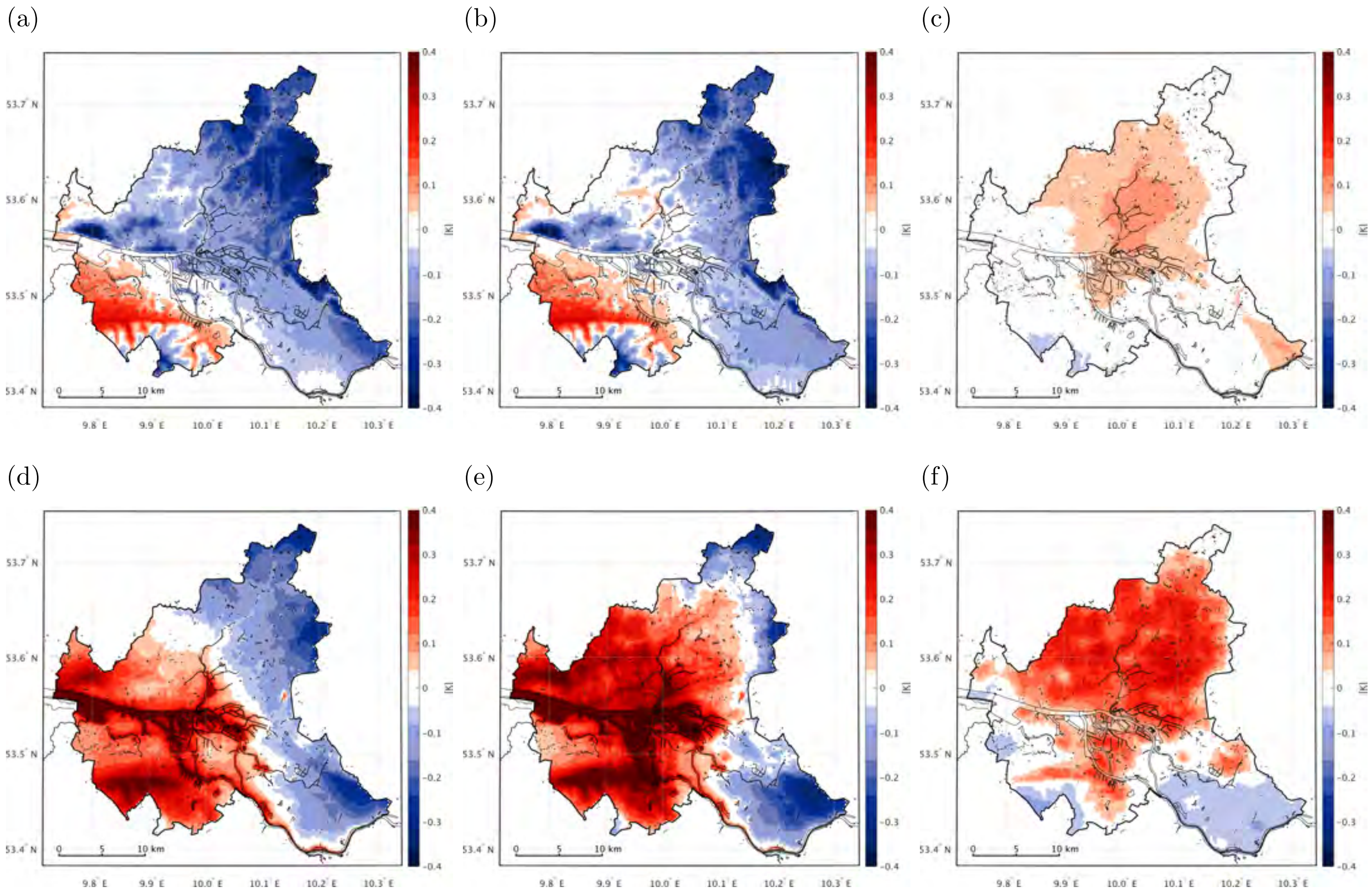

Figure 5.8: Mean spatial pattern at 10 m above ground for the temperature difference between urban and rural areas during (a),(b),(c) daytime (1100 LT to 1500 LT) and (d),(e),(f) nighttime (1800 LT to 0700 LT) for (a),(d) REF_WITH_SNOW, (b),(e) scenario s3 and (c),(f) scenario s3 minus REF_WITH_SNOW. Only areas within Hamburg are considered. The state boundaries of Hamburg are marked with a thick black line, water bodies are marked with thin black lines.

mean rural temperature (Figure 5.8b). The values of changes during daytime (0.06 K) are smaller than during nighttime (0.18 K) (Table 5.9).

The increased temperature at 10 m above ground influences the stratification of the atmosphere close to the surface. During daytime, the urban and rural areas of REF_WITH_SNOW and scenario s3 have an unstable stratification. During nighttime, all areas are stably stratified, but the urban areas of scenario s3 are less stable than the other areas. The stratification influences the vertical exchange and thus the wind speed at 10 m above ground. In REF_WITH_SNOW, the wind speed in the urban areas is lower than the wind speed in the rural areas during day- and nighttime (Table 5.8) and for the 24-hour mean (Figure 5.9c) due to the higher roughness length in the urban areas. Due to the more unstable stratification in scenario s3 than in REF_WITH_SNOW, the wind speed is higher (Figure 5.9d). During nighttime, the wind speed in the urban areas increases so that it is in the same as in the rural areas (Table 5.8) because of the less stable stratification of the atmosphere for urban areas in scenario s3. The effects of the changed roughness length in scenario s3 are less pronounced and therefore not visible in the resulting climate average wind field. The wind direction is not influenced by the changes in the wind speed and the atmospheric stratification (not shown).

The relative humidity and the cloud development influence the development of a UHI. The relative humidity in REF_WITH_SNOW is highest close to the water bodies and in the valley of the river Elbe (Figure 5.9a). It is higher during nighttime than during daytime (Table 5.8). The spatial pattern during day- and nighttime is the same as for the 24-hour mean (Figure 5.9a). In scenario s3 the specific humidity is higher due to the higher latent heat fluxes from the larger evaporative areas. The higher temperatures for the urban areas in scenario s3, however, lead to lower relative humidity (less than 1 %) in the urban areas (Figure 5.9b) despite the higher specific humidity. The effect is stronger during nighttime (still less than 1 %) but with the same spatial pattern for day- and nighttime and for the 24-hour mean.

The integral cloud water content (ICWC) is used as a proxy for cloud development, since a cloud cover is not available in the model results using a 250 m resolution in the focus domain. All clouds are resolved. The changes in the ICWC are small and not visible in Table 5.8. No systematic changes in time or space are found. Therefore, no systematic changes in the cloud development is induced by scenario s3 in the urban or rural areas.

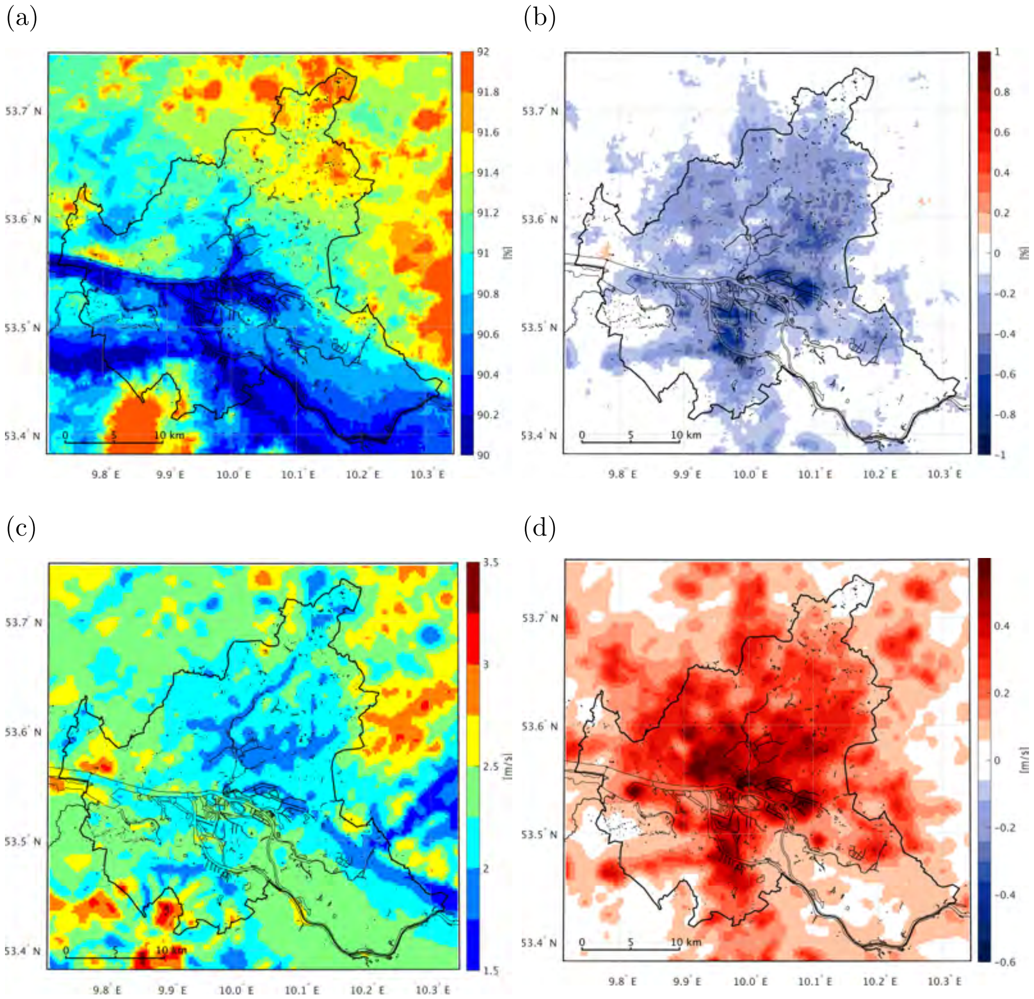

Figure 5.9: Mean spatial pattern at 10 m above ground as winter climate mean for (a),(b) relative humidity and (c),(d) wind speed. (a), (c) correspond to REF_WITH_SNOW, (b), (d) show differences of scenario s3 minus REF_WITH_SNOW. The boundaries of the state of Hamburg are marked with a thick black line, water bodies are outlined with thin black lines.

5.3.4 Comparison of results for urban development scenarios for winter and summer

The comparison of results of scenario s3 for summer and winter months shows that the most important influences on the seasonal climate due to climate adaptation measures differ from season to season for the MRH. During summer months with high incoming solar radiation, the increase of reflectivity in scenario s3 compared to the current surface covers induced by the increased albedo is most important to reduce the current UHI in the urban areas. During winter months, the incoming solar radiation is lower, so the exchange of energy between the surface and the atmosphere is more important and this introduces increasing temperatures. Thus, the effect of scenario s3 on temperature is opposite during summer and winter months. The effect of scenario s3 on the temperature at 10 m above ground is larger during winter months than during summer months.

The increased evaporation leads to higher latent heat fluxes and specific humidity for summer and winter months but because of the large effect on the temperature during winter months, the relative humidity increases only during summer months, while a decrease smaller than 1 % is found during winter months. The cooling introduced by the higher evaporation in scenario s3 is smaller than the cooling induced by the increased albedo during summer months and the warming induced by the increased exchange of energy between soil and atmosphere during winter months.

The changes in temperature during summer and winter months have opposite effects on the UCI and UHI. While during summer months, the target to reduce the UHI to off-set climate change is reached under scenario s3, during winter months, an increase of the UHI is found, although this may reduce the thermal cold stress during this season. Therfore, the increase of UHI is a positive change for a city with considerable lower winter than summer temperatures.

The wind speed is slightly decreased for the urban areas in scenario s3 compared to the reference surface cover during summer months and is clearly increased for the urban areas during winter months. The last is a result of the changed stratification of the atmosphere. During summer months, the decreased wind speed has nearly no impact on thermal heat stress (Chapter 4.4.3.1 and Chapter 4.4.3.2). During winter months, the increased wind speed may increase the thermal cold stress but this effect is counteracted by the increased temperature during this season. Nevertheless, the increased wind speed during winter month should be considered for urban planning to ensure wind comfort during winter months as well as during summer months.

5.4 Conclusions

The impact of scenario s3, which includes socio-economic changes on the winter climate of Hamburg is investigated with the numerical model METRAS using SDD with a non-uniform grid. The model is extended with a snow scheme to simulate winter months with occasional snow cover for the MRH. Three simulations of the 129 days shown as necessary to represent the statistics of the winter climate of the MRH were produced, one as a reference case without using the snow scheme (REF_NO_SNOW), one as a reference case using the snow scheme (REF_WITH_SNOW) and one as scenario s3 using the snow scheme.

Both reference cases are evaluated against observational data of 12 weather stations located in the model domain. The evaluation of REF_NO_SNOW shows good performances for METRAS, with values inside the range of the better 50 percent of typical model performances determined by Schlünzen et al. (2016). This implies that the method selected for this study of SDD connected with a non-uniform grid is suitable both to reduce the computing time with still good model results. This study also shows that the preparation of the orography data by merging data of a coarse and the final grid performs well for the 129 days simulated in capturing the winter climate of the MRH using bilinear interpolation and linearly decreasing weights for the coarse grid data in the non-uniform part of the model domain.

The evaluation of REF_WITH_SNOW shows lower performances than for REF_NO_SNOW but the results are still inside the better 50 percent of typical model performances. A cold bias is found for the air temperature which results in a larger bias for relative humidity and wind speed in REF_WITH_SNOW than in REF_NO_SNOW. The surface temperature is not evaluated because of a lack of observational data. Only in situations with snow cover the snow cover changes the temperature in REF_WITH_SNOW compared to REF_NO_SNOW. The larger bias in temperature therefore results from these situations. The decreased air temperatures in REF_WITH_SNOW result from the isolating of the snow cover and the reduced exchange of the atmosphere with the warmer soil. Therefore, the surface temperature is probably underestimated, too. As found by Jin et al. (1999), one reason for underestimating the surface temperature in a model with one snow layer using the force-restore method is the neglect of liquid water in the snow layer. Similar results are found by Boone and Etchevers (2001) and You et al. (2014). Attempts to include the effects of liquid water in the snow layer have been made by calculating the internal heat of a snow pack (Boone and Etchevers, 2001; You et al., 2014). An extension of the snow scheme in METRAS with a formulation of the internal heat of a snow pack may improve the model results. A validation of the snow scheme against other numerical models and against observational data from weather stations and satellites should then be performed.

Even if the evaluation of REF_WITH_SNOW shows slightly lower performances than the evaluation of REF_NO_SNOW, the introduction of the snow scheme is important because the impacts of the climate adaptation measures on the climate depend on the presence or absence of the isolating capacity of a snow layer. The largest increases of temperature were induced by the increased exchange of energy between the warm soil and the colder atmosphere due to earlier snow melt in areas with more unsealed surfaces. This implies for Hamburg, that the ratio of days with and without snow cover and the snow mass itself determine the strength of the impact of the climate adaptation measures on the winter climate as well as the mean temperatures of soil and atmosphere. The results of this study are therefore transferable to regions were the mean exchange of heat from the soil to the atmosphere is larger than the impact of the short-wave radiation balance and the cooling by evaporation. Shallow snow packs in combination with relatively warm soil and decreased amount of sealed areas result in an increased snow melt. This leads to higher temperatures. Areas with a thick snow layer may not be impacted by the increased exchange of energy between soil and atmosphere due to fewer sealed surfaces because a thick snow layer prevents the heat exchange between soil and atmosphere and does thus not increase the snow melt.

Due to the dependency of the impact of climate adaptation measures on the regional climate and especially on the amount of snow cover, the changes in globally induced regional climate may impact temperature changes for Hamburg. A decrease of the snow cover may reduce the impact of the climate adaptation measures and thus keep the temperatures at the level simulated for the reference surface cover. A higher number of days with a shallow snow cover may further increase the temperature in scenario s3 compared to REF_WITH_SNOW.

Results for scenario s3 show that implemented climate adaptation measures may provide benefit against increasing temperatures due to regional climate change during summer months and in addition may increase the thermal comfort due to increased temperatures in the urban areas during winter months.

6 Conclusions

In this thesis, the impacts of climate mitigation and adaptation measures on the climate of the metropolitan region of Hamburg (MRH) are quantified by using statistical-dynamical downscaling (SDD). The numerical model METRAS is used for analysing how urban development should be managed to increase human thermal comfort in possible future configurations of the city of Hamburg.

The first research question addressed in this thesis is how to represent the climate statistics of the climate of the MRH adequately for use in the statistical methods of the SDD, since simulations involving full datasets are computationally too expensive. The skill score following Perkins et al. (2007) (SSP) is used to calculate the number of days which sufficiently represent the climate needed to assess the impact of hypothetical large wind farms in the German Bight on the urban climate of Hamburg. The SSP does not consider non-linear relationships between meteorological variables so that the statistical representation of a probability density function (PDF) of a first variable in dependency of the PDF of a second variable is not kept necessarily. The relationships between different variables are important for assessing the impact of climate adaptation measures. Therefore, an additional statistical method, the bivariate skill score (BSS), is calculated to take this into account. The BSS method leads to a higher number of days necessary for the simulations to sufficiently represent the climate. For example, the SSP method achieves a good result by using ten days for representing the summer months while 55 days are needed to achieve a good result with the BSS method. The statistics of the summer and winter climates of Hamburg simulated with the BSS method show that the climate average is well represented. However, the number of days used in the simulations has to be determined with care and with respect to the particular application.

To further reduce the computational costs of simulating climate with mesoscale models, the use of a non-uniform grid is tested. This avoids several refinement steps from global to mesoscale horizontal grid resolution. To achieve this, a smoothing method for the boundaries and different interpolation methods between a uniform and the non-uniform grid as well as different weighting methods were tested. It turned out that the asymmetric orography is reduced best by using a bilinear interpolation with linear weights from a uniform grid to the non-uniform grid. The simulations using the non-uniform grid show a good performance that is within the better 50 percent of typical model performances following Schlünzen et al. (2016).

The second research question is what impact climate mitigation measures like wind farms have on the urban summer climate of Hamburg. The very large wind farms assumed to exist in the German Bight in the future result in slightly decreased summer climate average temperatures in Hamburg. This results from the reduced exchange of energy between the atmosphere and the sea surface of the German Bight, which is a source of heat for nearly the whole year. Therefore, the wind farms are not only a climate mitigation measure but also act as a climate adaptation measure in the summer. Nevertheless, these wind farms influence the development of the urban heat island (UHI) of Hamburg because of systematic changes in the cloud cover. The UHI increases even if the temperatures decrease. The urban effects of Hamburg therefore become more important, as do climate adaptation measures to reduce the UHI.

The third and fourth research questions concern the impact of climate adaptation measures on the urban summer and winter climates of Hamburg, respectively. To quantify the impact of the adaptation measures on the urban summer climate of Hamburg, three socio-economic scenarios are investigated. Two scenarios, scenario s1 and scenario s2, which project decreasing and stagnating numbers of inhabitants for Hamburg without or with only sporadic implementation of climate adaptation measures, have little impact on the urban summer climate of Hamburg. The third scenario, scenario s3, which assumes an increasing number of inhabitants and widespread implementation of climate adaptation measures, leads to a reduced UHI in Hamburg in the range of -0.1 K with small improvements in human thermal comfort of -0.1 K during summer months. During winter months, scenario s3 introduces increasing temperatures in the rage of 0.3 K during night for the MRH. These are larger values than the corresponding cooling during summer months. The strongest increases in temperatures are found for winter situations with snow cover where the snow cover is reduced by the impacts of scenario s3. Scenario s3 also shows slight increases in the UHI of Hamburg during the winter months. Therefore, under the conditions of scenario s3, there are improvements in human thermal comfort for the future summer climate of Hamburg. For the urban winter climate of Hamburg, however, the climate adaptation measures in the scenario introduce increasing temperatures and increasing wind speeds, which may affect human comfort both positively and negatively.

The results of the current investigations on the effects of climate mitigation and adaptation measures on the urban climate of Hamburg show that their impact depends on the processes that dominate the interaction of the particular climate mitigation or adaptation measure and the atmospheric values. The dominant effect of wind farms is a reduction of wind speed and thereby the process of heat and moisture exchange between the surface and the atmosphere is reduced within the wind farms and in their wake. The modified exchange of heat between the surface and the atmosphere is also the most important process for the climate adaptation measures of scenario s3 that modify the urban winter climate. It is most relevant because of the low incoming short wave radiation and low evaporation during winter months. During summer months, the incoming short wave radiation is high and the process of the modified net short wave radiation balance due to increased albedo becomes more important than the impact of the increased exchange of heat between the surface and the atmosphere. The identification of the dominant processes that are affected by the climate mitigation and adaptation measures investigated supports the possibility that the results of this study can be transferred from Hamburg to other regions with moist weather conditions during summer and winter and relatively warm soil during winter. Nevertheless, the quantitative impacts of the investigated measures need to be studied for each city because urban surface covers and the regional climate might lead to other non-linear effects from the interactions of all processes involved.

A possible hypothesis to explain the impact of large wind farms on the urban winter climate of Hamburg suggested by the results of this thesis is that the cooling effect of wind farms might be larger because of the larger temperature gradient between the water surface and the atmosphere. To assess this, the regional winter climate should be simulated with respect to non-linear effects when using the SDD technique. Additionally, the impact of the reduced exchange between the surface and the atmosphere on the sea surface temperature should be considered.

The interactions between the large wind farms in the German Bight and the socio-economic changes assumed in scenario s3 and their joint impact on the urban climate of Hamburg are still unknown. During summer months, scenario s3 reduces the UHI of Hamburg but increases it during winter months. In combination with the cooling from the wind farms, the temperature in the urban summer climate might be reduced more than the summed single effects of the climate mitigation and adaptation measures, due to the increased importance of urban effects related to the wind farms. For the urban winter climate of Hamburg, the effects of the large wind farms in the German Bight and scenario s3 are probably opposite. Therefore, the net effect is not determinable from the results of this thesis. In further calculations of the impact of climate adaptation measures, the future climate of Hamburg should be considered because of the large impact of changed snow cover. Furthermore, the calculation of thermal indices to assess the impact of the climate mitigation and adaptation measures on human thermal comfort may be necessary because an unfavourable combination of small changes in the meteorological variables may worsen human thermal comfort, even if there is a beneficial change to the temperature.

Acknowledgements

I thank my first supervisor K. Heinke Schlünzen for her excellent guidance during my PhD. Thanks for discussing the results of my work and pointing out new ideas. Thank you for supporting my PhD in a child compatible way.

I would like to thank Bernd Leitl for agreeing to be my second supervisor.

Peter Hoffmann and Robert Schoetter are acknowledged for their research in the project KLIMZUG-NORD. Their work was an essential base for my PhD. Additionally, I would like to thank them for being excellent colleagues.

I would like to thank Andrea Gierisch for her mental support and helpfulness. Many thanks for discussing the advantages and disadvantages of several snow schemes and proof-reading of parts of my thesis. Thank you for the great time during our PhD.

I would like to thank Jana Fischereit for a nice time and numerous inspiring and motivating discussions.

I would like to thank Volker Reinhardt for his assistance during programming and computing issues.

I would like to thank Jean Johnson, Jack Katzfay and Birgitt and Harald Linde for proof-reading.

David D. Flagg, David Grawe and Peter Kirschner are acknowledged for preparing the land-use and surface cover data and implementing more flexibility about the number of surface cover classes in METRAS.

Many thanks to all members of the MEMI working group for discussing a wide range of topics and having a great time.

Last but not least, many thanks to my parents, my husband and my daughter for their mental support.

Hermann-J. Lenhart is acknowledged for discussing the wind farm scenario and submitting the data. Wind turbine and wind farm data have been provided by the "Zukunft Küste - Coastal Futures" project founded through the German Federal Ministry of Education and Research under grant 03F0476 A-C.

The development of the urban development scenarios was done within the frame of the project KLIMZUG-NORD. I want to thank all colleagues who have been involved in the preconditioning of data and scenario development, especially Johanna Fink, Nicolas Klostermann, Elke Kruse, Lisa Kunert, Michael Martens, Elena Rottgardt, Katharina Schmidt, Julia Stockinger, Esther Verjans and Juliane Ziegler.

Sarah Wiesner is acknowledged for providing data about soil temperature and soil moisture.

This work is supported by the project KLIMZUG-NORD, funded under grant 01LR0805D by the German Federal Ministry of Education and Research and by the Cluster of Excellence 'CliSAP' (EXC177), University of Hamburg, funded through the German Science Foundation (DFG).

Surface cover data and information on building characteristics have been sourced from the "Freie und Hansestadt Hamburg, Landesbetrieb Geoinformation und Vermessung (Nr.102156)", the "Landesamt für Geoinformation und Landentwicklung Niedersachsen (LGN)", the "Landesvermessungsamt Schleswig-Holstein", the "Amt für Geoinformation" and the "Vermessungs- und Katasterwesen Mecklenburg-Vorpommern". Fees for these datasets were covered by the University of Hamburg as well as by the excellence cluster CLISAP.

Meteorological data for model forcing have been provided by European Centre for Medium-Range Weather Forecasts (ECMWF).

Meteorological observation data were provided by the German Meteorological Service (Deutscher Wetterdienst) (DWD).

The water surface temperatures have been retrieved from NOAA.

A Initialisation of snow data in METRAS

The initialisation data for the snow-related variables are provided to METRAS in the control file m3tras_TAPE70. The values are prepared from the ECMWF analysis data with a preprocessor and are horizontally interpolated to the METRAS grid (Section 2.2.1).

The first line of the control file indicates the number of the horizontal grid cells (nx1 and nx2 for x- and y-directions). The second line indicates if data for snow water equivalent (swecont) are provided or not. In the third line, the number of surface cover classes used in the m3tras_TAPE70 is provided. The number of SCCs may be equal to one or equal to the number of SCCs used in the METRAS model domain. If the number of SCCs is equal to one, the values for snow water equivalent found for a grid cell are applied to all SCCs. Otherwise, the data are read and separately applied for each SCC for each grid cell. The fourth and the following lines contain the indices for the horizontal grid cell, where the first column denotes the x-direction and the second column the y-direction. The third and any following columns give the values for the snow water equivalent for a whole grid cell or for each SCC. For the snow albedo (albedosnow) and the density of snow (rhosnow), the data are provided in the same control file, starting with a line analogous to the second line.

```
'NUMBER OF GRID POINTS: NX2 =' 20 ', NX1 =' 24
'swecont = ' .TRUE.
'NUMBER OF SURFACE COVER CLASSES = '   1
   0   0      0.00
   1   0      0.00
   2   0      0.00
   3   0      0.00
   4   0      0.01
   5   0      0.03

...

  23  21      0.00
  24  21      0.00
  25  21      0.00
'albedosnow = ' .TRUE.
'NUMBER OF SURFACE COVER CLASSES = '   1
   0   0   0.85
   1   0   0.85
   2   0   0.85
   3   0   0.85
   4   0   0.85
   5   0   0.85

...

  23  21   0.81
  24  21   0.81
  25  21   0.82
'rhosnow    = ' .TRUE.
'NUMBER OF SURFACE COVER CLASSES = '   1
   0   0 103.93
   1   0 101.98
   2   0 101.11
   3   0 103.22
   4   0 104.01
   5   0 104.03

...
```

B List of weather stations

Table B.1: WMO numbers of the weather stations used for assessing the needed number of to be simulated days. The 12 weather stations written in bold letters are located inside the model domain used for evaluating the winter climate simulations.

WMO number	weather station
06280	Groningen
06290	Twenthe
10015	Helgoland
10020	List
10035	**Schleswig**
10091	Arkona
10129	**Bremerhaven**
10130	**Elpersbüttel**
10131	**Cuxhaven**
10147	**Fuhlsbüttel**
10161	**Boltenhagen**
10162	**Schwerin**
10170	Rostock/Warnemünde
10184	Greifswald
10193	Ueckermünde
10224	**Bremen**
10249	**Lauenburg**
10261	**Seehausen**
10264	Marnik
10338	**Hannover**
10348	Braunschweig
10359	**Gardelegen**
10361	Magdeburg
10379	Potsdam
10384	Tempelhof
10385	Schönefeld
10393	Lindenberg

C Overview on results for single meteorological parameter

Figure C.1 to Figure C.8 show the SSPs as functions of the number of randomly chosen days for the individual seasons. The method to achieve these figures is discussed in Section 2.3.1.

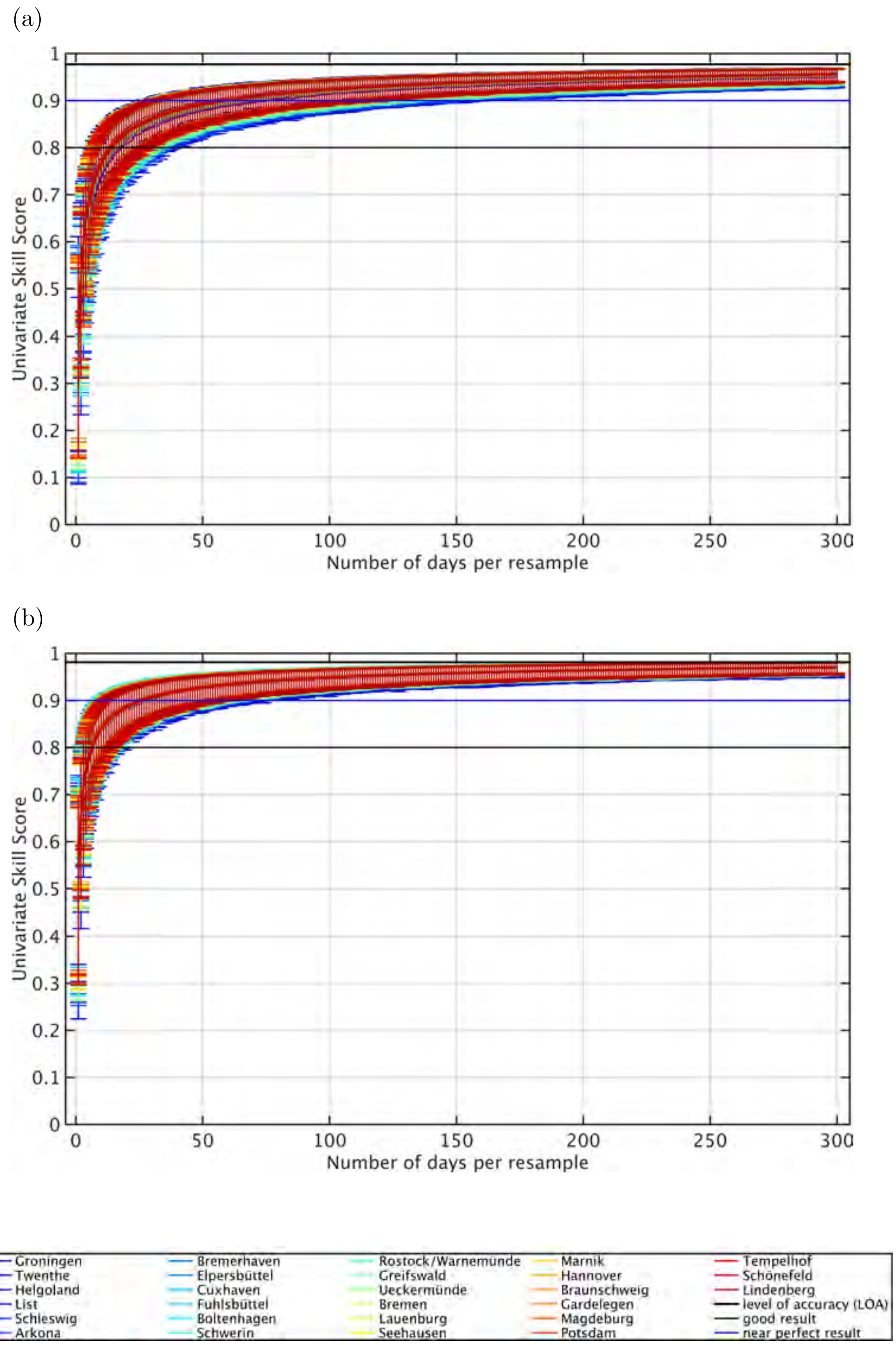

Figure C.1: Mean of the skill score following Perkins et al. (2007) (SSP) for each weather station for MAM for (a) TC and (b) RH with its 5th and 95th percentile shown by horizontal bars as a function of the number of randomly chosen days per resample. The thick black line marks the level of accuracy (LOA); the thin black (blue) line marks the good (near-perfect) agreement.

(a)

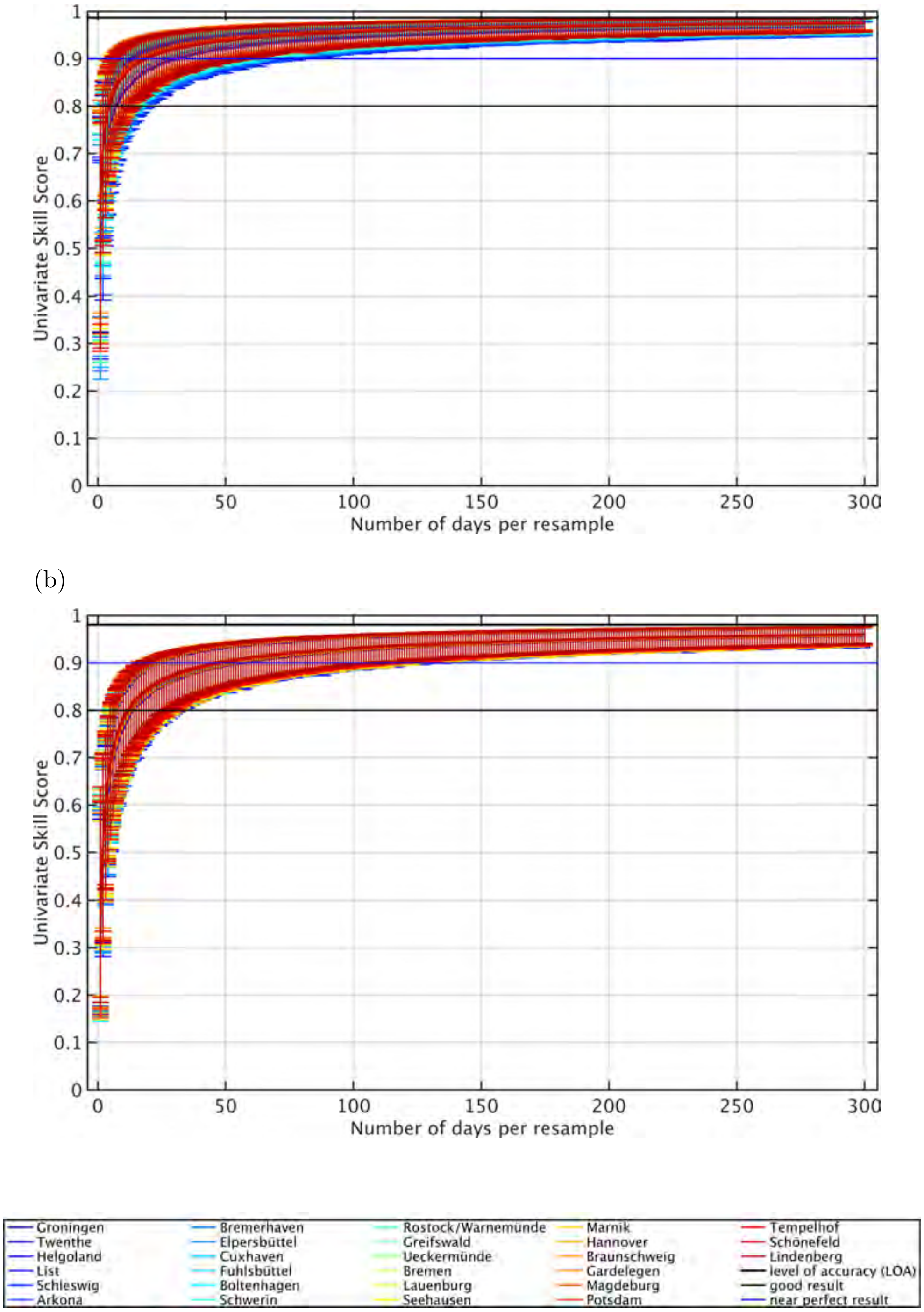

Figure C.2: Same as Figure C.1 but for (a) FF and (b) DD.

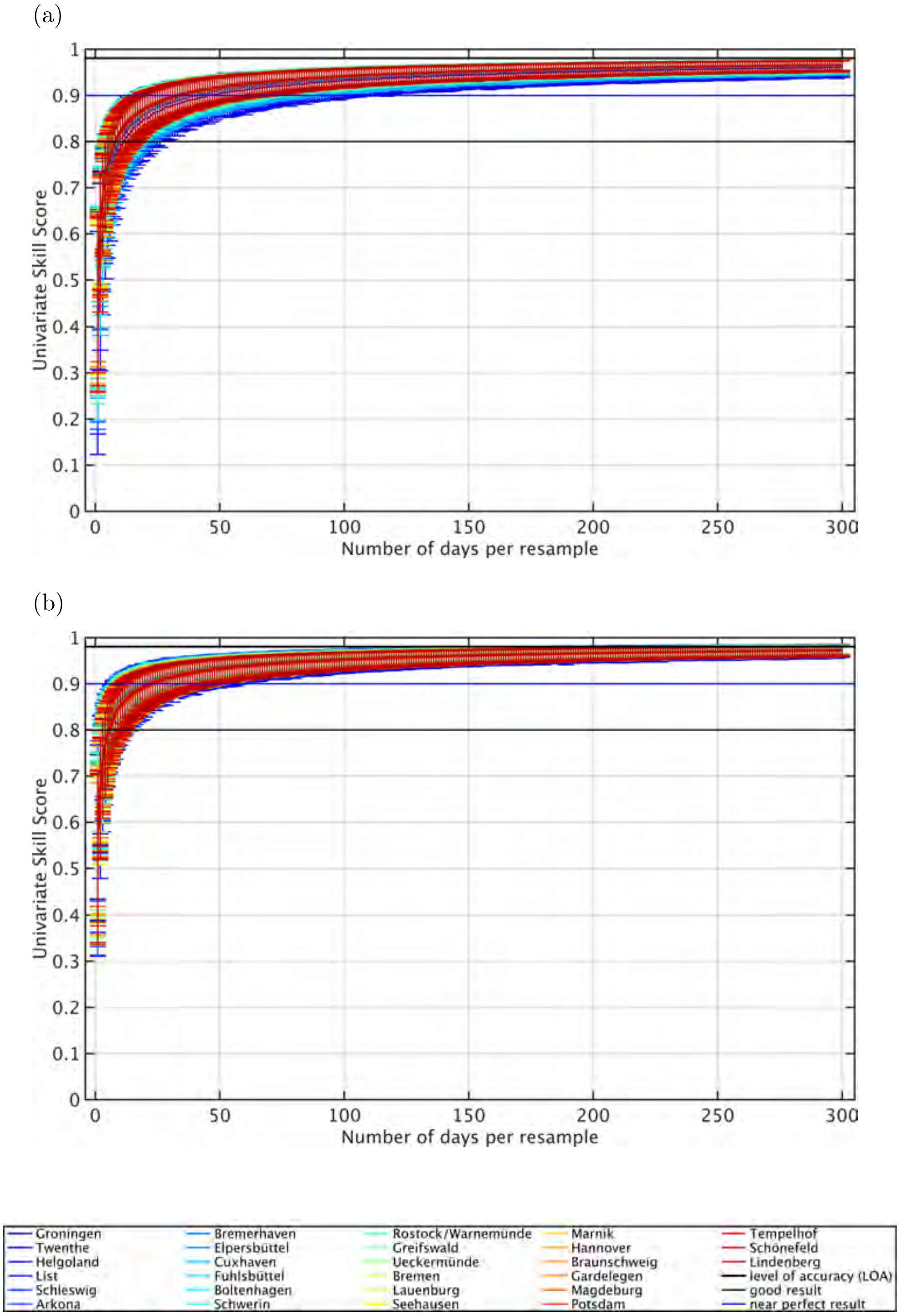

Figure C.3: Same as Figure C.1 but for JJA for (a) TC and (b) RH.

(a)

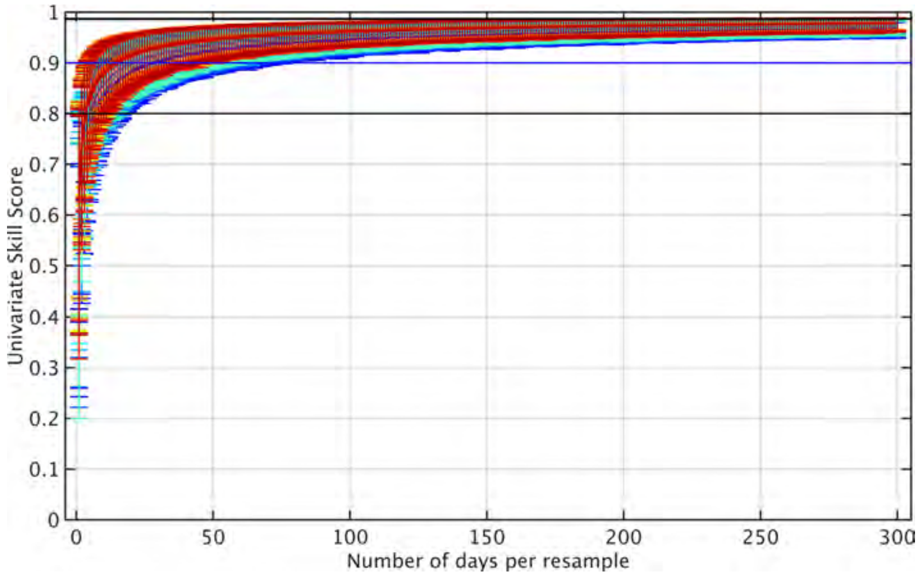

(b)

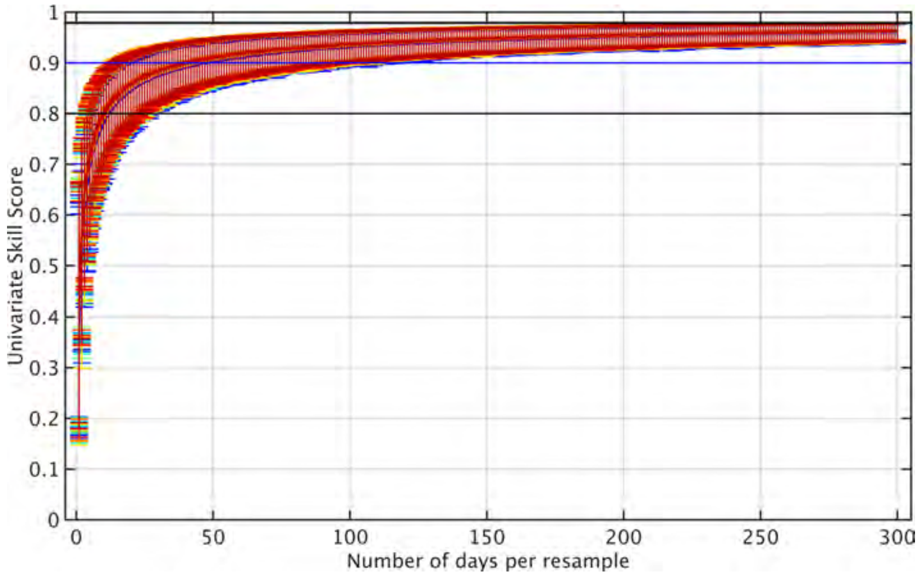

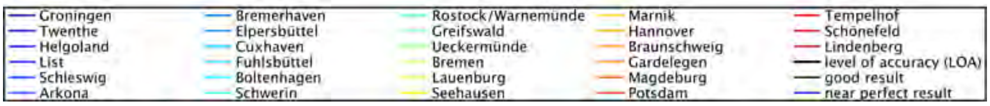

Figure C.4: Same as Figure C.1 but for JJA for (a) FF and (b) DD.

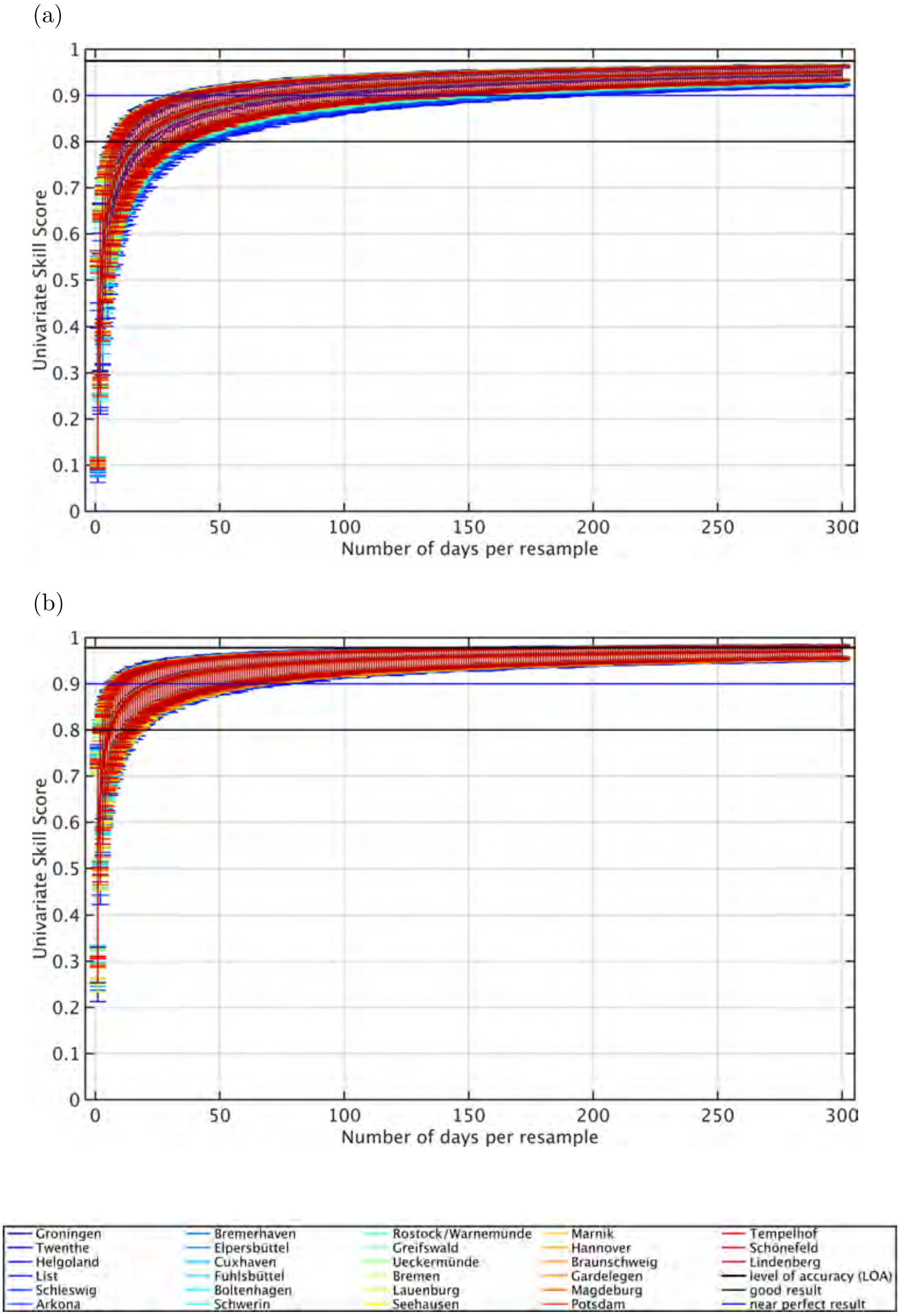

Figure C.5: Same as Figure C.1 but for SON for (a) TC and (b) RH.

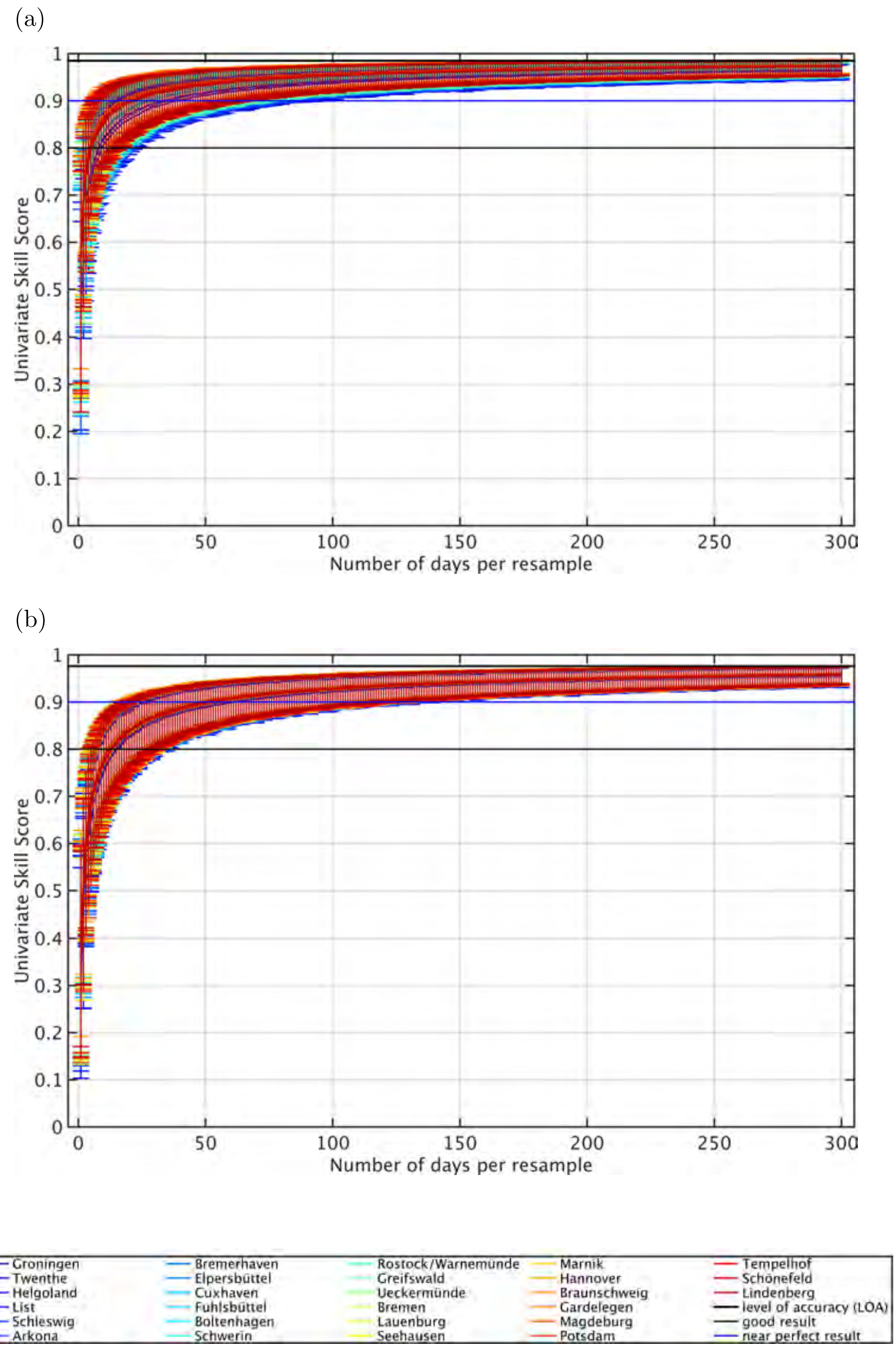

Figure C.6: Same as Figure C.1 but for SON for (a) FF and (b) DD.

(a)

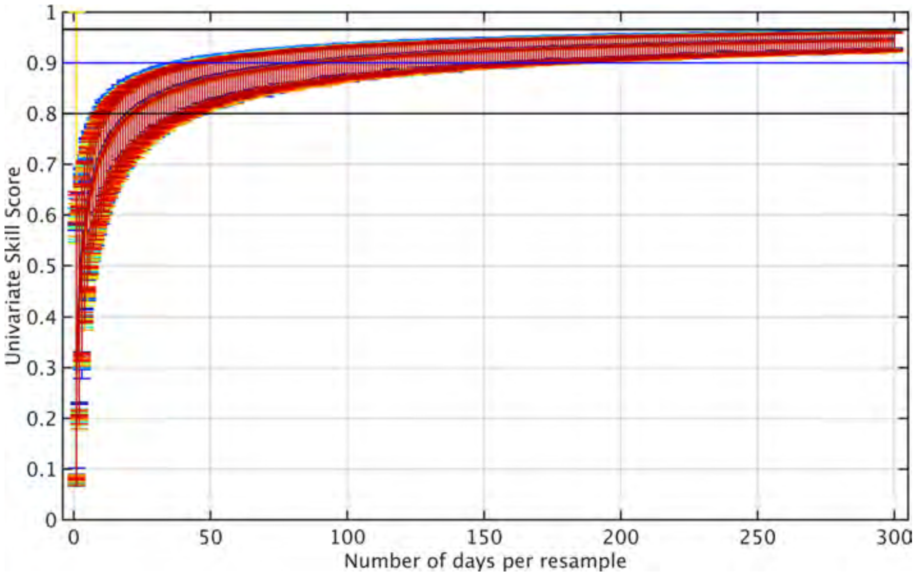

(b)

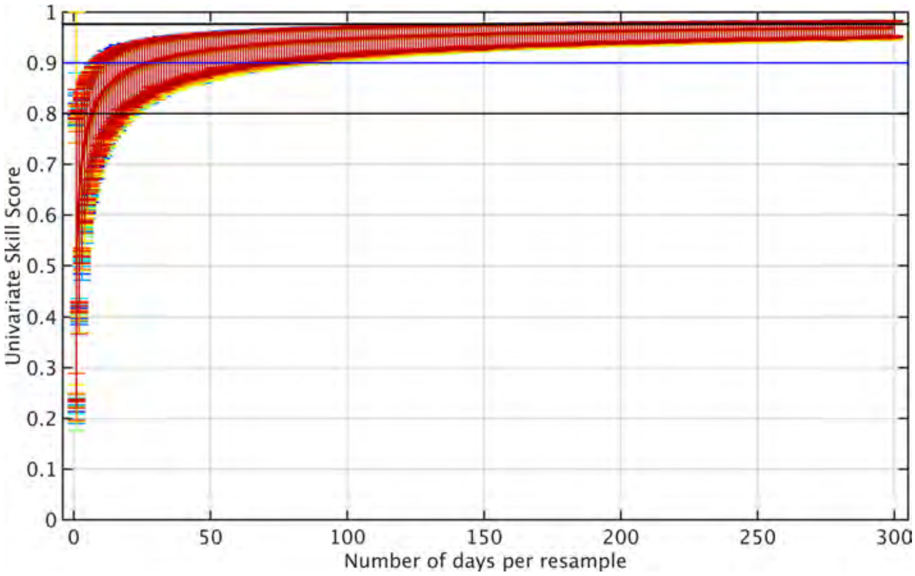

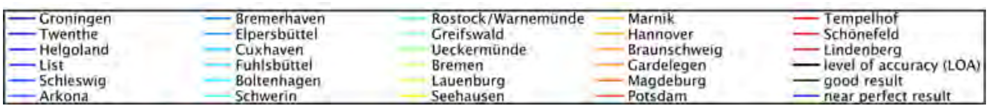

Figure C.7: Same as Figure C.1 but for DJF for (a) TC and (b) RH.

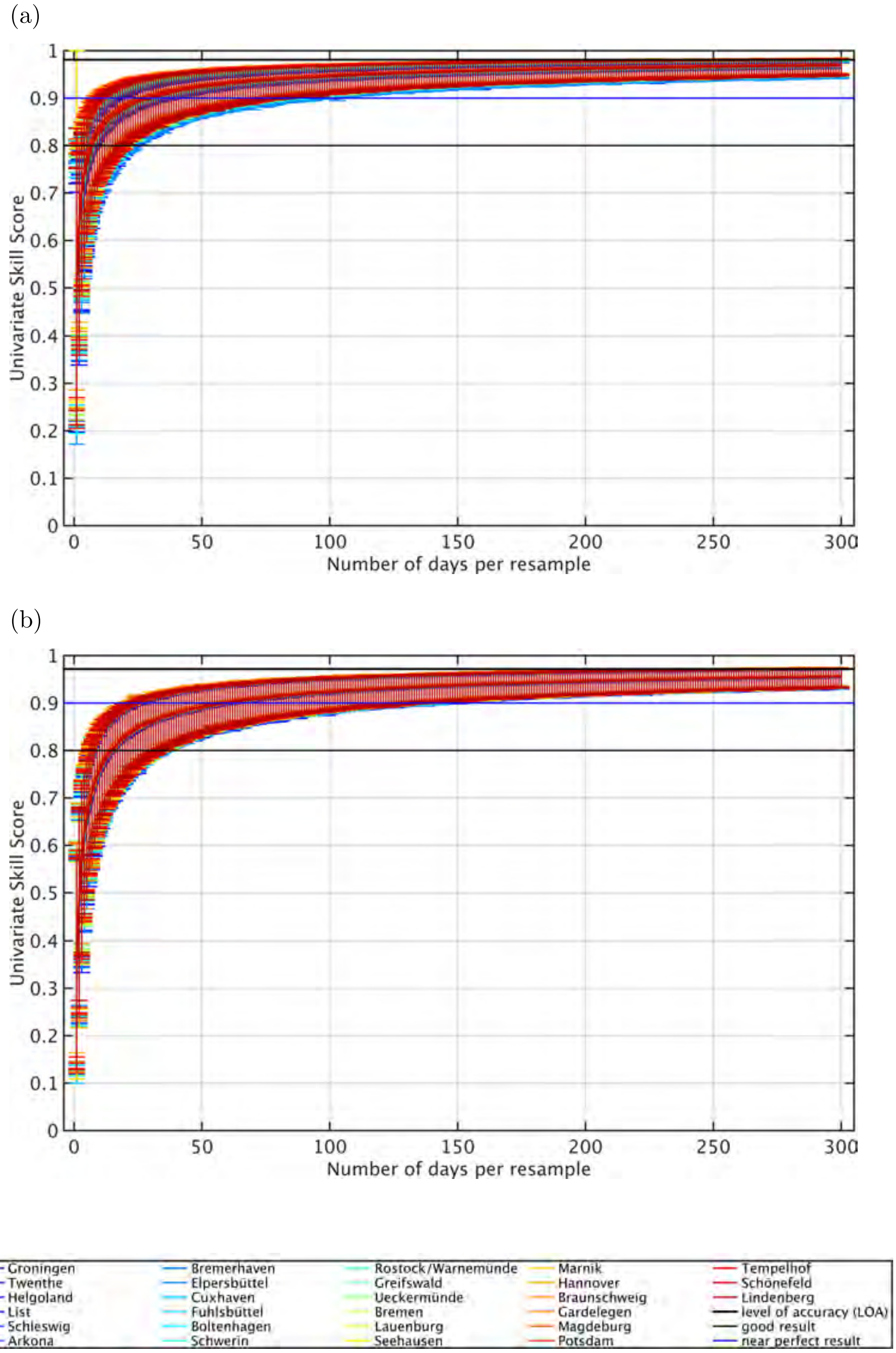

Figure C.8: Same as Figure C.1 but for DJF for (a) FF and (b) DD.

D Overview on results for combined meteorological parameter

Figure D.1 to Figure D.8 show the BSSs as functions of the number of randomly chosen days for the individual seasons. The method to achieve these figures is discussed in Section 2.3.2.

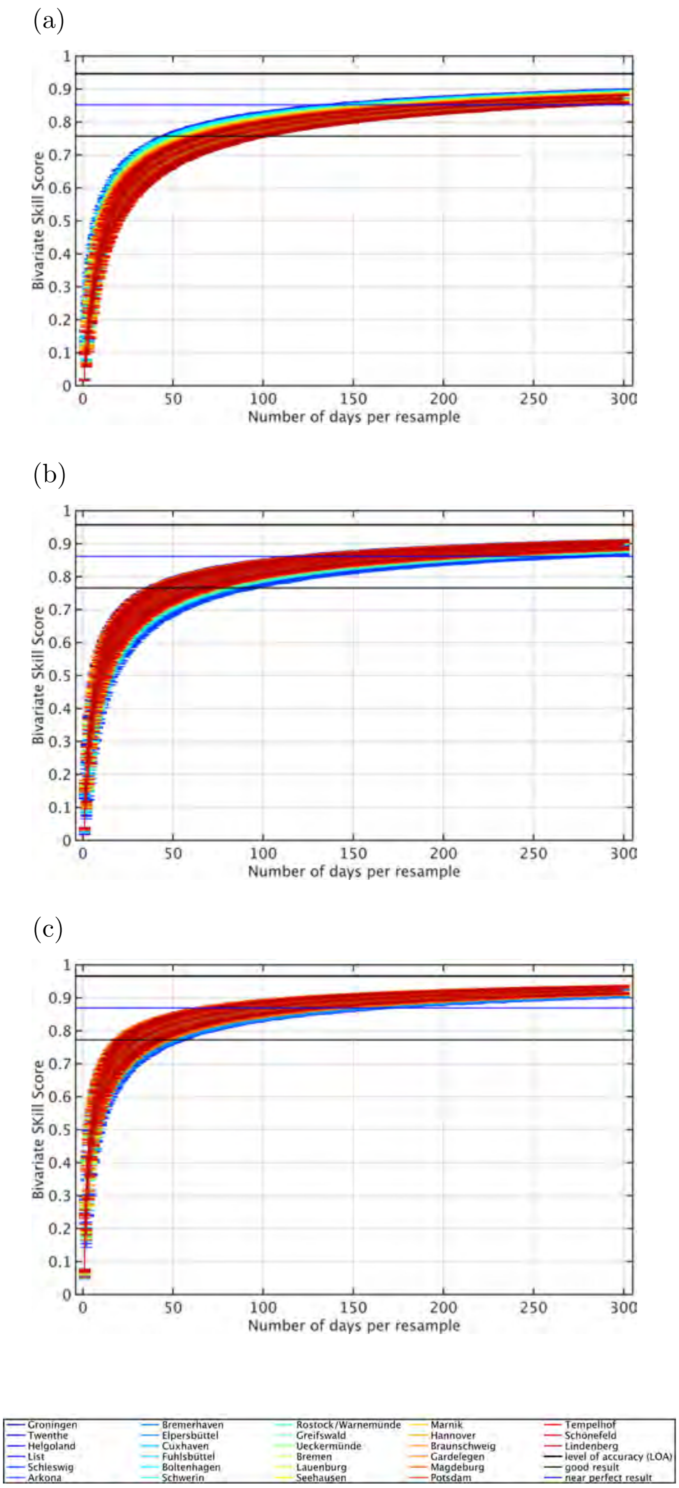

Figure D.1: Mean of the bivariate skill score (BSS) for MAM for (a) TC/RH, (b) TC/FF and (c) RH/FF for each weather station with its 5th and 95th percentile shown by horizontal bars as a function of the number of randomly chosen days per resample.

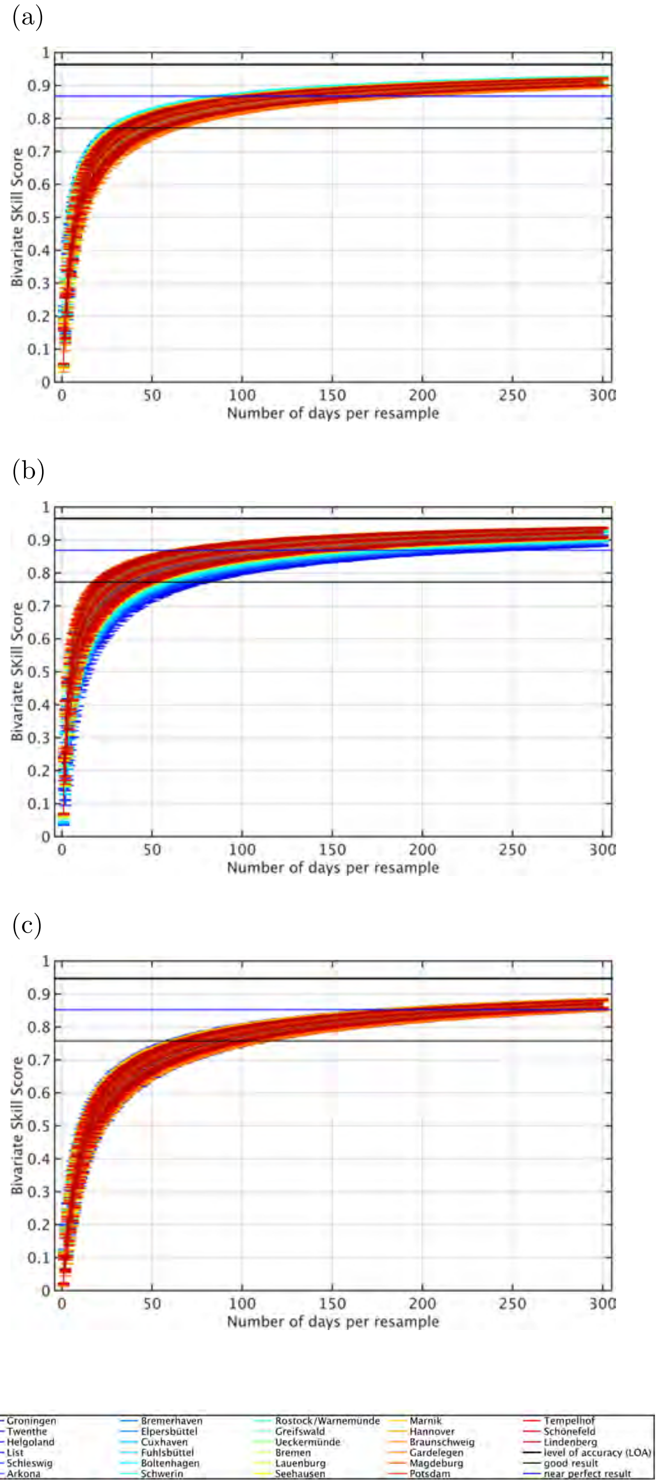

Figure D.2: Same as Figure D.1 but for (a) DD/RH, (b) DD/FF and (c) DD/TC.

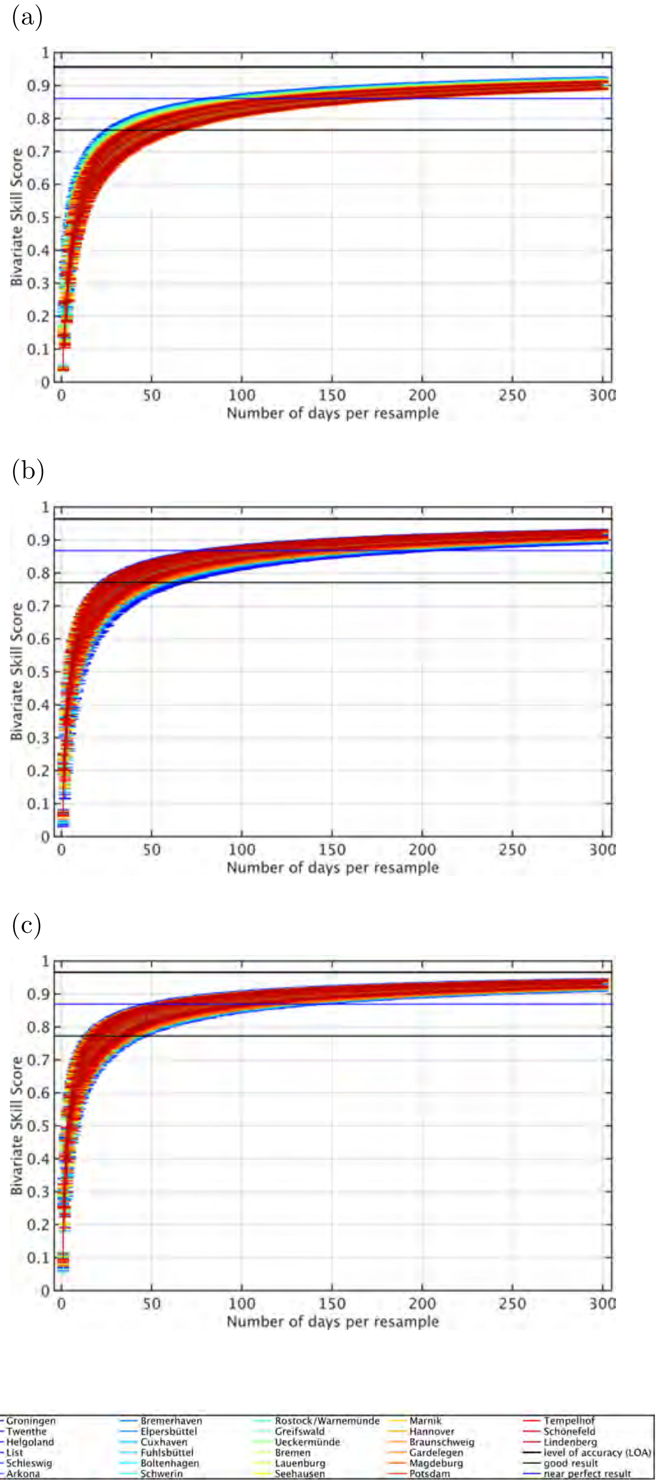

Figure D.3: Same as Figure D.1 but for JJA for (a) TC/RH, (b) TC/FF and (c) RH/FF.

(a)

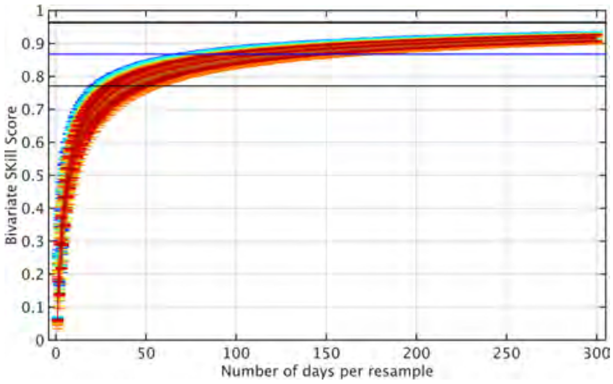

(b)

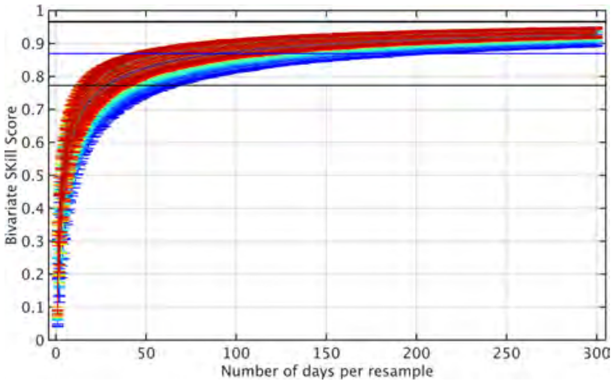

(c)

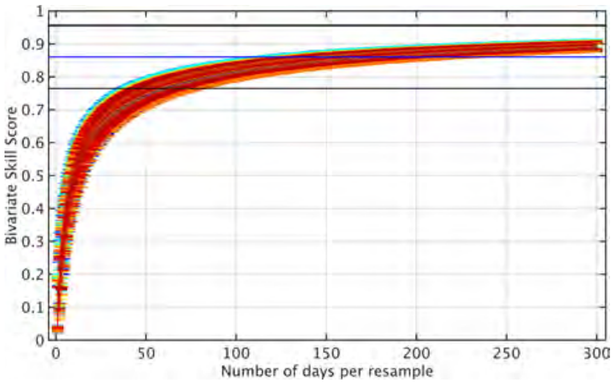

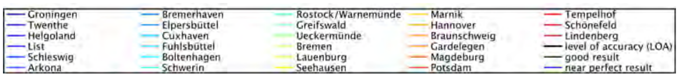

Figure D.4: Same as Figure D.1 but for JJA for (a) DD/RH, (b) DD/FF and (c) DD/TC.

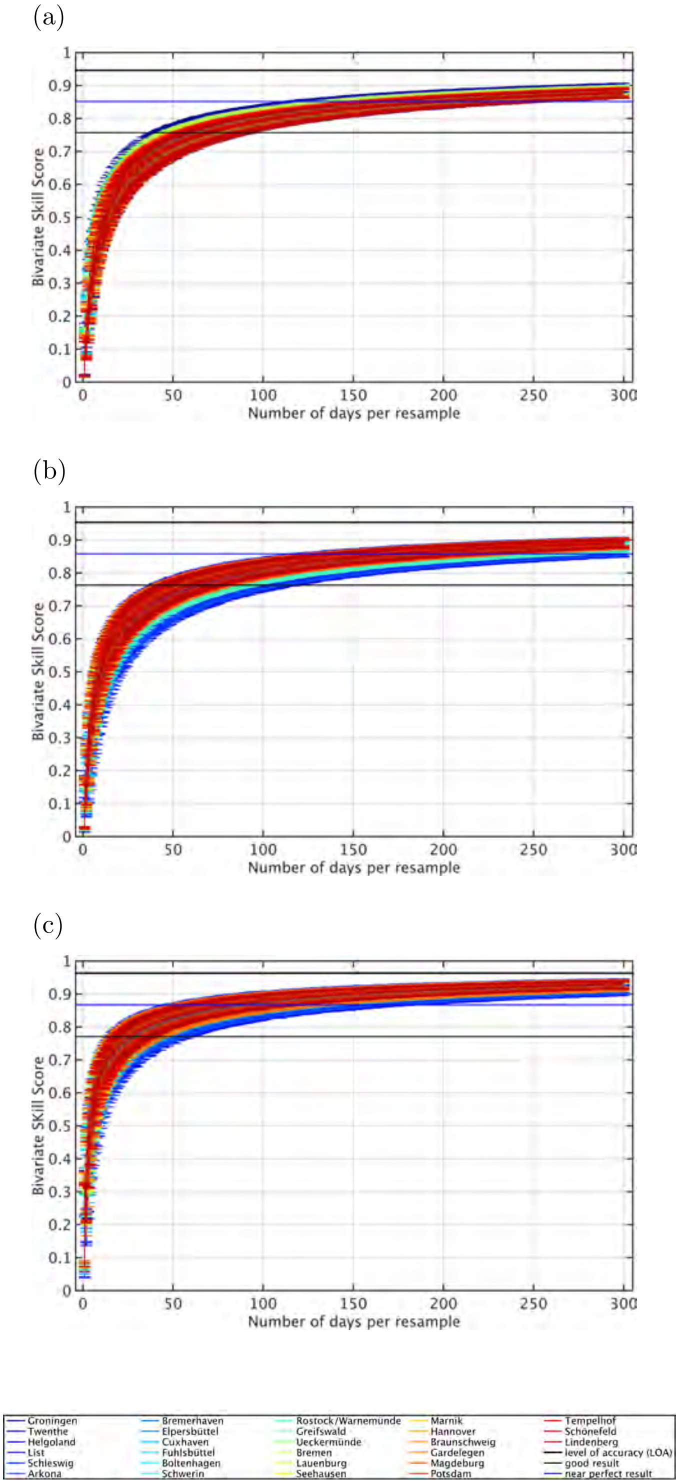

Figure D.5: Same as Figure D.1 but for SON for (a) TC/RH, (b) TC/FF and (c) RH/FF.

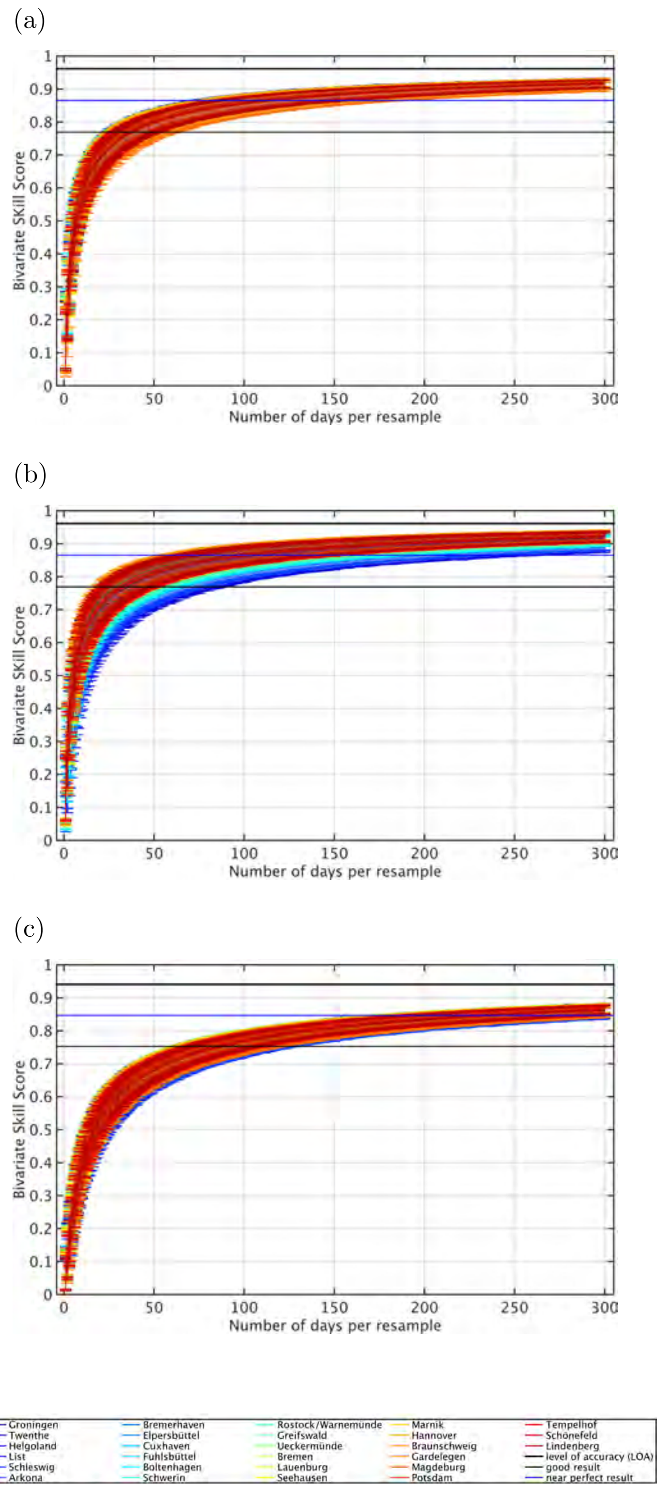

Figure D.6: Same as Figure D.1 but for SON for (a) DD/RH, (b) DD/FF and (c) DD/TC.

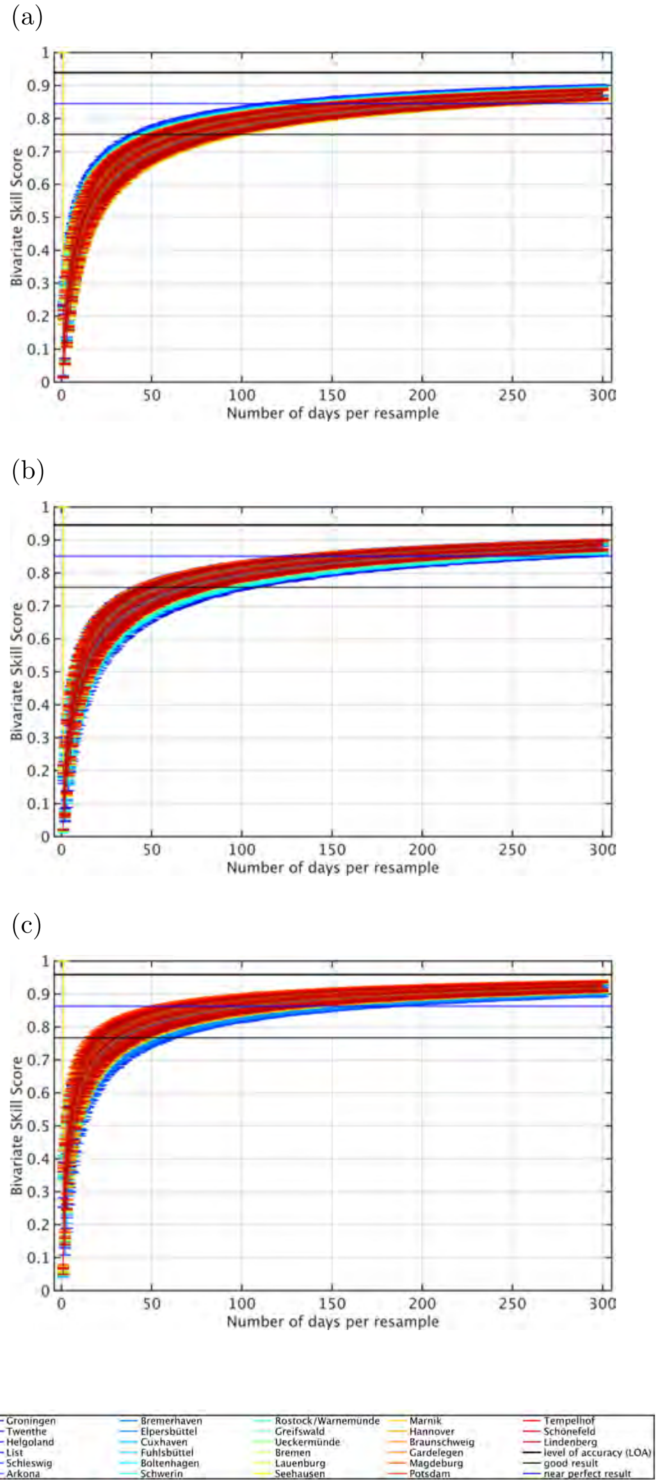

Figure D.7: Same as Figure D.1 but for DJF for (a) TC/RH, (b) TC/FF and (c) RH/FF.

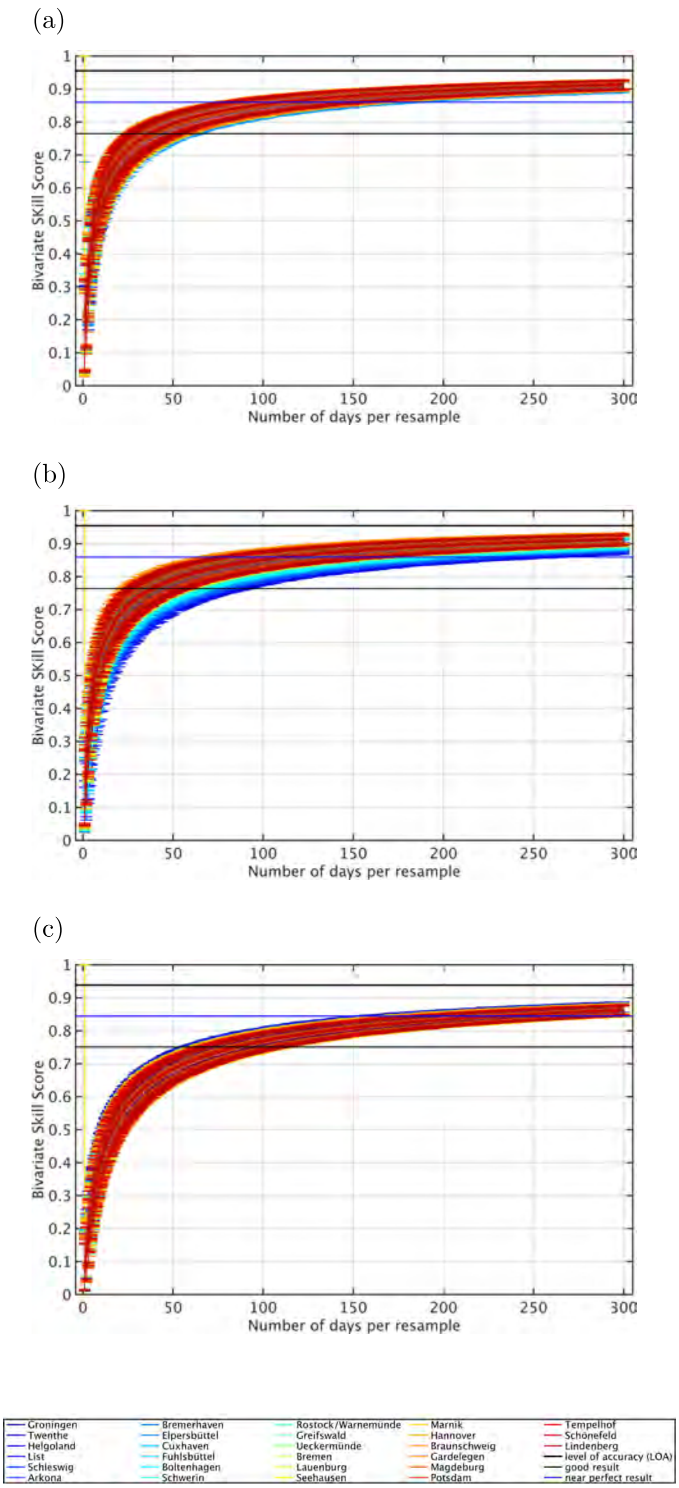

Figure D.8: Same as Figure D.1 but for DJF for (a) DD/RH, (b) DD/FF and (c) DD/TC.

E Determination of the thrust coefficient for wind turbines used in METRAS

Linde (2011) determined the thrust coefficient for a Nordex N80 / 2500 wind turbine from field measurements presented in Machielse et al. (2007). The thrust coefficients used in this study are decreased compared to the thrust coefficients from Linde (2011), because larger wind turbines seem to have lower power and thrust coefficients (Enercon, 2010).

The model METRAS was tested with different thrust coefficients. The result showed that METRAS results with the coarse grid resolution of 4×4 km^2 used in this study, are nearly independent from the thrust coefficient. Therefore, the thrust coefficients given in Table E.1 are considered to be sufficiently determined.

Table E.1: Thrust coefficient used in this study to parametrise the wind turbines.

wind speed [m/s]	thrust coefficient c_T
0.0	0.00
2.5	0.45
9.0	0.37
13.0	0.28
17.0	0.00

F Model characteristics of METRAS

Table F.1: Model characteristics of the employed model METRAS.

Model characteristic	METRAS
Equations	Reynolds-averaged equations in flux form for momentum, temperature, humidity and tracer
Approximations	anelastic approximation Boussinesq approximation Coriolis force is considered
Grid	Arakawa-C grid with terrain-following coordinates
Numerical schemes	Momentum advection is calculated with the Adams-Bashforth scheme with second-order central differences in space Advection of scalar quantities is calculated with the first-order upstream scheme in space and forward in time Seven point filter is used for smoothing of short waves resulting from Adams-Bashforth scheme Vertical diffusion is solved either explicitly or semi-implicitly with the Crank-Nicholson scheme, depending on time step needed for the different processes
Parameterisation of subgrid scale processes	first-order closure for turbulent fluxes resulting from Reynolds-averaging turbulent exchange coefficients are calculated using a mixing length approach for stable stratification and including a countergradient term for unstable stratification (Lüpkes and Schlünzen, 1996) flux aggregation method (Von Salzen et al., 1996) for calculating the subgrid scale surface cover effects Cloud and rain microphysics are calculated using the Kessler scheme (Kessler, 1969), falling of rain drops is simulated explicitly Radiation is calculated using a two-stream approximation scheme Bakan (1994)

continued on next page

continued from page before

Boundary conditions	Normal wind components at lateral boundaries calculated as far as possible zero-gradient for parallel wind components at lateral boundaries zero-gradient for horizontal wind components Vertical wind component are et to zero no slip condition for wind at surface zero-gradient for temperature at lateral boundaries and model top budget equation for temperature at surface zero-gradient for humidity at lateral boundaries and model top budget equation for humidity at surface
Nudging	for the horizontal wind components, temperature and humidity Cloud and rain water from forcing data are added to the specific humidity to allow for finer cloud developments in the nested simulation Nudging method following (Davies, 1976) ECMWF analysis data (ECMWF, 2009, 2010) are used for forcing the meteorological data Horizontal resolution of forcing data is 16 km after 26th January 2010 and of 25 km resolution before Data of sea surface temperature are taken from NOAA Optimum Interpolation Sea Surface Temperatures V2 (Reynolds et al., 2002)

G Days simulated to represent the winter climate of Hamburg

Table G.1 provides the names and dates of days simulated for the winter months. The simulations are started five hours before the first results are used in the analyses. The simulations are initialised for day zero, 1900 LT. The number of days to dry the soil is used in the 1D version of METRAS where the soil model is integrated for the time (number of days) given. This ensures a realistic soil moisture during model initialisation. The number of days to dry the soil results from a visual inspection of precipitation data for the model area for the day before day zero of the simulation. It indicates the time without rain before model initialisation, given in days (Table G.1).

The simulations are executed with a maximum of 200 allowed iterations for the pressure solver. However, due to numerical instabilities caused by the pressure solver, the number of maximum iterations allowed is set to 400 in some simulations. These simulations are marked with an 'A' for the numerics used (Table G.1). For some simulations, the lateral boundary conditions for the specific humidity are set from zero gradient to large-scale values obtained from the ECMWF analysis data, also because of numerical reasons resulting from the humidity values at the boundaries. These simulations are marked with a 'B' for the numerics used (Table G.1).

METRAS dynamically calculates the length of the time-steps needed for the model integration in a numerically stable mode, depending on the physics and numerics used. This calculation is not executed during every model iteration to save computing time but at a constant time interval. Due to abrupt changes in the forcing, the wind speed changes greatly in the simulation LIWI10 during one of these constant intervals. This effect leads to a violation of the Courant-Friedrichs-Lewy-Criterion for some time-steps. As a consequence, the simulation becomes numerically unstable. To avoid this, the length of the calculated time-steps for the simulation LIWI10 is reduced by 37.5 % (rcfl = 0.5 instead of rcfl = 0.8) after day 2, 1500 LT. This is marked with 'rcfl' in Table G.1. The simulations of LIWI01 and LIWI08 aborted in at least one of the three scenario simulations. They are completely left out of the evaluation and the statistics are calculated without the simulations of LIWI01 and LIWI08. The reasons for abortion need further investigations.

Table G.1: Days assessed for the winter season. The number of days to dry the soil is applied in the 1D version of METRAS. Some simulations have an increased number of allowed iterations for the pressure solver (marked with an 'A'), some simulations additionally use different lateral boundary conditions for relative humidity (marked with a 'B'). The aborted simulations are not used in the analyses. Simulations including snow cover anywhere in the model domain are marked with italic letters. The simulations marked with bold italic letters include snow cover in the focus domain. The simulations marked with a star include snow cover at Fuhlsbüttel.

Name of simulation	Day 1	Day 2	Day 3	number of days to dry the soil	Numeric used
LIWI01	2006-02-03	2006-02-04	2006-02-05	1	aborted
LIWI02	2006-02-10	2006-02-11	2006-02-12	1	-
LIWI03	2006-12-09	2006-12-10	2006-12-11	1	B
LIWI04	2006-12-19	2006-12-20	2006-12-21	1	-
LIWI05	2006-12-23	2006-12-24	2006-12-25	1	B
LIWI06	2006-12-31	2007-01-01	2007-01-02	1	-
LIWI07	2007-01-06	2007-01-07	2007-01-08	1	A
LIWI08	2007-01-18	2007-01-19	2007-01-20	1	aborted
LIWI09	2007-01-25	2007-01-26	2007-01-27	1	-
LIWI10	2007-01-28	2007-01-29	2007-01-30	1	rcfl
LIWI11	2007-02-03	2007-02-04	2007-02-05	1	-
LIWI12 ⋆	2007-02-10	2007-02-11	2007-02-12	1	-
LIWI13	2007-02-15	2007-02-16	2007-02-17	1	-
LIWI14	2007-02-26	2007-02-27	2007-02-28	1	-
LIWI15	2007-12-03	2007-12-04	2007-12-05	1	A
LIWI16	2007-12-14	2007-12-15	2007-12-16	1	A
LIWI17	2007-12-21	2007-12-22	2007-12-23	3	-
LIWI18 ⋆	2008-01-03	2008-01-04	2008-01-05	1	A
LIWI19	2008-01-07	2008-01-08	2008-01-09	1	A
LIWI20	2008-01-15	2008-01-16	2008-01-17	1	B
LIWI21	2008-01-23	2008-01-24	2008-01-25	1	A
LIWI22	2008-02-08	2008-02-09	2008-02-10	1	-

continued on next page

continued from page before

Name of simulation	Day 1	Day 2	Day 3	number of days to dry the soil	Numeric used
LIWI23	2008-02-12	2008-02-13	2008-02-14	1	-
LIWI24	2008-12-02	2008-12-03	2008-12-04	1	-
LIWI25	2008-12-15	2008-12-16	2008-12-17	1	-
LIWI26	2008-12-23	2008-12-24	2008-12-25	1	-
LIWI27 ⋆	2009-01-10	2009-01-11	2009-01-12	1	-
LIWI28	2009-01-22	2009-01-23	2009-01-24	1	-
LIWI29	2009-02-01	2009-02-02	2009-02-03	1	-
LIWI30	2009-02-04	2009-02-05	2009-02-06	1	-
LIWI31	2009-02-08	2009-02-09	2009-02-10	1	-
LIWI32	2009-02-19	2009-02-20	2009-02-21	2	-
LIWI33	2009-12-01	2009-12-02	2009-12-03	1	-
LIWI34	2009-12-07	2009-12-08	2009-12-09	1	-
LIWI35	2009-12-15	2009-12-16	2009-12-17	1	-
LIWI36	2009-12-28	2009-12-29	2009-12-30	1	A
LIWI37 ⋆	2010-01-19	2010-01-20	2010-01-21	1	-
LIWI38	2010-01-29	2010-01-30	2010-01-31	1	-
LIWI39 ⋆	2010-02-13	2010-02-14	2010-02-15	1	-
LIWI40 ⋆	2010-02-19	2010-02-20	2010-02-21	1	-
LIWI41	2008-02-26	2008-02-27	2008-02-28	1	-
LIWI42	2008-12-06	2008-12-07	2008-12-08	1	-
LIWI43	2008-12-31	2009-01-01	2009-01-02	1	-
LIWI44 ⋆	2009-02-13	2009-02-14	2009-02-15	1	-
LIWI45 ⋆	2010-02-05	2010-02-06	2010-02-07	1	-

List of important Acronyms

R	correlation coefficient
REF_NO_SNOW	reference case without using the snow scheme
REF_WITH_SNOW	reference case with using the snow scheme
2D-PDF	two-dimensional probability density function
ADC	actuator disc concept
BEP	urban parametrisation scheme (building effect parametrisation)
BIAS	BIAS of model results
BSS	bivariate skill score
DD	wind direction
DJF	December, January and February
DWD	German Meteorological Service (Deutscher Wetterdienst)
ECMWF	European Centre for Medium-Range Weather Forecasts
FF	wind speed
Fuhlsbüttel	weather station at the Hamburg airport
GCM	global circulation model
HH1	METRAS grid with 1 km horizontal grid resolution
HH250	METRAS grid with 250 m horizontal grid resolution
HH4	METRAS grid with 4 km horizontal grid resolution
HITRATE	HITRATE of model results
HUSCO	Hamburg Urban Soil Climate Observatory
ICWC	integral cloud water content
IPCC	Intergovernmental Panel on Climate Change

JJA	June, July and August
LATE	time period from 2100 LT to 2400 LT
LIWI	name for winter simulations 01 to 45
LOA	level of accuracy
LT	local time
MAM	March, April and May
METRAS	mesoscale transport and stream model of the atmosphere
MRH	metropolitan region of Hamburg
NOAA OISST	NOAA Optimum Interpolation Sea Surface Temperature V2
NOON	time period from 1000 LT to 1600 LT
PDF	probability density function
PT	perceived temperature
RCM	regional climate model
RH	relative humidity
RMSE	root mean square error
SCC	surface cover class
SDD	statistical-dynamical downscaling
SON	September, October and November
SSP	skill score following Perkins et al. (2007)
SWE	snow water equivalent
TC	temperature in degree Celsius
UCI	urban cool island
UHI	urban heat island

WMO	World Meteorological Organization
WP	weather pattern, name for summer simulations 1C to 7C for cluster centre, 1M to 7M for cluster mean and 1T to 7T for threshold UHI
WPC	weather pattern classification

List of important Symbols

Greek Letters

α	[.]	albedo of a snow pack
α_j	[.]	albedo of a specific surface cover class
α_{min}	[.]	maximum albedo of a snow pack
α_{min}	[.]	minimum albedo of a snow pack
$\alpha_{q,j}$	[.]	soil water availability of a specific surface cover class
β	[.]	empirical factor
Δt	$[s]$	length of the time-step
ϵ	[.]	parameter
$\theta_\star$	$[K]$	scaling value for heat
θ	$[K]$	potential temperature
$\theta_{S,j}$	$[K]$	potential surface temperature for each surface cover class
$\theta_{\star,j}$	$[K]$	scaling value for heat of a specific surface cover class
$\theta(z_{k=1})$	$[K]$	potential temperature in the lowest model layer
κ	[.]	Karman constant
λ	[.]	empirical scaling factor
μ_j	[.]	parameter to calculate the short wave radiation budget
ν_j	$[W/Km]$	thermal conductivity of a specific surface cover class
ν_g	$[W/Km]$	thermal conductivity
$\nu_{snow,j}$	$[W/Km]$	thermal conductivity through a layer of snow
$\nu_{soil,j}$	$[W/Km]$	thermal conductivity through a layer of soil
$\rho_{0,surf}$	$[kg/m^3]$	air density of the basic state at the surface
ρ	$[kg/m^3]$	air density
ρ_{max}	$[kg/m^3]$	maximum density of snow
ρ_{min}	$[kg/m^3]$	minimum density of snow
ρ_{snow}	$[kg/m^3]$	density of snow
ρ_{water}	$[kg/m^3]$	density of water
σ	$[W/K^4m^2]$	Stefan-Boltzmann-constant
τ	$[s]$	period of the temperature wave
τ_1	$[s]$	empirical factor

τ_a	[.]	empirical factor
τ_f	[.]	empirical factor
χ	[.]	scalar variable
ψ_h	[.]	stability functions of heat
ψ_m	[.]	stability functions of momentum
ω	$[1/s]$	frequency of the temperature wave

Latin Letters

A	$[W/m^2]$	reflected radiation flux
A_0	$[K]$	amplitude of the temperature wave
A_1	$[m^2]$	rotor parallel area far upwind of a wind turbine in Chapter 3, reflected radiation flux for visible range 1 everywhere else $[W/m^2]$
A_2	$[m^2]$	rotor parallel area far downwind of a wind turbine in Chapter 3, reflected radiation flux for the near infrared range 2 everywhere else $[W/m^2]$
A'	$[m^2]$	rotor area
$\hat{C}_{\chi,j}$	[.]	near-surface effective transfer coefficients of a scalar variable
$\hat{C}_{m,j}$	[.]	near-surface effective transfer coefficients of momentum
$\hat{C}_{q,j}$	[.]	near-surface effective transfer coefficients of specific humidity
$\hat{C}_{\theta,j}$	[.]	near-surface effective transfer coefficients of potential temperature
c_{ice}	$[W/Km]$	thermal conductivity of ice
c_p	$[J/kgK]$	specific heat capacity of dry air at constant pressure
c_{snow}	$[W/Km]$	thermal conductivity of snow
$c_{surface}$	$[W/Km^2]$	heat transfer coefficient from the surface into the snow pack
c_T	[.]	thrust coefficient
D	$[m]$	rotor diameter in Chapter 3, accuracy for HITRATE everywhere else
D_j	$[m]$	depth of soil layer
d	$[m]$	distance between the rotor and the reference rotor in Chapter 3, damping depth everywhere else

$d_{snow,j}$	$[m]$	damping depth for snow
$d_{soil,j}$	$[m]$	damping depth for soil
E	$[W/m^2]$	incoming radiation flux
E_0	$[W/m^2]$	solar constant
E_{01}	$[W/m^2]$	solar constant for the visible range 1
E_{02}	$[W/m^2]$	solar constant for the near infrared range 2
E_1	$[W/m^2]$	incoming radiation flux for the visible range 1
E_2	$[W/m^2]$	incoming radiation flux for the near infrared range 2
E_{melt}	$[J/m^2]$	energy necessary for melting
E_{snow}	$[m/s]$	rate of evaporation of snow
F_j	$[W/m^2]$	anthropogenic heat emission for each surface cover class
f_A	$[.]$	function for the albedo
f_j	$[.]$	fraction of a specific surface cover class in an individual grid cell
G	$[W/m^2]$	heat flux to the soil
$G_{S,j}$	$[W/m^2]$	heat flux to the soil at the surface for each surface cover class
$G_{snow,j}$	$[W/m^2]$	heat flux through a layer of snow
$G_{soil,j}$	$[W/m^2]$	heat flux through a layer of soil
H	$[W/m^2]$	sensible heat flux
H_j	$[W/m^2]$	sensible heat flux for each surface cover class
h	$[m]$	depth where the temperature is assumed to be constant
h_j	$[m]$	depth of daily temperature wave
$h_{snow,j}$	$[m]$	depth of temperature wave for snow
$h_{soil,j}$	$[m]$	depth of temperature wave for soil
I_∞	$[W/m^2]$	incoming solar radiation constant
j	$[.]$	specific surface cover class
k_j	$[m^2/s]$	thermal diffusivity of a specific surface cover class
$k_{snow,j}$	$[m^2/s]$	thermal diffusivity of snow for a specific surface cover class
$k_{soil,j}$	$[m^2/s]$	thermal diffusivity of soil for a specific surface cover class
L	$[W/m^2]$	latent heat flux

L_f	$[J/kg]$	latent heat of fusion
L_j	$[W/m^2]$	latent heat flux for each surface cover class
$L_{MO,j}$	$[m]$	Monin-Obukhov-Length for each surface cover class
$LW_{net,j}$	$[W/m^2]$	net long wave radiation flux
l_{21}	$[J/kg]$	latent heat of evaporation of water
l_b	$[m]$	blending height
M	$[W/m^2]$	momentum flux
$\bar{M}$	$[.]$	mean of model results
M_i	$[.]$	model result
M_{snow}	$[m/s]$	rate of melting
m	$[.]$	number of bins of a probability density function
N	$[.]$	sample size
n	$[.]$	number of bins of a probability density function
$\bar{O}$	$[.]$	mean of observations
O_i	$[.]$	observation
P	$[mm/h]$	precipitation
P_{snow}	$[m/s]$	rate of snowfall
$p_{snow_{z0}}$	$[.]$	snow cover fraction
q	$[.]$	specific humidity
$q_1^1(z_{k=1})$	$[kg/kg]$	specific humidity in the lowest model layer
$q_{1sat,j}^1$	$[kg/kg]$	saturation value of the specific humidity at the surface
$q_{1S,j}^1$	$[kg/kg]$	specific humidity at the surface
$q_\star$	$[kg/kg]$	scaling value for moisture
$q_{\star,j}$	$[kg/kg]$	scaling value for moisture of a specific surface cover class
$Re_\star$	$[.]$	roughness Reynoldsnumber
S	$[W/m^2]$	net solar radiation flux
SWE	$[m]$	snow water equivalent
$SW_{net,j}$	$[W/m^2]$	net short wave radiation budget of a specific surface cover class
T'	$[N]$	rotor thrust
T_0	$[K]$	melting point
$T_{0_{mean}}$	$[K]$	mean temperature

T_D	[.]	transmission factors for absorption and scattering by aerosols
T_E	[.]	transmission factors for Rayleigh scattering
T_h	$[K]$	soil temperature in the deep h_j
T_L	[.]	transmission factors for absorption and scattering by liquid water
T_{max}	$[N]$	maximum rotor thrust
T_S	$[K]$	surface temperature
$T_{S,j}$	$[K]$	sub-grid scale surface temperature
$T_{snow,j}$	$[K]$	snow temperature
$T_{soil,j}$	$[K]$	soil temperature
T_V	[.]	transmission factors for absorption by water vapour
t	$[s]$	time
$u_\star$	$[m/s]$	scaling value for momentum
$u_{\star,j}$	$[m/s]$	scaling value for momentum of a specific surface cover class
$V(z_{k=1})$	$[m/s]$	horizontal wind speed in the lowest model layer
v'	$[m/s]$	mean wind speed at a wind turbine
v_1	$[m/s]$	mean wind speed far upwind of a wind turbine
v_2	$[m/s]$	mean wind speed far downwind of a wind turbine
$W_{k,j}$	$[m]$	saturation value for soil water content of a specific surface cover class
Z	[.]	zenith angle of the sun
Z_M	[.]	probability density function
Z_{M_i}	[.]	bin of a probability density function
$Z_{M_{ik}}$	[.]	bin of a two-dimensional probability density function
Z_{O_i}	[.]	bin of a probability density function
Z_O	[.]	probability density function
$Z_{O_{ik}}$	[.]	bin of a two-dimensional probability density function
z	$[m]$	depth
z_0	$[m]$	effective roughness length
$z_{0,j}$	$[m]$	roughness length of a specific surface cover class
$z_{0_{psnow}}$	$[m]$	roughness length for the partly snow-covered surface
z_{0q}	$[m]$	effective roughness length for moisture
$z_{0q,j}$	$[m]$	sub-grid scale roughness length for moisture

$z_{0_{snow}}$	$[m]$	roughness length for snow
$z_{0\theta}$	$[m]$	effective roughness length for heat
$z_{0\theta,j}$	$[m]$	sub-grid scale roughness length for heat
$z_{g,j}$	$[m]$	depth of snow-soil-interface
z_{snow}	$[m]$	depth of snow

References

ADACHI, S. A., F. KIMURA, H. KUSAKA, T. INOUE, H. UEDA, 2012: Comparison of the impact of global climate changes and urbanization on summertime future climate in the tokyo metropolitan area. – Journal of Applied Meteorology and Climatology **51**(8), 1441–1454.

BACK, L., 2011: Stadtentwicklungsplan Klima: urbane Lebensqualität im Klimawandel sichern – Kulturbuch-Verlag, 84 pp.

BAIDYA ROY, S., 2011: Simulating impacts of wind farms on local hydrometeorology. – Journal of Wind Engineering and Industrial Aerodynamics 491–498.

BAIDYA ROY, S., J. J. TRAITEUR, 2010: Impacts of wind farms on surface air temperatures. – Proceedings of the National Academy of Sciences **107**(42), 17899–17904.

BAIDYA ROY, S., S. W. PACALA, R. L. WALKO, 2004: Can large wind farms affect local meteorology?. – J. Geophys. Res. 109 1–6.

BAKAN, S., 1994: Eine einfache Strahlungsparameterisierung für ein mesoskaliges Modell. – Interner Bericht. Max-Planck-Institut für Meteorologie, Hamburg, Deutschland, 21 pp.

BAKER, D. G., D. L. RUSCHY, D. B. WALL, 1990: The albedo decay of prairie snows. – Journal of Applied Meteorology **29**(2), 179–187.

BECHTEL, B., K. J. SCHMIDT, 2011: Floristic mapping data as a proxy for the mean urban heat island. – Climate Research **49**(1), 45–58.

BECKER, G. A., 1981: Beiträge zur Hydrographie und Wärmebilanz der Nordsee. – Deutsche Hydrografische Zeitschrift **34**(5), 167–262.

BEST, M. J., C. S. B. GRIMMOND, 2015: Key conclusions of the first international urban land surface model comparison project. – Bulletin of the American Meteorological Society **96**(5), 805–819.

BHUMRALKAR, C. M., 1975: Numerical experiments on the computation of ground surface temperature in an atmospheric general circulation model.. – Journal of Applied Meteorology **14**, 1246–1258.

Boettcher, M., P. Hoffmann, H.-J. Lenhart, K. H. Schlünzen, R. Schoetter, 2015: Influence of large offshore wind farms on north german climate. – Meteorologische Zeitschrift, 465–480.

Boone, A., P. Etchevers, 2001: An intercomparison of three snow schemes of varying complexity coupled to the same land surface model: Local-scale evaluation at an alpine site.. – Journal of Hydrometeorology **2**(4), 374–394.

Bowler, D. E., L. Buyung-Ali, T. M. Knight, A. S. Pullin, 2010: Urban greening to cool towns and cities: A systematic review of the empirical evidence. – Landscape and urban planning **97**(3), 147–155.

Brutsaert, W., 1975: The roughness length for water vapor sensible heat, and other scalars. – Journal of the Atmospheric Sciences **32**(10), 2028–2031.

Brutsaert, W., 1982: Evaporation into the atmosphere, volume 1 – D. Reidl Pubblishing Company, Dordrecht, 302 pp.

Bungert, U. M., 2008: Einfluss der Nestung auf die Ergebnisse meteorologischer Modelle Ph.D. thesis, University of Hamburg, 140 pp.

Burkhard, B., 2006: Nordsee 2055 - Zukunftsszenarien für die Küste. – EcoSys Suppl. Bd. 46 70–89.

Ca, V. T., T. Asaeda, E. M. Abu, 1998: Reductions in air conditioning energy caused by a nearby park. – Energy and Buildings **29**(1), 83–92.

Cheng, V., E. Ng, C. Chan, B. Givoni, 2012: Outdoor thermal comfort study in a sub-tropical climate: a longitudinal study based in hong kong. – International Journal of Biometeorology **56**(1), 43–56.

Christiansen, M. B., C. B. Hasager, 2005: Wake effects of large offshore wind farms identified from satellite sar. – Remote sensing of environment 98, 251-268 12–15.

Clarke, R. H., 1970: Recommended methods for the treatment of the boundary layer in numerical models. – Australian Meteorological Magazine **18**, 51–71.

Daschkeit, A., 2011: Das Klima der Region und mögliche Entwicklungen in der Zukunft bis 2100, in von Storch, H. and Claussen, M. and KlimaCampus Team – Klimabericht für die Metropolregion Hamburg. Berlin, Heidelberg: Springer Verlag, 61-90.

Davies, H., 1976: A laterul boundary formulation for multi-level prediction models. – Quarterly Journal of the Royal Meteorological Society **102**(432), 405–418.

De Freitas, C. R., E. A. Grigorieva, 2015: A comprehensive catalogue and classification of human thermal climate indices. – International Journal of Biometeorology **59**(1), 109–120.

Deardorff, J. W., 1978: Efficient prediction of ground surface temperature and moisture, with inclusion of a layer of vegetation. – Journal of Geophysical Research: Oceans **83**(C4), 1889–1903.

Douville, H., J.-F. Royer, J.-F. Mahfouf, 1995: A new snow parameterization for the meteo-france climate model. – Climate Dynamics **12**(1), 21–35.

Drusch, M., D. Vasiljevic, P. Viterbo, 2004: Ecmwf's global snow analysis: Assessment and revision based on satellite observations. – Journal of Applied Meteorology **43**(9), 1282–1294.

Dutra, E., G. Balsamo, P. Viterbo, P. M. A. Miranda, A. Beljaars, C. Schär, K. Elder, 2010: An improved snow scheme for the ecmwf land surface model: description and offline validation. – Journal of Hydrometeorology **11**(4), 899–916.

ECMWF, 2009: Part ii: Data assimilation. – IFS DOCUMENTATION - Cy33r1 Operational implementation 3 June 2008 160 pp.

ECMWF, 2010: Part vii: Data assimilation. – IFS DOCUMENTATION - Cy36r1 Operational implementation 26 January 2010 168 pp.

Eichhorn, A., 2013: Determining reasons for impacts of offshore wind farms on meteorological parameters in North-Western Germany. – Bachelorarbeit Meteorologie, Univ. Hamburg, 29 pp.

El Kasmi, A., C. Masson, 2008: An extended k–ε model for turbulent flow through horizontal-axis wind turbines. – Journal of Wind Engineering and Industrial Aerodynamics **96**(1), 103–122.

Emeis, S., 2010: A simple analytical wind park model considering atmospheric stability. – Wind Energy **13**(5), 459–469.

Enercon, 2010: ENERCON Windenergieanlagen, Produktübersicht, status 07/10. – ENERCON GmbH 23 pp.

FITCH, A. C., J. B. OLSON, J. K. LUNDQUIST, J. DUDHIA, A. K. GUPTA, J. MICHALAKES, I. BARSTAD, 2012: Local and mesoscale impacts of wind farms as parameterized in a mesoscale NWP model. – Monthly Weather Review **140**(9), 3017–3038.

FITCH, A. C., J. K. LUNDQUIST, J. B. OLSON, 2013: Mesoscale influences of wind farms throughout a diurnal cycle. – Monthly Weather Review **141**(7), 2173–2198.

GEORGESCU, M., M. MOUSTAOUI, A. MAHALOV, J. DUDHIA, 2013: Summer-time climate impacts of projected megapolitan expansion in Arizona. – Nature Climate Change **3**(1), 37–41.

GEORGESCU, M., P. E. MOREFIELD, B. G. BIERWAGEN, C. P. WEAVER, 2014: Urban adaptation can roll back warming of emerging megapolitan regions. – Proceedings of the National Academy of Sciences **111**(8), 2909–2914.

GILL, S. E., J. F. HANDLEY, A. R. ENNOS, S. PAULEIT, 2007: Adapting cities for climate change: the role of the green infrastructure. – Built Environment **33**(1), 115–133.

GOLCHERT, H. J., 1981: Mittlere monatliche Globalstrahlungsverteilungen in der Bundesrepublik Deutschland. – Meteorologische Rundschau **34**, 143–151.

GRAWE, D., H. L. THOMPSON, J. A. SALMOND, X.-M. CAI, K. H. SCHLÜNZEN, 2013: Modelling the impact of urbanisation on regional climate in the Greater London Area. – International Journal of Climatology **33**(10), 2388–2401.

GROSS, G., 2010: Numerical simulations to the diurnal variation of wakes behind wind turbines. – Meteorologische Zeitschrift **19**(1), 91–99.

GROSS, G., 2012: Numerical simulation of greening effects for idealised roofs with regional climate forcing. – Meteorologische Zeitschrift **21**(2), 173–181.

HAMDI, R., G. SCHAYES, 2008: Sensitivity study of the urban heat island intensity to urban characteristics. – International Journal of Climatology **28**(7), 973–982.

HAU, E., 2002: Windkraftanlagen: Grundlagen, Technik, Einsatz, Wirtschaftlichkeit – Springer, 997 pp.

HIROTA, T., J. W. POMEROY, R. J. GRANGER, C. P. MAULE, 2002: An extension of the force-restore method to estimating soil temperature at depth and evaluation for frozen soils under snow. – Journal of Geophysical Research: Atmospheres (1984–2012) **107**(D24), 10 pp.

Hoffmann, P., 2012: Quantifying the influence of climate change on the urban heat island of Hamburg using different downscaling methods Ph.D. thesis, University of Hamburg, 138 pp.

Hoffmann, P., K. H. Schlünzen, 2013: Weather pattern classification to represent the urban heat island in present and future climate. – Journal of Applied Meteorology and Climatology **52**(12), 2699–2714.

Hoffmann, P., O. Krueger, K. H. Schlünzen, 2012: A statistical model for the urban heat island and its application to a climate change scenario. – International Journal of Climatology **32**(8), 1238–1248.

Hoffmann, P., R. Schoetter, K. H. Schlünzen, 2016: Statistical-dynamical downscaling of the urban heat island in Hamburg, Germany. – Meteorologische Zeitschrift 21 pp.

Hollweg, H.-D., U. Böhm, I. Fast, B. Hennemuth, K. Keuler, E. Keup-Thiel, M. Lautenschlager, S. Legutke, K. Radtke, B. Rockel, others, 2008: Ensemble simulations over Europe with the regional climate model CLM forced with IPCC AR4 global scenarios. – M & D Technical Report **3**, 152 pp.

Honjo, T., T. Takakura, 1991: Simulation of thermal effects of urban green areas on their surrounding areas. – Energy and Buildings **15**(3-4), 443–446.

Huth, R., C. Beck, A. Philipp, M. Demuzere, Z. Ustrnul, M. Cahynová, J. Kyselỳ, O. E. Tveito, 2008: Classifications of atmospheric circulation patterns. – Annals of the New York Academy of Sciences **1146**(1), 105–152.

IPCC's Fifth Assessment Report (AR5), 2013: Climate change 2013: The physical science basis. contribution of working group I to the fifth assessment report of the intergovernmental panel on climate change. – Cambridge University Press, Cambridge, United Kingdom and New York, NY, USA 1535.

Jacob, D., R. Podzun, 1997: Sensitivity studies with the regional climate model remo. – Meteorology and Atmospheric Physics **63**(1), 119–129.

JACOB, D., H. GÖTTEL, S. KOTLARSKI, P. LORENZ, K. SIECK, 2008: Klimaauswirkungen und Anpassung in Deutschland-Phase 1: Erstellung regionaler Klimaszenarien für Deutschland.

JACOB, D., E. NILSON, L. TOMASSINI, K. BÜLOW, 2009: REMO climate of the 20th century run and A1B scenario run, BfG project, 0.088 degree resolution. – World Data Center for Climate. CERA-Database

JACOBSON, M. Z., J. E. TEN HOEVE, 2012: Effects of urban surfaces and white roofs on global and regional climate. – Journal of Climate **25**(3), 1028–1044.

JÄNICKE, B., F. MEIER, D. FENNER, U. FEHRENBACH, A. HOLTMANN, D. SCHERER, 2016: Urban–rural differences in near-surface air temperature as resolved by the Central Europe Refined analysis (CER): sensitivity to planetary boundary layer schemes and urban canopy models. – International Journal of Climatology 2063–2079.

JIN, J., X. GAO, Z.-L. YANG, R. C. BALES, S. SOROOSHIAN, R. E. DICKINSON, S. F. SUN, G. X. WU, 1999: Comparative analyses of physically based snowmelt models for climate simulations. – Journal of Climate **12**(8), 2643–2657.

JUNGCLAUS, J. H., N. KEENLYSIDE, M. BOTZET, H. HAAK, J.-J. LUO, M. LATIF, J. MAROTZKE, U. MIKOLAJEWICZ, E. ROECKNER, 2006: Ocean circulation and tropical variability in the coupled model ECHAM5/MPI-OM. – Journal of Climate **19**(16), 3952–3972.

KANDA, M., M. KANEGA, T. KAWAI, R. MORIWAKI, H. SUGAWARA, 2007: Roughness lengths for momentum and heat derived from outdoor urban scale models. – Journal of Applied Meteorology and Climatology **46**(7), 1067–1079.

KEITH, D. W., J. F. DECAROLIS, D. C. DENKENBERGER, D. H. LENSCHOW, S. L. MALYSHEV, S. PACALA, P. J. RASCH, 2004: The influence of large-scale wind power on global climate. – Proceedings of the National Academy of Sciences of the United States of America **101**(46), 16115–16120.

KESSLER, E., 1969: On the distribution and continuity of water substance in atmospheric circulations. – Meteorological Monographs 1–84.

KLINK, K., C. J. WILLMOTT, 1994: Influence of soil moisture and surface roughness heterogeneity on modeled climate. – Climate Research **4**, 105–18.

Kottek, M., J. Grieser, C. Beck, B. Rudolf, F. Rubel, 2006: World Map of the Köppen-Geiger climate classification updated. – Meteorologische Zeitschrift **15**(3), 259–263.

Kruse, E., J. Ziegler, N. Klostermann, J. Fink, 2014: Eingangsparameter für die Modellierung. – Kruse, E., T. Zimmermann, A. Kittel, W. Dickhaut, J. Knieling, C. Sörensen (Hrsg.) (2014): Stadtentwicklung und Klimaanpassung-beispielhaft dargestellt am Einzugsgebiet der Wandse, Hamburg. Berichte aus dem KLIMZUG-NORD Modellgebieten, Band 4, TuTech Verlag, Hamburg, Germany: 158-161

Lange, M., B. Burkhard, S. Garthe, K. Gee, A. Kannen, H.-J. Lenhart, W. Windhorst, 2010: Analyzing coastal and marine changes: Offshore wind farming as a case study, Zukunft Küste - Coastal Futures Synthesis Report. – LOICZ Research and Studies No. 36. GKSS Reasearch Center, Geesthacht **10**, 212 pp.

Lemonsu, A., S. Bélair, J. Mailhot, S. Leroyer, 2010: Evaluation of the town energy balance model in cold and snowy conditions during the montreal urban snow experiment 2005. – Journal of Applied Meteorology and Climatology **49**(3), 346–362.

Linde, M., 2011: Modellierung des Einflusses von Windkraftanlagen auf das umgebende Windfeld. Master's thesis, Meteorological Institute, KlimaCampus, University of Hamburg, 101 pp.

Lüpkes, C., K. H. Schlünzen, 1996: Modelling the arctic convective boundary-layer with different turbulence parameterizations. – Boundary-Layer Meteorology **79**(1), 107–130.

Luce, C. H., D. G. Tarboton, 2001: A modified force-restore approach to modeling snow-surface heat fluxes. – Elder, Kelly, ed. Proceedings of the Western Snow Conference: Sun Valley, Idaho, April 16-19, 2001, sixty-ninth annual meeting. Fort Collins, CO: Colorado State University: 103-114

Lynch-Stieglitz, M., 1994: The development and validation of a simple snow model for the GISS GCM. – Journal of Climate **7**(12), 1842–1855.

Machielse, L. A. H., P. J. Eecen, H. Korterink, van der S. P. Pijl, J. G. Schepers, 2007: ECN test farm measurements for validation of wake models. – Energy research Centre of the Netherlands, 12pp.

Martens, M., 2012: Untersuchung des Klimas der Norddeutschen Tiefebene mittels Datenanalyse und Downscaling Master's thesis, Meteorological Institute, University of Hamburg, 112 pp.

Martilli, A., A. Clappier, M. W. Rotach, 2002: An urban surface exchange parameterisation for mesoscale models. – Boundary-Layer Meteorology **104**(2), 261–304.

Meyer, E. M. I., K. H. Schlünzen, 2011: The influence of emission changes on ozone concentrations and nitrogen deposition into the southern North Sea. – Meteorologische Zeitschrift **20**(1), 75–84.

Michaelsen, K., U. Krell, V. Reinhardt, H. Grassl, L. Kaufeld, 1998: Climate of the north sea. – Selbstverlag des Deutschen Wetterdienstes, Offenbach am Main, Einzelveröffentlichungen Nr. 118 277 pp.

Mikkelsen, R. F., 2003: Actuator disc methods applied to wind turbines. – PhD Thesis, Technical University of Denmark, 121pp.

Miller, L. M., F. Gans, A. Kleidon, 2011: Estimating maximum global land surface wind power extractability and associated climatic consequences. – Earth System Dynamics **2**, 1–12.

Molly, J.-P., 1978: Windenergie in Theorie und Praxis - Grundlagen und Einsatz – Verlag C. F. Müller Karlsruhe, 138 pp.

Müller, N., W. Kuttler, A.-B. Barlag, 2014: Counteracting urban climate change: adaptation measures and their effect on thermal comfort. – Theoretical and Applied Climatology **115**(1-2), 243–257.

Perkins, S. E., A. J. Pitman, N. J. Holbrook, J. McAneney, 2007: Evaluation of the AR4 climate models' simulated daily maximum temperature, minimum temperature, and precipitation over Australia using probability density functions. – Journal of Climate **20**(17), 4356–4376.

Philipp, A., P. M. Della-Marta, J. Jacobeit, D. R. Fereday, P. D. Jones, A. Moberg, H. Wanner, 2007: Long-term variability of daily North Atlantic-European pressure patterns since 1850 classified by simulated annealing clustering. – Journal of Climate **20**(16), 4065–4095.

Pielke, R. A., 1984: Mesoscale Meteorological Modeling – Academic Press, 612 pp.

Prospathopoulos, J. M., 2010: Discussion after a presentation at first WAUDIT summer school in Pamplona, Spain. – Personal communication

Rechid, D., J. Petersen, R. Schoetter, D. Jacob, 2014: Klimaprojektionen für die Metropolregion Hamburg. – Berichte aus den KLIMZUG-NORD Modellgebieten, Band 1, TuTech Verlag, Hamburg, Germany 59 pp.

Reynolds, R. W., N. A. Rayner, T. M. Smith, D. C. Stokes, W. Wang, 2002: An improved in situ and satellite SST analysis for climate. – Journal of Climate **15**(13), 1609–1625.

Reynolds, R. W., T. M. Smith, C. Liu, D. B. Chelton, K. S. Casey, M. G. Schlax, 2007: Daily high-resolution-blended analyses for sea surface temperature. – Journal of Climate **20**(22), 5473–5496.

Riecke, W., G. Rosenhagen, 2010: Das Klima in Hamburg - Entwicklung in Hamburg und der Metropolregion von Wolfgang Riecke und Gudrun Rosenhagen. Berichte des Deutschen Wetterdienstes 234 – Selbstverl. des Dt. Wetterdienstes, Offenbach, 82 pp.

Roeckner, E., G. Bäuml, L. Bonaventura, R. Brokopf, M. Esch, M. Giorgetta, S. Hagemann, I. Kirchner, L. Kornblueh, E. Manzini, others, 2003: The atmospheric general circulation model ECHAM 5. PART I: Model description.

Rottgardt, E., R. Schoetter, E. Kruse, L. Kunert, K. Schmidt, J. Stockinger, E. Verjans, 2014: Entwicklungsszenarien, Strategien und Anpassungsmaßnahmen. – Kruse,E., T. Zimmermann, A. Kittel, W. Dickhaut, J. Knieling, C. Sörensen (Hrsg.) (2014): Stadtentwicklung und Klimaanpassung-beispielhaft dargestellt am Einzugsgebiet der Wandse, Hamburg. Berichte aus dem KLIMZUG-NORD Modellgebieten, Band 4, TuTech Verlag, Hamburg, Germany: 80-86

Schlünzen, K., R. Sokhi, 2008: Overview of tools and methods for meteorological and air pollution mesoscale model evaluation and user training. – Joint report by WMO and COST, 728 116 pp.

Schlünzen, K. H., 1990: Numerical studies on the inland penetration of sea breeze fronts at a coastline with tidally flooded mudflats. – Beitr. Phys. Atmosph. **63**, 243–256.

SCHLÜNZEN, K. H., 1997: On the validation of high-resolution atmospheric mesoscale models. – Journal of Wind Engineering and Industrial Aerodynamics **67**, 479–492.

SCHLÜNZEN, K. H., J. J. KATZFEY, 2003: Relevance of sub-grid-scale land-use effects for mesoscale models. – Tellus A **55**(3), 232–246.

SCHLÜNZEN, K. H., T. STAHLSCHMIDT, A. REBERS, U. NIEMEIER, M. KRIEWS, W. DANNECKER, 1997: Atmospheric input of lead into the German Bight-a high resolution measurement and model case study. – Marine Ecology Progress Series **156**, 299–309.

SCHLÜNZEN, K. H., P. HOFFMANN, G. ROSENHAGEN, W. RIECKE, 2010: Long-term changes and regional differences in temperature and precipitation in the metropolitan area of Hamburg. – International Journal of Climatology **30**(8), 1121–1136.

SCHLÜNZEN, K. H., D. GRAWE, S. I. BOHNENSTENGEL, I. SCHLÜTER, R. KOPPMANN, 2011: Joint modelling of obstacle induced and mesoscale changes-Current limits and challenges. – Journal of Wind Engineering and Industrial Aerodynamics **99**(4), 217 – 225.

SCHLÜNZEN, K. H., D. D. FLAGG, B. H. FOCK, A. GIERISCH, V. REINHARDT, C. SPENSBERGER, 2012: Scientific Documentation of the Multiscale Model System M-SYS (METRAS, MITRAS, MECTM, MICTM, MESIM). – MEMI Technical Report 4. Meteorologisches Institut, KlimaCampus, Universität Hamburg 138pp.

SCHLÜNZEN, K. H., K. CONRADY, C. PURR, 2016: Typical performances of mesoscale meteorology models. – In: Air Pollution Modeling and its Application XXIV, Springer, 447–457.

SCHLÜNZEN, K. H., U. KRELL, 2004: Atmospheric parameters for the North Sea: a review. – Senckenbergiana maritima **34**(1-2), 1–52.

SCHOETTER, R., 2013: Can local adaptation measures compensate for regional climate change Ph.D. thesis, University of Hamburg, 69-77.

SCHOETTER, R., D. GRAWE, P. HOFFMANN, P. KIRSCHNER, A. GRÄTZ, K. H. SCHLÜNZEN, 2013: Impact of local adaptation measures and regional climate change on perceived temperature. – Meteorologische Zeitschrift **22**(2), 117–130.

Schroeder, G., K. H. Schlünzen, 2009: Numerical dispersion of gravity waves. – Monthly Weather Review **137**(12), 4344–4354.

Spensberger, C., 2010: Einfluss von Schiffsemissionen auf die Meereis-Albedo Master's thesis, University of Hamburg, 94 pp.

Spronken-Smith, R. A., T. R. Oke, 1998: The thermal regime of urban parks in two cities with different summer climates. – International Journal of Remote Sensing **19**(11), 2085–2104.

Spronken-Smith, R. A., T. R. Oke, W. P. Lowry, 2000: Advection and the surface energy balance across an irrigated urban park. – International Journal of Climatology **20**(9), 1033–1047.

Staiger, H., G. Laschewski, A. Grätz, 2012: The perceived temperature–a versatile index for the assessment of the human thermal environment. Part A: scientific basics. – International Journal of Biometeorology **56**(1), 165–176.

statista, 2017a: Bevölkerungswachstum in Deutschlands Grossstädten. – https://de.statista.com/statistik/daten/studie/160101/umfrage/bevoelkerungswachstum-in-deutschlands-grossstaedten/, date of last visit: 1 March 2017

statista, 2017b: Entwicklung der Bevölkerung von Hamburg seit 1961. – https://de.statista.com/statistik/daten/studie/155147/umfrage/entwicklung-der-bevoelkerung-von-hamburg-seit-1961/, date of last visit: 1 March 2017

Stütz, E., G. Steinfeld, D. Heinemann, J. Peinke, 2012: Parametrisierung von Windparks in COSMO. – Abstract METTOOLS VIII, Mitteilungen aus dem Institut für Meteorologie der Universität Leipzig 15 p.

Stubbenhagen, A.-L., 2017: Städtische Wärmesinsel im Winterklima - Modelluntersuchungen von Anpassungsmaßnahmen für Hamburg Master's thesis, University of Hamburg, 106 pp.

Taha, H., 1997: Urban climates and heat islands: albedo, evapotranspiration, and anthropogenic heat. – Energy and Buildings **25**(2), 99–103.

Takebayashi, H., M. Moriyama, 2012: Study on surface heat budget of various pavements for urban heat island mitigation. – Advances in Materials Science and Engineering **2012**, 11 pp.

THEEUWES, N. E., A. SOLCEROVÁ, G. J. STEENEVELD, 2013: Modeling the influence of open water surfaces on the summertime temperature and thermal comfort in the city. – Journal of Geophysical Research: Atmospheres **118**(16), 8881–8896.

UPPALA, S. M., P. KÅLLBERG, A. SIMMONS, U. ANDRAE, V. BECHTOLD, M. FIORINO, J. GIBSON, J. HASELER, A. HERNANDEZ, G. KELLY, OTHERS, 2005: The ERA-40 re-analysis. – Quarterly Journal of the Royal Meteorological Society **131**(612), 2961–3012.

VANOS, J. K., J. S. WARLAND, T. J. GILLESPIE, N. A. KENNY, 2012: Thermal comfort modelling of body temperature and psychological variations of a human exercising in an outdoor environment. – International Journal of Biometeorology **56**(1), 21–32.

VDI 3783 BLATT 16, 2015: Umweltmeteorologie; Prognostische mesoskalige Windfeldmodelle; Verfahren zur Anwendung in Genehmigungsverfahren nach TA Luft. – Berlin: Beuth Verlag

VERSEGHY, D. L., 1991: CLASS A Canadian land surface scheme for GCMs. I. Soil model. – International Journal of Climatology **11**(2), 111–133.

VON SALZEN, K., K. H. SCHLÜNZEN, 1999: A prognostic physico-chemical model of secondary and marine inorganic multicomponent aerosols I. Model description. – Atmospheric Environment **33**(4), 567–576.

VON SALZEN, K., M. CLAUSSEN, K. H. SCHLÜNZEN, 1996: Application of the concept of blending height to the calculation of surface fluxes in a mesoscale model. – Meteorologische Zeitschrift **5**, 60–66.

WANG, C., R. G. PRINN, 2010: Potential climatic impacts and reliability of very large-scale wind farms. – Atmos. Chem. Phys. **10**, 2053–2061.

WIESNER, S., 2017: HUSCO-Hamburg Urban Soil Climate Observatory. www.clisap.de/husco.

WIESNER, S., A. ESCHENBACH, F. AMENT, 2014: Urban air temperature anomalies and their relation to soil moisture observed in the city of Hamburg. – Meteorologische Zeitschrift 143–157.

YANG, L., D. NIYOGI, M. TEWARI, D. ALIAGA, F. CHEN, F. TIAN, G. NI, 2016: Contrasting impacts of urban forms on the future thermal environment: example of Beijing metropolitan area. – Environmental Research Letters **11**(3), 034018.

You, J., D. G. Tarboton, C. H. Luce, 2014: Modeling the snow surface temperature with a one-layer energy balance snowmelt model. – Hydrology and Earth System Sciences **18**(12), 5061–5076.

Yu, C., W. Hien, 2006: Thermal benefits of city parks. – Energy and Buildings **38**(2), 105–120.

Zhou, L., Y. Tian, S. Baidya Roy, C. Thorncroft, L. F. Bosart, Y. Hu, 2012: Impacts of wind farms on land surface temperature. – Nature Climate Change **1505**, 1–5.

Eidesstattliche Versicherung

Hiermit erkläre ich, Marita Böttcher, an Eides statt, dass ich die vorliegende Dissertationsschrift selbst verfasst und keine anderen als die angegebenen Quellen und Hilfsmittel benutzt habe.

Einer Veröffentlichung dieser Arbeit stimme ich zu.

Hamburg, den 4. Juli 2017